UNIVERSITÀ
DEGLI STUDI
DI PADOVA

UNIVERSITA' DEGLI STUDI DI PADOVA

CENTRO INTERDIPARTIMENTALE "*Centro Ricerche Fusione*"

UNIVERSIDADE TÉCNICA DE LISBOA

JOINT RESEARCH DOCTORATE IN FUSION SCIENCE AND ENGINEERING

CYCLE XXIV (2009/2011)

PhD THESIS

DEVELOPMENT AND VALIDATION OF NUMERICAL MODELS FOR THE OPTIMIZATION OF MAGNETIC FIELD CONFIGURATIONS IN FUSION DEVICES

Coordinator :

Chiar.mo Prof. Piero MARTIN

Supervisor(s):

Chiar.mo Prof. Giuseppe Chitarin

Ing. Anton Soppelsa

Doctoral Student:
Ing. Nicolò Marconato

To Alice

Contents

Abstract

This thesis presents the work carried out in the context of two different activities, both involving development of Finite Element models for magnetic analysis regarding the optimization of fusion devices. In particular, the thesis deals with the design of the electrostatic accelerator of the ITER Neutral Beam Injector (NBI) prototype and with the MHD active control system of the RFX-mod Reverse Field Pinch (RFP) experiment, respectively under construction and operating at Consorzio RFX in Padua.

ITER, the first fusion experimental reactor under construction in Cadarache, will be equipped with two NBIs, each of them capable to inject into the plasma up to 16.5 MW, by accelerating negative hydrogen or deuterium ions up to energy of 1MeV. The needs of very high voltages and of the use of negative ions represent the main issues relating to this new technology, and efforts have still to be spent in order to overcome them. Therefore, in this regard, the construction of a test facility housing the ITER neutral beam prototypes was deemed required. In the present status of advancement of the ITER neutral beam test facility PRIMA (Padova Research on Injectors Megavolt Accelerated), the design and optimization of several features relating both physics and engineering aspects required massive use of modelling tools. An important role in the ion source and accelerator physics is played by the magnetic field here present, which has to be determined and optimized accurately, and its distribution has also to be provided as input for physics simulation codes.

The analyses regarding the ITER NBI, carried out in the framework of Fusion for Energy grants for the final design of the source and accelerator prototype SPIDER (Source for Productions of Ions of Deuterium Extracted from a Radio-frequency plasma) and of the full NBI prototype MITICA (Megavolt ITER Injector and Concept Advancement), aim at optimizing the magnetic configuration inside the ion source and accelerator, in order to improve the performances in terms of ion beam optics and aiming, and to obtain an efficient filter for the extracted electrons. Several 2D and 3D models have been developed in order to assess different features, on different scales

of magnitude, from the local configuration inside a single aperture to the global non-uniformity effects near the external edges of the device. This has been fulfilled mainly by means of the commercial FEM software ANSYS®, which has allowed to chose between several formulations to perform magnetostatic analyses in presence of permanent magnets, ferromagnetic material and current bus-bars with rather complex geometry at the same time. In such condition the development and verification of the models was not straightforward. Auxiliary numerical tools have been also developed for specific post- processing purposes.

The second work presented in this thesis concerns the modelling of the electromagnetic response of the RFX-mod MHD active control system. RFX-mod, the world's largest RFP experiment, has the most complete and flexible (magnetic) feedback control system of MHD instabilities, made by 192 radial field coils fully covering the toroidal surface of the machine. Their independent power supplies, together with as many sensor coils inside the stabilizing copper shell, allow the implementation of advanced control scheme for the active stabilization of slow timescale MHD modes. The shell and the other conductive structures interposed between active coils and sensors introduce a dynamic behaviour in the input-output response of the system. Ths behaviour results strongly affected by the presence of 3D features, like the gaps required for the penetration of the axisymmetric field components, which introduce poloidal and toroidal mode coupling in the system response to an external magnetic field.

This activity has been carried out by the implementation of an optimized mesh of the system of coils and conductive structures, suited for the custom FEM software CARIDDI developed by CREATE consortium, and by the following derivation of the state-space representation of this model. Large part of the work has been accomplished through the implementation of Matlab® routines required for building the mesh and for pos-processing purposes. There are three main results of this activity. The first is the in-depth understanding of the symmetry properties of the machine. The second is the implementation of a new control algorithm based on the developed model able to compensate in real time the effect introduced by the 3D wall. The third is the proposal of a new measurement cleaning algorithm to be introduced in the control scheme, again based on the developed model and therefore, contrary to the presently implemented one, able to take into account the actual toroidal geometry.

The thesis is organized as follows:

- **Chapter 1** contains an overview on the advancements of the research and technology of nuclear fusion as possible sustainable energy source for the future. In the context of the current word energy source availability, the nuclear fusion is introduced. Some fundamental physics and engineering concepts are presented, together with the progresses obtained in the latest years, leading to the ITER project. In this framework, the concept and available technology about plasma heating is described, with a particularly detailed description of the NBI, anticipating topics required for a good understanding of the PhD work described in further chapters. A description of the RFX-mod experiment is also given, in order to introduce concepts related to the second subject of this dissertation.
- **Chapter 2** focuses on the mathematical formulations at the basis of the numerical solution of magnetic problems. The several magnetic formulations are described with the twofold purpose of underling the wide range of methods suited to solve particular cases and of providing references for the following paragraphs and chapters. Few words are spent to describe the edge-element approach to finite element methods and its advantages. Finally a brief description of both the ANSYS® and CARIDDI code is given.
- **Chapter 3** deals with the development of FEM models for the optimization of the magnetic field configuration in the extraction and accelerator area of SPIDER. First a description of the magnetic sources and the aim of the optimization are given. Then the optimization procedure made by 2D models is reported. Finally the assessment of the optimized configuration with 3D model and its final implementation, together with the new features introduced are described.
- In **chapter 4** the work done for MITICA is discussed. The several alternative magnetic design concepts considered are described and compared.
- **Chapter 5** presents the modelling activity done on the RFX-mod MHD active control system. A brief description of the system is recalled and the effect of the conductive structure on shaping its response, together with the concept of modal decoupler is introduced. Then the procedure to derive the state-space representation from the FEM model determined with the CARIDDI code is reported. The optimization of the mesh and the experimental benchmark of the results take up a large part of the chapter. Then the development and implementation of the so called modal decoupler is described in detail,

and some preliminary experimental results are shown. In the last paragraph, a new measurement cleaning algorithm based on the developed toroidal model is proposed.

- Finally, **chapter 6** summarizes the results obtained, providing some conclusions and suggesting some future developments.

Prefazione

Questa tesi espone il lavoro realizzato nell'ambito di due diverse attività, entrambe riguardanti lo sviluppo di modelli magnetici agli elementi finiti per l'ottimizzazione di macchine per la fusione. In particolare gli argomenti trattati riguardano la progettazione dell'acceleratore elettrostatico del prototipo di Iniettore di Neutri (NBI) per ITER e del sistema di controllo attivo delle instabilità MHD di cui è dotato l'esperimento RFX-mod in configurazione Reverse Field Pinch (RFP), rispettivamente il primo in costruzione e il secondo già operante al Consorzio RFX a Padova.

ITER, il primo reattore sperimentale a fusione in costruzione a Cadarache (Francia), sarà dotato di due NBI, ciascuno in grado di iniettare nel plasma fino ad una potenza di 16.5 MW, mediante l'accelerazione di ioni negativi di idrogeno o deuterio con energia fino a 1MeV. La necessità dell'impiego di tensioni così elevate e dell'uso di ioni negativi costituisce la principale difficoltà per lo sviluppo di questa giovane tecnologia, difficoltà che richiede ancora molti sforzi per essere superata con successo. La realizzazione di una facility per testare un prototipo dei vari componenti che costituiscono l'iniettore è pertanto considerata necessaria. Allo stato attuale di avanzamento nella realizzazione di tale facility, chiamata PRIMA (Padova Research on Injectors Megavolt Accelerated), il progetto e l'ottimizzazione di diversi aspetti, sia di fisica che d'ingegneria, richiedono un massiccio utilizzo di codici di simulazione.

Un ruolo molto importante nella fisica della sorgente e nell'acceleratore di ioni è giocato dal campo magnetico * presente, il quale deve essere pertanto accuratamente determinato e ottimizzato, e la cui distribuzione deve poter essere disponibile come input per altri codici di simulazione. Le analisi relative all'NBI di ITER, realizzate nell'ambito di contratti con Fusion for Energy per il progetto definitivo del prototipo di sorgente e acceleratore SPIDER (Source for Productions of Ions of Deuterium Extracted from a Radio-frequency plasma) e del prototipo completo MITICA (Megavolt ITER Injector and Concept Advancement), sono finalizzate all'ottimizzazione della configurazione magnetica all'interno della sorgente e dell'acceleratore di ioni, al fine di migliorare le loro performance in termini di ottica e direzione del fascio, e per

ottenere un'efficiente filtraggio degli elettroni congiuntamente estratti. Sono stati realizzati alcuni modelli 2D e 3D per valutare diversi aspetti, su differenti scale di grandezza, dalla configurazione locale all'interno di un singolo foro delle griglie alla disuniformità globale ai bordi di queste. Ciò è stato svolto principalmente mediante l'uso del software FEM commerciale ANSYS®, il quale permette di scegliere tra numerose formulazioni per la realizzazione di analisi magnetostatiche, anche con la contemporanea presenza di magneti permanenti, materiali ferromagnetici e conduttori di corrente con geometrie complesse. In tali condizioni, infatti, lo sviluppo e la verifica dei modelli non sono affatto immediati. Sono inoltre stati sviluppati strumenti numerici ausiliari utilizzati in fase di post-processing.

Il secondo lavoro illustrato in questa tesi riguarda la modellizzazione della risposta elettromagnetica del sistema di controllo attivo MHD di RFX-mod.

RFX-mod è il più grande esperimento in configurazione RFP attualmente presente al mondo ed è dotato del più completo e flessibile sistema di controllo (magnetico) attivo delle instabilità MHD, costituito da 192 bobine di campo radiale che ricoprono interamente la superficie toroidale della macchina. Ognuna di esse è alimentata indipendentemente e ad ognuna corrisponde un sensore di campo radiale posizionato all'interno della scocca stabilizzatrice in rame. Tale sistema permette l'implementazione di avanzati schemi di controllo feedback per la stabilizzazione attiva dei modi MHD caratterizzati da dinamiche troppo lente perché siano stabilizzati passivamente dalla scocca conduttrice. Questa, insieme alle altre strutture conduttrici interposte tra bobine attuatrici e sensori, introduce un comportamento dinamico nella risposta input-output del sistema. Tale dinamica risulta fortemente influenzata dalla caratteristica tipicamente 3D delle strutture conduttrici, in particolare dovuta ai tagli necessari per la penetrazione delle componenti di campo assialsimmetriche, i quali introducono accoppiamenti modali poloidali e toroidali nella risposta del sistema ad un campo magnetico esterno.

Quest'attività ha previsto la realizzazione e ottimizzazione di una mesh del sistema di bobine e strutture conduttrici, adatta al codice FEM CARIDDI sviluppato dal consorzio CREATE, e dalla successiva derivazione di una rappresentazione state-space del modello ottenuto. Buona parte del lavoro è stata impiegata nell'implementazione di routine Matlab® sviluppate per la costruzione della mesh e per fini di post-processing. Tale attività ha portato a tre principali risultati. Il primo è stato l'approfondimento della comprensione delle proprietà di simmetria che caratterizzano la macchina. Il secondo è stato l'implementazione di un nuovo algoritmo di controllo basato sul

modello sviluppato, in grado di compensare in tempo reale l'effetto introdotto dalle strutture 3D. Per ultimo, si è arrivati alla proposta di un nuovo algoritmo di ripulitura delle misure da introdurre nello schema di controllo, anch'esso basato sul modello sviluppato e per questo in grado di tener conto dell'effettiva geometria toroidale, a differenza di quello attualmente utilizzato che si basa su un modello cilindrico.

La tesi è organizzata come segue:

- Nel **capitolo 1** è presentata una panoramica sui progressi della ricerca e della tecnologia per lo sviluppo della fusione nucleare come possibile fonte di energia sostenibile per il futuro. La fusione nucleare viene considerata nel contesto dell'attuale disponibilità di risorse energetiche nel mondo. Vengono poi richiamati alcuni concetti fondamentali di fisica ed ingegneria, insieme ai progressi ottenuti negli ultimi anni che hanno portato al progetto internazionale ITER. In quest'ambito sono inseriti il concetto e le metodologie per il riscaldamento del plasma, con una descrizione più dettagliata del NBI e dello stato dell'arte, anticipando concetti necessari alla comprensione del lavoro di dottorato descritto nei capitoli successivi. È fornita inoltre una breve descrizione dell'esperimento RFX-mod, anche questa necessaria per introdurre concetti relativi al secondo soggetto della tesi, descritto nell'ultimo capitolo.
- Il **capitolo 2** si focalizza sulle formulazioni matematiche alla base della soluzione numerica di problemi magnetici. Le diverse formulazioni vengono elencate con il doppio scopo di evidenziare la grande varietà di metodi adatti a risolvere casi specifici e di fornire riferimenti a quanto trattato nei seguenti paragrafi e capitoli. Qualche parola è spesa anche per descrivere l'approccio edge-element nel metodo degli elementi finiti e i vantaggi connessi al suo utilizzo. Infine è fornita una breve descrizione dei software ANSYS® e CARIDDI.
- Il **capitolo 3** tratta del lavoro relativo ai modelli FEM sviluppati per l'ottimizzazione della configurazione magnetica nella regione di estrazione ed accelerazione di SPIDER. Inizialmente vengono descritte le sorgenti magnetiche presenti e successivamente la procedura di ottimizzazione mediante modelli 2D. Infine vengono descritte la verifica della configurazione ottimizzata mediante modelli 3D, la sua definitiva implementazione e le novità introdotte.

- Nel **capitolo 4** è riportato il lavoro svolto per la configurazione magnetica dell'esperimento MITICA. I diversi concetti di design alternativi presi in considerazione sono descritti e confrontati. Alla fine si propone quella che è ritenuta la soluzione più performante.
- Il **capitolo 5** presenta l'attività di modellizzazione sul sistema di controllo attivo MHD di RFX-mod. Viene prima richiamata una breve descrizione del sistema e poi vengono introdotti gli effetti delle strutture conduttive nell'influenzarne la risposta, insieme al concetto di disaccoppiatore modale. Successivamente è descritta la procedura per derivare la rappresentazione state-space dal modello determinato con il codice CARIDDI. L'ottimizzazione della mesh e il benchmark sperimentale dei risultati occupano gran parte del capitolo. Vengono poi descritti dettagliatamente lo sviluppo e l'implementazione del cosiddetto disaccoppiatore modale e sono esposti alcuni risultati sperimentali preliminari. Nell'ultimo paragrafo è descritto il nuovo algoritmo di ripulitura delle misure che viene proposto.
- Il **capitolo 6**, infine, riassume i risultati ottenuti, fornisce le conclusioni e suggerisce alcuni possibili sviluppi futuri.

1 Introduction

This chapter wants to introduce the basic concepts about the possible exploitation of nuclear fusion power as one of the alternatives to cover the increasing energy demand of the world, as well as some of the most critical issues of the research in this field, without any claim of completeness. The intention is to give the minimum information required to set this PhD work in the context of fusion research.

First a very brief overview on the energetic problem will be given, then the current development of nuclear fusion technology will be described, with particular attention to the ITER project, representing the next step in the near future of fusion research. Here a section dedicated to give a background of the neutral beam injection as one of the possible auxiliary systems required to start the fusion reaction is introduced, constituting one of the main arguments of this PhD thesis. Finally the distinctive features that make RFX-mod, a smaller machine currently working in Padua, one of the most advanced experiment for the active control of MHD plasma instabilities will be set out in order to provide the context where the second PhD activity, described in the last chapter, is inserted.

1.1 The World Energy problem

During their evolution, humans have ever increased their own energy consumption as a result of both the population growth and the progress of the technology. Starting from the primary energy source, consisting on the food, humans learned to exploit other sources of energy in order to go beyond the mere survival, increasing their intellectual progress and well-being. During the most of the human history, the exploited sources of energy can be considered renewable sources, whether these are the animal power, the fire from biomass, the wind or water power. However,

everything changed after the so called industrial revolution, when humans learnt to take advantage of the higher power density released in the combustion of the hydrocarbons and later in the fission of the uranium. This technologic revolution has doubtless led to a progress and well-being level unheard-of, culminating in an exponential population growth, but it entailed also a number of issues which today must be taken into account with the utmost seriousness by all the world countries. Two are in particular these issues, but several the implications: the resources of fossil fuel and uranium are limited, and both the carbon dioxide (CO_2) emissions due to the combustion and the radioactivity which can be released during accidents in nuclear power plants or in nuclear waste repositories heavily weigh on the climate and the environment.

Leaving out arguments about the sustainability of the development model currently adopted by industrialized and emerging countries, but highlighting the concept of the fundamental importance of efficiency and energy savings, it is possible to say that human development is closely related to energy consumption. Several studies in this regard, as for instance [1], evidence there is a clear correlation between the per capita electricity consumption and human development as measured by the Human Development Index (HDI), a measure of human well-being compiled annually by the United Nations for each country which takes into account figures like life expectancy, literacy and Gross Domestic Product (GDP).

Except for coal, the supply of gas and oil at present rate of consumption will last in few decades and geopolitical crises, such as the gas crisis between Russia and Ukraine in 2006 and a possible future oil crisis, make the energy supply of many countries even more precarious. If the models of the energy generation mix for the near future forecasted in the recent years foresee an increased employment of nuclear energy, referring in this case to the only mature technology of conventional nuclear fission, they probably would be revised taking into account the effect on the public opinion of the world's second-worst nuclear accident occurred at Fukushima in 2011.

The renewable energies represent the most long term alternative, including wind power, hydroelectric power, tidal power, combustion of wood and biomass, geothermal power and solar energy. Unfortunately, even if they will contribute much more in the future, thanks to likely future cost reduction, improvements on efficiency and on energy storage systems, which are required to assure continuity by most of renewable sources, they are not expected to be able to satisfy the total demand.

In this context, two are the carbon-free technology which could assure respectively a middle-long and very long term power supply able to maintain current consumption rates and those of developing countries: Generation-IV fission reactor and fusion reactor. The former technology can extract at least 50 times more energy than current fission reactors from a given quantity of uranium, thanks to the exploitation of a closed fuel cycle, involving repeated recycling though reprocessing of discharged spent fuel in order to remove fissile material, which consequently allows also to reduce the amount of waste. The latter has the potential to provide a sustainable, large-scale and intrinsically safe solution to global energy needs, using fuels that are universally available.

Their technical and economical feasibility remains to be proven, but the current circumstances may drive an acceleration on their achievement.

1.2 Thermonuclear fusion

As already mentioned, nuclear fission is not the only process able to free energy from atoms. Nuclear fusion is the inverse process by which a couple of atomic nuclei join together to form a heavier one. The nuclear energy production exploits the unbalance between the mass of the reactants with respect to the reaction products, according to the Einstein relationship $E = mc^2$, where E is the released energy and Δm the mass defect between the reactant and product. This mass defect results in a production of energy, as the atoms are bound together or split as a consequence of the reaction. If the nuclear mass of the product element is less than that of iron (Fe), which corresponds to the peak of the binding energy curve, then the nuclear particles will be more tightly bound than they were in the lighter nuclei; vice versa for elements heavier than iron. This is the reason why the two inverse nuclear processes exist.

Nuclear fusion reactions happen naturally in the stars, where high temperature and pressure allow hydrogen nuclei to get close enough for the short-range attractive nuclear (strong) force to bind them together overcoming by quantum tunneling the Coulomb repulsive force. This is possible if the two reactants collide with high enough thermal energy, hence the name thermonuclear fusion. It is usually specified in contrast with the so called cold fusion, where the problem of winning the Coulomb barrier is faced by means of other effects.

For a significant fraction of fusion reactions to occur, matter has thus to be brought to high densities and temperatures for a sufficiently long time; conditions which in stars are created by

the gravitational force. In such conditions, matter is in the plasma state, a fully ionised gas entirely made of electrons and positive ions freely moving in the space, resulting in a macroscopically neutral mean.

Apart from the gravitational confinement, there are other two methods which can be exploited to recreate the required conditions of temperature and pressure for the thermonuclear fusion reactions to happen. One is based on the momentum conservation and it is called inertial confinement, the other is based on the Lorentz force and therefore it is called magnetic confinement.

The magnetically confined thermonuclear fusion relies just on the fact that at the working conditions the reactants are in the plasma state. As a matter of fact, charged particles interact with the magnetic field through the Lorentz's force and for this reason they can actually be confined by a properly shaped magnetic field. Macroscopically, an ionised gas at high temperature is a good conductor which can be subjected to a flow of electric current. The interaction between this current and the surrounding magnetic field gives rise to the confining force.

Among the several possible nuclear fusion reactions, the most favourable one for being achieved on the earth is the fusion between deuterium D^+ and tritium T^+ nuclei, which are the two hydrogen isotopes; the first widespread in nature, while the second is unstable with a half-life of 12 years. Indeed, the cross section for the deuterium-tritium reaction is so that it can balance the radiative losses of a confined plasma with the given density at the lowest possible temperature.

Interest on nuclear fusion stems from its positive features relative to both the environment preservation and the availability of fuel. As a matter of fact, a future reactor would be intrinsically safe since, contrary to fission, conditions for fusion reactions to occur require an input power which can be interrupted at any time in case of failure or accident. Radioactivity is limited to that of tritium, which would be produced by neutron reaction of lithium and consumed in situ within a closed loop, and of the short-term activation of the structural material. Deuterium and lithium are abundantly widespread on Earth, in particular in sea water.

Research into the field of plasma physics began in the 1950s and still continues to this day. Since its beginning, the research activity in the field of magnetically confined thermonuclear fusion has been tightly linked with the development of the machines used for the plasma confinement inside their vacuum chamber. Over the years several machines, corresponding to several different magnetic configurations, have beenbuilt and tested. The most successful have proved to be those

based on toroidal geometry, which are free from the problem of losses at the ends of the linear configuration, at the expense of a greater complexity. Together with complexity, also the size of such devices has grown gradually, from the initial major radius of about half a meter to the several meters of the current biggest devices, in order to reduce the losses per unit plasma volume.

Presently the Tokamak, the Stellarator and the Reversed Field Pinch (RFP) magnetic configurations are in use. All of them share the toroidal concept but the magnetic configuration is rather different. The magnetic field is always arranged in order to obtain helical field lines whose goal is to contain the losses of particles, but how this is obtained varies among the configurations. In Tokamaks and Reversed Field Pinches a toroidal current is induced in the plasma as if it is the secondary winding of a transformer and a toroidal field is applied with convenient toroidal field coils. Poloidal field windings are used to introduce a magnetic field component required to control the plasma shape and position. However the two configurations differ in the intensity of the toroidal component with respect the poloidal one: while they are comparable in RFP, the first is about ten times higher in Tokamak. Moreover, in RFP the toroidal field change sign moving from the plasma centre along its minor radius.

Stellarators are indeed quite different because they do not make use of an induced toroidal current to confine the plasma. This naturally allows for operations in steady state, but on the other hand this configuration requires the design and building of coils with complex, non-planar shapes.

Today the research in the field of magnetically confined thermonuclear fusion is carried out at Universities, Laboratories and Research Centres all around the world. The operating machines where it is possible to perform experimental exploitation of magnetically confined plasmas are now a few tens and other machines are currently being build. The research reported in this document has been carried out at Consorzio RFX in Padova, where a RFP upgraded machine is present, namely the Reversed-Field eXperiment (RFX-mod). Consorzio RFX has also been selected for developing and testing the prototype of the negative ion driven Neutral Beam Injector (NBI) for the international project ITER, which will be the world's largest and most advanced experimental Tokamak nuclear fusion reactor with the aim of demonstrating the feasibility of the technology.

1.2.1 MHD theory and plasma stability

The simplest physics model of the behavior of magnetically confined plasmas is the so called *magnetohydrodynamic* (MHD) theory. This academic discipline studies the macroscopic behaviour of electrically conducting fluids immersed within magnetic field. The starting point of the theory is a set of equations comprehensive of the Navier-Stokes equations of fluid dynamics, the Maxwell's equations of electromagnetism and a plasma state equation involving the thermo-dynamical quantities. Depending on the applications, this set of equations can be already too much to explain the basic plasma dynamic in a magnetic field. Different simplifying assumptions can be made and several suited theories are derived to study different physics aspects. One of the most important simplifications is to consider the plasma resistivity equal to zero, which leads to the so called *ideal MHD*. In this case the plasma becomes a perfect conductor able to freeze the magnetic field lines in their original configuration. Depending on the working hypothesis, other names are commonly in use; for instance, *resistive MHD* considers the plasma resistivity, and *two-fluid MHD*, where ions and electrons are treated as different fluids.

However, even the most general MHD theory has limits. This model requires a Maxwellian distribution of the particles forming the fluid to be applicable. Since in fusion plasmas the mean free path of the particles can be as big as thousand times the size of the machine, this hypothesis is not automatically verified. This could be the reason why macroscopic phenomena exist which cannot be explained by a fluid theory. Efforts are spent in developing a more effective and inclusive kinetic theory, able to take into account, for example, the effects of a non Maxwellian distribution of the plasma particles.

However, the ideal MHD remains almost invariably the first model considered by experimental physicists and engineers because of its simplicity and ability of capturing many of the important properties of plasma dynamics, and being often also qualitatively accurate.

Ideal MHD theory can provide quite accurate information when applied to analyze the plasma behaviour in the neighbourhood of a given equilibrium state. A plasma is in equilibrium if no net forces are acting macroscopically accelerating any part of it. If the equilibrium is stable to a small perturbation, the plasma would react in order to go back in the original configuration. If not it will grow, eventually causing the collapse of the magnetic configuration, the lost of the confinement and the premature end of the discharge. Therefore, the understanding and control of the plasma instabilities is one of primary issue to achieve magnetically confined fusion reaction.

The plasma instabilities which can be predicted by and analyzed with the help of the MHD theory are called MHD instabilities. Examples of these instabilities are the resistive wall mode (RWM) instability and the neoclassical tearing mode (NTM) instability. If a plasma were within a continuous and perfectly conductive chamber, every movements of it would be counteracted by the actions of the eddy currents induced in the chamber walls. If instead the chamber is not perfectly conductive, the counteraction intensity decays with a timescale related to the chamber resistivity; this is the case of the NTMs, which therefore develop in a relatively long timescale. On the contrary, RWMs develop in a timescale linked to the plasma resistivity and therefore are much faster.

An example of a more trivially contollable instability is the vertical instability affecting Tokamaks with elongated, non-circular plasma profiles.

1.3 ITER

At the present time, the most promising configuration to achieve a fusion reactor is the Tokamak, whose name came from the Russian acronym standing for toroidal chamber with magnetic coils. Indeed, it results in a much more stable plasma configuration with respect the RFP, to be set up with a much more simpler machine than Stellarator. This is the reason way, since toroidal geometry configurations have been studied in the russian laboratories in '60 and '70, the Tokamak became the dominant concept in the fusion research community and currently it is the most advanced. It has allowed to achieve the best performance in terms of confinement time, which is a measure of the rate at which the plasma loses energy to the environment defined as the ratio between its energy content and losses, and to get some power from fusion reaction. In this regard, it is defined *fusion gain factor* the quantity $Q = P_{fus}/P_{aux}$, where P_{fus} is the fusion power and P_{aux} the power needed by auxiliary systems to heat and maintain the plasma. The best performances have been achieved in the Joint European Torus (JET) experiment in 1997, corresponding to a factor $Q = 0.7$. JET is a project run in the framework of the European Fusion Development Agreement (EFDA) by the United Kingdom Atomic Energy Agency (UKAEA) at Culham, in the United Kingdom, and currently it is the world's largest Tokamak device. The large experimental database obtained in the last decade with JET and tens of experiments all around the world, together with improving capability of numerical simulations, have provided the international community the physics basis for designing a burning plasma experiment based on the Tokamak concept, called ITER. The name is the acronym for International Thermonuclear Experimental Reactor, since it is a collaborative project which foresees the participation of most of the industrialized countries involved in fusion research. On November 21, 2006, the seven participants (European Union, Japan, Russian Federation, People's Republic of China, South Korea, India and United States of America) formally agreed to fund the project, whose program is anticipated to last for 30 years – 10 years for construction and 20 years of operation. The site preparation is in progress and the first plasma operation is expected in 2019. In Table 1 the main ITER characteristics are reported.

ITER Parameters		
Fusion Power	500	[MW]
Fusion Gain Factor (Q)	≥ 10	
Major Radius	6.02	[m]
Minor Radius	2	[m]
Machine Height	26	[m]
Machine Diameter	29	[m]
Plasma Volume	837	[m^3]
Maximum toroidal feld	5.03	[T]
Plasma Current	15	[MA]
Pulse length	≥ 400	[s]

Table 1: Main Parameters of the ITER Tokamak.

ITER is going to be built in order to investigate burning plasma conditions presently not yet explored and to test several technological issues required for a future commercial reactor able to output energy to be converted in electricity. The principal aims of ITER are:

- the fusion of 0.5 g of deuterium/tritium mixture in its approximately 840 m^3 reactor chamber;
- to achieve extended burn in inductively-driven plasmas, overcoming the so called breakeven point ($Q = 1$) with a gain factor $Q \geq 10$. This point must be demonstrated at nominal fusion power output of about 500 MW in so called conventional operating scenarios, which foresee a duration sufficient (≈ 400 s) to achieve stationary plasma conditions;
- to test the possibility of achieving steady state operation using non-inductive current drive with a ratio of fusion to input power of at least 5;
- to explore the possibility of high Q operation exploitation, if favourable confinement conditions can be achieved;
- to test several concept for breeding tritium by lithium modules exposed to neutron flux inside the plasma chamber;
- to test several technological issues in particular related to the first wall materials subject to highly localized heat loads and EM forces in presence of intense neutron fluxes.

The several parts forming the ITER machine have been assigned to be developed by the different parties of the project and in many case a same component is developed by several countries together, in order to help cooperation and synergies, sharing knowledge acquired by each one.

ITER is predicted to produce inductively driven D-T plasmas. These plasmas will have a density $n_e \approx 10^{20}$ and core electron and ion temperatures respectively of $T_e \approx 8.8$ keV and $T_i \approx 8$ keV. New physics regimes and a variety of technological issues will be explored with ITER. For example, the effect of having a high quantity alpha particles produced by the fusion reactions contributes significantly to the plasma pressure, with the relating plasma instabilities which can be studied in depth for the first time in this new device. Furthermore, as already mentioned, a variety of technological issues will also be studied in ITER, like the test of advanced materials facing very intense heat and neutron fluxes, the test of concepts for tritium breeding, the superconducting technology under high neutron flux and many others.

Again, ITER will be a test bed for the auxiliary and control systems needed to achieve the conditions expected to be required for a fusion reactor. In ITER an external heating and current drive capability of 73 MW will be available, shared among 2 NBI for 16.5 MW each, an Electron Cyclotron Resonant Heating (ECRH) system and a Ion Cyclotron Resonant Heating (ICRH) system for 20 MW each. At most only two of these technologies it is deemed can be chosen for a future reactor. Several advanced diagnostics will be installed for both analysis and plasma control.

ITER is considered to be the last experimental device to solve many of the scientific and engineering issues concerning a burning plasma, which will demonstrate a Tokamak can get to be a power plant.

1.3.1 Auxiliary Heating and Current Drive

In order for fusion reactions to occur, the confined plasma must be brought to extremely high temperature, of about 10 keV. In Tokamak plasmas the temperature is intrinsically raised by the plasma current through ohmic heating. So the generated heat depends on the resistance of the plasma and on the intensity of the current. Unfortunately, in a Tokamak the required temperature cannot be achieved by ohmic heating, since as the temperature of heated plasma rises, its resistance decreases and the plasma current is limited by the toroidal field, in turns limited by technological restrictions. The maximum plasma temperature which can be reached by ohmic heating in a tokamak seems to be about 2 keV. Therefore, additional heating systems are required to achieve the goal of 10 keV.

Two are the possible solutions. One way, called radiofrequency heating, is the exploitation of the resonance of electromagnetic waves with the plasma to radiate power inside it. Radiating waves

with particular frequency coinciding with characteristic frequencies of the plasma, the electromagnetic power associate to the wave is transferred to the charged particles, which in turn collide with other plasma particles increasing its overall temperature. The second option, called neutral beam injection, foresees to fire very energetic particles into the machine, where they will transfer their momentum to the plasma particles by collisions. It is worth noticing that both these methods are also able to drive the plasma current, hence they are useful to control and optimize the plasma current profile and to contribute to sustain the plasma current during long-pulse/steady state advanced operating scenarios. A schematic of plasma heating and current drive systems is reported in Figure 1.

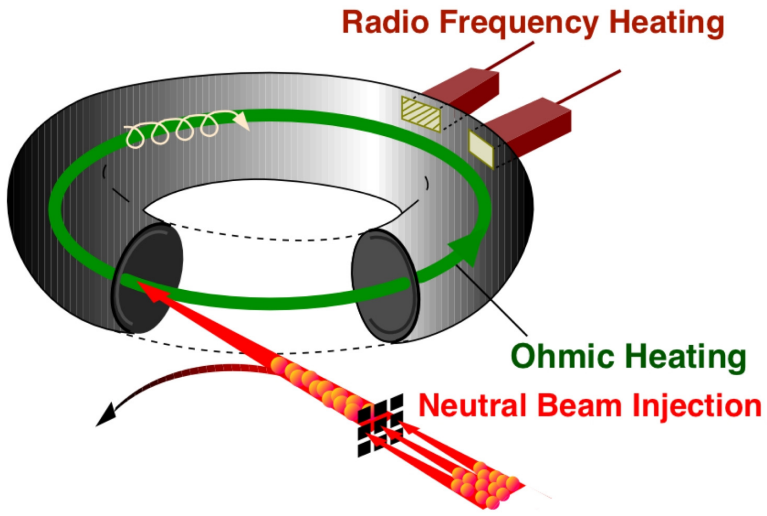

Figure 1: Schematic of an heating and current drive system featuring radiofrequency antennas and neutral beam injection

The neutral beam injection heating will be treated more in detail in the next paragraph, being one of the topics of this thesis work.

1.3.2 Neutral Beam Injection

As already mentioned, a way to heat up a plasma to very high temperatures is by using a neutral beam injector (NBI). The name comes from the fact that the injected particles, in order to not be deviated by the magnetic field and so reach the plasma centre, need to be neutral particles. Since the injected particles have no charge they can penetrate the strong magnetic field devoted to confine the plasma, transfer their energy to plasma particles and thus increase the overall temperature by collisions. If injected tangentially with respect to the plasma column, such beam can be used to increase the efficiency of the current drive. Moreover, the use of NBIs has allowed to discover an enhanced confinement scenario, called H mode, causing the transition from the

(normal) lower level of confinement of the plasma, defined as L mode. H mode regimes exhibit edge transport barriers which allow to achieve higher core ion temperature and an increasing of the energy confinement time of roughly a factor two higher than in L mode.

An important issue of the NBI technology is that neutral particles cannot be accelerated, and this affects in particular high energy neutral beams, as it will be explain in the following. As a matter of fact, the only way to accelerate particles to the energy required to effectively heat the plasma is to exploit electromagnetic fields. Thus, in principle, positive or negative ions have to be produced inside an ion source. Then they are accelerated as an ion beam by means of strong electric field between different grids of an electrostatic accelerator. Once achieved the required energy, they are neutralized by charge exchange processes within a neutral gas stripper. The neutral beam is then deprived of the remaining not neutralized ions by means of strong magnetic field inside a so-called Residual Ion dump (RID), while the neutral beam proceed towards the Tokamak chamber. As the neutrals enter the plasma, they are gradually ionized, remaining trapped by the magnetic field of the device. The choice of the beam energy depends on the minor radius of the plasma and on its density: bigger and denser the plasma higher the energy in order to deposit most of the power at the plasma core. The ions created in the source can be either positive or negative; the choice depends on the beam energy. For low energy neutral beam injector positive ions are used, since they are more easily produced and the efficiency is not affected by the concurrent acceleration of electrons. In high energy neutral beam injectors instead the use of negative ions is compulsory, since the neutralization efficiency for positive ions sharply drops above energy of about 100 keV (depending on the species), as it is shown in Figure 2. On the contrary, for the negative ion beam the low binding energy of the additional electron (0.75 eV) enables an easy detachment of this electron, causing the neutralization efficiency to stay at about 60% even for the highest energies.

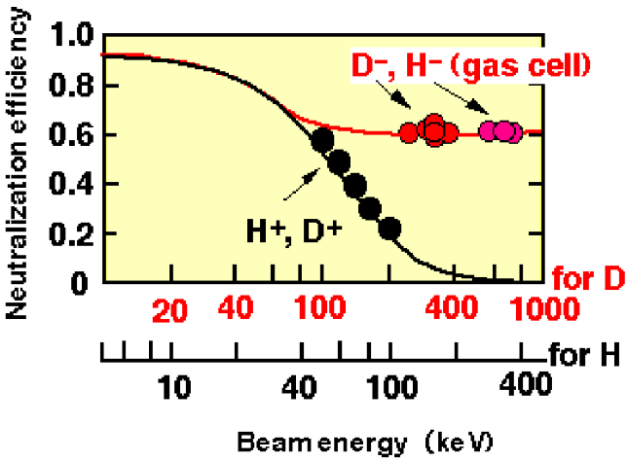

Figure 2: Neutralization efficiency for positive and negative deuterium and hydrogen ions against beam energy per nucleon

The development of negative ion-based NBI systems for fusion is progressing steadily, addressing and solving the issues found when increasing the required performance, and year after year there is an increasing confidence in this promising field: in 1992 the first complete negative ion-based beamline produced 100 kW of 100 keV D^0 beams in the framework of a collaboration between JAERI and CEA, 16 A of H^- were produced at Nagoya in 1994, and 40 mA H^- beams were accelerated to 700 keV at JAERI in 1995 [5]. After these successful small power injectors, large negative ion-based systems have been installed on the JT60-U Tokamak and on the LHD stellarator, achieving maximum parameters of 400 keV, 17.4 A and 180 keV, 34.5 A, respectively [6, 7, 8]. A negative ion-based system with two 1 MeV, 40 MW ion beamlines is proposed for ITER, in order to inject into its plasma two 16.5 MW neutral beams [9, 10].

1.3.2.1 Negative ion source

The attractive feature of negative ions to set up high energy neutral beam, their low electron affinity, is a drawback when production or acceleration is considered: firstly it is difficult to attach this additional electron; secondly many negative ions are destroyed ("stripped") by collisions with plasma or neutral particles before being extracted from the sources or accelerated to the final energy. The present higher performance has been obtained in particular from large caesium seeded sources. As a matter of fact, negative ions can be obtained through two distinct processes: volume production, which consists in the attachment to neutral particle of free electrons in the plasma, while surface production is the "jump" of electrons from the conduction band of metal surfaces surrounding the plasma toward the electron affinity level of the particle approaching the walls.

As far as the negative ion production by surface reactions on the plasma grid is concerned, the probability of electron capture during backscattering of hydrogen atoms or ions to the plasma grid depends on the work function of the surface and on the velocity of the impacting ions. The negative ion yield per *H* impact on a wall can be predicted by the following equation:

$$Y\left(H^- / H\right) = \exp\left(-\frac{\phi - A}{C \cdot v_\perp}\right) \tag{1.1}$$

where *C* is a constant, $v_\perp$ is the perpendicular velocity of the impacting ions to the wall and $\phi - A$ represents the energy difference between the Fermi level of the surface and the affinity level, which should be as small as possible to enhance the electron capture probability. The most widely used method to lower the surface work function of the source wall surfaces is to coat them with caesium, which indeed has the lowest work function of all metals (1.8 eV).

The volume production is given by a dissociative attachment of electrons to *H* molecules, described as:

$$H_2 + e = H^- + H_0 \tag{1.2}$$

The cross-section of this reaction is enhanced (up to a factor of five) when the hydrogen molecules are in high vibrational states. The energy needed in reactions to excite the hydrogen molecules is about 10eV, while the reaction 1.2 with excited electrons needs the capture of an electron with lower energy, about 1e; moreover the newly created H^- lifetime is greatly shortened by the presence of energetic electrons, which easily can destroy the negative ions. Therefore, negative ion sources are equipped with some kind of filter to separate two electron populations, depending on their energy. The first realization utilized a two chambers source structure (*tandem concept*), but then a simplest solution was preferred, constituting in using a transverse magnetic filter close to the plasma grid (*filter field*) to separate the two populations in the same chamber. The produced fast electrons are rejected back by the mirror effect due to the gradient of the magnetic filter field. On the contrary, cold electrons pass through the filter field lines more easily, being much more collisional. The direct consequence of this effect is that the average electron temperature falls rapidly with distance perpendicular to the filter field. The schematic of the process is reported in Figure 3.

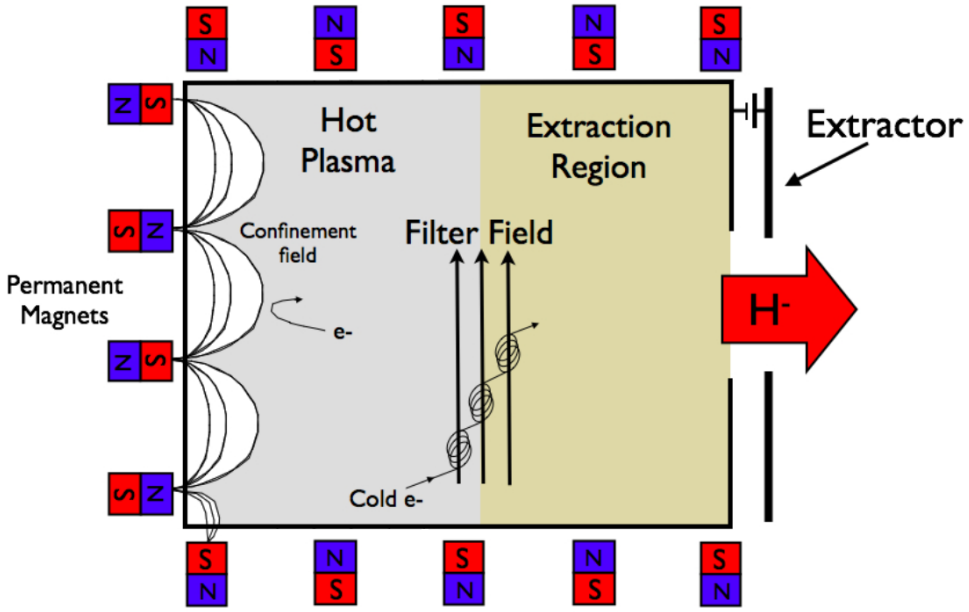

Figure 3: Schematic of a negative ion source. Note the presence of the confinement field produced by permanents magnets array devoted to limit the plasma to touch the source walls, and the filter field, preventing hot electrons to reach the extraction region.

Another issue which made more complex negative ion production with respect positive ions is the extracted current: the electric field acts both on the negative ions and on the electrons hampering the exit of former from the plasma. From the design point of view, this aspect has important consequences on the gap lengths, dimension and number of holes in the grids. The "reverse" electric field in the plasma sheath causes further complications in the design of the negative ion source; in order to extract the required negative current, it is necessary to provide a strong magnetic field in front of the plasma grid to filter the electrons from the main plasma; moreover, the plasma grid should be positively polarised with respect the plasma potential, in order to repel the positive ions that are present inside the plasma.

There are basically two different concepts to produce the plasma required as ion source: Arc sources and Radio Frequency (RF) sources.

In an arc source, electrons are emitted from a hot cathode and accelerated by a DC voltage typically of 100 V towards the source walls. The accelerated electrons ionize the gas molecules leading to the desired plasma.

The RF source concept utilizes the oscillating electric field induced by a RF coil in order to accelerate electrons to ionize the gas molecules. A typical frequency for RF sources is 1 MHz, with typical RF powers of 100 kW [11]. Main advantages of a RF source with respect to the arc source are:

- long lifetime due to the absence of filaments having a limited thermal cycle time;
- low cost due to the easy electrical insulation of the RF generators from the high potential plasma source walls;
- better control, during beam modulation, of the extracted ion current due to the fast response of the ion density in the source to changes of the RF input power; this makes active beam current control possible;
- reduced complexity of the source having less electrical connections compared to arc sources, making remote handling easier.

Due to these advantages, an RF source has been recently chosen as the reference design for the 1 MeV negative ion injectors of ITER.

1.3.2.2 Negative ion extraction and acceleration

The electrostatic acceleration of the ions is the more efficient solution to produce the large current values required by fusion NBIs. The ion acceleration can be distinguished in two steps: the extraction of the ions from the source and the following acceleration to full energy by other electrostatic steps.

The design of such an accelerator is an optimization process to get the best optic performance of the accelerated beam, constrained by the need to avoid electrical breakdowns and related high capacitive energy dissipation. As already mentioned, the design of negative ion accelerators, beside to be used in case of higher energies and so high voltages, has the further complication of dealing with co-extracted and stripped electrons.

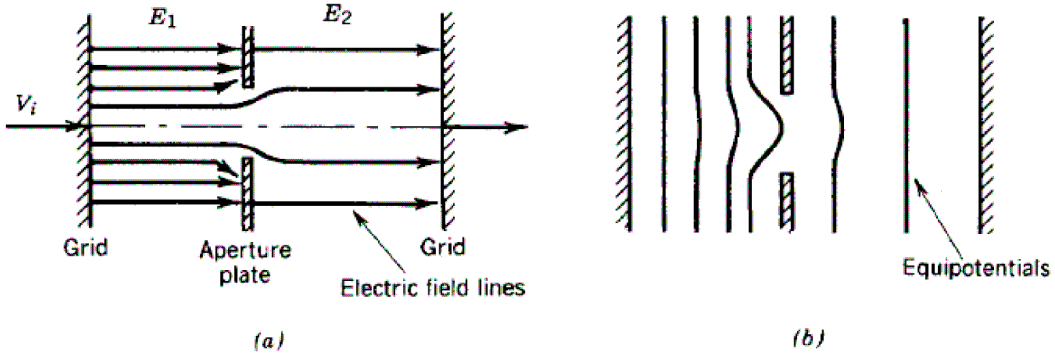

Figure 4: Electrostatic aperture lens, electric field (a) and equipotential lines (b).

The physics describing the electrostatic acceleration and beam focussing has some common points with geometric optics [12]. The aperture on a plate acts as a lens (see Figure 4) connecting

two regions with different electric field intensity with the same direction. This difference causes a curvature of the field lines which converges or diverges the accelerated beam (see Figure 5).

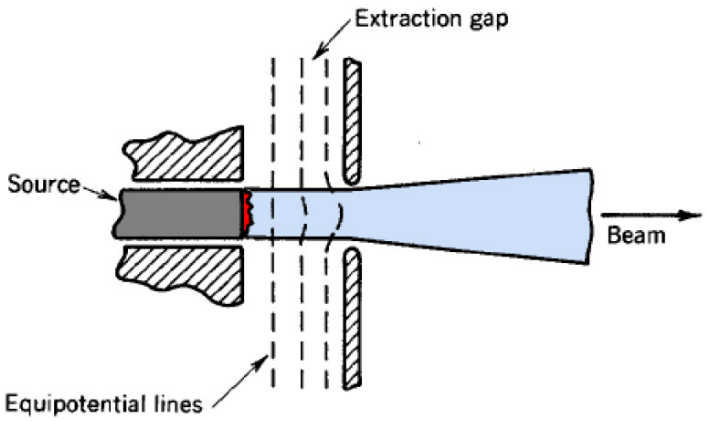

Figure 5: The negative (defocusing) lens.

A suitable choice of voltage and gaps between the grids allows transferring the required energy to the extracted beamlet with the proper focus.

An ion beam is typically composed of several beamlets, each of them being extracted from the ion source separately from the others. This is achieved by assembling a set of carefully aligned grids, in which a number of cylindrical or conical apertures are drilled. These grids are polarized at various voltages in order to create the desired electric field distribution. The geometry of the accelerating channels and the gaps between the grids are carefully designed to optimize beam optics.

The first grid, called Plasma Grid (PG), separates the source plasma from the accelerator. In the second grid, usually called Extraction Grid (EG), permanent magnets are inserted in order to deflect the stray electrons and to prevent them from being further accelerated. This magnetic field breaks the axial symmetry of the acceleration channel.

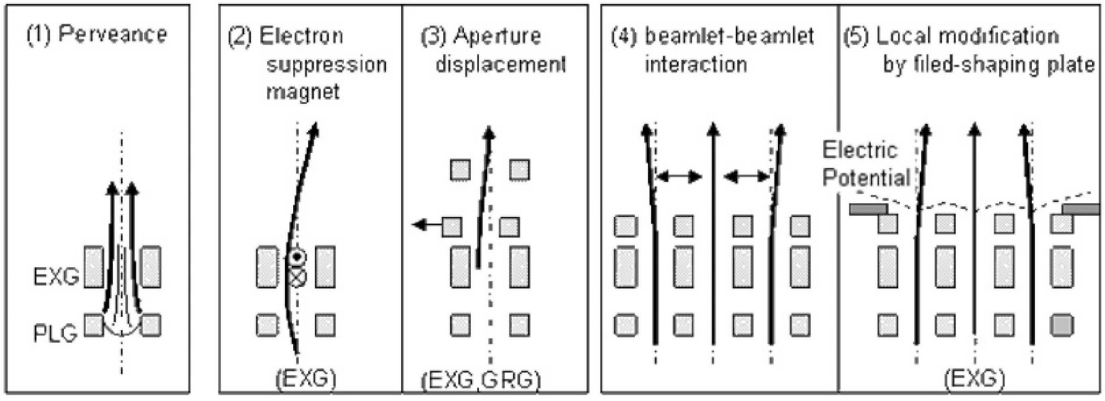

Figure 6: Main causes that influence beam optics.

In Figure 6 the main features that influence charged particle beam optics are shown, in detail it is possible to distinguish:

1. The perveance effect is related to the influence of spatial charge on the beam divergence.
2. The presence of magnetic field permanently deflects an accelerated beam.
3. Also aperture displacements deflect the beam path, particularly in the first stages being lower the particle velocity.
4. The beamlet-beamlet interaction is present due to the spatial charge effect between each beamlet.
5. A compensation for the beam aiming can be obtained by a local modification of the equipotential lines, in particular by inserting suitable plates downstream the extraction grid.

In order to increase the filter field inside the source, a DC current can flow through the plasma grid in the y direction: the superposition of this magnetic field with the field produced by the permanent magnets inside the source and embedded in the extraction grid produces a magnetic field that isn't uniform in space, resulting in a non-uniform beam with aberration. This aspect could lead to deposit the neutral beam power inside the device or in the duct connecting the NBI with the toroidal plasma chamber and as a consequence, to decrease the lifetime of the injector. This issue has been one of the main arguments of this PhD work and it will be described in detail in chapter 3 and 4.

A schematic picture of a RF source for negative ions is shown in Figure 7.

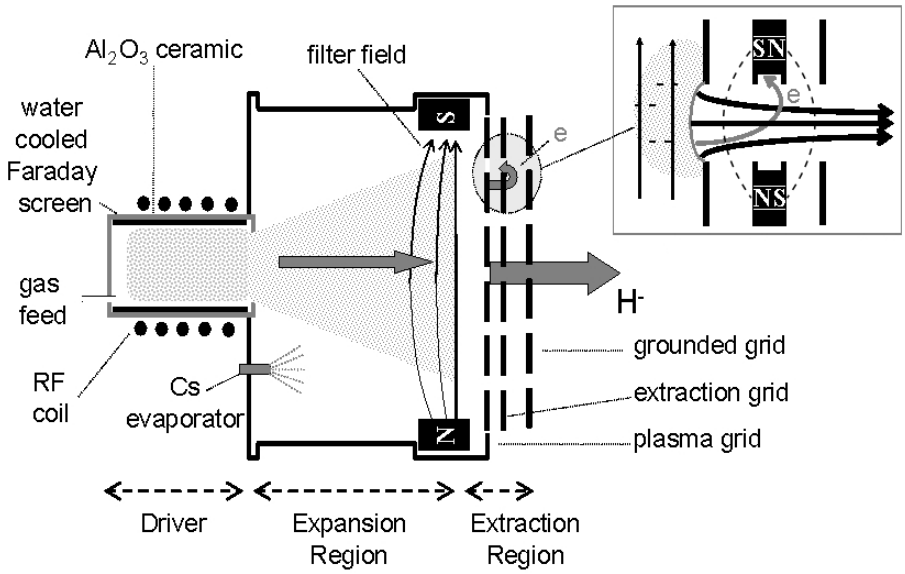

Figure 7: Schematic of the RF source for negative ions.

1.3.3 The ITER Neutral Beam Test Facility

In the framework of the activity planned by the ITER Organization for the research and development of the NBIs (design optimization, construction and operation), Consorzio RFX in Padova was chosen to host a test facility, called PRIMA (acronym for Padova Research on ITER Megavolt Accelerator), where the complete prototype will be built. It will include two experiments: a full size plasma source with a lower extraction voltage and a complete full size NBI, which should achieve the nominal power and voltage up to 1 MV. The first experiment is called SPIDER (acronym for Source for Productions of Ions of Deuterium Extracted from a Radio-frequency plasma) while the second is called MITICA (Megavolt ITER Injector and Concept Advancement).

1.3.3.1 SPIDER

SPIDER is the first experimental device which will be completed and operated, aimed at achieving the required performance in terms of current density, aiming and their uniformity, of a negative ion beam (made of H^- and in a later stage D^- ions) from an ITER size ion source. A sketch of its design is reported in Figure 8, while the main requirements are resumed in .

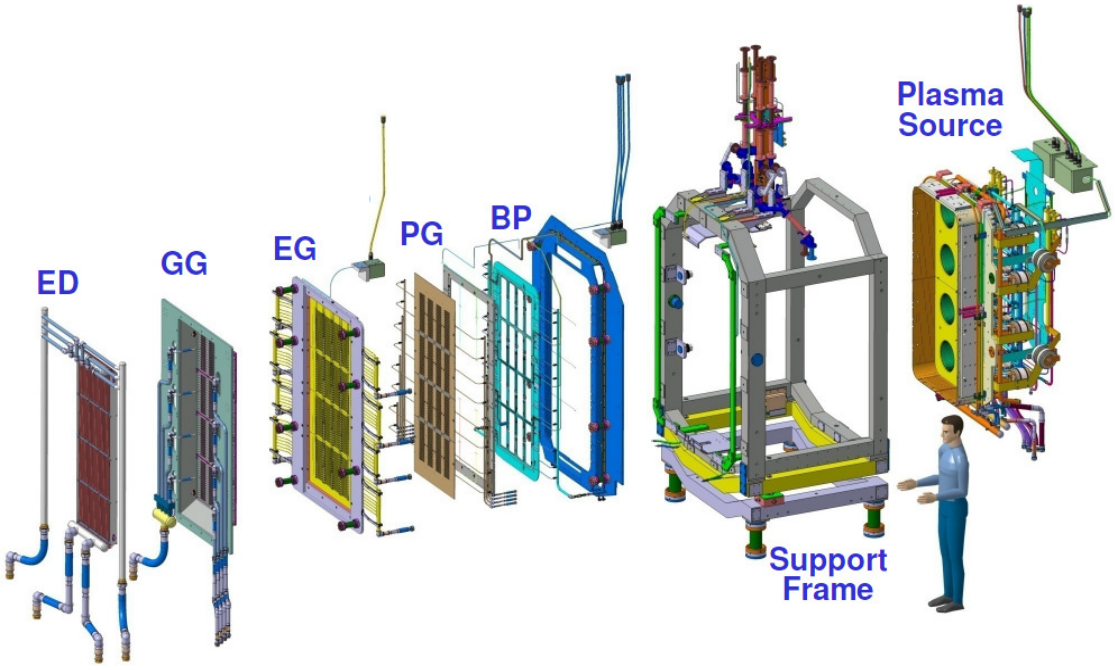

Figure 8: Exploded view of the SPIDER device.

The SPIDER device is composed by a radiofrequency (RF) ion source, an electrostatic accelerator and a target calorimeter. The extraction and accelerator system is composed of three grids: the Plasma Grid (PG), the Extraction Grid (EG) and the Grounded Grid (GG). The gap

between the grids and the aperture shape and diameter are important parameters to allow a proper focus to the extracted beam, which have been optimized in the design phase. The PG, which is the grid directly facing the plasma, is required to operate at a temperature of about 150°C in order to enhance the effect of the caesium injected in the plasma chamber for negative ion surface generation [2]. Moreover, the plasma side of the PG is Molybdenum coated in order to reduce the sputtering yield. The apertures are designed with conical chamfers on the upstream and downstream sides of the grid. The PG is maintained slightly polarized with respect to the plasma potential in order to reduce the unavoidable co-extracted electron current. A transverse magnetic field is generated close to the PG in order to maximize the negative ion volume production and to further reduce co-extracted electrons, as it is described more in detail in chapter 3. Moreover some suppression magnets are embedded in the extraction grid to deviate the trajectories of the co-extracted electrons, forcing them to impinge on the EG surface. The EG has an electric potential higher than the PG (depending on the extracted current density), so that the negative charged ions can be properly extracted from the RF expansion chamber. The GG has the function to accelerate the ion beamlets up to a potential of about 100 kV and also it results loaded by co-extracted and stripped electrons. Each grid of the ITER NBI is divided in 4 vertical segments of 320 apertures each, for a surface of 2000 cm^2. Each segment contains 4 horizontal groups of apertures arranged in a regular 5x16 rectangular array. All the grids required to be actively cooled and thus they are made by electro-deposition of pure copper onto a copper base plate. Indeed, this technique permits to obtain a very complex geometric shape, with very small cooling channels and grooves for embedded magnets inside the grid, and to have good mechanical properties, due to the high purity and to the very small grain size of copper. EG and GG are critical from the structural point of view, since they are thin and wide item subject to power loads which are expected to be quite high and concentrated.

SPIDER Parameters			
Ion Species	$\mathbf{D^-}$	$\mathbf{H^-}$	
Beam Energy	100	100	[keV]
Beam Current	40	60	[A]
Extracted current density	285	355	[A/mm^2]
Pulse Length	3600	3600	[s]
Source filling pressure	0.3	0.3	[Pa]
Extracted electron to ion ratio	≤ 1	≤ 0.5	

Table 2: Main parameters of the SPIDER source

In the last design update SPIDER was also equipped with an electron dump system, consisting of consecutive arrays of cooling pipes devoted to dump the high divergence electrons exiting the accelerator, preserving more delicate structures [3].

The main objective of SPIDER is to demonstrate the feasibility of extracting the nominal ion current density from a very large ion radio-frequency source, focusing on its values and uniformity across the beam section together with the containment of electrons leakages. As a matter of fact, SPIDER will be the first ITER-like radio-frequency source, whose concept is presently tested only on small size sources (BATMAN and only recently ELISE sources at IPP Garching [4]). In particular, the electron to ion ratio should be limited to less than 1 and the admissible ion current non-homogeneity should be less than 10% on the whole beam cross-section. Most of this information can be extracted by an instrumented calorimeter, a diagnostic system made of a slanting target intercepting the beam after the acceleration stage, able to evaluate uniformity, divergence and value of the beam current.

Some SPIDER shots will also be dedicated to test an important requirement for the ITER NBI, which is the production and extraction of a negative ion beam for pulses up to an hour. Finally, the capability of optimization of the cesium consumption and the tolerance to the presence of impurities will be studied in depth.

As already mentioned, in SPIDER a RF plasma source will be adopted, including eight RF drivers placed on the backside of the source.

1.3.3.2 MITICA

MITICA is a full size prototype of the ITER neutral beam injector, designed to answer to all the requirements. It will operate in Padua in order to be experimentally optimized in view of the final devices to be installed in ITER, where no other modifications will be adopted. The main parameters of the experiment are reported table 1.3.

MITICA Parameters			
Ion Species	$\mathbf{D^-}$	$\mathbf{H^-}$	
Beam Energy	1	1	[MeV]
Beam Current	40	60	[A]
Extracted current density	285	355	[A/mm^2]
Beamlet divergence	≤ 7	≤ 7	[mrad]
Pulse Length	3600	3600	[s]
Source filling pressure	0.3	0.3	[Pa]
Extracted electron to ion ratio	≤ 1	≤ 0.5	

Table 3: Main parameters of MITICA injector.

Differently from SPIDER whose aim is the achievement of the requirements of the ion source, the most of the technical specifications of MITICA are strongly connected to the problem of optimizing the interaction with the ITER plasma. For instance the energy parameters for the beam must satisfy the need to penetrate up to the plasma core, where the heat is efficiently deposited. Since the ionizing cross section of the beam decreases with the beam energy, in order to allow the beam to reach the plasma core without being completely ionized before, high beam energy is required. On the other hand, the beam energy value has the limit to minimize the fraction of high energy neutral particles reaching the internal wall of the vessel. Further constrain in the choice of the beam energy is that high voltages need high insulating distances, while the dimension of the injector are fixed to do not exceed the ITER duct dimension. Taking into account these different needs, a value around 1MeV was selected as the best choice for the beam energy of the ITER NBIs.

Taking into account the loss factors of the various processes the ion beam is subject from its extraction to its neutralization, it was estimated a delivered power from each injector around 17 MW. Considering the extraction surface the requirement on ion current density is obtained, as reported in the previous table.

Differently for SPIDER, MITICA include also the Neutralizer and the Residual ion dump (RID), devoted to remove the fraction of charged particles still present in the beam.

A schematic of MITCA, including all the mentioned components is given in Figure 9.

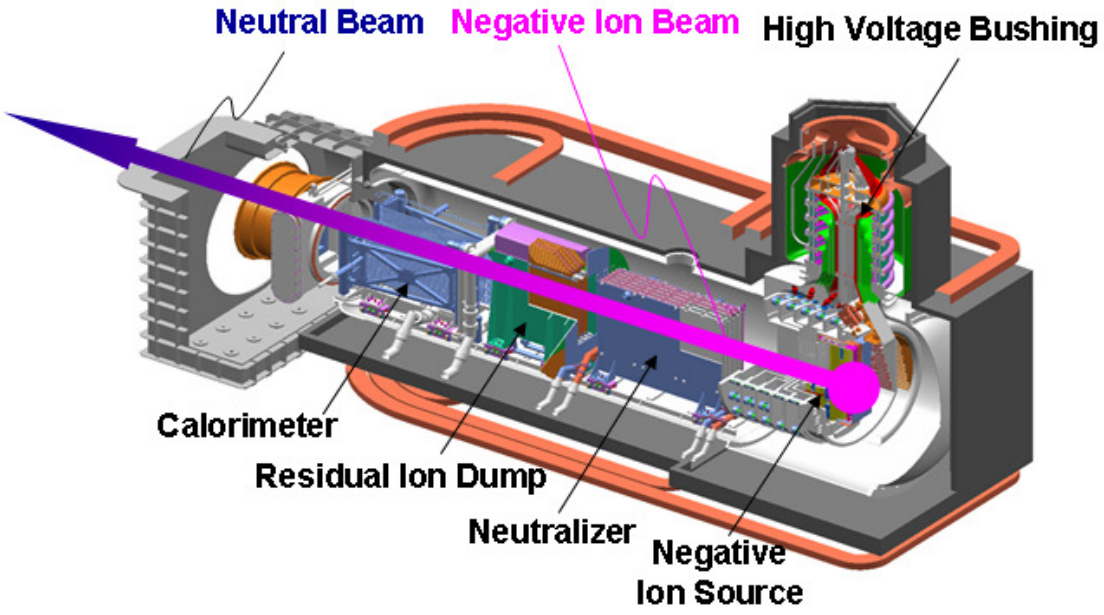

Figure 9: Sketch of the MITICA injector.

1.4 RFX-mod

RFX is the acronym standing for “Reversed Field eXperiment”, the biggest RFP even today which started the operations in the 1992, in the framework of a joint EURATOM-ENEA-CNR association. It has been then upgraded after a fire that in the 1999 destroyed part of its power supplies, introducing so considerable modifications to even change its name in RFX-mod, back in operation in 2004. The details of the major modifications of RFX-mod have been reported in the papers [13].

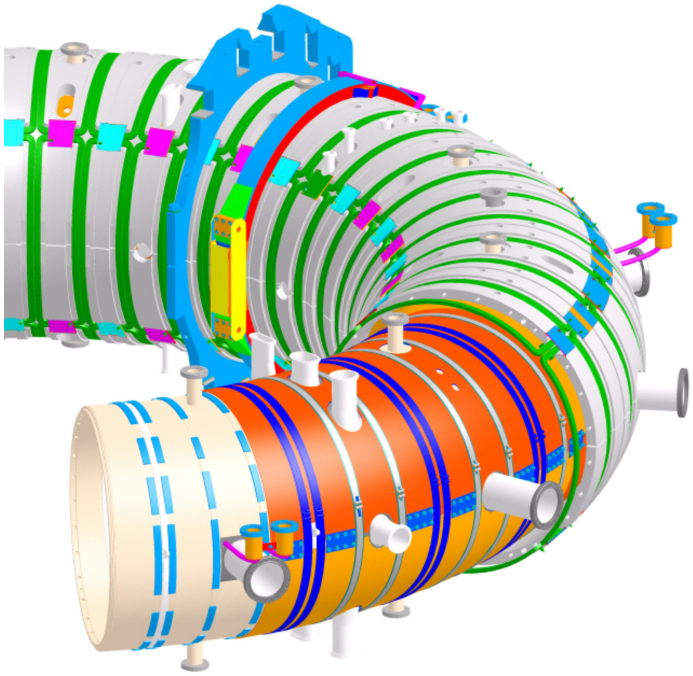

Figure 10: RFX-mod assembly.

The structure of RFX-mod is that of a typical RFP, consisting of a toroidal vacuum vessel within a conductive shell and related magnetic system. This is formed by a poloidal field system, in turn consisting of an air magnetizing system and further coils for the plasma shape and position, the toroidal field system and a radial magnetic field system for the active control of MHD instabilities as well, which constitutes the main modification of the machine. Overall, the maximum peak power of an RFX-mod pulse requires 200 MVA, directly taken from the 400 kV 50 Hz Italian grid. Figure 10 shows the RFX-mod assembly, the poloidal and toroidal field systems excepted. The main parameters of the RFX machine are listed in Table 4.

RFX-mod Parameters		
Major radius, R_0	2.0	[m]
Minor radius, a	0.5	[m]
Maximum plasma current, I_p	2.0	[MA]
Maximum applied toroidal field, b_φ	0.7	[T]
Current rise time	15-50	[ms]
Flat top time	250	[ms]
Core flux swing	15	[Vs]
Inductive storage	72.5	[MJ]
Vacuum vessel toroidal resistance	1.1	[mΩ]

Table 4: RFX-mod main parameters.

The vacuum vessel is a toroidal rigid structure made of INCONEL 625, composed of 72 elements welded together. Its inner surface is fully covered by graphite tiles, periodically baked at temperature about 180°C. The vacuum vessel is equipped with 96 ports for vacuum pumping, gas inflow and diagnostic systems. In RFX-mod the vacuum vessel is surrounded by a close fitting 3 mm thick copper shell, which replaced the old 65 mm aluminium shell. The purpose of this structure, common in RFP machines, is to provide a passive stabilisation of the fast MHD instabilities. The thickness is a compromise between the conflicting requirements of passive control of the fast instabilities and of penetration of externally induced magnetic fields to actively control of slower MHD modes. The shell has one inner equatorial cut, as well as a poloidal gap with a toroidal overlap of 23° (Figure 11), in order to allow the penetration of the axialsymmetric toroidal magnetic field, the equilibrium vertical field and the axialsymmetric toroidal electric field. The outer equatorial gap is short-circuited with bolted copper plates. The shell is clamped to the vessel through stainless steel bands (in blue in Figure 10) that sustain the electrodynamic forces arising in the shell. This component, together with the active control system of the MHD instabilities, is one of the fundamental components for the present PhD thesis.

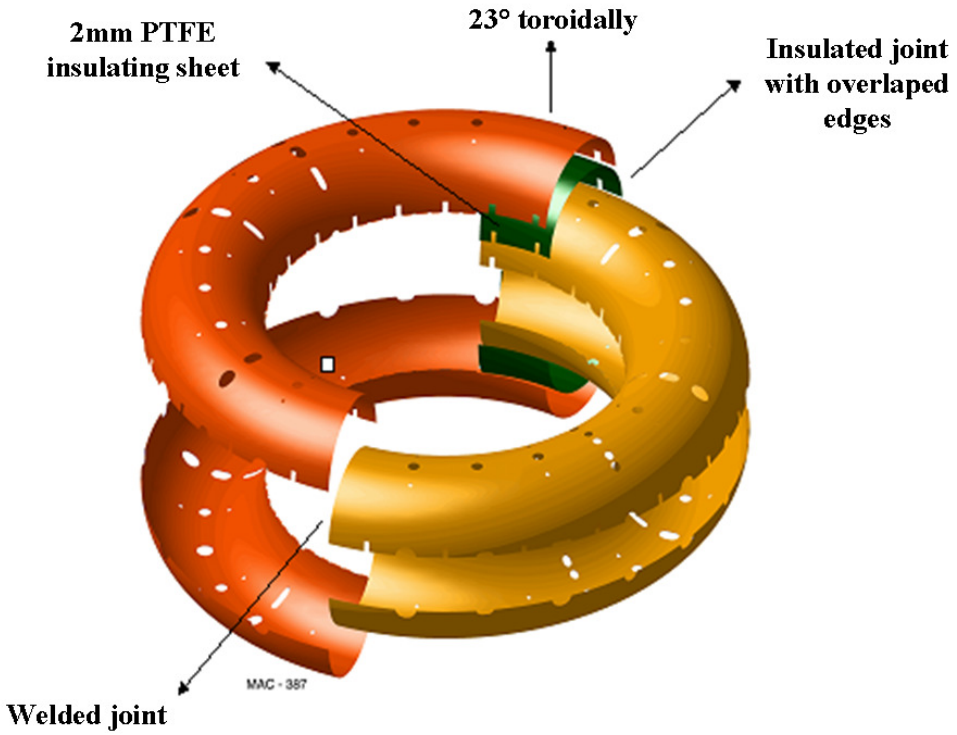

Figure 11: 3 mm copper shell exploded view.

Outside the stabilising shell, a toroidal structure provides the necessary mechanical support to the machine assembly, including 48 toroidal field coils, 8+8 field shaping coils and 192 local coils called saddle coils (in green in Figure 10 and Figure 12).

The saddle coils system has been introduced in order to implement an active control of the MHD instabilities, in particular for the control of the RWMs. It is formed by 192 independently fed coils, hosted by grooves conveniently cut on the outer surface of the toroidal support structure at $r = r_c = 0.582$ m and have been arranged as a bi-dimensional Cartesian grid of adjacent coils, as shown in Figure 12. Each coil is made of a 60 turns copper winding having four legs them laying on a toroidal surface, two of them in the poloidal direction, the other two in the toroidal direction. The coils are placed tightly close together, so that a single groove hosts the legs of two poloidally or toroidally adjacent coils. Neglecting the size of their section, the interior surface of these coils is an exact covering of the toroidal surface they lay on. The grid forms an array made of 48 coils along the toroidal direction and 4 coils along the poloidal direction. Each coil spans a poloidal angle of 90 degrees and a toroidal angle of 7.5 degree.

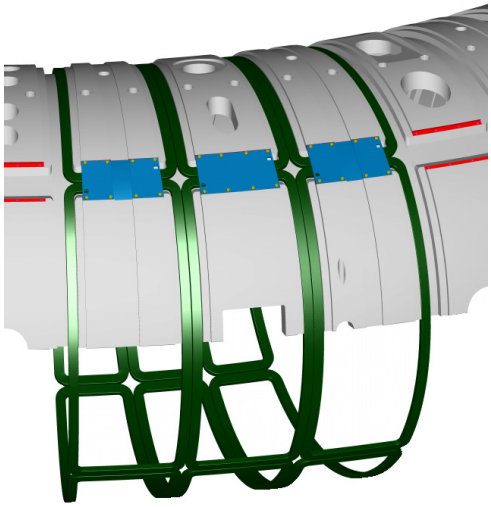

Figure 12: Sketch of the RFX-mod support structure and active coils.

For their shape and position, the saddle coils can produce a relatively strong local magnetic field with a substantially radial component in its neighbourhood. The coils are designed to carry a maximum current of 400 A for 300 ms, producing a maximum local radial field b_r of about 50 mT.

The RFX-mod magnetic field sensors are also of primary interest for this PhD work, in particular the integral radial field sensors laid down on the outer surface of the vacuum vessel at r_s = 0.507 m. These sensors are one turn coils with a geometry analogous to the one of the active coils. In Figure 13 the radial field sensors position together with the other poloidal and toroidal field pick-up coils on the vacuum chamber is shown.

The collection of a saddle coil, the sensor lying below it and eventually the power amplifier which feed it is called MHD unit.

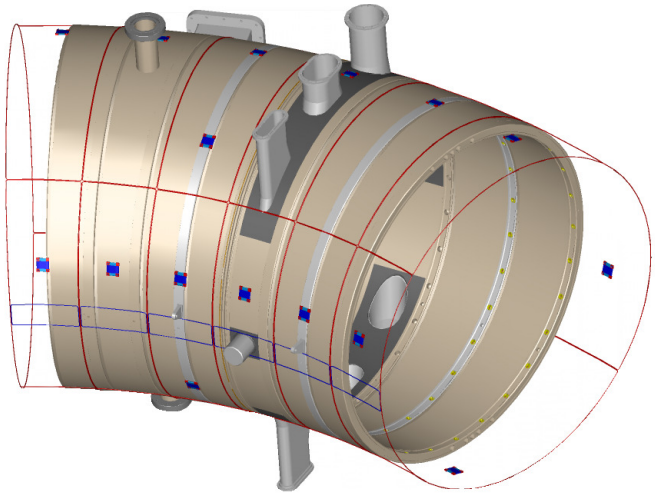

Figure 13: Sketch of a part of RFX-mod vessel and relative position of magnetic sensors.

1.4.1 RFX-mod MHD active control system

The saddle coil set of RFX-mod, together with their amplifiers and the radial field sensors, represents the most advanced magnetic system for active control of MHD instabilities in fusion devices. Of course, the system is made by the electronic equipment for the acquisition and processing of the relevant control variables as well. Core of the system is a computer implementing the feed-forward and feed-back algorithms allowing the system to work effectively.

From a systemic point of view, three components can be distinguished:

1. the power amplifiers feeding the saddle coils;
2. the electromagnetic system made up of the active coils, the radial sensors and the passive structures of the machine assembly,
3. the control systems, consisting of the data acquisition equipment and the processing units.

These components usually work in loop configuration: inputs of the active coils system are the output voltages of the power amplifiers, inputs of the radial sensors are the fluxes generated by the coils together with the plasma, which are then processed by control algorithms and resulting quantities are sent back to the power amplifiers as references or set points.

Without going into detail about the model of the amplifiers, being beyond the purpose of this work, it is worth noticing that the power amplifiers themselves can be seen as a controlled dynamic system. Depending on their parameter configuration, they can be voltage controlled, current controlled or flux controlled. In the first case the electronic logic of the amplifiers interprets input signals simply as a scaled voltage reference, giving a proportional voltage in output. In the second case, the input signal is interpreted as a scaled current reference and a feedback controller implemented in the power amplifiers measures the output current and change the output voltage trying to follow the reference. In the third case the, the input signal is the error (difference) between the reference and the flux measured by the underlying sensor.

The electromagnetic system is basically a dynamic inductive system. It is made by 192 fed coils (the active coils), 192 sensor coils (the radial field sensors) and the conductive structures in between the two sets. Neglecting the latter, the set of 384 coils can be modeled as an ideal inductive system, satisfying the following relation among the currents:

$$\begin{bmatrix} v_1(t) \\ v_2(t) \end{bmatrix} = \begin{bmatrix} L_{11} & L_{12} \\ L_{21} & L_{22} \end{bmatrix} \frac{d}{dt} \begin{bmatrix} i_1(t) \\ i_2(t) \end{bmatrix} + \begin{bmatrix} R_{11} & 0 \\ 0 & R_{22} \end{bmatrix} \begin{bmatrix} i_1(t) \\ i_2(t) \end{bmatrix} \tag{1.3}$$

where v and i denotes voltage and current vector respectively. The index 1 refers to the active coils, index 2 to the sensors. L_{ij} are partitions of a global inductance matrix (containing both auto and mutual terms), while R_{ii} are diagonal resistance matrices. The voltage at the ends of the sensor coils is integrated to produce the flux measure. The integrating electronic is assumed to have a very small effect on the measured system so that the relation $i_2(t) = 0$ is reasonable. This consideration leads to the equations

$$\begin{aligned} v_1(t) &= L_{11}\frac{d}{dt}i_1(t) + R_{11}i_1(t) \\ \psi_2(t) &= L_{21}i_1(t) \end{aligned} \tag{1.4}$$

where $\psi_2(t)$ is the flux vector measured by the radial field sensors.

However, these equations are valid only in a space free of passive structures. In their presence a linear multiple-input-multiple-output (MIMO) model of the relation between the input voltages (or currents) and the output fluxes can still be derived, but require more effort in the modeling, being the resulting transfer matrices frequency dependent.

Development of a model able to take into account the effect of the eddy current induced in the passive structure and its conversion in state-space representation, have been central object of this PhD thesis, as widely described in chapter 5.

2 Finite Element Methods for magnetic problems

2.1 Introduction

Determination of magnetic and electric field distributions and calculation of related quantities with the desired accuracy in most of practical cases cannot be carried out by analytical procedures. The difficulties of factors such as complicated geometry, multiple material, presence of solid material where eddy currents can be induced, anisotropy, saturation and hysteresis effects in iron mean that a numerical method is required.

Nowadays computer performances, together with the theory on numerical methods for the solution of magnetic field problems are advanced enough to cover almost any kind of problem with satisfactory results.

Several methods have been developed in the last decades, the main available ones are:

- finite difference
- finite element
- boundary element and other integral approaches.

All have their advantages and drawbacks; however finite element method incorporates most of the advantages of the other two techniques without incurring significant disadvantages. For instance the finite difference method is not well suited to model irregular geometries including slants and curved surfaces (lower accuracy), and cannot deal with material properties depending on the spatial coordinate (e.g. ferromagnetic material with localized different saturation level).

Boundary element technique indeed works efficiently with linear materials and not with non-linear ones. Thus, finite element method is best suited to be a general purpose tool able to treat most of the cases.

Nevertheless, the variety of conditions and the inherent complexity of magnetic problems require advance knowledge to choose the proper formulation in order to get good enough results with the minimum demand of computer resources.

This chapter doesn't claim to give a thorough description of the finite element method applied to magnetic field problems, but only to recall the various formulations and their scope, in particular in relation to those which have been used to carry out the activities described in the following chapters.

In paragraph 2.5 a brief description of the ANSYS code, in particular with regard to the formulations used, will be given as far as possible, since the information provided by the manufacture are not completely exhaustive.

In paragraph 2.6 a brief description of the CARIDDI code will be given, with particular emphasis to the peculiarity of the formulation which allows getting an electromagnetic model in state-space form, together with the drawbacks which it implies in terms of high demand of computer resources.

2.2 Magnetic formulations

Finite element methods have been successful in electromagnetics largely because the conventional field equations permit numerous different reformulations in terms of potentials, each of them results particularly suited in specific cases.

Electromagnetic field problems occupy a relatively favourable position in engineering and physics since their governing laws can be expressed very concisely by a single set of four equations, the well known Maxwell equations. Each of these may be function of three space coordinates x, y, z and the time t. The four Maxwell equations in differential form are usually written as follows:

$$\nabla \times \mathbf{E} = -\frac{\partial \mathbf{B}}{\partial t} \tag{2.1}$$

$$\nabla \times \mathbf{H} = \mathbf{J} + \frac{\partial \mathbf{D}}{\partial t} \tag{2.2}$$

$$\nabla \cdot \mathbf{D} = \rho \tag{2.3}$$

$$\nabla \cdot \mathbf{B} = 0 \tag{2.4}$$

where **E** is the electric field intensity [*V*/*m*], **H** is the magnetic field intensity [*A*/*m*], **D** is the electric flux density [*C*/*m*], **B** is the magnetic flux density [*T*], **J** is the electric current density [A/m^2] and ρ is the electric charge density [C/m^3].

To solve the system of the Maxwell equations the constitutive relations have to be considered:

$$\mathbf{D} = \varepsilon\mathbf{E} \tag{2.5}$$

$$\mathbf{B} = \mu\mathbf{H} \tag{2.6}$$

$$\mathbf{J} = \sigma\mathbf{E} \tag{2.7}$$

which describe the macroscopic properties of the medium being dealt with in terms of its electric permittivity ε, magnetic permeability μ and electric conductivity σ. These quantities are not necessarily constants; a notable exception is the case of ferromagnetic materials for which the **B-H** relationship may be a complex non linear law; moreover, they could be represented as a tensor in the case of anisotropic materials.

The system of the above equations has a general validity and numerical techniques to solve general electromagnetic problems exist, but the rest of the chapter will focus on the magnetostatic and magneto quasi-static formulations only.

2.2.1 Magnetostatic

The equations governing the study of static magnetic field distributions are the following:

$$\begin{cases} \nabla \times \mathbf{H} = \mathbf{J} \\ \nabla \cdot \mathbf{B} = 0 \end{cases} \quad \text{in } V \tag{2.8}$$

where the current density **J** has been assigned, to which must be added:

- a constitutive relation:

$$\mathbf{B} = \mu\mathbf{H} \tag{2.9}$$

- interface conditions on any discontinuity surface Σ:

$$\begin{cases} \left\| \mathbf{H} \times \hat{\mathbf{n}} \right\| = 0 \\ \left\| \mathbf{B} \cdot \hat{\mathbf{n}} \right\| = 0 \end{cases} \tag{2.10}$$

  where ||·|| stands for the jump of the quantity at the interface;

- boundary conditions on the border of V ($\partial V = \Sigma_B \cup \Sigma_H \cup \Sigma_\infty$) which assures the uniqueness of the solution, as for instance the following:

$$\begin{cases} \mathbf{H}\times\hat{\mathbf{n}}\big|_{\Sigma_H} = 0 \\ \mathbf{B}\cdot\hat{\mathbf{n}}\big|_{\Sigma_B} = 0 \\ |\mathbf{B}|_{r\to\infty} \to 0 \quad as \quad \dfrac{1}{r^3} \end{cases} \tag{2.11}$$

The magnetostatic case has peculiarities which lead it to be the more complex among the static problems and they can be summarized as follows:

- Most of the magnetic material of interest are strongly non-linear and show hysteretic behaviour.
- The use of scalar potential is not allowed in general. There is this opportunity only under particular conditions which will be explained in the following. Magnetostatic (or more in general magnetic) problems are intrinsically vectorial and thus, in general, three times more heavy to be solved.
- Magnetic problems are in general free bounded and thus they have to be solved on unlimited domain, unless to admit some approximations.

Therefore, to investigate in depth the different possibility to formulate the model is essential in order to be able to choose the more adequate for each specific situation.

2.2.1.1 *A* formulation: magnetic vector potential

The most general way to solve a magnetostatic problem is by introducing a magnetic *vector potential* **A** such as:

$$\mathbf{B} = \nabla\times\mathbf{A} \tag{2.12}$$

This is true since **B** is a solenoidal vector field and it allows to automatically solve the first of (2.8):

$$\nabla\times\left(\frac{1}{\mu}\nabla\times\mathbf{A}\right) = \mathbf{J} \tag{2.13}$$

to which boundary and connection conditions have to be added:

$$\begin{cases} \dfrac{1}{\mu}\left\|\nabla\times\mathbf{A}\right\|\times\hat{\mathbf{n}} = 0 \\ \left\|\nabla\times\mathbf{A}\right\|\cdot\hat{\mathbf{n}} = 0 \end{cases} \text{ on } \Sigma \tag{2.14}$$

$$\begin{cases} \dfrac{1}{\mu}(\nabla \times \mathbf{A}) \times \hat{\mathbf{n}}\Big|_{\Sigma_H} = 0 \\ (\nabla \times \mathbf{A}) \cdot \hat{\mathbf{n}}\big|_{\Sigma_B} = 0 \\ |\mathbf{A}|_{r\to\infty} \to 0 \quad as \quad \dfrac{1}{r^2} \end{cases} \tag{2.15}$$

This formulation has two drawbacks:

- the unknown **A** is a vectorial quantity;
- the equation (2.13) in general doesn't admit an unique solution in terms of **A**.

As a matter of fact, for any assigned field **B** equation (2.12) doesn't identify univocally **A,** indeed nothing change by adding to **A** the gradient of any scalar function:

$$\mathbf{B} = \nabla \times \mathbf{A} = \nabla \times (\mathbf{A} + \nabla \xi) \quad \forall \xi$$

The uniqueness of the solution is assured only by the addition of a *gauge condition*. In static condition the most classic is the Coulomb gauge:

$$\nabla \cdot \mathbf{A} = 0 \tag{2.16}$$

A further used one is the two components gauge [18]:

$$\mathbf{A} \cdot \mathbf{w} = 0 \tag{2.17}$$

where **w** is any vector field without closed field lines. This condition prescribes the component of the vector potential along the director determined by an arbitrarily chosen non-vanishing vector field **w,** which does not posses closed field lines, to be zero. This gauge is computational useful when the edge element approach is adopted (see paragraph 2.4), since it is easily imposed by considering **w** pointed as the sides of any tree associated to the discretized domain grid and eliminating the unknowns associated to these edges. This condition eliminates one of the three components of the vector potential, thus reducing the total number of scalar unknown from three to two.

In bi-dimensional geometry both the issues above don't exist: the problem is reduced to solve a scalar equation and the gauge assuring the uniqueness of the solution is automatically satisfied. Indeed, considering a Cartesian reference system (*x, y, z*), the current density can only be orthogonal to the plane, for instance pointed towards *z* and depending on *x* and *y*: $\mathbf{J} = J(x, y)\mathbf{i}_z$. Therefore **B** has only components along *x* and *y*, and the vector potential satisfying the Coulomb gouge is:

$$\mathbf{A} = A(x, y)\mathbf{i}_z \tag{2.18}$$

and thus:

$$\mathbf{B} = \nabla \times \mathbf{A} = \nabla A \times \mathbf{i}_z \tag{2.19}$$

In this case the equation to be solved results:

$$\nabla \cdot \left(\frac{1}{\mu} \nabla A \right) = -J \tag{2.20}$$

which corresponds to a Poisson equation. Dirichelet and Neumann boundary condition have to be added:

$$\begin{cases} \dfrac{1}{\mu} \dfrac{\partial A}{\partial n}\bigg|_{\Sigma_H} = 0 \\ A\big|_{\Sigma_B} = \text{const} \end{cases} \tag{2.21}$$

together with connection conditions:

$$\begin{cases} \dfrac{1}{\mu} \left\| \dfrac{\partial A}{\partial n} \right\| = 0 \\ \|A\| = 0 \end{cases} \quad \text{on } \Sigma \tag{2.22}$$

Similarly is valid in axial symmetry as well.

2.2.1.2 φ formulation: reduced magnetic scalar potential

Let's introduce the *source* magnetic field $\mathbf{H_s}$ as the magnetic field in vacuum due to the assigned current density, which implies:

$$\begin{cases} \nabla \times \mathbf{H_s} = \mathbf{J} \\ \nabla \cdot (\mu_0 \mathbf{H_s}) = 0 \end{cases} \quad \text{everywhere} \tag{2.23}$$

$\mathbf{H_s}$ can be easily determined through the Biot-Savart integral:

$$\mathbf{H_s}(\mathbf{r}) = \frac{\mathbf{1}}{\mathbf{4\pi}} \int_{V_J} \frac{\mathbf{J}(\mathbf{r'}) \times (\mathbf{r} - \mathbf{r'})}{|\mathbf{r} - \mathbf{r'}|^3} dV' \tag{2.24}$$

where V_J is the volume limiting the current density.

As it can be seen by comparing equations (2.8) and (2.23), the difference between the total magnetic field $\mathbf{H}$ and $\mathbf{H_s}$ is conservative, and thus setting:

$$\mathbf{H} = \mathbf{H_s} - \nabla \varphi \tag{2.25}$$

the first of (2.8) is automatically satisfied. The scalar field φ is called *reduced magnetic scalar potential* and it can be found through the second of the (2.8):

$$\nabla \cdot (\mu \nabla \varphi) = \nabla \cdot (\mu \mathbf{H_s}) \quad \text{in } V \tag{2.26}$$

while the connection and boundary conditions are:

$$\begin{cases} \left\| \mu \dfrac{\partial \varphi}{\partial n} - \mu \mathbf{H_s} \cdot \hat{\mathbf{n}} \right\| = 0 \\ \left\| \varphi \right\| = 0 \end{cases} \quad \text{on } \Sigma \tag{2.27}$$

$$\begin{cases} \varphi|_{\Sigma_H} = \text{assigned} \\ \left.\dfrac{\partial \varphi}{\partial n}\right|_{\Sigma_B} = \mathbf{H_s} \cdot \hat{\mathbf{n}}|_{\Sigma_B} \\ \varphi_{r\to\infty} \to 0 \quad as \quad \dfrac{1}{r^2} \end{cases} \tag{2.28}$$

where the value of φ on Σ_H can be found by conveniently integrating the tangential component to Σ_H of $\mathbf{H_s}$.

The introduction of the reduced scalar potential reduces again the problem to solve a Poisson equation with Dirichlet and Neumann boundary condition with a scalar unknown. However this implies the following drawbacks:

- the integral (2.24) has to be computed for any point where we want to know **H**;
- this formulation can give large errors in regions of high permeability due to cancellation errors.

This second point of course is the most critic and it originates from the fact that in high permeability regions the magnetic field **H** has a low amplitude and in any case much lower than the value it would assumes in vacuum, corresponding to $\mathbf{H_s}$. Indeed, because it is determine as difference of two quantities (equation (2.25)), both with absolute value much higher than **H** itself. Therefore, little errors in the evaluation of $\mathbf{H_s}$ and $\nabla\varphi$, which are unavoidable when numerically determined, leads to big errors in the **H** evaluation.

2.2.1.3 φ - ψ formulation: reduced-total magnetic scalar potential

In order to overcome the problem of cancellation in the evaluation of the magnetic field in high permeability regions (V_m), here can be introduced a *total scalar potential* ψ, such that:

$$\mathbf{H} = -\nabla\psi \quad \text{in } V_m \tag{2.29}$$

$$\mathbf{H} = \mathbf{H_s} - \nabla\varphi \quad \text{in } V - V_m \tag{2.30}$$

The equations to be solved become the following two:

$$\nabla \cdot (\mu \nabla \psi) = 0 \quad \text{in } V_m \tag{2.31}$$

$$\nabla \cdot (\mu \nabla \varphi) = \nabla \cdot (\mu \mathbf{H_s}) \quad \text{in } V - V_m \tag{2.32}$$

with boundary and connection conditions, which are similar to those in (2.27) and (2.28).

Again, in this case Poisson equations have to be solved, or better Laplace equation if μ is constant in V_m, with Dirichelet and Neumann boundary conditions. Obviously, so that equation (2.29) can be valid, the following conditions have to be verified:

- in high permeable regions the magnetic field has to be conservative ($\nabla \times \mathbf{H} = 0$ in V_m), that is here no current density is allowed;
- V_m has to be simply connected, or, if multiply connected, it cannot link current-carrying conductors.

While the first point absolutely must be verified, if indeed the second not, equation (2.29) can still be used as long as appropriate cuts are introduced in V_m, which means discontinuity surfaces for ψ.

The φ - ψ formulation is the most used in magnetostatics, since it combines the property to have scalar unknowns to the absence of cancellation problems. Anyhow, if the conditions on V_m are not verified, other formulations have to be preferred.

However, there is a drawback: since the magnetic field has two different representations in V_m and V - V_m, connection conditions are required also on the surface Σ_m which divides the two domains. These conditions are deduced again from equations (2.8) and results the following:

$$\begin{cases} \left(\mathbf{H_s} - \nabla\varphi\right)\times\hat{\mathbf{n}}\big|_{\Sigma_{m\varphi}} = -\nabla\psi\times\hat{\mathbf{n}}\big|_{\Sigma_{m\psi}} \\ \mu\left(\mathbf{H_s}\cdot\hat{\mathbf{n}} - \dfrac{\partial\varphi}{\partial n}\right)\Big|_{\Sigma_{m\varphi}} = -\dfrac{\partial\psi}{\partial n}\Big|_{\Sigma_{m\psi}} \end{cases} \tag{2.33}$$

where $\Sigma_{m\varphi}$ and $\Sigma_{m\psi}$ are the two sides of Σ_m which face to the reduced and total potential regions respectively.

2.2.1.4 *A* - ψ formulation: magnetic vector-scalar potential

When there are regions best represented by scalar potential domain, where no current sources are present, and others by vector potential domain, with presence of currents, the two potential methods can be combined, getting:

$$\begin{aligned} \mathbf{B} &= \nabla\times\mathbf{A} \quad \text{in}\, V_A \\ \mathbf{H} &= -\nabla\psi \quad \text{in}\, V_\psi \end{aligned} \tag{2.34}$$

and thus the equations to be solved result:

$$\begin{aligned} \nabla\times\left(\frac{1}{\mu}\nabla\times\mathbf{A}\right) &= \mathbf{J} \quad \text{in}\, V_A \\ \nabla\cdot(\mu\nabla\psi) &= 0 \quad \text{in}\, V_\psi \end{aligned} \tag{2.35}$$

with related boundary and connection condition.

The drawbacks of the formulation evidently are the following:

- a vector unknown has to be found in V_A;
- solution in terms of **A** is not unique unless a gauge condition is imposed;
- connection conditions on the surface $\Sigma_{A\text{-}\varphi}$ are required.

With regards to this last point, the continuity of the normal component of flux density and tangential component of field intensity are used to couple the two potentials [14, 15]. Of particular interest is to see how the numerical equation set can be symmetrised. Let's consider the application of the Galerkin weighted residual method to equations (2.35), which results in the following integral equations:

$$\int_{V_A}\mathbf{N}\cdot\nabla\times\left(\frac{1}{\mu}\nabla\times\mathbf{A}\right)dV = \int_{V_A}\mathbf{N}\cdot\mathbf{J}dV \tag{2.36}$$

$$\int_{V_\psi} w\cdot\nabla\cdot(\mu\nabla\psi)dV = 0 \tag{2.37}$$

where the terms **N** and w are the element shape functions. After integrating by parts they result:

$$\int_{V_A}\nabla\times\mathbf{N}\cdot\frac{1}{\mu}\nabla\times\mathbf{A}dV - \int_{\Sigma_A}\left(\mathbf{N}\times\frac{1}{\mu}\nabla\times\mathbf{A}\right)\cdot\mathbf{n}_A d\varsigma = \int_{V_A}\mathbf{N}\cdot\mathbf{J}dV \tag{2.38}$$

$$-\int_{V\psi}\nabla w\cdot\mu\nabla\psi dV + \int_{\Sigma_\psi} w\cdot\mu\nabla\psi\cdot\mathbf{n}_\psi d\varsigma = 0 \tag{2.39}$$

The two regions can be coupled exactly by imposing the continuity conditions (2.10). The continuity of the tangential component of the field intensity across the interface implies the following equation:

$$-\int_{\Sigma_A}\left(\mathbf{N}\times\frac{1}{\mu}\nabla\times\mathbf{A}\right)\cdot\mathbf{n}_A d\varsigma = \int_{\Sigma_A}(\mathbf{N}\times\nabla\psi)\cdot\mathbf{n}_A d\varsigma \tag{2.40}$$

Similarly, the continuity of the normal component of flux density:

$$\int_{\Sigma_\psi} w\cdot\mu\nabla\psi\cdot\mathbf{n}_\psi d\varsigma = -\int_{\Sigma_\psi} w\cdot\nabla\times\mathbf{A}\cdot\mathbf{n}_\psi d\varsigma \tag{2.41}$$

The two interface terms on the right hand side of equations (2.40) and (2.41) are asymmetric, but can be symmetrised by using the following procedure. Let's apply the vector identity $\nabla\times(\psi\mathbf{A})=\psi\nabla\times\mathbf{A}+\nabla\psi\times\mathbf{A}$ to the interface condition (2.41):

$$-\int_{\Sigma_\psi} w\cdot\nabla\times\mathbf{A}\cdot\mathbf{n}_\psi d\varsigma=\int_{\Sigma_\psi}(\nabla\psi\times\mathbf{A})\cdot\mathbf{n}_\psi d\varsigma-\int_{\Sigma_\psi}\nabla\times(w\mathbf{A})\cdot\mathbf{n}_\psi d\varsigma \tag{2.42}$$

and by applying the Stokes theorem to the second member of the right hand side, the second interface term is provided:

$$\int_{\Sigma_\psi}(\nabla\psi\times\mathbf{A})\cdot\mathbf{n}_\psi d\varsigma-\int_{\partial\Sigma_\psi} w\mathbf{A}dl \tag{2.43}$$

The interface term on the right hand side of equations (2.40) and the interface term (2.43) are now symmetric (since n_A and n_ψ are in opposite direction), provided the condition

$$\int_{\partial\Sigma_\psi} w\mathbf{A}dl=0 \tag{2.44}$$

is true. This is the case if the interface is completely within the domain, since integrals over internal edge will cancel. In plane of symmetry, tangential component of **A** will be zero, and since condition (2.44) depends on tangential **A**, it will apply. The symmetry condition is also assured if the scalar potential is prescribed, since this implies the equations referring to w will be deleted.

2.2.2 Magneto-quasi static

In case of time varying currents, magnetostatics is no more valid and in general one has to solve the whole Maxwell's equations, in terms of wave equations. In most situations, however, provided that the velocities involved are small compared to the speed of light, one may invoke the quasi-static approximation. In other terms, regarding the magnetic case, the displacement current (time variation of the electric flux density) can be neglected with good approximation. This case is also called eddy current problem.

The equations governing the study of magnetic field distributions in quasi-static approximation are the following:

$$\begin{cases}\nabla\times\mathbf{E}=-\dfrac{\partial\mathbf{B}}{\partial t}\\ \nabla\times\mathbf{H}=\mathbf{J}\end{cases}\qquad\text{in } V \tag{2.45}$$

where the current density **J** is unknown in the conductive part (V_c) of the domain, while it is assigned (equal to $\mathbf{J_s}$) in the remaining part (V - V_c). The problem is closed by:

- the initial conditions, which guarantees $\nabla \cdot \mathbf{B} = 0$;
- two constitutive relations, supposed linear:

$$\begin{aligned} \mathbf{B} &= \mu \mathbf{H} \quad \text{in } V \\ \mathbf{J} &= \sigma \mathbf{E} \quad \text{in } V_c \end{aligned} \tag{2.46}$$

- interface conditions on any discontinuity surface Σ:

$$\begin{cases} \left\| \mathbf{H} \times \hat{\mathbf{n}} \right\| = \left\| \mathbf{E} \times \hat{\mathbf{n}} \right\| = 0 \\ \left\| \mathbf{J} \cdot \hat{\mathbf{n}} \right\| = \left\| \mathbf{B} \cdot \hat{\mathbf{n}} \right\| = 0 \end{cases} \tag{2.47}$$

  where ||·|| stands for the jump of the quantity at the interface;
- boundary conditions on the border of V assuring the uniqueness of the solution, which depend on the particular formulation.

The observation that in $V - V_c$ the current density is assigned naturally leads to the following division of the equations:

$$\begin{cases} \nabla \times \mathbf{E} = -\dfrac{\partial \mathbf{B}}{\partial t} \\ \nabla \times \mathbf{H} = \mathbf{J} \end{cases} \quad \text{in } V_c \tag{2.48}$$

$$\begin{cases} \nabla \times \mathbf{H} = \mathbf{J_s} \\ \nabla \cdot \mathbf{B} = \mathbf{0} \end{cases} \quad \text{in } V - V_c \tag{2.49}$$

Therefore, the magneto-quasi static model results in coupling a quasi-static model in the conductive region and the magnetostatic one in the non conductive region.

From the point of view of the calculation, the major difficulty introduced by the magneto-quasi static equation is the coupling of a static model with a diffusive one, which have to be joint with suitable connection conditions on the surface dividing the conductive and non-conductive regions.

Several formulation are possible for the solution of the magneto-quasi static problem, each of them with its own advantages and drawbacks. They belong roughly to two categories: *magnetic formulations*, in terms of magnetic quantities, and electric formulations, in terms of electric quantities. In both cases the formulations can be in terms of field, of potentials or mixed.

Unlike in the case of magnetostatics where some formulations are in terms of scalar quantities, the presence of unknown currents prevents scalar formulations in magneto-quasi static case.

2.2.2.1 *H* formulation: magnetic formulation in terms of field

All the equations to be solved, (2.48) and (2.49), are expressed in terms of the magnetic field **H**, exploiting the constitutive relations (2.46):

$$\nabla\times\left(\sigma^{-1}\nabla\times\mathbf{H}\right)+\mu\frac{\partial\mathbf{H}}{\partial t}=0 \text{ in } V_c \tag{2.50}$$

$$\begin{cases}\nabla\times\mathbf{H}=\mathbf{J}\\ \nabla\cdot\mu\mathbf{H}=\mathbf{0}\end{cases}\text{ in } V-V_c \tag{2.51}$$

Moreover, initial, boundary and connection conditions have to be added. These connections are expressed as follows:

$$\begin{cases}\left\|\mathbf{H}\times\hat{\mathbf{n}}\right\|=0\\ \left\|\mu\mathbf{H}\cdot\hat{\mathbf{n}}\right\|=0\end{cases}\text{ in }\Sigma \tag{2.52}$$

This formulation is unattractive both from a computational point of view, since the problem is expressed in terms of a vector quantity, as well as for applying the continuity conditions (2.52). Indeed, while the tangential component of **H** is continuous, its normal component cannot if the permeability μ is discontinuous. Therefore, this formulation cannot be used in the case discontinuity of the permeability are present in the solution domain, unless by adopting advanced technique, as Edge Elements and Cell method.

2.2.2.2 *H - Ω* formulation: mixed magnetic formulation

Equations concerning the non conductive domain $V - V_c$, as already mentioned, are formally the same of the magnetostatics. Therefore it is possible to try to express them, at least in this region, in terms of a scalar unknown.

Let's introduce again the *source* magnetic field $\mathbf{H_s}$ such as:

$$\begin{cases}\nabla\times\mathbf{H}_s=\mathbf{J}_s\\ \nabla\cdot\mu\mathbf{H}_s=\mathbf{0}\end{cases}\text{ in } V \tag{2.53}$$

which corresponds to the field produced in the whole space by a source current $\mathbf{J_s}$ without eddy currents induced in any conductive material. Despite the current $\mathbf{J_s}$ is time varying, this field immediately diffuses in the whole space. Moreover, let's suppose $\mathbf{J_s}$ is zero in the conductive domain V_c and $\mathbf{H_s}$ satisfies the all boundary and connection conditions. Then it is possible define *reaction field* the difference:

$$\mathbf{H_r}=\mathbf{H}-\mathbf{H_s} \tag{2.54}$$

which represents the reaction of the current induced in the conductive material. It has to satisfies the following equations:

$$\nabla\times\left(\sigma^{-1}\nabla\times\mathbf{H}_\mathbf{r}\right)+\mu\frac{\partial\mathbf{H}_\mathbf{r}}{\partial t}=-\mu\frac{\partial\mathbf{H}_\mathbf{s}}{\partial t}\quad\text{in } V_c \tag{2.55}$$

$$\begin{cases}\nabla\times\mathbf{H}_\mathbf{r}=0\\ \nabla\cdot\mu\mathbf{H}_\mathbf{r}=0\end{cases}\quad\text{in } V-V_c \tag{2.56}$$

to which initial and connection conditions have to be added, while no boundary conditions have to be imposed because they are satisfied by $\mathbf{H_s}$.

Since $\mathbf{H_r}$ is irrotational, it allows the introduction of a scalar potential, denoted with Ω, such as:

$$\mathbf{H}_\mathbf{r}=-\nabla\Omega\quad\text{in } V-V_c \tag{2.57}$$

Therefore the equations result:

$$\nabla\times\left(\sigma^{-1}\nabla\times\mathbf{H}_\mathbf{r}\right)+\mu\frac{\partial\mathbf{H}_\mathbf{r}}{\partial t}=-\mu\frac{\partial\mathbf{H}_\mathbf{s}}{\partial t}\quad\text{in } V_c \tag{2.58}$$

$$\nabla\cdot\left(\mu\nabla\Omega\right)=0\quad\text{in } V-V_c \tag{2.59}$$

However, this formulation has the following drawbacks:

- $\mathbf{H_s}$ has to be computed solving a magnetostatic problem for each time step.
- Connection conditions have to be imposed on the conductive surface, since the magnetic field representation is different across it.
- The issue related to the continuity conditions mentioned before persists.
- In presence of strong skin effect, the reaction field compensates almost completely the source field; therefore the computation of the total field can be affected by cancellation errors.

2.2.2.3 *T - Ω - Ω* formulation: magnetic formulation in terms of potentials

The classic way to avoid the issue of the continuity conditions is by introducing of potentials. Since **J** has to be solenoidal so that the second of the (2.45) equations is valid, an *electric vector potential* **T** can be introduced such as:

$$\mathbf{J}=\nabla\times\mathbf{T}\qquad\text{in } V_c \tag{2.60}$$

Maintaining the notations of the previous paragraph, it is possible to write:

$$\nabla\times\mathbf{H}_\mathbf{r}=\nabla\times\mathbf{T}\Leftrightarrow\mathbf{H}_\mathbf{r}=\mathbf{T}-\nabla\Omega\quad\text{in } V_c \tag{2.61}$$

and the equations to be solved become:

$$\nabla\times\left(\sigma^{-1}\nabla\times\mathbf{T}\right)+\mu\frac{\partial\left(\mathbf{T}-\nabla\Omega\right)}{\partial t}=-\mu\frac{\partial\mathbf{H}_{\mathrm{s}}}{\partial t}\quad\text{in } V_{\mathrm{c}} \tag{2.62}$$

$$\nabla\cdot\left(\mu\nabla\Omega\right)=0\quad\text{in } V-V_{\mathrm{c}} \tag{2.63}$$

In this way $\mathbf{T}$ and Ω can be continuous, and $\mathbf{H_r}$ can have normal component discontinuous in case of discontinuity of the permeability, if $\partial\Omega/\partial n$ is discontinuous. The price is the need of a gauge condition to guarantee the uniqueness of $\mathbf{T}$ and Ω separately.

Usually the Coulomb gauge or the two components gauge are used, already defined, but also the Lorenz gauge:

$$\nabla\cdot\mathbf{T}=\mu\sigma\,\partial\Omega/\partial t \tag{2.64}$$

Further drawback is the possibility of incurring in cancellation problems, since the reaction field is computed as difference of the two quantities $\mathbf{T}$ and $\nabla\Omega$.

2.2.2.4 *A** formulation: electric formulation in terms of field

In electric formulations primary quantities are directly related to the electric field, in particular to the quantity $\mathbf{A^*}$ defined as follows:

$$\mathbf{A^*}=\mathbf{A}+\int\nabla\varphi dt \tag{2.65}$$

and such as:

$$\partial\mathbf{A}^*/\partial t=-\mathbf{E}\Rightarrow\mathbf{B}=\nabla\times\mathbf{A}^* \tag{2.66}$$

Its solution is unique provided opportune initial conditions are given. The equations to be solved in this case are:

$$\nabla\times\left(\mu^{-1}\nabla\times\mathbf{A}^*\right)+\sigma\frac{\partial\mathbf{A}^*}{\partial t}=0\text{ in } V_{\mathrm{c}} \tag{2.67}$$

$$\begin{cases}\nabla\times\left(\mu^{-1}\nabla\times\mathbf{A}^*\right)=\mathbf{J}_{\mathrm{s}}\\ \nabla\cdot\varepsilon\mathbf{A}^*=0\end{cases}\qquad\text{in } V-V_c \tag{2.68}$$

with initial, boundary and the following connection conditions:

$$\begin{cases}\left\|\mathbf{A}^*\times\hat{\mathbf{n}}\right\|=0\\ \left\|\sigma\mathbf{A}^*\cdot\hat{\mathbf{n}}\right\|=0\end{cases}\quad\text{in }\Sigma \tag{2.69}$$

The second of the (2.68) equations is the Gauss law in absence of charge density and it is necessary to find the temporal integral of the electric field $\mathbf{A^*}$ outside the conductive material.

As for the magnetic formulations, in this case discontinuity of σ are not allowed unless conveniently treated, since a component of $\mathbf{A^*}$ should result discontinuous.

2.2.2.5 *A* - Ω* formulation: mixed electric formulation

In order to reduce the number of unknowns, outside the conductive region a scalar potential can be used by following the same argument as for the mixed magnetic formulation, and so getting:

$$\nabla \times \left(\mu^{-1} \nabla \times \mathbf{A}^*\right) + \sigma \frac{\partial \mathbf{A}^*}{\partial t} = 0 \text{ in } V_c \tag{2.70}$$

$$\nabla \cdot \left(\mu \nabla \Omega\right) = 0 \text{ in } V - V_c \tag{2.71}$$

with initial, boundary and connection conditions. Particular attention has to be paid to the connection conditions, since inside and outside the conductive region the unknowns are different, one is an electric quantity and the other is magnetic.

2.2.2.6 *A - φ - Ω* formulation: electric formulation in terms of potentials

In order to avoid the issue of the continuity conditions, also in the case of electric quantities are used, the problem can be solved in terms of potentials. In this case it is the magnetic vector potential together with the electric scalar potential, such as:

$$\mathbf{B} = \nabla \times \mathbf{A} \Rightarrow \mathbf{E} = -\partial \mathbf{A} / \partial t - \nabla \varphi \tag{2.72}$$

By following similar arguments as before, the equations are:

$$\nabla \times \left(\mu^{-1} \nabla \times \mathbf{A}\right) + \sigma \frac{\partial \left(\mathbf{A} + \nabla \varphi\right)}{\partial t} = 0 \quad \text{in } V_c \tag{2.73}$$

$$\nabla \cdot \left(\mu \nabla \Omega\right) = 0 \text{ in } V - V_c \tag{2.74}$$

In order to assure the uniqueness of each quantity, similar gauge conditions as before have to be imposed.

This formulation represents the eddy current case of the magnetostatic formulation described in paragraph 2.2.1.4; similar comments are valid regarding the coupling of the two magnetic potentials.

2.3 Integral formulations

Up to now formulations have been consider able to determine the magnetic field or related quantities in every points of the domain. They are expressed in terms of differential operators which act on the unknown. For this reason they are called differential formulations. In their numerical implementation, they have advantages related to the sparsity of the resulting matrices. On the other hand they have the drawback to require to model, in general, a huge domain since the equations involve also the surrounding vacuum (air) region.

A different approach is based on the calculation of the fields in a limited number of points as integration of the contribution of each source in these points; in the magnetic case this is done by applying the Biot-Savart law. In magnetostatics this is trivial, since all the sources are known, while in the magneto-quasi-static case some of the sources are unknown. However, it is possible to assume these unknown sources as the unknowns of the problem, obtaining formulations which involve the unknowns through integral operators. For this reason they are called *integral formulations*.

This has the advantage of requiring modeling the only conductive regions and so, in general, reducing and simplifying a lot the mesh. A drawback is related to the difficulty of appling the method to magnetic materials, since they result like sources and this imply a quite complex treatment.

Considering the magneto-quasi-static case, the unknowns are currents induced in conductive materials V_c. Neglecting the presence of magnetic materials, the equations to be solved are the (2.45) together with the constitutive relations (2.46). The first of the equations (2.45) is automatically satisfied by assuming:

$$\mathbf{E} = -\partial\mathbf{A}/\partial t - \nabla\varphi \tag{2.75}$$

Introducing the magnetic vector potential (with the Coulomb gauge), the **B** solenoidality is automatically satisfied and the Biot-Savart law:

$$\mathbf{A}(\mathbf{r},\mathrm{t}) = \frac{\mu_0}{4\pi}\int_{V_c}\frac{\mathbf{J}(\mathbf{r}',\mathrm{t})}{|\mathbf{r}-\mathbf{r}'|}dV' + \mathbf{A}_\mathbf{s}(\mathbf{r},\mathrm{t}) \tag{2.76}$$

allows to satisfy the second of the (2.45) and the first of the (2.46). $\mathbf{A_s}$ is the magnetic vector potential given by the known sources located in $V - V_c$ and it is expressed in terms of the known current density $\mathbf{J_s}$ as:

$$\mathbf{A_s}(\mathbf{r},\mathrm{t}) = \frac{\mu_0}{4\pi}\int_{V-V_c}\frac{\mathbf{J_s}(\mathbf{r'},\mathbf{t})}{|\mathbf{r}-\mathbf{r'}|}dV' \tag{2.77}$$

Therefore, the problem is closed by satisfying the second of the (2.46):

$$\sigma^{-1}\mathbf{J}(\mathbf{r}) + \frac{\mu_0}{4\pi}\frac{\partial}{\partial t}\left(\int_{V_c}\frac{\mathbf{J}(\mathbf{r'})}{|\mathbf{r}-\mathbf{r'}|}dV'\right) + \frac{\partial \mathbf{A}_s}{\partial t} + \nabla\varphi = 0 \quad \text{in } V_c \tag{2.78}$$

The unknown **J** has to satisfy the following conditions:

- $\mathbf{J}\cdot\hat{\mathbf{n}}\big|_{\Sigma_c} = 0$
- $\nabla\cdot\mathbf{J} = 0 \quad \text{in } V_c$
- $\left\|\mathbf{J}\cdot\hat{\mathbf{n}}\right\| = 0 \quad \text{in } V_c$

Being **J'** a test function with the same properties of **J**, the weak form of equation (2.78) results:

$$\int_{V_c}\mathbf{J'}(\mathbf{r},\mathrm{t})\cdot\left\{\sigma^{-1}\mathbf{J}(\mathbf{r},\mathrm{t}) + \frac{\mu_0}{4\pi}\frac{\partial}{\partial t}\int_{V_c}\frac{\mathbf{J}(\mathbf{r'},\mathrm{t})}{|\mathbf{r}-\mathbf{r'}|}dV' + \frac{\partial \mathbf{A}_s}{\partial t}\right\}dV = 0 \quad \forall\mathbf{J'} \tag{2.79}$$

where the term involving $\nabla\varphi$ doesn't contribute thanks to the properties of the test functions **J'**[1].

2.4 Edge-element approach

According to the previous paragraphs, the continuity of the tangential component of **E**, **H**, **A** and **T**, as well as the normal component of **B**, **D** and **J**, is required at any material interface. The normal component of **E**, **H**, **A** and **T**, as well as the tangential component of **B**, **D** and **J**, are instead free to jump. Moreover, the scalar potential φ, ψ and Ω should be continuous.

Particular care has to be paid in the discretization process involved in the finite element approach, since the use of the more common nodal shape function forces all the component of fields and potentials to be continuous across neighboring elements. Therefore, when scalar potential formulations cannot be adopted in presence of materials with very different characteristics, the use of edge elements may be the best choice. As a matter of fact, the solution of the nodal vector potential formulation has been found to be incorrect when the normal component of the vector potential is significant at the interface between elements of different permeability [16].

---

[1] Given a conservative vector field $\boldsymbol{v}_{cons}(P,t) = -\nabla f(P,t)$ and a solenoidal field $\boldsymbol{v}_{sol}(P,t)$, being at least one of them equal zero outside the limited volume τ_v, it results $\int_{\tau_v}\boldsymbol{v}_{cons}(P,t)\cdot\boldsymbol{v}_{cons}(P,t)d\tau = 0$.

The degree of freedom of the edge elements are not to be interpreted as components of some vector fields at mesh nodes, but as circulations of the field along element edge, or rather they are associated with the tangential components along the edges of the elements. In this way, the adoption of edge elements for the representation of vector fields **E** and **H**, as well as vector potentials **A** and **T**, automatically guarantees the continuity of the tangential components. It is fair to say that edge-elements are part of a discrete algebraic structure (*Whitney's complex*) which closely matches the continuous differential one (*de Rahm's complex*) in which eddy-current equations lay [17]. Edge-elements are more natural in modeling magnetic and eddy-currents conditions, and in general best suited for solving 3D problems in presence of materials with different permeability.

Without going into detail, in the following the properties of edge-element shape function will be recalled. Denoted with N_k the shape function associated with the node *k*-th and with $\mathbf{N}_e$ the shape function associated with the edge $e = \{i, j\}$, connecting *i*-th and *j*-th nodes:

- The line integral of $\mathbf{N}_e$ along the edge $e = \{i, j\}$ is unity:

$$\int_{\{i,j\}} \mathbf{N}_e d\mathbf{l} = -\int_{\{i,j\}} \mathbf{N}_e d\mathbf{l} = 1 \tag{2.80}$$

- The line integral of $\mathbf{N}_e$ along any other edge is zero:

$$\int_{\{k,l\}} \mathbf{N}_e d\mathbf{l} = -\int_{\{l,k\}} \mathbf{N}_e d\mathbf{l} = 0 \quad \{i, j\} \neq \{k, l\} \tag{2.81}$$

- The tangential components of $\mathbf{N}_e$ are continuous across the facets of adjacent elements.
- The normal components of $\mathbf{N}_e$ are not necessarily continuous.
- $\mathbf{N}_e$ and $\nabla \mathrm{N_k}$ belong to the same functional space: the gradient of a nodal shape function is given by a linear combination of the edge shape functions having in common that node:

$$\nabla N_k = \sum_{e=1,E} \mathrm{G_{ek}} \mathbf{N}_e \tag{2.82}$$

  where E is the number of edges of the mesh and **G** is the *Ex**NP*** (where *NP* is the number of nodes of the mesh) incidence matrix defined as:

$$\mathrm{G_{em}} = \begin{cases} +1 & \text{if} \quad e = \{i, j\} \quad \text{and} \quad m = j \\ -1 & \text{if} \quad e = \{i, j\} \quad \text{and} \quad m = i \\ 0 & \text{otherwise} \end{cases} \tag{2.83}$$

2.5 Brief overview on the ANSYS code

ANSYS [29] code is a commercial general purpose package for computer-based engineering simulation, implementing the finite element method. It allows to perform simulations in almost any fields of physics of interest in engineering, such as structural mechanics, fluid dynamics, explicit dynamics, heat transfer and electromagnetism.

It integrates different graphical environments where the user can perform its analysis, from the creation of the mesh to the visualization of the results. Different environments have different characteristics in terms of building or import of the mesh and of ability to solve particular physics.

The so called Workbench platform is a particular user-friendly environment, which has the advantage of making quicker and easier the implementation of the model, but on the other hand it could result too automated leaving not enough freedom both in the building of the mesh and in the choice of the formulation. This is particularly true for electromagnetic cases, which by their very nature must be solved by a formulation rather than another according to the specific case. For this reason, the best environment for electromagnetic analysis is the classic one, where user can apply the best suited formulation by choosing the appropriate Element Type.

Here also the building of the mesh is leaved more free, since the user is able to create structured mesh in almost any part of the geometry by imposing the partition of each line. Indeed, in general, it is possible to choose between tetrahedral (only mapped parts) or hexahedra elements and then mixed structured and unstructured mesh parts are automatically joined by prismatic or pyramidal elements. The most of analysis types can be solved with linear or quadratic elements, by choosing the suitable Element Type.

Regarding to magnetics, ANSYS classic allows to solve 2D and 3D static, harmonic and transient problems, in presence of both linear and non-linear material. It allows to model current sources, permanent magnets and ferromagnetic materials, as well as to solve different type of coupled analysis. In particular regarding current sources, they can be stranded coils or massive conductors, both obtained by a meshed geometry or by primitives consisting of predefined geometries. Coils and conductors can be current or voltage fed, as well as connected to an electric circuit.

Any kind of 2D magnetic problem is, evidently, solved in terms of magnetic vector potential **A** which in these cases reduces to a scalar quantity, its A_z component.

As already mentioned in the previous paragraph, in 3D geometry several formulations can be adopted to solve magnetic problems. ANSYS implements both nodal and edge-element approach in terms of magnetic vector potential **A** to solve harmonic and transient problems. In case of magnetostatic problems one has to choose among the following options:

- *Magnetic scalar potential*: it can be used when solenoidality of current sources is assured. In turn it is divided in the following three solution strategies:
    - *Reduced Scalar Potential*: it can be adopted if no current sources or no iron region are within the problem domain at the same time. The RSP strategy uses a one-step procedure solving equations (2.24) and (2.26).
    - *Difference Scalar Potential*: it can be adopted when current sources and singly connected iron region exist within the problem domain at the same time. The DSP strategy uses a two-step procedure, which results in solving equations (2.31) and (2.32), with connection conditions (2.33) on the surface separating the high permeability region to the rest of the domain.
    - *General Scalar Potential*: it can be adopted when current sources and multiply connected iron region exist within the problem domain. The GSP strategy uses a three-step solution procedure, as the following:
        1. In the first step $\mathbf{H_s}$ is assumed solution on the air region, while in the iron region **H** is the solution of equation (2.26) having the second of the equations (2.28) as boundary condition for this region.
        2. In the second step a solution only in the air region is performed by solving here equation (2.26) and constraining the potential solution φ at the surface of the iron to be what it was calculated in the first step.
        3. In the third step the final value of the total field in the whole domain is calculated by applying equation (2.26) assuming as source field in the iron and air regions the fields determined in the first and second step respectively.
- *Magnetic vector potential* (*nodal*): it has a more general application but it is not recommended for models containing materials with different permeability. The solution

has been found to be incorrect when the normal component of the vector potential is significant at the interface of elements of different permeability [16].

- *Mixed scalar-vector potential*: It allows to get the advantages of using the scalar potential in regions where it can be used also when in some region it cannot. Here the nodal vector potential is used and the two formulation are coupled through a specified surface. This interface cannot be an air-iron boundary. This option is limited only to those cases in which the Reduced Scalar Potential formulation can be used. Non-eddy current iron domain can be placed in the scalar potential region, taking care to possible cancellation errors. The normal component of the vector potential has to be imposed equal to zero in order to ensure the vector potential solution is unique satisfying in this way the Coulomb gauge condition. In order to assure the symmetry of the system of equation, as illustrated in paragraph 2.2.1.4, the vector-scalar potential interface has to be completely within the domain. Otherwise part of the interface can be on the boundary of the domain only if it lays on a plane of symmetry or here the scalar potential is prescribed.
- *Edge flux degree of freedom*: It allows eliminating the shortcoming of the nodal based continuous vector potential formulation, leaving the normal component of the vector potential free to be not continuous. This formulation makes use of the so called Edge flux degree of freedom associated to the mid-side nodes of the elements. It corresponds to the component of the vector potential **A**, tangential to the element edge. In this way, the magnetic flux crossing an element face corresponds to the closed line integral of the vector potential. Thus, the sum of the DoFs supported by side nodes around a face is the flux crossing the face.

2.6 Brief overview on the CARIDDI code

CARIDDI [19] is a specific finite elements code for three-dimensional magneto-quasi-static problems, which was born for the analysis of eddy current induced in nonmagnetic conductor, and later extended to magnetic material. It is based on an integral formulation [18] and thus it requires a discretization only of the conducting structures, which can be also topologically complex. It allows also an easy coupling with external electric circuits [22] via suitable electrodes corresponding to a number of identified element surfaces. The introduction of a two-component electric vector potential and the use of first-order hexahedral edge elements give rise to a very accurate code, which closely parallels the correct solution by allowing to impose the right continuity conditions. It results to be also very effective, since it is able to deal with arbitrary 3D geometries of conducting structures, being them either massive structures or thin shell, with a minimal number of unknowns.

The mathematical formulation (considering the nonmagnetic material version) is that described in paragraph 2.3 and a numerical solution is obtained by applying Galerkin's method to equation (2.79). The unknown is the current density vector $\mathbf{J}$ which is represented as the linear combination of n basis functions $\mathbf{J}_f$ with the same properties of $\mathbf{J}$:

$$\mathbf{J}(\mathbf{r},\mathbf{t}) = \sum_{k=1,n} \mathrm{I}_{\mathrm{k}}(\mathbf{t})\mathbf{J}_k(\mathbf{r}). \tag{2.84}$$

According to the Galerkin's method n independent weighting functions are chosen to be the same basis function: $\mathbf{J'}_k = \mathbf{J}_k$.

Expanding $\mathbf{J}$ in terms of facet elements does not automatically assure its solenoidality, since the flux of $\mathbf{J}_k$ would be equal to zero across any face of the mesh except face k. However, the condition that the basic function $\mathbf{J}_k$ have the required properties of the unknown current density $\mathbf{J}$ can be satisfied by introducing the electric vector potential $\mathbf{T}$ ($\mathbf{J} = \nabla\times\mathbf{T}$), assuring the solenoidality of $\mathbf{J}$ and the continuity of its normal component, and adopting edge element shape functions for $\mathbf{T}$, allowing also to impose the boundary condition $\mathbf{J}_k = 0$ on Σ_c directly on the weight functions. The uniqueness of the vector potential is assured by the gauge $\mathbf{T}\cdot\mathbf{w} = 0$, where $\mathbf{w}$ is an arbitrary vector field which does not possess closed field lines. The discrete analogue of this gauge is conveniently imposed directly on the basis functions, introducing the tree-cotree decomposition of the mesh and eliminating the degrees of freedom associated to the tree edges

[18]. The shape functions are therefore derived from the *n* basis functions for the gauged vector potential:

$$\mathbf{J}_k = \nabla \times \mathbf{T}_k \tag{2.85}$$

where **T** is expressed as a linear combination of edge element shape functions $\mathbf{N}_e$:

$$\mathbf{T} = \sum_{e=1,E} \mathrm{T_e}(\mathbf{t})\mathbf{N}_e(\mathbf{r}) \tag{2.86}$$

where *E* is the total number of the element edges and the coefficient T_e provides the line integral of **T** along the oriented edge *e*.

Thus, applying Galerkin's method to equation (2.79), it reduces to the following linear system of ordinary differential equations, which can be solved by the use of a time stepping method:

$$\{L\}\frac{d}{dt}[I] + \{R\}[I] = [U] \tag{2.87}$$

where [*I*] is the column vector made of the I_k instant basis function coefficients, corresponding to the coefficient T_e associated to the activated[2] oriented edge *e* of the selected co-tree, and:

$$L_{ij} = \frac{\mu_0}{4\pi}\int_{V_c}\int_{V_c} \frac{\nabla \times \mathbf{N}_i(\mathbf{r}) \cdot \nabla \times \mathbf{N}_j(\mathbf{r}')}{|\mathbf{r} - \mathbf{r}'|} dV dV'' \tag{2.88}$$

$$R_{ij} = \frac{\mu_0}{4\pi}\int_{V_c} \nabla \times \mathbf{N}_i(\mathbf{r}) \cdot \sigma^{-1} \nabla \times \mathbf{N}_j(\mathbf{r}') dV \tag{2.89}$$

$$U_i = -\int_{V_c} \nabla \times \mathbf{N}_i(\mathbf{r}) \cdot \frac{\partial}{\partial t}\mathbf{A}_s dV \tag{2.90}$$

The major of the computational burden is the numerical calculation of the $\{L\}$ matrix, due to the double volume integral. Furthermore, it is worth noticing that particular care has to be paid to the singular contribution of $1/|\mathbf{r}\text{-}\mathbf{r}'|$. This is due to the attempt of approximating a continuous distribution with a discrete one and a method is implemented by considering uniformly charged spheres of adequate radius instead of point charges when these latter would coincide.

Further drawback of the formulation is that the $\{L\}$ matrix is completely full and accordingly the memory space it occupies goes with the square of the number of DoF.

On the other hand, a particularity of this formulation is to obtain the dynamic representation of the system which has been modelled. So, once the matrices have been calculated, CARIDDI can

[2] In order to impose the boundary condition $\mathbf{J}_k = 0$ on Σ_c, a procedure to deactivate those edges of the co-tree closing independent loop with the edges of the tree, which lay on the boundary of the mesh and thus correspond to current exiting external element surface, is implemented

calculate a predefined transient analysis, but it is also possible to re-arrange the matrices in order to get the model in the most convenient form, as for instance in state-space form.

3 Optimization of SPIDER magnetic configuration

3.1 Introduction

SPIDER is a full-size Negative Ion Source and a multi-beamlet 100 kV Accelerator, presently under construction in Padova and is part of PRIMA, the test bed for the full development of the Heating Neutral Beam system for ITER. During the final design, the SPIDER extractor and accelerator system has been improved with respect to the original configuration. In particular, the magnetic configuration has been optimized in order to improve the performances in terms of ion beam optics and aiming, and to obtain an efficient filter for the extracted electrons.

The purpose of SPIDER is to optimize the Ion Source performances by maximizing the extracted negative ion current density and its spatial uniformity and by minimizing the co-extracted electrons. Nominal operating current is 60 A with H^- ions (and later 40 A with D^- ions) and an energy of 100 kV.

As a matter of fact, the negative ion source of the neutral beam injectors for ITER requires that the electron current, which is co-extracted out of the ion source across the plasma grid, is not larger than the negative ion current [24]. To reduce the number of extracted electrons, the reference design [25] is characterized by a magnetic field configuration generated by a current flowing in the plasma grid and by two permanent magnets on either side of the source [9]. In this configuration however the magnetic field is not uniform across the beam.

A careful distribution of the filter field current can provide a more efficient extraction of negative ions with respect to electrons. The use of ferromagnetic material can reduce the magnetic field downstream with respect to the accelerator, resulting in lower beam deflection.

The work described in this chapter has involved the development of 2D and 3D magnetostatic models, mainly with the commercial finite element ANSYS code, for optimizing the magnetic field distribution inside the plasma source and accelerator region of the SPIDER device.

In particular paragraph 3.3 focuses on the adopted strategies aimed at optimizing the horizontal magnetic field distribution and improving the beam optics, based on two-dimensional magnetic field simulations.

Paragraph 3.5 describes the three-dimensional simulation carried out to address the vertical uniformity of the field, to analyze the vertical magnetic field contribution introduced by permanent magnets embedded in the EG, taking into account the effects of their finite extension, and optimizing the return PG current path.

3.2 Magnetic field sources in SPIDER reference design

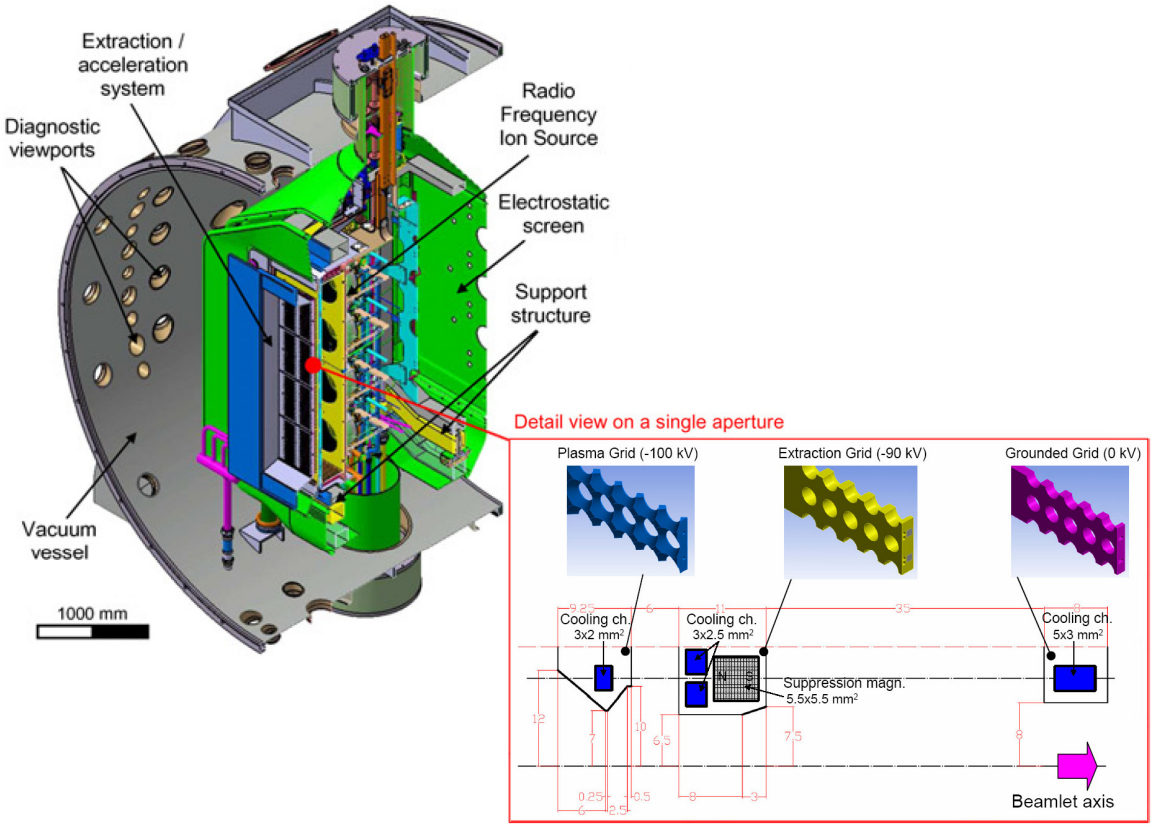

Figure 14: Design overview of the SPIDER extractor/accelerator system

The SPIDER ion source extraction and accelerator system, sketched in Figure 14, is composed of three grids: the Plasma Grid (PG), the Extraction Grid (EG) and the Grounded Grid (GG). The magnetic configuration in the SPIDER device is based on two different contributions, which in a first analysis can be considered separately: the Filter Field (FF) and the Suppression Field (SF).

The FF principally lies on the horizontal plane and should be as parallel as possible to the grids in the region immediately upstream relative to the PG. Its purpose is twofold: first is to separate

source electrons into two populations with different temperature in the same chamber, as described in paragraph 1.3.2.1; second aim is to reduce the electron current extracted through the PG apertures by forcing the electrons to hit the PG or the source walls, thanks to their lower Larmor radius than the ions. In the ITER reference design [25] the FF is generated by a current flowing in the PG, along its height, and by two permanent magnets on either side of the source [9]. The B_x component of the FF has to be maximized with respect to the others, since the vertical B_y and parallel horizontal B_z components are side effects due to the finite dimensions of permanent magnets and current path, as well as of the non-uniformity of the latter for the presence of the PG apertures and water manifolds, which may introduce magnetic field in-homogeneities and a possible path for the electrons to escape through the grid apertures.

The SF has a main vertical transverse magnetic field component (B_y) generated in the front and on the back of the EG apertures by permanent magnets embedded in the EG. Therefore the co-extracted electrons are deflected onto the EG, while the Ion trajectories, thanks to their grater Larmour radius, are only slightly deflected to the left or to the right, according to the sign of the vertical component of the SF, which changes on each subsequent aperture row (as it can be deduced by observing in Figure 14 the orientation of the permanent magnets). The ion beamlets are consequently subjected to a horizontal crisscross deflection, cause of non-homogenous power deposition on the GG and of distortion of the beamlet pattern, which deteriorates the overall beam aiming. The standard solution to mitigate this effect is an electrostatic action on the ions achieved by off-setting the EG apertures on the proper direction (see Figure 6). The drawback is its dependence on the grid voltages. Given the prototypal/experimental character of SPIDER, a more flexible solution based on magnetic deflection has been tested, proposed and accepted. It will be described in detail in paragraph 3.5.2.

In Figure 15 a horizontal section of the SPIDER ion source and accelerator is shown, where the FF sources as foreseen in the reference design are highlighted in color.

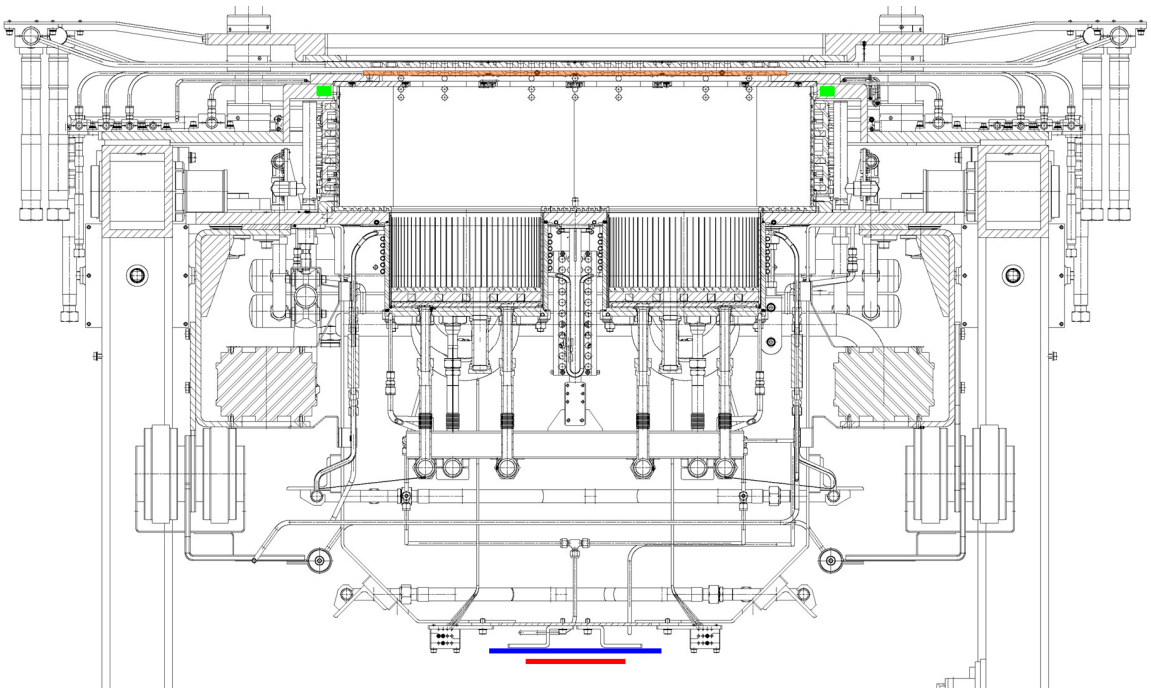

Figure 15: Horizontal section of the SPIDER ion source and accelerator, with highlighted in color the FF sources as foreseen in the reference design. In orange the PG, in green the two side permanent magnets, in blue a ferromagnetic shield and in red the conductor for the return path of the PG current.

According to [25], the FF has foreseen to be produced by two permanent magnets on the sides of the grids (green) and by 4 kA flowing through the PG (orange). PG current is closed through a conductor placed on the back side of the whole ion source system (red). A ferromagnetic layer (blue) is interposed to shield the magnetic field related to the return path of the PG current, in particular to limit the stray field in the region of the RF drivers.

3.3 2D analyses

The magnetic field configuration inside the plasma source and extraction/accelerator region has been initially optimized on the basis of 2D magnetostatic analyses, involving the FF only, using the commercial FEM software ANSYS. The SF was not considered at this stage, because it involves a mainly vertical component of the magnetic field, which cannot be represented in the 2D model used for the FF. Specifically in this stage the following objectives have been pursued:

- uniformity of magnetic field in the ion source;
- reduction of the axial component of the magnetic field in the ion source;
- reduction of the horizontal component of the magnetic field inside the accelerator;
- reduction of the horizontal magnetic field downstream relatively to the grounded grid.

Similar investigations have already been carried out by other authors. For instance, [26] describes the increase of source uniformity using the magnetic configuration frequently adopted in positive ions sources, featuring a tent-shaped magnetic field due to a suitable arrangement of permanent magnets. In [27] the authors have investigated the possibility of improving the uniformity of the magnetic field configuration by machining the plasma grid (PG) so that the PG current is forced to follow specific paths.

The approach adopted in the present work aims at simplifying the design of the magnetic configuration and at making it more flexible. Several magnetic field configurations have been considered, including the roles of ferromagnetic material, suitable currents and permanent magnets.

In the following, the magnetic field sources will be introduced along with the ANSYS numerical model; then the results of the best cases will be presented. A comparison of the proposed solutions in terms of particle trajectories will be given.

3.3.1 2D model description

A horizontal section of the ion source and accelerator was considered. Only half of this section has been modeled, thanks to the intrinsic symmetries. A representation of the model used, which summarizes the different configurations tested, is reported in Figure 16.

The model considers the grids, PG, EG and GG; the filter field permanent magnet; another conductor on the side where the PG current can be diverted; also the conductor for the current return was included, and several positions and configurations were tested for the return path of the current. More precisely, the conductor for the current return initially was located on the back side of the device (dark green bar called Return Conductor A in Figure 16), behind a ferromagnetic plate (blue bar in Figure 16 called Magnetic Shield); other solutions were also tested and in particular the best one consists of three conductors placed on the back side of the plasma source among the RF drivers, as it is shown in Fig. 1 with the tag Return Conductor B.

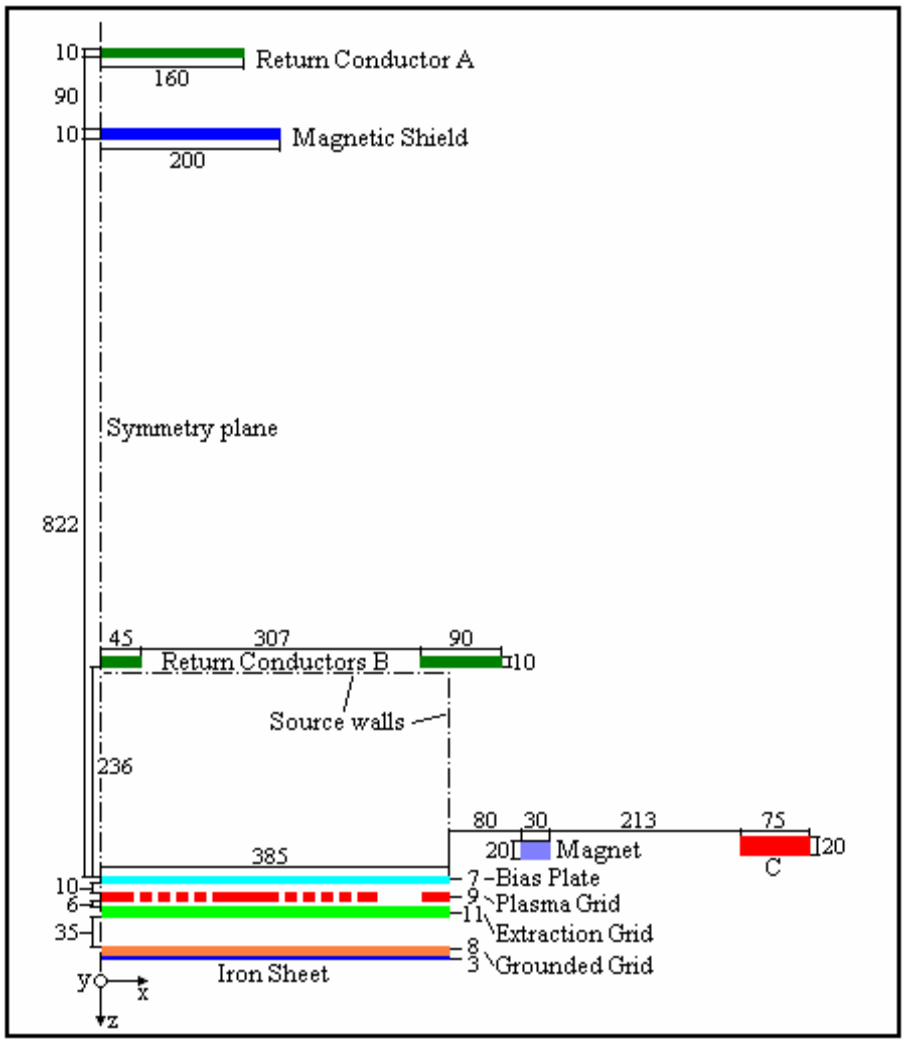

Figure 16: Representation of the 2D ANSYS model; source wall are indicated (RF drivers are not shown). The beam is along z; numbers indicates dimensions in mm.

Several configurations have been tested including various methods to modify the magnetic field: return current partially flowing in additional conductors; forward current partially flowing in additional conductors as well; ferromagnetic inserts in PG, among the beamlet groups, as is highlighted in blue colour in Figure 17; the effect of a ferromagnetic plate on the GG, on the downstream side (blue colour), etc. The reference case and the most promising results will be described in detail in the paragraph below.

Because of the beamlet apertures and the cooling water manifold, the current flowing in the PG is characterized by a non uniform current density. To build a two-dimensional model sufficiently realistic, the PG has been modeled, instead of a simple bar, as a bar interrupted as many times as the apertures, in order to take this fact into account. These "equivalent 2D holes" have a width which is given by the ratio between "vacuum" volume and solid volume, multiplied by grid

length and divided by aperture number. The lateral hole on the PG represents the coolant manifold.

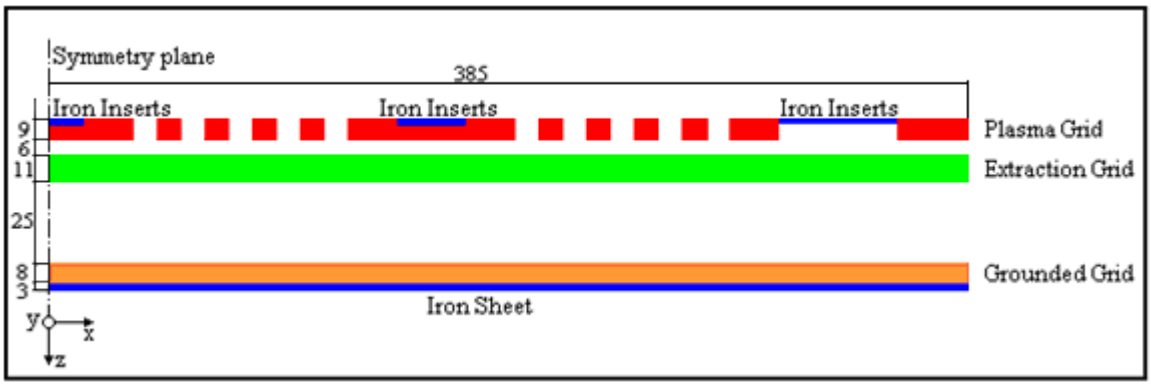

Figure 17: Zoom of the grid region in the 2D ANSYS model.

3.3.2 2D magnetic field computations

In this paragraph the four most significant cases are described; these are:

Case A: the reference case [25], which considers the magnetic field due to the FF magnets and that due to the 4 kA current flowing through the PG and its return through the return conductors A (see Figure 16);

Case B: current return as in A; filter magnets as in A; higher FF current distributed between the PG, 3 kA, and conductors C (Figure 16), 2x1.5 kA; 3 mm ferromagnetic plate in the GG;

Case C: same as B, but the return of the total current is divided in the three conductors B (Figure 16) placed on the back side of the plasma source, among the RF drivers: the central one has a current of 3 kA, while those in the side have 1.5 kA each one;

Case D: the same case as the former without the FF permanent magnets.

3.3.2.1 Case A

In this case, two permanent magnets are located on the grid sides and a current of 4 kA flows through the PG to form the FF. The orientation of the permanent magnetsis such that the two horizontal components of the magnetic field are added upstream the Plasma Grid, while they are subtracted downstream, in order to obtain a high horizontal field in the ion source and a lower one in the accelerator and downstream.

As shown in Figure 18, the field obtained is not uniform upstream of the PG from the grid centre (left side of the picture) to the edges, where the magnetic field is stronger. This can be seen also in Figure 19: the central beamlet group is subject to a field of about 4-5 mT upstream PG and 2

mT downstream, while the lateral group is subject to a field of about 5-6 mT upstream PG and less than 1 mT downstream. Figure 20 shows a high axial component of the magnetic field in the lateral beamlet group compared to the horizontal one, about 20÷30%. This means a large angle between field lines and the *x* axis in this region, as seen in Figure 18. Large electron extraction can result from the side beamlet groups, which has to be avoided.

These considerations, as well as those for the subsequent cases, are supported by the analysis of field profiles along some paths shown in Figure 32 to Figure 39, where the profiles are shown together in order to compare the four cases.

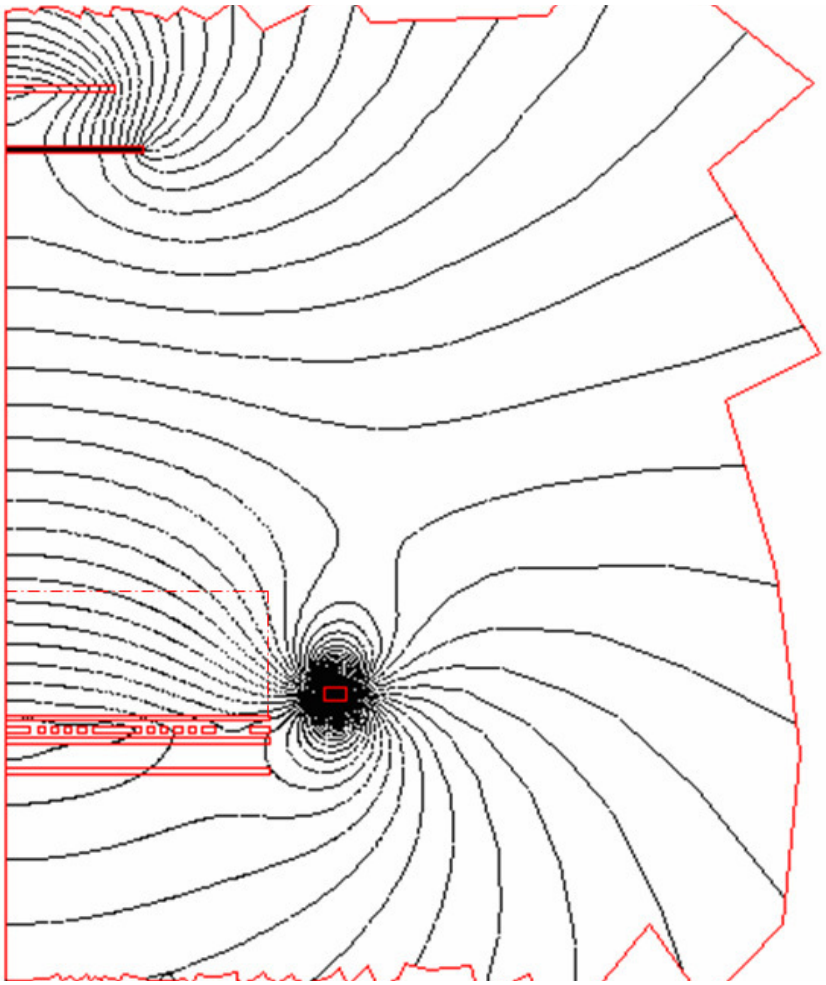

Figure 18: Magnetic equiflux lines in the device, reference case (A).

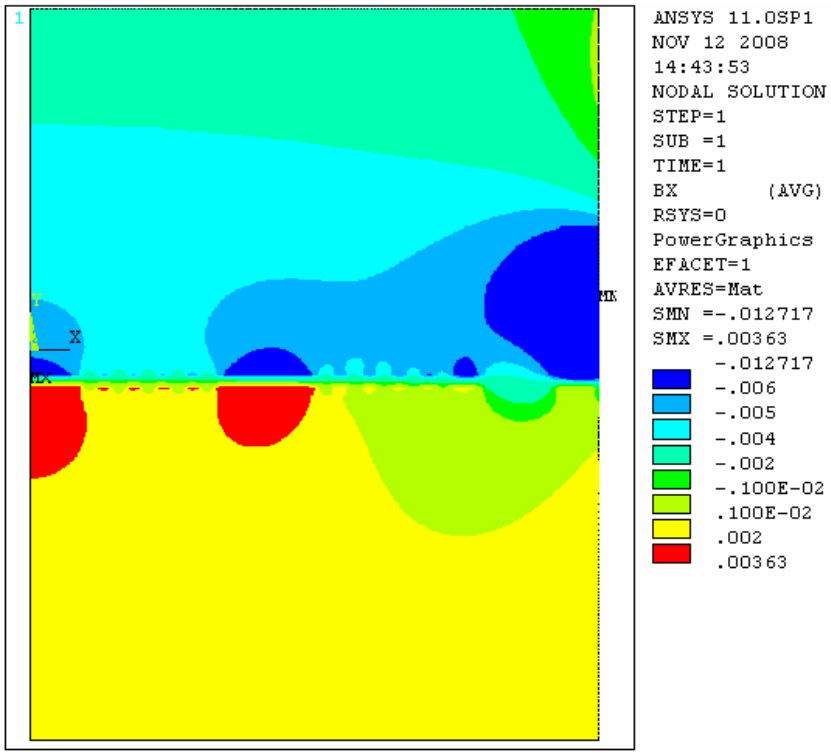

Figure 19: Horizontal (X) component of magnetic field in the ion accelerator, reference case (A).

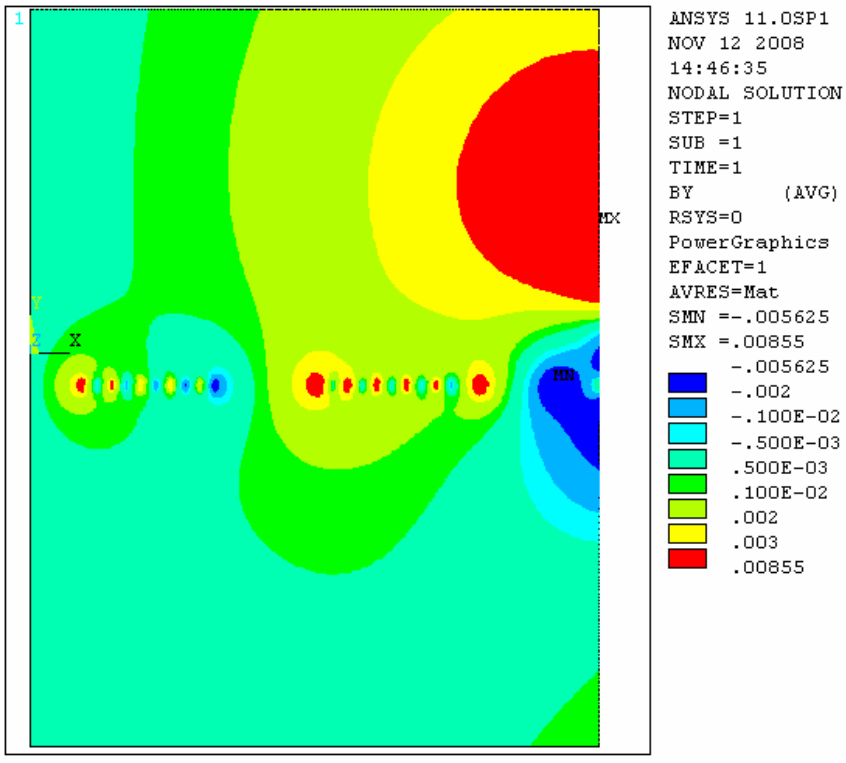

Figure 20: Axial (Z) component of the magnetic field in the ion accelerator, reference case (A).

3.3.2.2 Case B

The best configuration found to improve the magnetic uniformity upstream the PG and to reduce the field downstream the GG, while maintaining the current return in the back side of the device, has been obtained with a current of 3 kA through the PG and another forward current of 1.5 kA in both side conductors, and a ferromagnetic plate on the downstream side of the GG.

In Figure 21 and Figure 22 it can be seen that the use of the additional two conductors increases the magnetic horizontal uniformity: as a matter of fact upstream of the PG the B_x component of the magnetic field is more uniform, about 5 mT. The figures also show the effect of a ferromagnetic plate in reducing the B_x component downstream PG, even below 1 mT.

As it can be inferred from Figure 21 and Figure 23, the field lines on the side of the grid are not parallel to the grid.

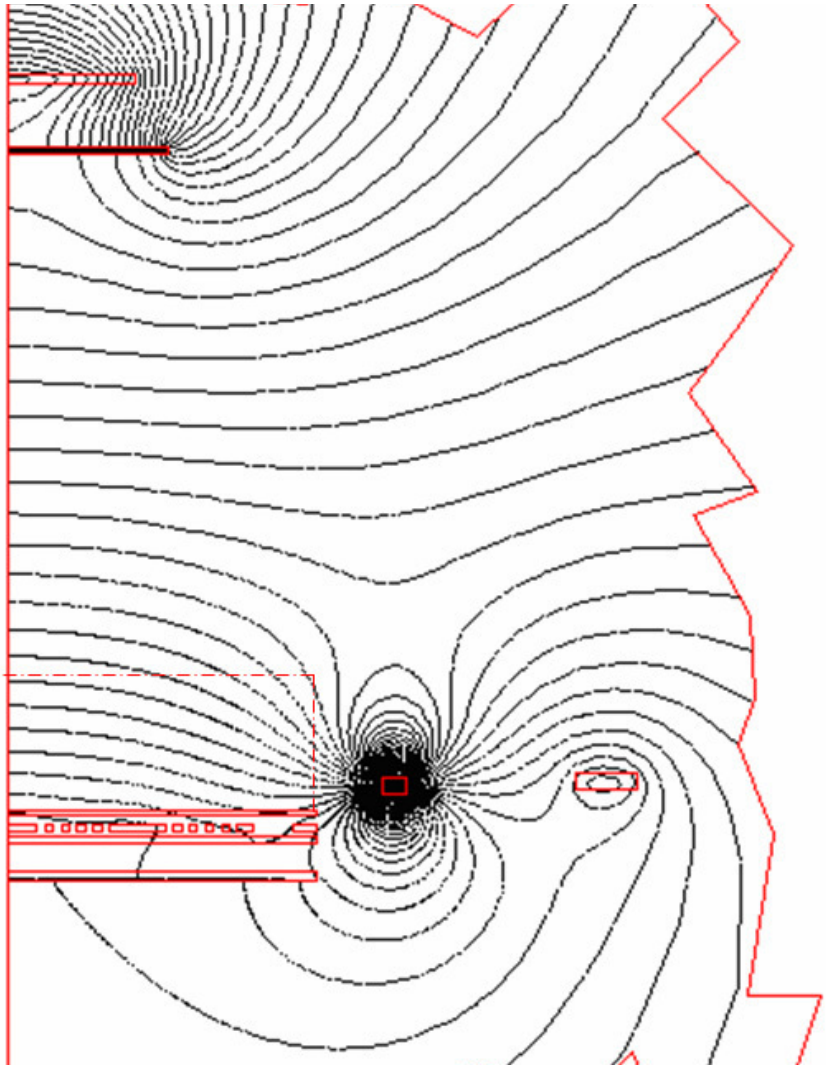

Figure 21: Magnetic equiflux lines in the device (case B).

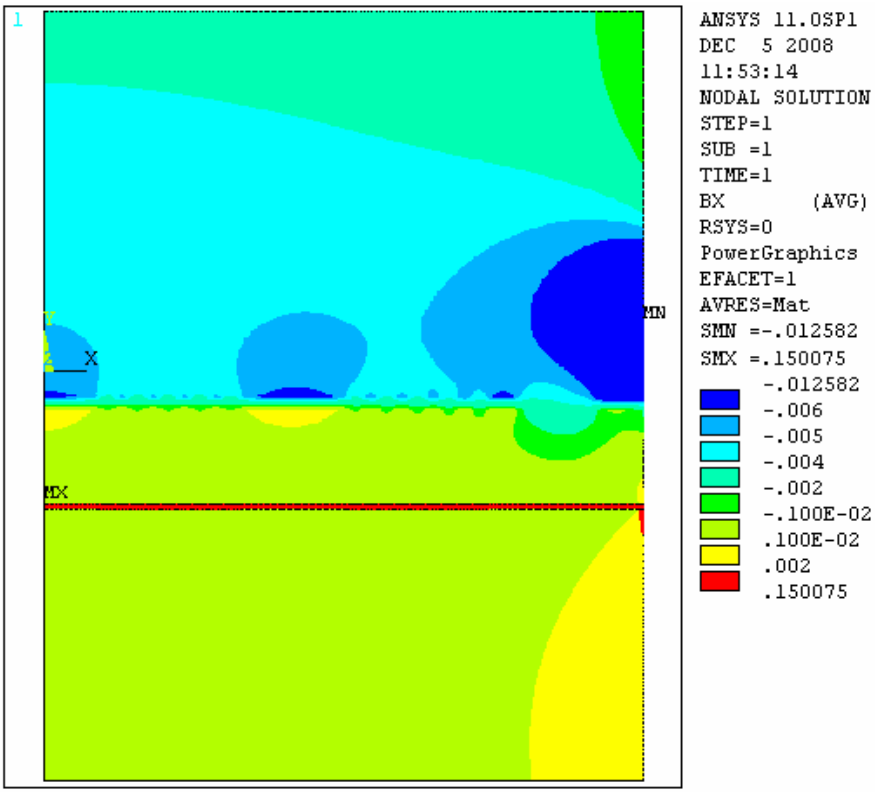

Figure 22: Horizontal (X) component of the magnetic field in the ion accelerator (case B).

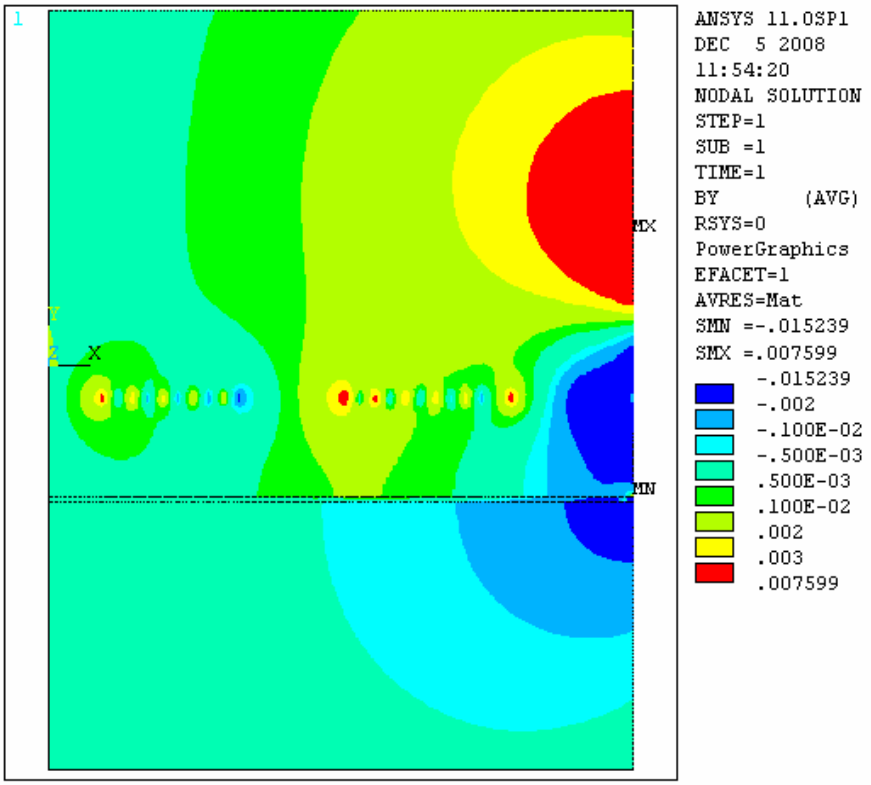

Figure 23: Axial (Z) component of the magnetic field in the ion accelerator (case B).

3.3.2.3 Case C

A configuration “more similar to a solenoid” could improve the intensity and the uniformity in the plasma source, and also reduce the field outside the solenoid, downstream the PG. So the return current was placed nearer to the PG and distributed along it: the return current was evenly divided in the three conductors B Figure 16, placed in the back plate of the plasma source, between the RF drivers.

Figure 24 shows that the magnetic field downstream the GG is almost negligible and displays the profile of the field lines. In Figure 25 it can be seen that better uniformity of the horizontal component of the magnetic field upstream of the PG has been obtained, together with its lower value downstream.

The axial component of the magnetic field is also reduced, as it can be seen in Figure 26, below 1 mT except in the outermost aperture of the side beamlet groups.

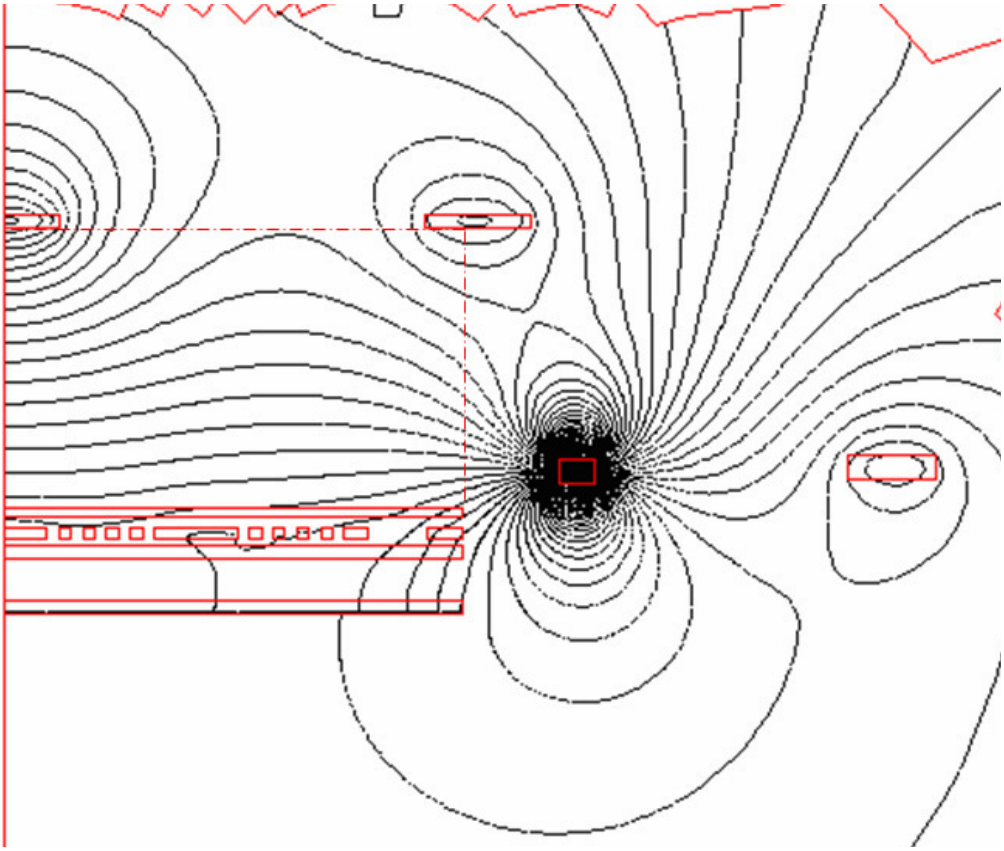

Figure 24: Magnetic equiflux lines in the device (case C).

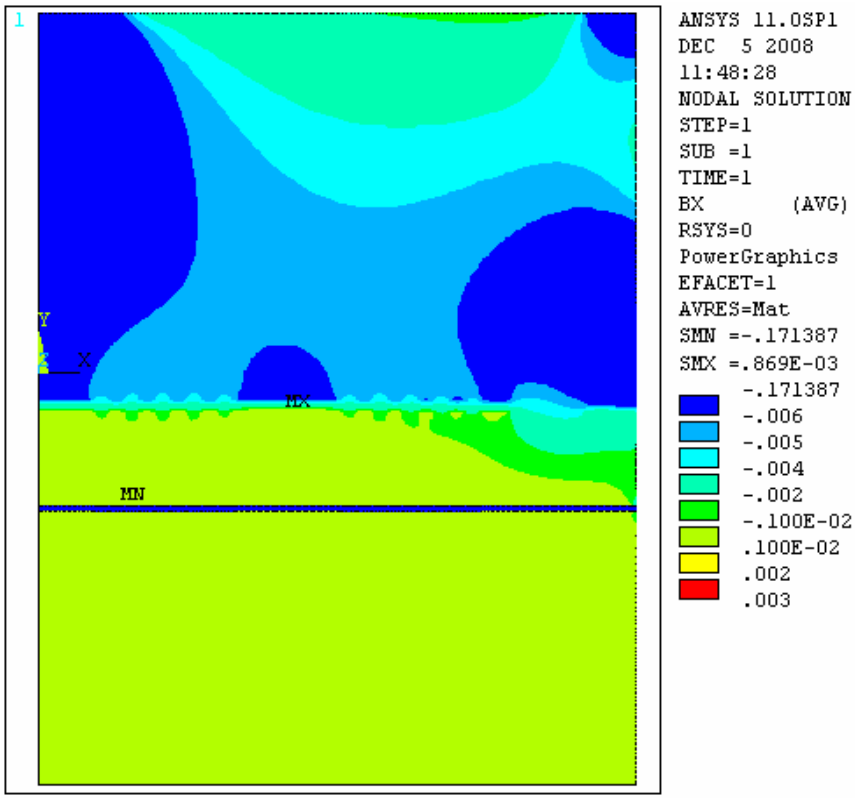

Figure 25: Horizontal (X) component of the magnetic field in the ion accelerator (case C).

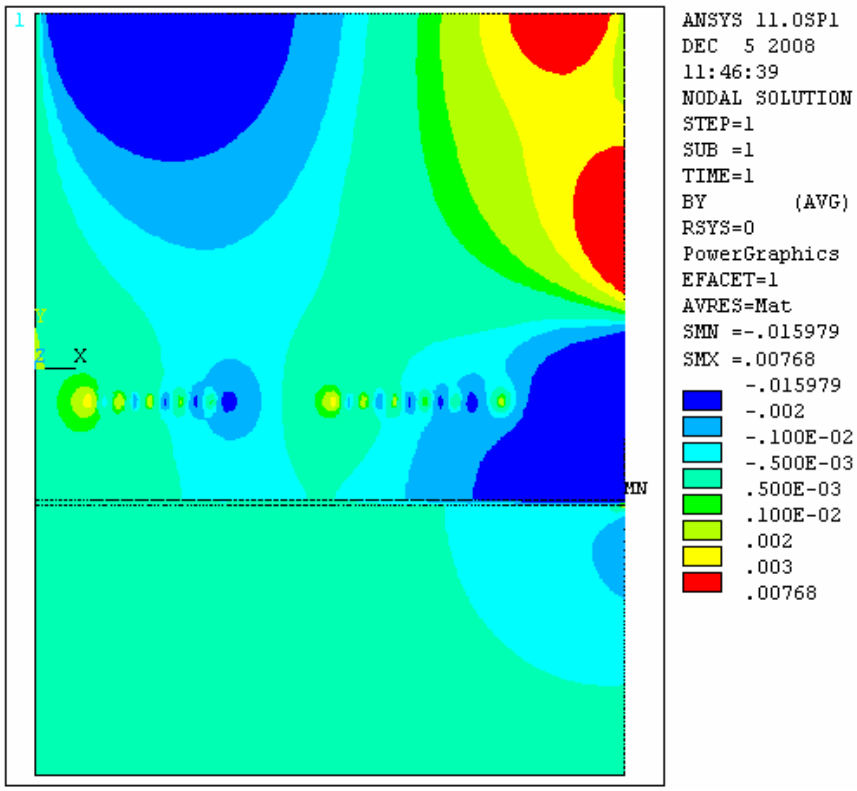

Figure 26: Axial (Z) component of the magnetic field in the ion accelerator (case C).

3.3.2.4 Case D

In order to improve the uniformity of the FF on the lateral beamlet groups and to ensure the field lines upstream of the PG are parallel to the grid, a new set of configurations was considered. These configurations do not include permanent magnets and rely only on the current busbars for the production of the FF.

Figure 27 and Figure 28 show that the combined effect of bringing the return current nearer to the PG and the absence of the filter field magnets improves the uniformity upstream the PG and reduces the magnetic field downstream. In particular there are no more field lines which connect directly the plasma source to the beamlet apertures: this prevents electrons which follow the magnetic field lines from crossing the apertures and maximizes the ratio of negative ion current to electron current, being minimum the ratio of axial to horizontal magnetic field components.

In addition, by varying the current, this solution gives the possibility to regulate the FF strength being the magnetic configuration completely produced by currents, while the spatial distribution remains unchanged.

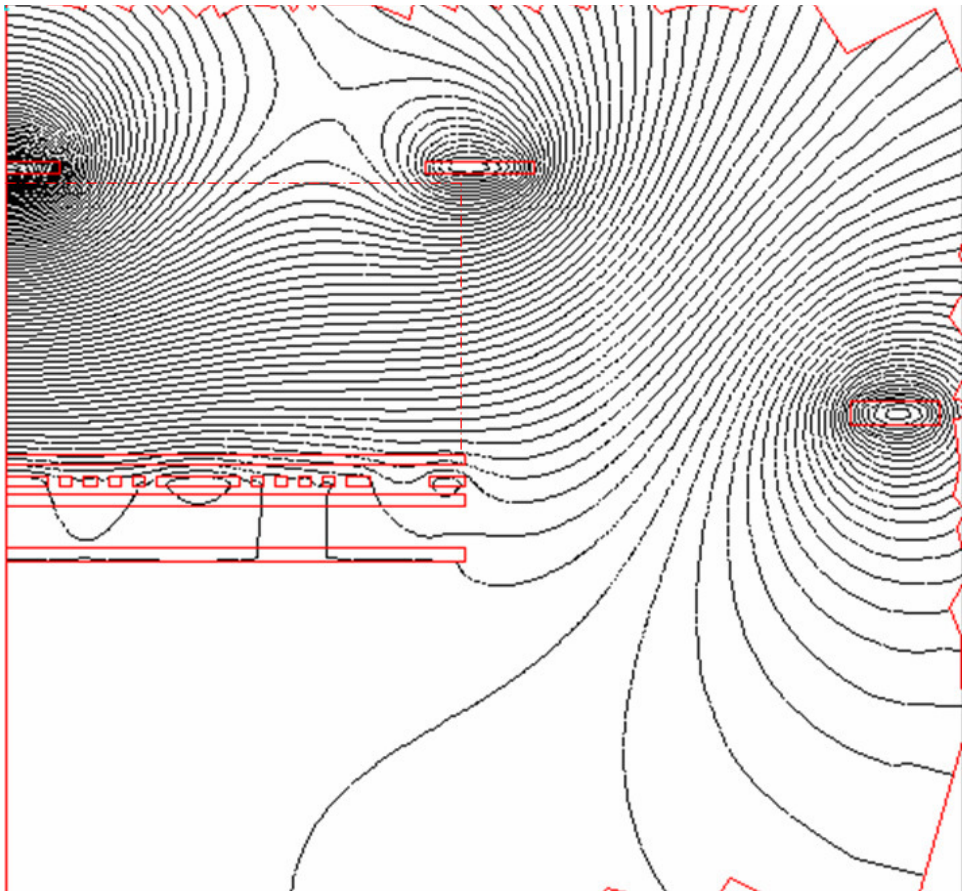

Figure 27: Magnetic equiflux lines in the device (case D).

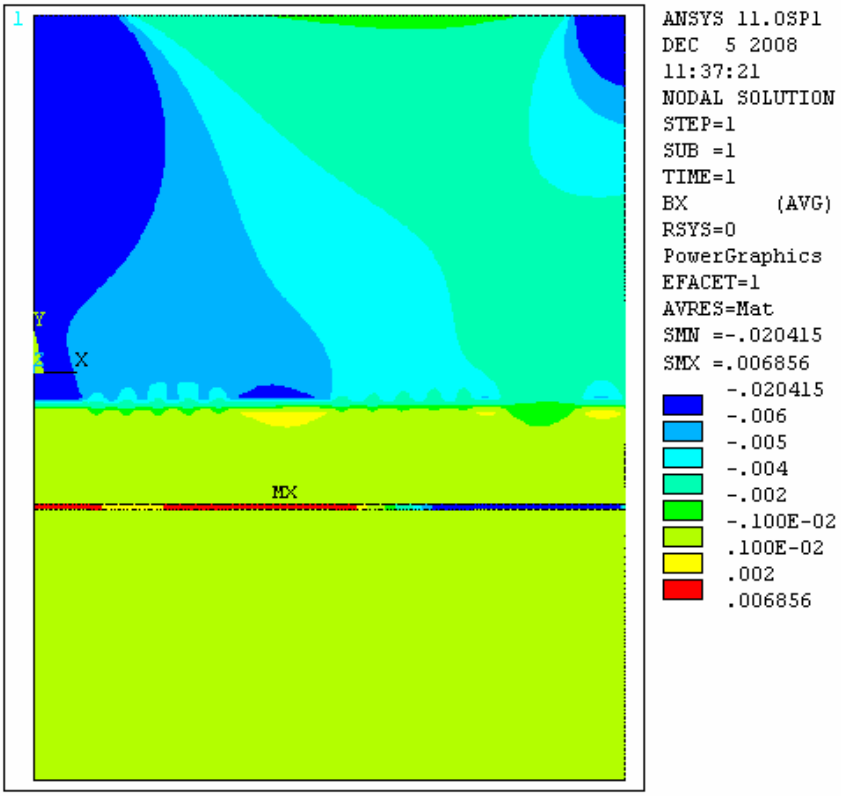

Figure 28: Horizontal (X) component of the magnetic field in the ion accelerator (case D).

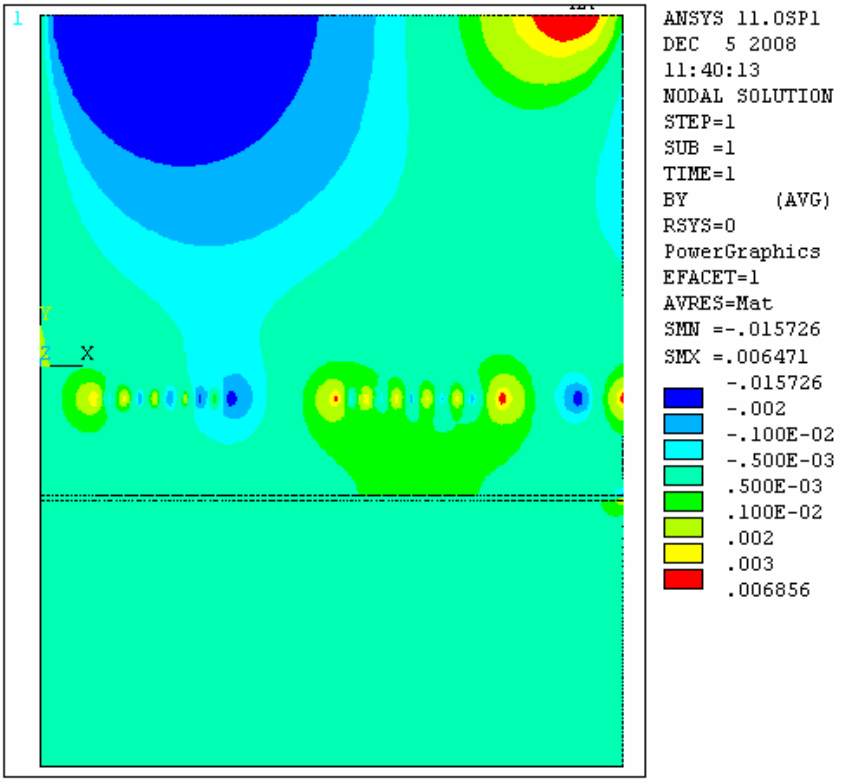

Figure 29: Axial (Z) component of the magnetic field in the ion accelerator (case D).

3.3.2.5 Comparison among configurations

In Figure 30 the magnetic flux lines in the ion accelerator of the four different cases described before are compared. It is easy to see that from case A to D the magnetic flux density downstream the GG decreases, while upstream the PG it increases.

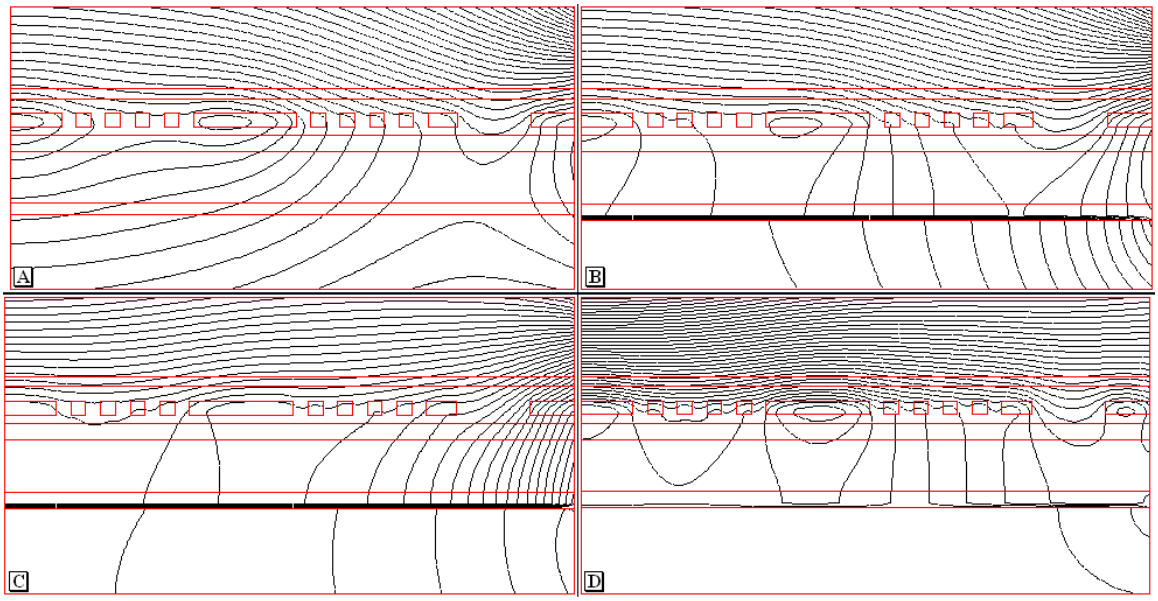

Figure 30: Comparison of the magnetic equiflux lines in the accelerator among the four different cases.

Moreover, in cases A and B many of the magnetic flux lines, which lie inside the source and run parallel to the grids upstream the central beamlet group, go inside the holes of the lateral beamlet groups, dragging many electrons of the plasma source in these apertures. In case C only some flux lines which come from the source sides enter some beamlet apertutes. On the contrary, in case D the flux lines which reach the holes come from the region upstream of the PG where the plasma has a lower density. Therefore case D probably minimizes the electrons extracted from PG.

It must also be noticed that, thanks to the absence of the permanent magnets, the magnetic configuration in case D does not behave like a magnetic mirror on the sides of the plasma grid, thus avoiding the accumulation of high energy electrons near the PG.

In the following, the B_x and B_z magnetic field components are plotted along several paths, whose location is sketched in Figure 31. The magnetic field profiles are displayed together in the next figures in order to have a more careful comparison of the four cases.

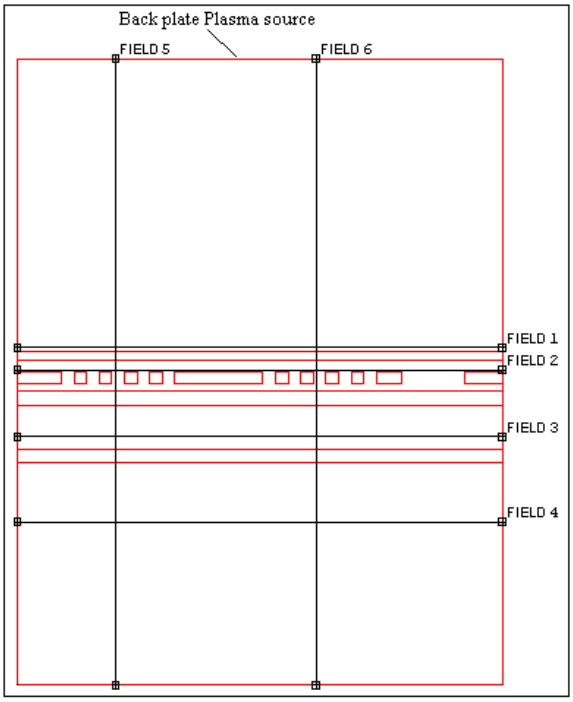

Figure 31: Paths for the following figures.

In Figure 32 through Figure 37, the red vertical lines represent the area occupied by the two beamlet groups, while the blue vertical lines correspond to the axis of each beamlet.

In Figure 32 the horizontal component of the magnetic field along a path parallel to the grids 20 mm upstream PG is displayed. The best would seem the case C since it shows the best B_x uniformity among beamlet groups as well as the highest values.

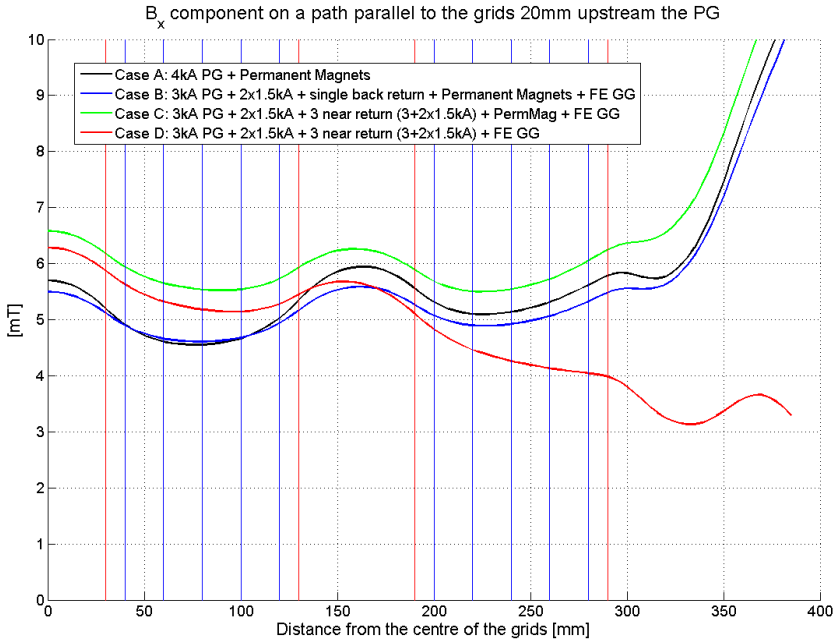

Figure 32: B_x component along a path parallel to the grids 20 mm upstream the PG (FIELD1 in Figure 31).

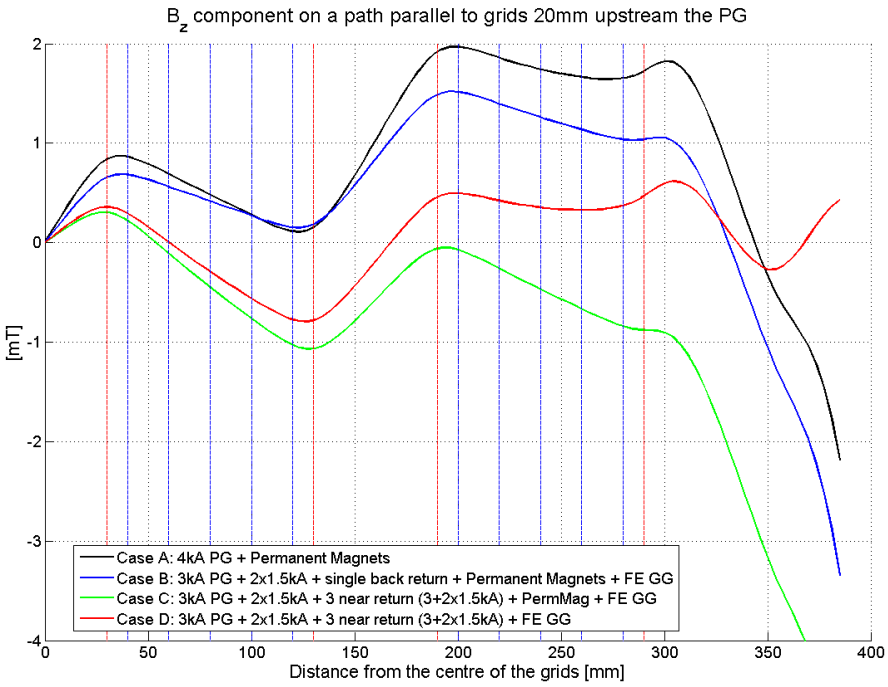

Figure 33: B_z component along a path parallel to the grids 20 mm upstream the PG (FIELD1 in Figure 31).

Figure 33 shows the axial component of the magnetic field along the same path as Figure 32. Case D is a little better than the others because the maximum values are lower than case C; however this difference is less meaningful because of the larger B_x of case C.

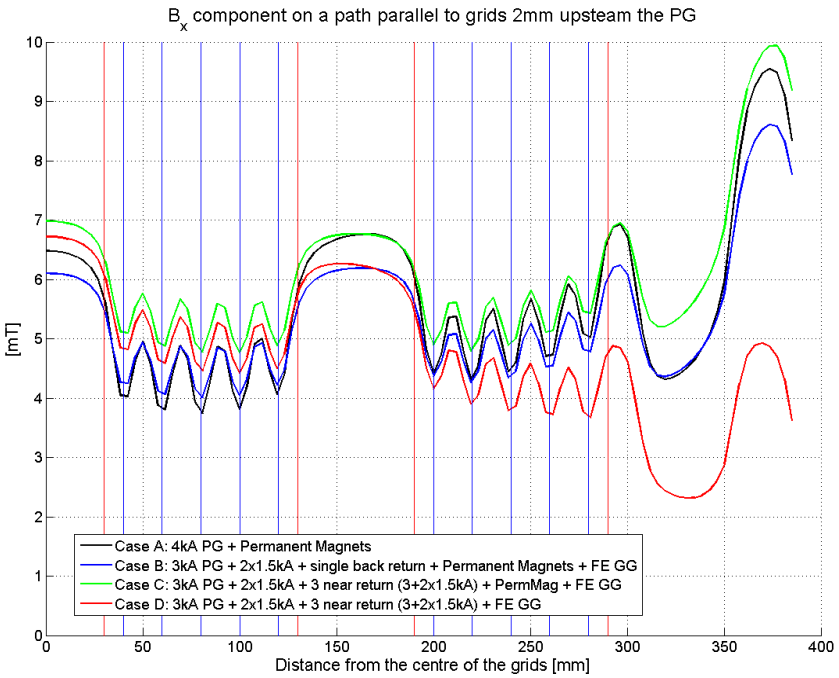

Figure 34: B_x component along a path parallel to the grids 2 mm upstream the PG (FIELD2 in Figure 31).

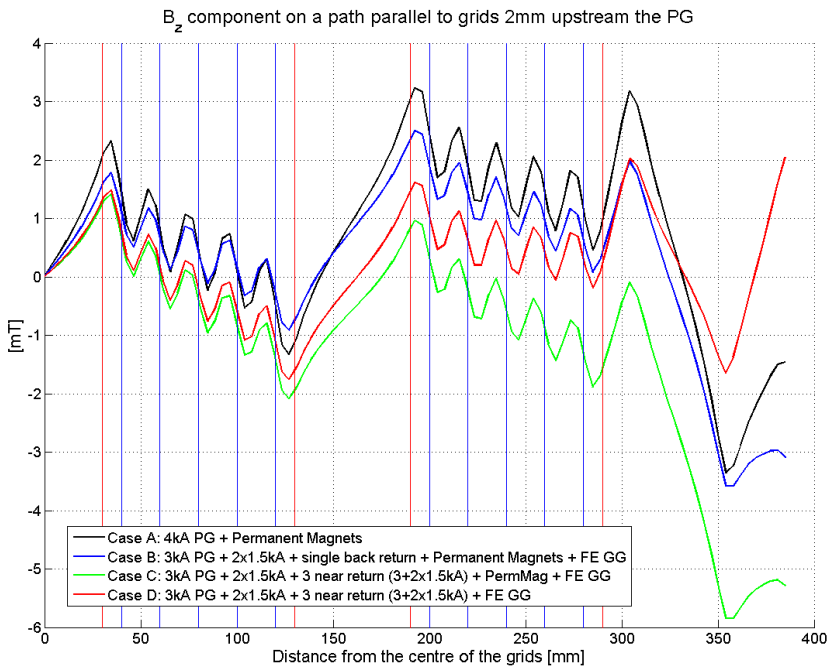

Figure 35: B_z component along a path parallel to the grids 2 mm upstream the PG (FIELD2 in Figure 31).

Similarly, Figure 34 and Figure 35 show the horizontal and axial component respectively of the magnetic field along a path parallel to the grids 2 mm upstream the PG. In this case the effect of the apertures is obviously more manifest.

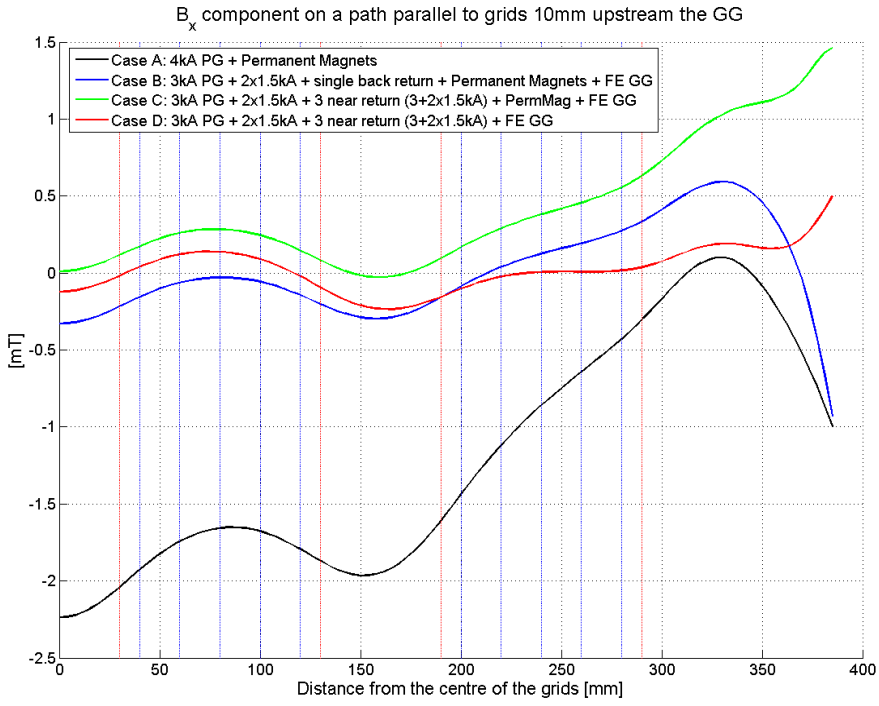

Figure 36: B_x component along a path parallel to the grids 10 mm upstream the GG (FIELD3 in Figure 31).

From the observation of Figure 36, which shows the horizontal component B_x of the magnetic field along a path 10 mm upstream the GG (between the EG and the GG), case D would seem the best, since in this region the B_x component of the field is the lowest, resulting in a lower beamlet vertical deflection. Anyway, the large reduction compared to the reference case is clear.

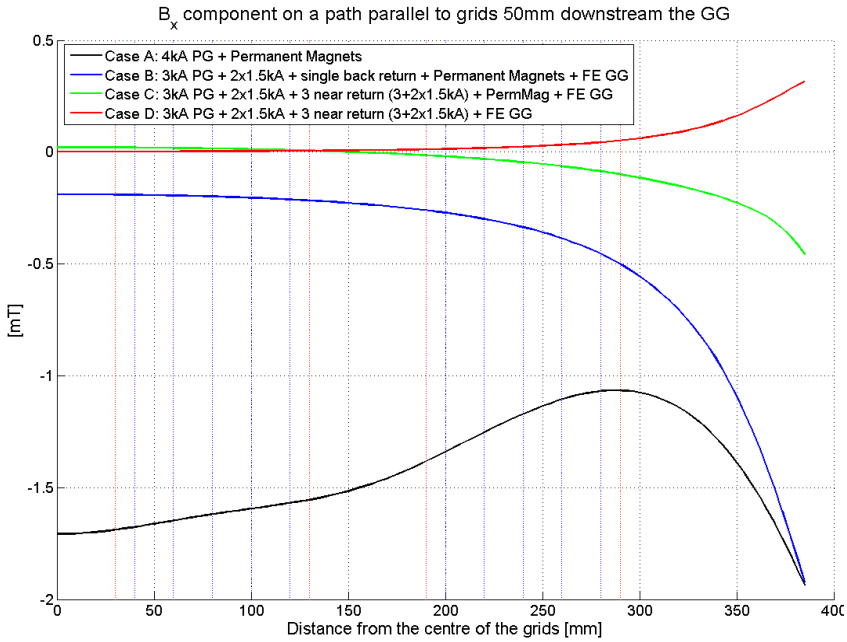

Figure 37: B_x component along a path parallel to the grids 50 mm downstream the GG (FIELD4 in Figure 31).

Figure 37 shows the horizontal component of the magnetic field along a path parallel to the grids 50 mm downstream the GG, outside the ion accelerator. The improvement of the optimized cases with respect to the reference is obvious, in terms of reduction of stray magnetic field and uniformity. In particular case D is the best; also case C is very good, with a slightly higher B_x component.

Figure 38 and Figure 39 display the horizontal component of the magnetic field along a particle trajectory in the centre of the central beamlet group and in the centre of the lateral beamlet group respectively. Case C is the best in terms of field strength in the plasma source, whereas case D is the best in terms of lower field downstream the PG; both conclusions are true also for the lateral beamlet group.

On the basis of the features of the magnetic field, it can be concluded that the best conditions seem to be those of case D; anyway the subsequent introduction of the two side permanent magnets will be leaved available.

In the following the effect of the magnetic field on particle motion will be studied.

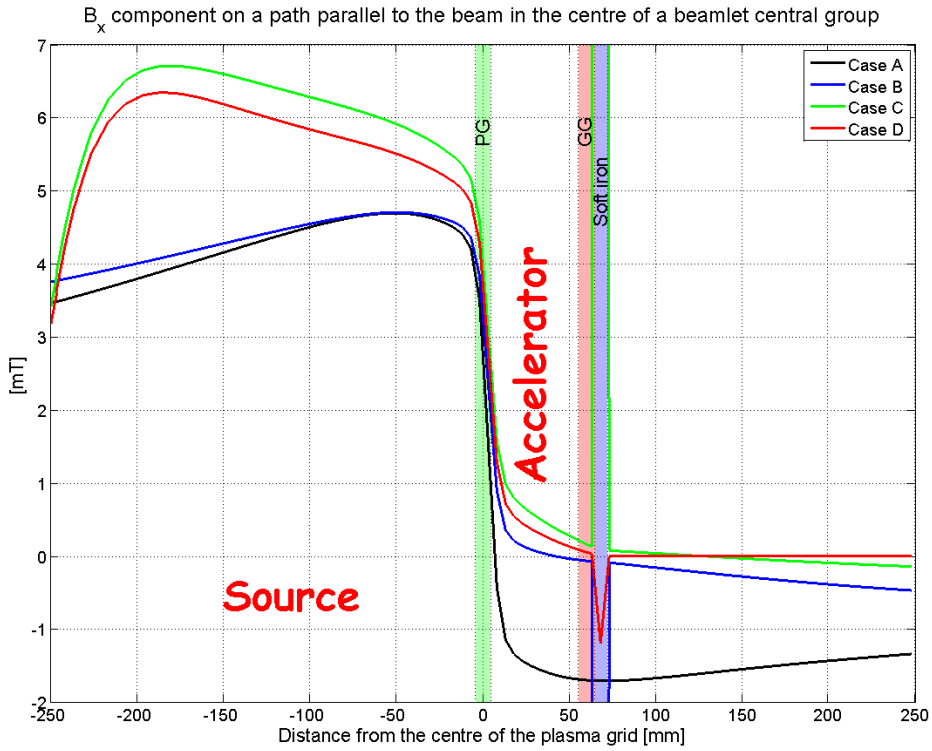

Figure 38: Bx component along a path parallel to the particle trajectory in the centre of the central beamlet group (FIELD5 in Figure 31).

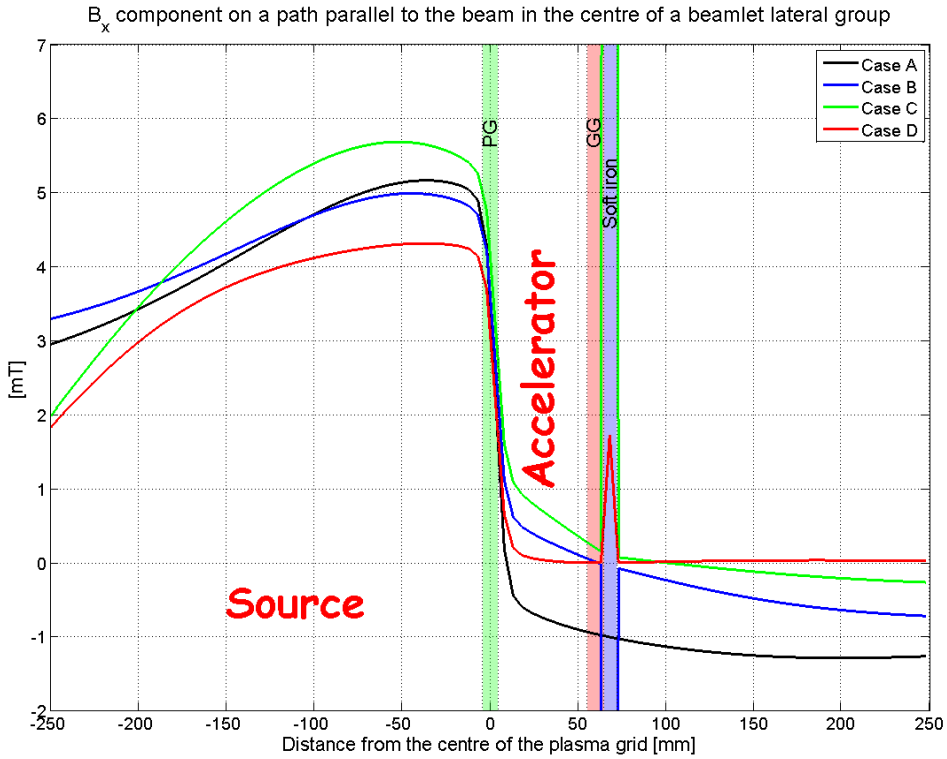

Figure 39: Bx component along a path parallel to the particle trajectory in the centre of the lateral beamlet group (FIELD6 in Figure 31).

3.3.3 Computation of deflection angle and offset

The magnetic field necessary for the suppression of co-extracted electrons also produces a deflection of the ion beamlets. One of the main objectives of the present work is the reduction of the effect of this magnetic field on the trajectories of negative ions. The uniformity of the deflection is also important, because it allows the compensation by tilting the source. Hence the various magnetic configurations have been compared also in terms of deflection of the particle trajectories. As the beamlet trajectories are mainly along the z direction, the x component of the FF generates a vertical deflection (along y).

The vertical deflection angle θ can be defined, in the vertical plane, as the angle between the beamlet direction and the geometrical axis of the apertures. The vertical offset, defined as the vertical distance between beamlet centre and geometrical axis, is approximately proportional to the deflection angle for a given accelerator and position.

The code EAMCC (Version 3.1) [28] was used to calculate the beamlet trajectories inside the accelerator. Table 5 shows that the difference between the deflection angles calculated at the "Central" and "Lateral" positions, 18 mm downstream with respect to the GG, is about 2 mrad with magnetic configuration A, about 1 mrad with configuration B, about 0.5 mrad with configuration C and about 0.2 mrad with configuration D.

	Deflection angle "Central" beamlet [mrad]	Deflection angle "Lateral" beamlet [mrad]	Differential deflection between beamlets [mrad]
Case A	-3	-1	2
Case B	+0.5	+1.5	1
Case C	+1.5	+2	0.5
Case D	+1	+0.8	0.2

Table 5: Deflection of "Central" and "Lateral" beamlets for the four cases investigated.

Hence, it is confirmed that the magnetic configuration D gives the best results in terms of deflection uniformity.

The evaluation of the vertical deflection of the beamlets by the EAMCC code is a time-consuming task when the computation must be carried out for a long distance downstream relatively to the GG.

In the paraxial approximation, $\partial y/\partial z << 1$, where the curvature radius is $R_{yz} \approx mv_z/(qB_z)$ and the velocity $v \approx v_z$ is related to the electrostatic potential by the classical conservation of the total energy:

$$v_z = \sqrt{v_0 - \frac{2 \cdot q}{m}(U_0 - U)} \tag{3.1}$$

where U is the electric potential on the z axis, U_0 its value at extraction and v_0 the initial speed at extraction, the ion deflection angle $\theta = \partial y/\partial y$ can be derived by integrating along the beam direction z the following expression:

$$\frac{\partial^2 y}{\partial z^2} \approx \frac{q\left(B_x(z) + \frac{dy}{dz}\frac{dU}{dz}\right)}{m\sqrt{v_0^2 + \frac{2q}{m}(U_0 - U(z))}} \tag{3.2}$$

In order to determine the trajectories of 5+5 ion beamlets produced in different horizontal position, equation (3.1) has been numerically integrated.

The results of the integrals are shown in Figure 40 for all cases under investigation, negative ions H^- (m = 1.675.10^{-27} [kg] and ^{q} = 1.602.10^{-19} [C]) and 1 m downstream relative to the PG. The vertical deflection of all beamlets has been greatly reduced with the proposed magnetic configuration, from around 20 mrad to about 0.5 mrad; moreover, the maximum difference among the beamlets decreased from 5 mrad to 0.4 mrad.

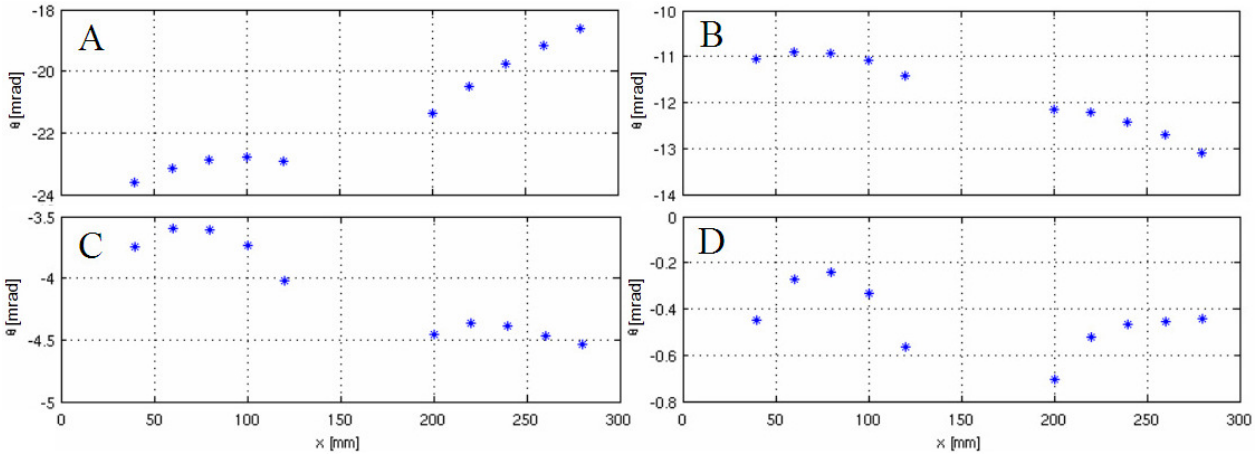

Figure 40: Calculation of the deflection angle [mrad] up 1 m downstream relative to the PG for each beamlet

3.4 Implementation of SPIDER source design

The magnetic configuration of case D has thus been implemented in the mechanical design of the beam source for SPIDER (Figure 41). The two conductors for forward PG current are copper bars having a section of 100×15 mm^2 each. The return current is distributed on three parallel copper bars, having a section of 90×10 mm^2 each, which are placed in between the copper and the stainless steel driver plates of the RF source and insulated from them (Figure 42). The current generating the FF flows through the following path:

- the current enters the PG through the top element;
- it comes back in the rear side of the plasma source through the central return conductor;
- on the top it is divided to the two lateral forward conductors through a junction element;
- finally it goes up flowing through the return lateral conductors, at the end of which it is united again.

At the top of the beam source all conductors are connected to the in-vacuum end of the power supply transmission line.

A first concept foresaw to have both forward and return lateral conductors in parallel to the PG and central conductor respectively, allowing to regulate the sharing of the current between the PG and the two side bars within few percent by changing suitable junction elements with others having different electrical resistance. This concept has been abandoned in order to exploit the 4 kA power supply already defined for the reference design, allowing a 25% margin of increasing the current and consequently the magnetic field.

The most critical element from a thermal point of view is the central return bar, having the highest current density. The thermal power dissipated by it will be approximately 270 W at the level of current considered in the design (3 kA PG current and 1.5 kA current in the two bars parallel to PG). This power level should not constitute any problem, as it could be easily removed by conduction along the copper bars and by radiation to surrounding structures.

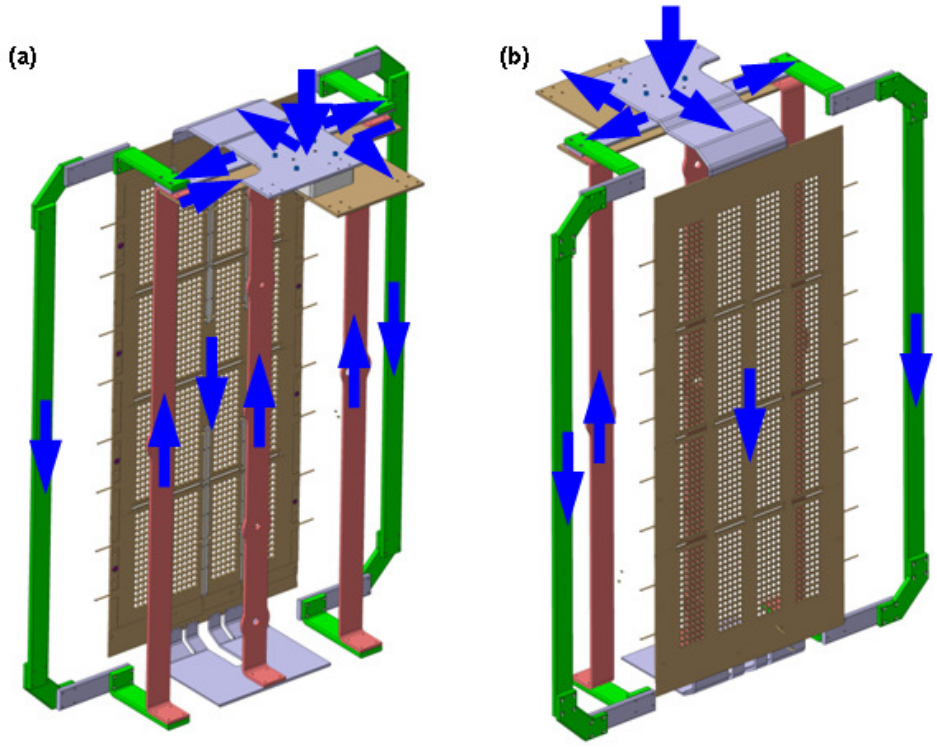

Figure 41: Implementation of the FF electrical circuit in the beam source of SPIDER: (a) rear axonometric projection (b) frontal axonometric projection. Lateral forward conductors are in parallel to each others as well as the return current conductors and both pairs are in series with PG and central return conductor.

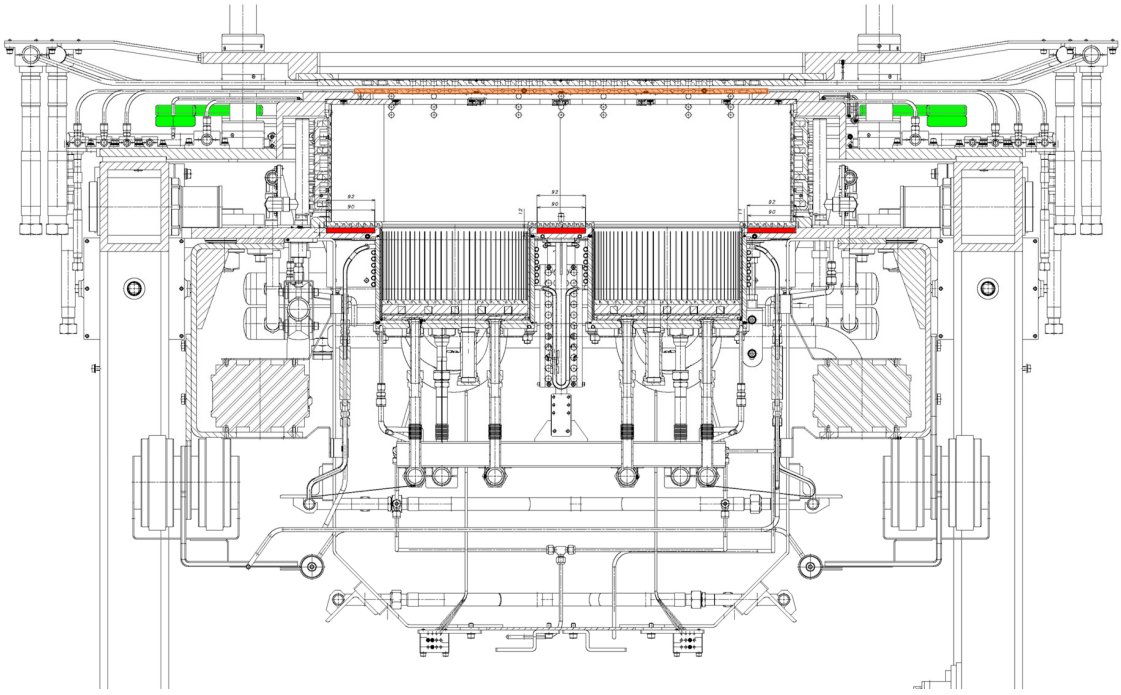

Figure 42: Horizontal section of the SPIDER ion source and accelerator, with highlighted in color the optimized configuration of the FF sources. In orange the PG, in green the two side forward current bars and in red the three bars for the return path of the PG current.

3.5 3D analyses

Three-dimensional analyses on the optimized configuration were carried out in order to assess the reliability of 2D analysis and the vertical uniformity of the magnetic field, but also to evaluate the detailed 3D magnetic field profiles inside the beamlet apertures and to obtain a map of the actual magnetic field distribution for particle tracking simulations.

In particular, two different 3D models have been built because of the two different needs to assess global and detailed features, and for the geometrical complexity of the device, where overall large dimensions (of the order of meter) and small details (beamlet apertures and thin grid thickness of the order of few millimeters) coexist at the same time. This fact inevitably leads to a very high number of mesh elements and consequently heavy computational demands.

Although the problem to be solved is static, the presence of current flowing in solid conductors with complex geometry and ferromagnetic material at the same time, together with the large number of unknowns, makes its solution not trivial and rather time consuming.

3.5.1 Simplified global model

First a simplified 3D model of the overall magnetic field source system has been built, mainly to assess the vertical uniformity of the magnetic field. Since this analysis aims at assessing global features, the local details of the model have been simplified as far as possible in order to reduce the computational complexity. For this reason, the model includes only the FF source and the ferromagnetic layer on the downstream side of the GG. SF magnets have indeed not been considered in order to model only half geometry exploiting the intrinsic symmetry, as in the case of the 2D model.

The number of elements has been strongly reduced as well by leaving out to model the beamlets apertures in the PG and in the ferromagnetic layer, considering instead uniform equivalent electric resistivity and magnetic permeability values in the region of the beamlet groups. The equivalent resistivity value have been determined by FEM analysis on a suitable sub-model. The same has been done to simplify the modeling of the PG water manifolds.

In Figure 43 a sketch of the model mesh is shown.

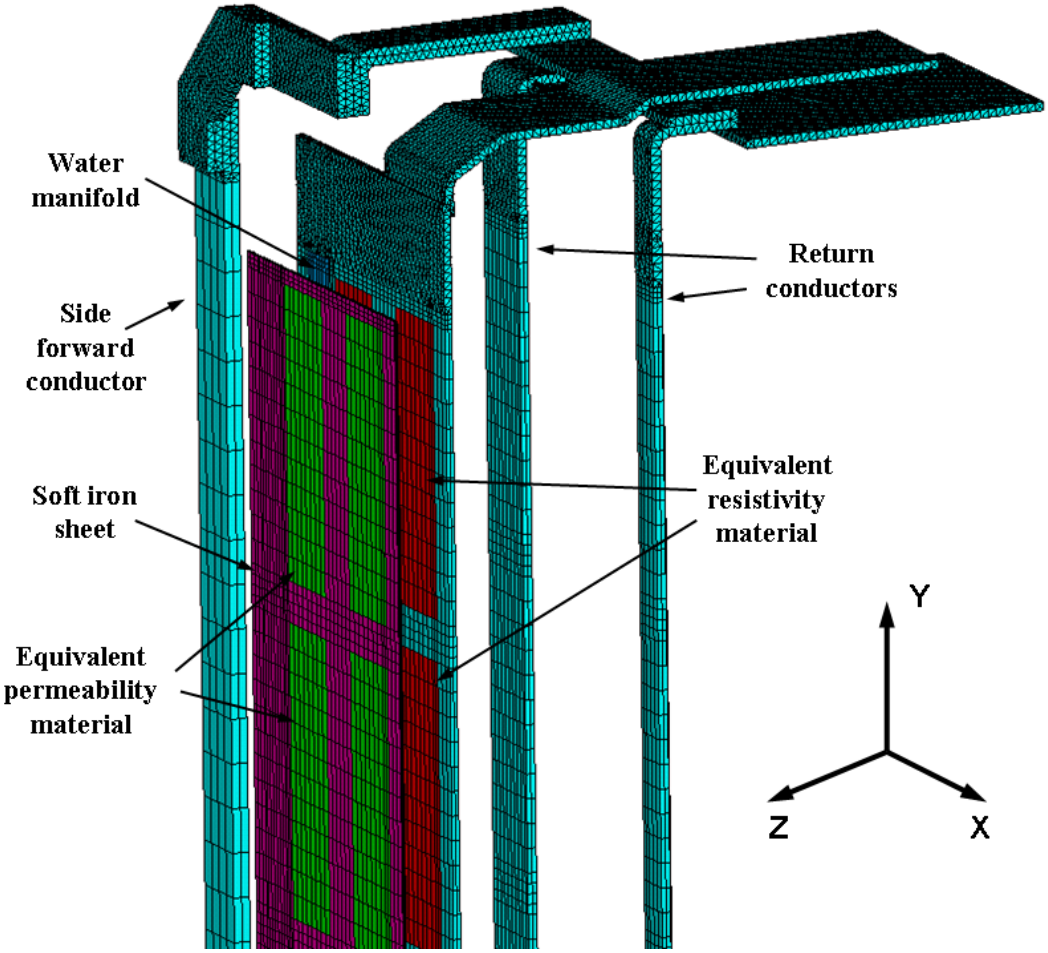

Figure 43: Part of the mesh of conductors in the simplified 3D model of the FF configuration.

Given the small value of the magnetic field involved, which reaches at most about 100 mT in the iron, constant magnetic permeability has been assumed everywhere. A value of 1000 is assumed for the relative magnetic permeability of the ferromagnetic sheet and an equivalent permeability value of 262 for the beamlet group regions, based on the ratio of the iron volume end total volume.

The first step of the calculations consists on a steady-state current conduction analysis to determine the actual current density distribution, followed by a magnetostatic 3D analysis.

The classical formulation to solve 3D magnetostatic problem in presence of current sources and simply connected iron region is the (magnetic) Difference Scalar Potential (DSP) strategy. However, in ANSYS this formulation can be applied only to current sources formed by primitives (SOURC36 element type) and not to meshed ones.

The standard 3D nodal magnetic vector potential formulation is not suitable to carry out this magnetostatic analysis, because the solution can be incorrect when the normal component of the vector potential is significant at the interface between elements of different permeability [16].

A solution based on the vector potential formulation using edge elements was initially tested. As a matter of fact, this formulation is the most general for the solution of magnetostatic problems, since it makes use of the magnetic vector potential and leaves its normal component free to jump at any material interface (see paragraph 2.4), while the usual nodal shape functions forces the fields to be continuous all over the mesh. However, unsatisfactory results have been obtained as the only boundary conditions allowed to simulate the far-field decay in this case is the parallel flux condition, which is ill-suited to the problem, unless to model a very big air volume.

A mixed nodal scalar and vector potential formulation has been chosen, thus allowing to reduce the number of unknowns and to efficiently simulate the far-field decay boundary conditions, having the option of using the INFIN111 element type which allows to model an open boundary of a 3D unbounded field problem. The vector potential formulation is used in a volume containing the bus-bars and a little part of air. In the remaining current-free volume, where the ferromagnetic material is present, the scalar potential formulation is applied. The normal component of the vector potential at the vector-scalar interface has to be set to zero for satisfying the Coulomb gauge and thus ensuring the uniqueness of the vector potential solution. Normal magnetic field condition has been imposed on the symmetry plane. This corresponds to imposing a zero normal component of the vector potential and zero scalar potential in the symmetry surfaces corresponding to the region where they are respectively defined. Prescribed (zero) scalar potential on the symmetry surface also assures the symmetry of the coefficient matrix (see paragraph 2.2.1.4). This is not the usual application of the coupled nodal-vector potential formulation, but the results have been found in good agreement with the 2D analysis and therefore considered correct.

As an example of the results obtained, in Figure 45 contour plots of the B_x magnetic field component on a vertical (xy) surface are reported. This surface corresponds to the vertical area occupied by the bus-bar system, at the same horizontal z coordinates of the paths represented in Figure 31 (FIELD1 to FIELD4 correspond to Figure 31-a to b, respectively). The boundary of the beamlet groups are highlighted in black and the B_x values on their corners are reported.

In Figure 44 the B_x component along horizontal paths parallel to the grids 20 mm upstream respect to the PG (FIELD1 of Figure 31) in three different vertical positions is reported. The three curves are compared also with the result of the 2D analysis, showing a good agreement.

In the actual 3D geometry the uniformity is not as good as that obtained in the 2D analysis, considering infinitely high conductors. Anyway, both the pictures show that the uniformity of the *Bx* component is in general better along the vertical dimension than along the horizontal one. Therefore, no action has been considered necessary to improve the vertical uniformity and the new design has been accepted from this perspective.

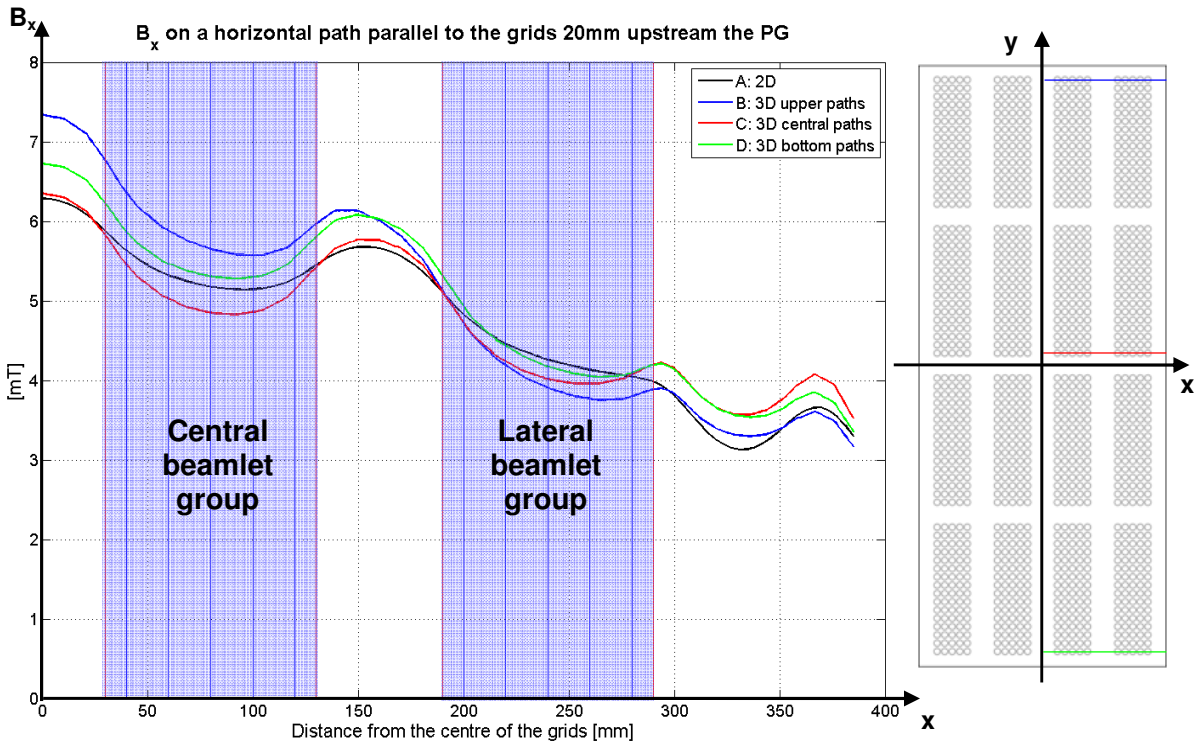

Figure 44: Space distribution of B_x along horizontal paths located 20 mm upstream of the PG. The 3D results relative to the top (blue line), the centre (red line) and the bottom (green line) of the grid, are compared, together with the result of the 2D analysis (black line).

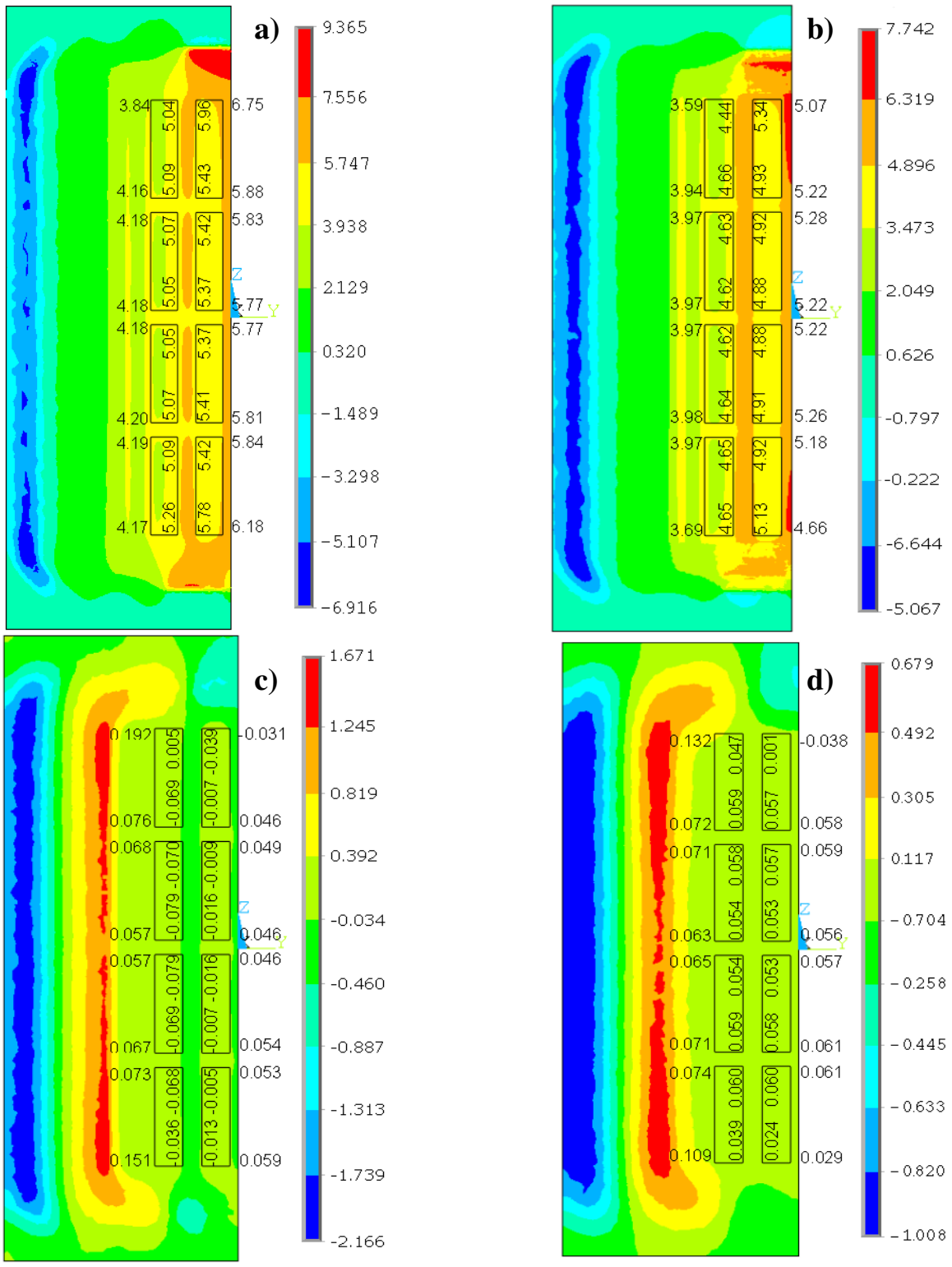

Figure 45: Contour plots of the Bx component on vertical (xy) surfaces at the same z coordinates of the paths represented in Figure 31: a) 20mm upstream PG, b) 2mm upstream PG, c) 10mm upstream GG and d) 50mm downstream GG .

3.5.2 Detailed local model

Once the new design has been assessed with regard to the uniformity of the magnetic field from a global perspective, the local features have been investigated through a dedicated model, in particular to check the effect of the beamlet apertures on the current distribution and accordingly on the local magnetic field uniformity.

This "detailed" 3D model has been developed to verify the accuracy of the approximations introduced in the 2D model as well as for the investigation of the magnetic field non-uniformities on the scale of a single aperture, which can affect particle trajectories.

The model considers a portion of the entire system corresponding to the whole horizontal geometry and three beamlet apertures along the vertical dimension (see Figure 46), plunged in a disc of air of suitable dimensions. Here all the magnetic field sources are taken into account, including the SF permanent magnets on the EG. For this reason no intrinsic symmetries could be exploited to reduce the mesh dimension.

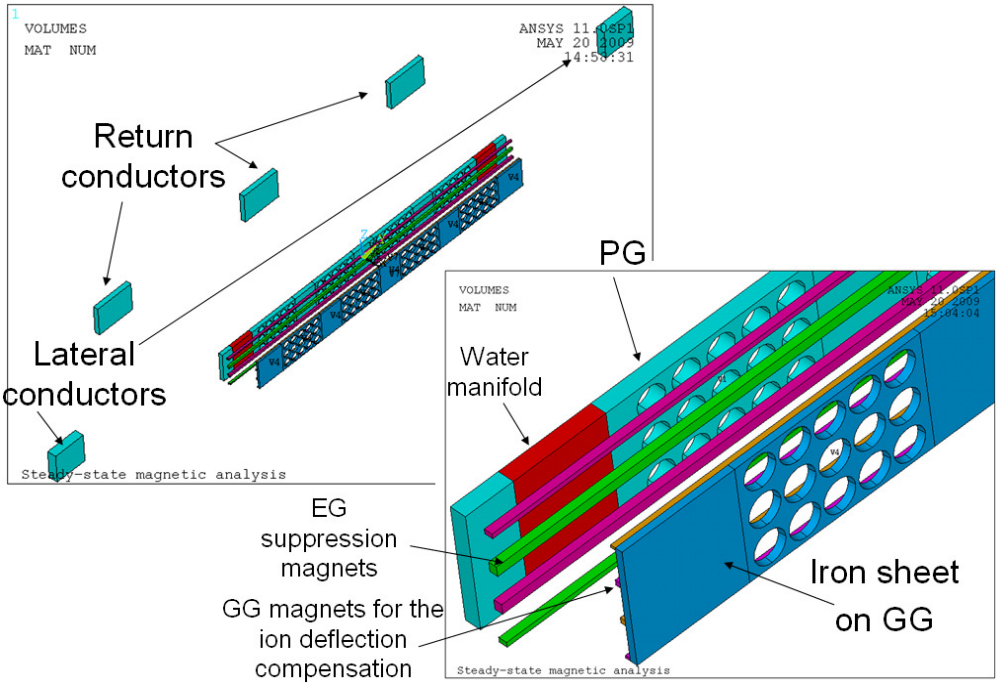

Figure 46: Detailed 3D model with FF source, SF magnets, soft iron layer and compensation magnets on the GG

The geometry of the model and therefore the resulting boundary conditions are compatible with the edge element formulation. Indeed, in this case tangential magnetic field is the natural condition to be imposed on the top and bottom planes of the model for applying vertical periodicity, and the same condition fits well enough the field on the side boundary, if this is placed far enough away from the current sources.

On the contrary, the mixed scalar-vector potential formulation doesn't work in this case, although it should (according to the theory [15], ANSYS would seem to apply [29]). Indeed, the imposition of a zero tangential component of the vector potential on the upper and bottom planes of the model for imposing the flux parallel condition, should assure the symmetry of the coefficient matrix and consequently a correct solution. Anyway, the ANSYS support service has not been helpful in understand the reason for this.

Also in this case the magnetostatic analysis is preceded by a steady-state current conduction analysis to determine the actual current density distribution in the PG.

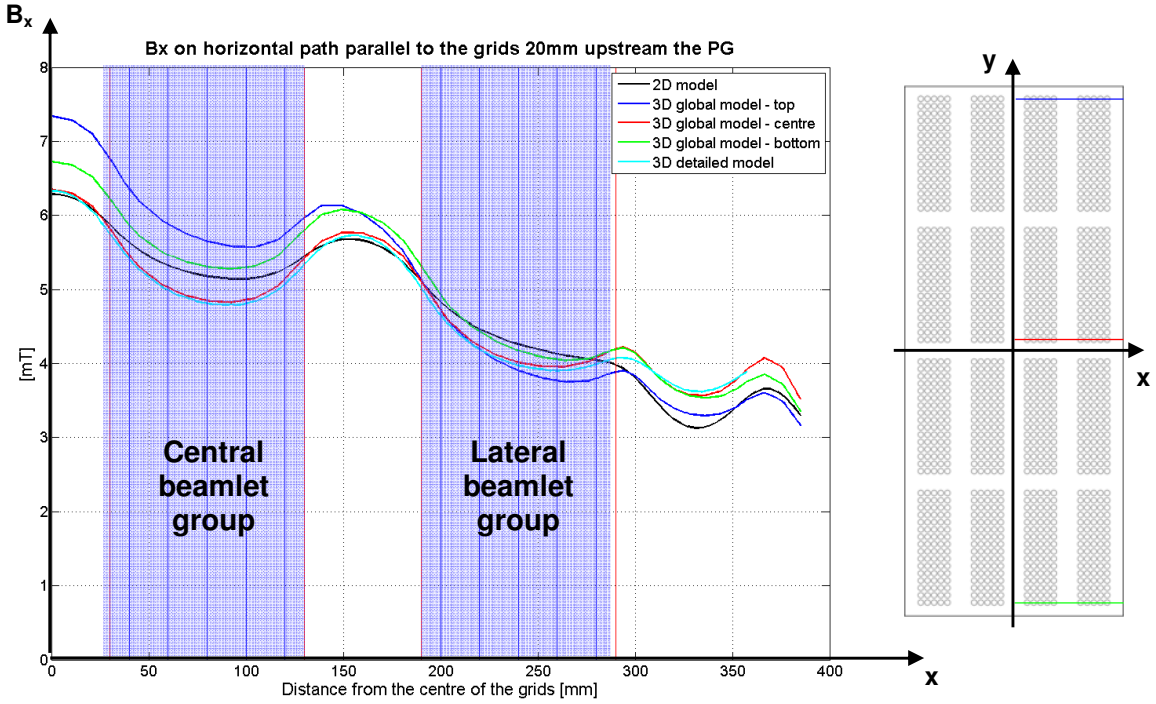

Figure 47: Space distribution of B_x along horizontal paths located 20 mm upstream of the PG. Comparison of all models: the detailed 3D model (light blue line), the global 3D model relatively to the top (blue line), the centre (red line) and the bottom (green line) of the grid, the 2D model (black line).

In Figure 47 a comparison of all the models is shown, consisting in the same spatial distribution of the B_x component along horizontal paths 20 mm upstream with respect to the PG as illustrated in Figure 44. The figure shows as the results of this "detailed" model and those of the previous "global" model, with regard to a central region of the grids with respect to the vertical dimension, are in good agreement.

This 3D model has been used also to analyze a possible method for magnetically compensating the crisscross horizontal ion deflection due to the alternate polarity of the SF permanent magnets (see Figure 46). The ions exiting the PG are indeed subject to a vertical magnetic field, which

changes direction on the two side of the EG. Moreover, since this field doesn't reach zero value at the PG and it is still present in the plasma source, the accelerating ions are subject to a non-zero line integral of this field, with the consequence of a net deflection. Furthermore, the field has opposite direction in each neighbour row and therefore it determines a horizontal deflection in opposite direction considering following rows. In the negative ion accelerators presently operating, this deflection is compensated by electrostatic means, i.e. introducing an offset on the axis of the EG apertures (see paragraph 1.3.2.2).

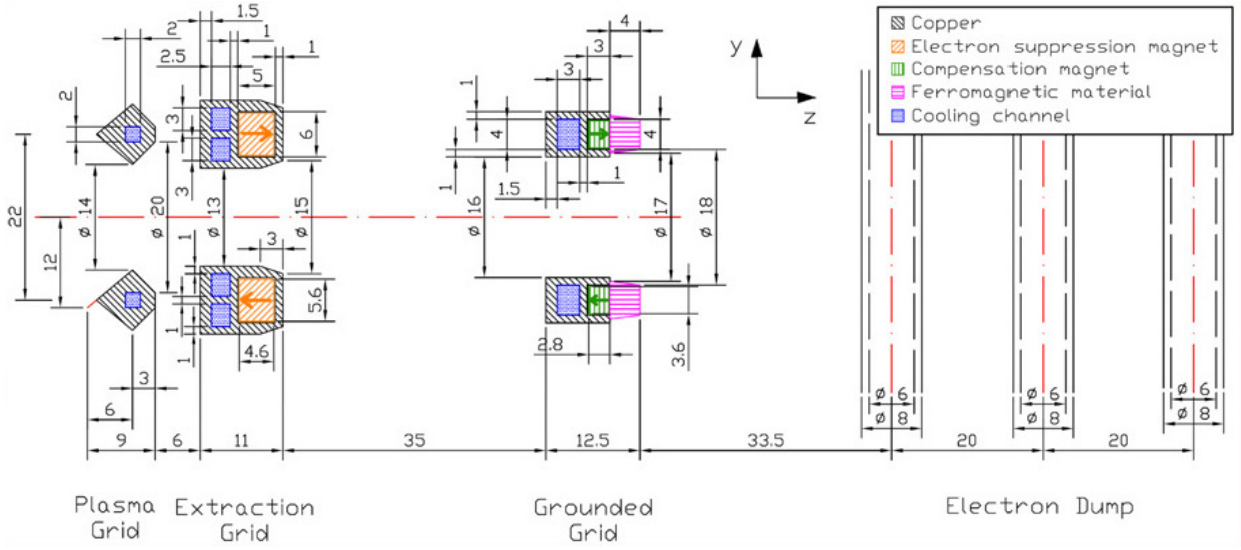

Figure 48: View of a vertical section of the SPIDER extractor/accelerator system optimized design, together with the electron dump, correspondent to the centre of a beamlet aperture. All the dimensions are in mm.

The layout, shown in Figure 48, includes a new set of permanent magnets in direct contact with the soft iron layer on the downstream side of the GG, which can compensate the deflection previously introduced by the SF. Contrary to the electrostatic means, this magnetic compensation is totally independent on the beam acceleration voltage [3]. Figure 48 shows also a new component, called electron dump (ED), which has been introduced in order to dump the electrons exiting the accelerator more deflected by the new set of magnets embedded in the GG, thus avoiding they load the calorimeter and the vessel. The ED is composed of a series of vertical pipes surrounding the apertures and located downstream of the GG.

Figure 49 shows the profile of vertical component of the magnetic field (B_y) along the beam direction z, in five positions within the left aperture of the central beamlet group. Thanks to the ferromagnetic layer, the Compensation Field (CF), in the region in front of the apertures, is only present on the upstream side of the GG. In this way, the ions passing through the CF are subject to a horizontal deflection only in one direction. Therefore, by calibrating the CF intensity with

respect to that of the SF, a complete compensation of the ion deflection is obtained in a large range of accelerating voltage.

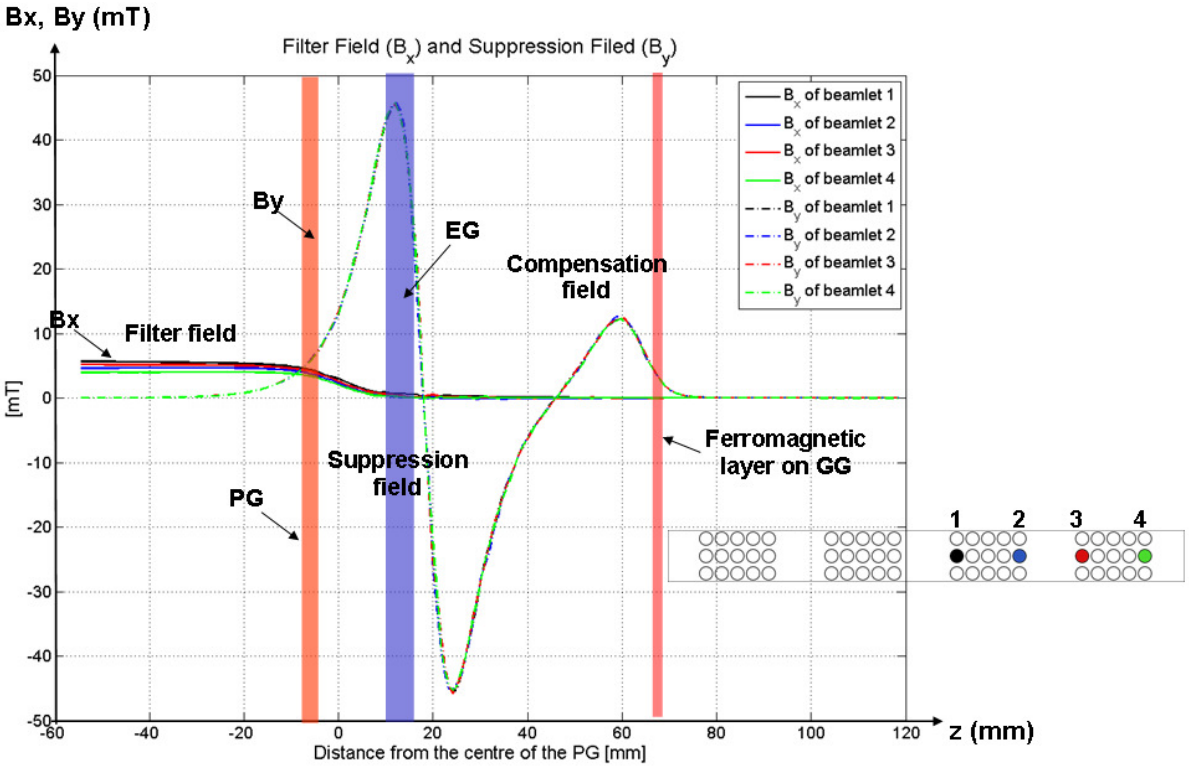

Figure 49: Profile of the horizontal (Bx) and vertical (By) components of the magnetic field along four different beamlet axes

Several analyses have been carried out in order to tune the compensation magnets and the ferromagnetic material in the GG for an optimal compensation of the beam deflection given by the suppression magnets. Taking into account all the constraints, the compensation magnets have been designed with a section of 3.6×2.8mm2 and with a magnetic remanence of 0.4 T, and the ferromagnetic plate with a thickness of 4 mm.

The solution based on GG offset loses effectiveness if the extracted current is different from the nominal one, since if the extracted current density is varied, for acceptable beam optics also the grid voltages must be varied. Moreover, this is a rigid solution (not modifiable without changing the whole GG). This is a disadvantage if we consider that the estimations of the beam deflection are affected by some uncertainties and have not been experimentally validated so far.

The solution based on compensating magnets in the GG should work efficiently also with an extracted current different from the nominal one. Moreover, it is expected to be more flexible. In fact, it is possible to change the compensation magnets in the GG and/or the thickness of the ferromagnetic plate without changing the GG.

3.6 Choice of permanent magnets

The requirements for the SPIDER magnets are reported in Table 1.

The dimensions A, B and C are referred to the convention shown in Figure 1:

- the A dimension is parallel to the magnetization;
- the B dimension is the shorter dimension perpendicular to A;
- the C dimension is the longer dimension perpendicular to A.

Magnet location	A [mm]	Toler. On A [mm]	B [mm]	Toler. On B [mm]	C [mm]	Toler. On C [mm]	Magnetic Remanence [T]	Total quantity
Extraction grid	4.6	+0.1	5.6	+0.1	43	-0.2	1.1	816
Grounded grid	2.8	+0.1	3.6	+0.1	43	-0.2	0.4	1020
Ion source Later. Wall	20	±0.1	10	±0.1	60	-0.2	1.1	264
	20	±0.1	10	±0.1	25	-0.2	1.1	40
Drivers	13	±0.1	9	±0.1	50	-0.2	1.1	232
	13	±0.1	9	±0.1	25	-0.2	1.1	280

Table 6: SPIDER magnets requirements

Moreover, all the magnets are required to resist to high temperature (up to 250°C) and to have a small temperature coefficient of the residual field. In other words, they have to be magnetically stable with respect to temperature variations.

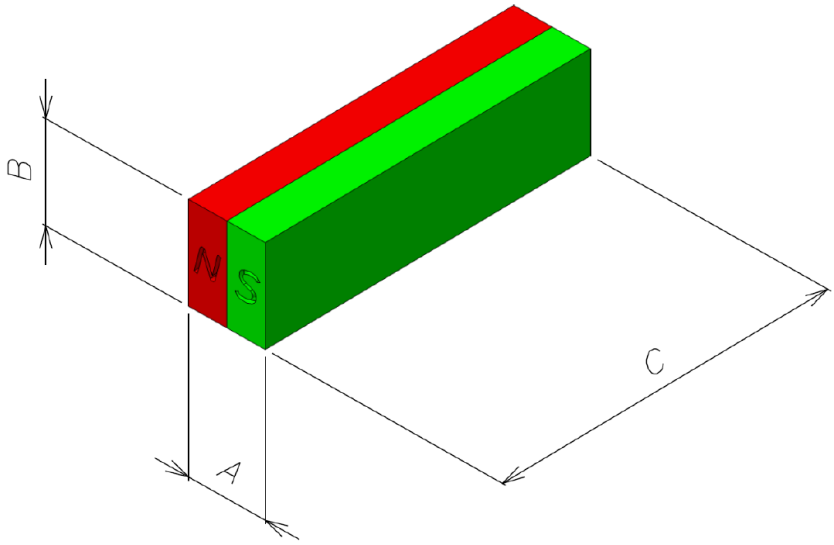

Figure 50: Convention on magnets dimensions

A market survey has been carried out in order to find magnets with suitable characteristics. Several manufacturers have been found which produce permanent magnets with required magnetic characteristics and also able to resist to temperature higher than 250°C for long periods.

The remanence temperature coefficient of the residual field declared by the various suppliers is also acceptable (always about -0.03, which means a decreasing of the produced flux of 3% for an increasing of 100°C).

The most promising materials to be chosen for the different magnets are the following:

- Sm_2Co_{17} for the magnets of the EG, lateral wall and drivers. This type of magnets combines high values of remanence (over the required level of 1.1 T) and energy density with a good stability at high temperature (up to 250°C).
- Ferrite magnets for the magnets of the GG. These magnets have a remanence around 0.4 T, which is the suitable value for the compensation of the deflection due to the SF, and can work up to 250°C. This material has been chosen because a good uniformity in the material magnetization can be ensured. A material with a higher remanence could be also used after partial de-magnetization; however in this case the magnetization could result to be not sufficiently uniform.

In Figure 51 the magnetization curves for different operating temperature of one of the most promising candidate for supplying the Sm_2Co_{17} magnets are reported.

In order to reduce brittleness of the magnets and for a better behaviour in vacuum conditions, a Nickel coating of 10 μm is prescribed for all the magnets.

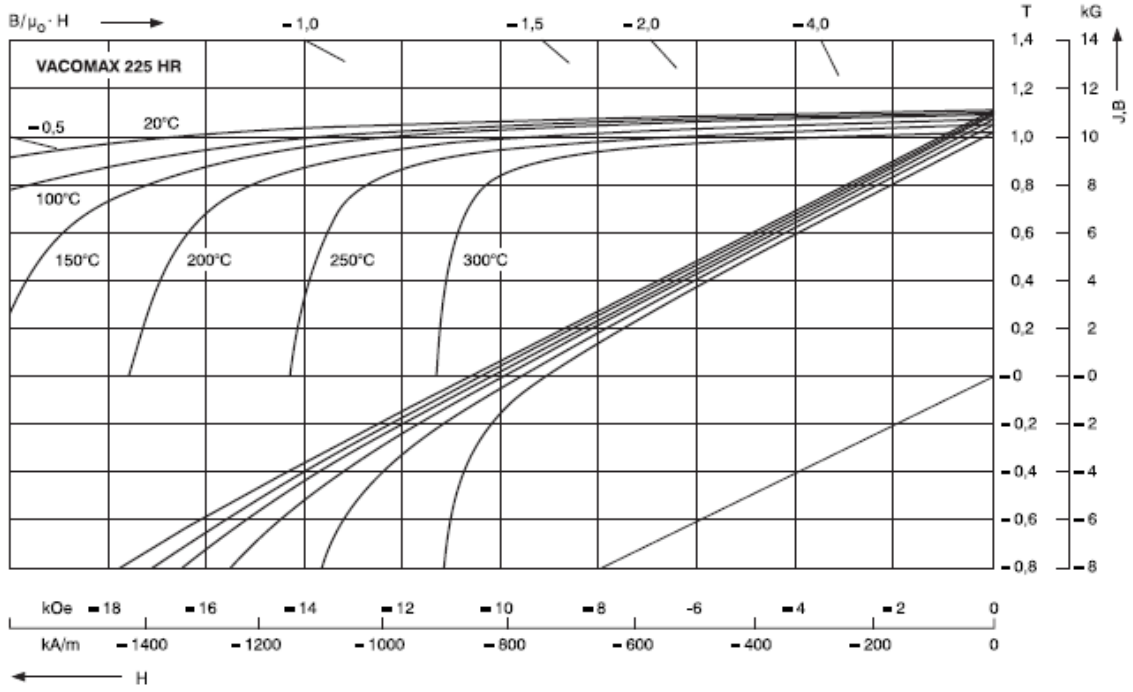

Figure 51: Typical demagnetization curves of a Sm_2Co_{17} magnet from Vacuumschmelze.

4 Optimization of MITICA magnetic configuration

4.1 Introduction

MITICA (Megavolt ITER Injector Concept Advancement) is the prototype of the full-size Heating and Current Drive Neutral Beam Injectors for the ITER Tokamak reactor [30] planned to be built at Consorzio RFX. The core of MITICA [31] is constituted by a RF-driven negative ion source and by a multi-grid electrostatic Accelerator (Figure 52), which shall produce a 60A H^- ion beam (or a 40A D^- ion Beam) with a specific energy up to 1 MeV. The beam is formed by 1280 individual negative ion beamlets (16 groups of 16×5 circular apertures) with an overall cross-section of ~600×1600 mm^2, which are to be extracted, accelerated and neutralized under well-controlled conditions in order to produce a focused 1 MeV, 17 MW Neutral Beam on a 400×560 mm^2 target at ~25 m. The magnetic configuration inside the accelerator is of crucial importance for the achievement of the required beam optic quality, with the correction of undesired ion beamlet deflections, and also of a good beam efficiency, with the early deflection of the co-extracted and stripped electrons.

Several alternative magnetic design concepts have been considered, comparing in detail the magnetic and beam optics simulation results, evidencing the advantages and drawbacks of each solution, both from the physics and engineering point of view.

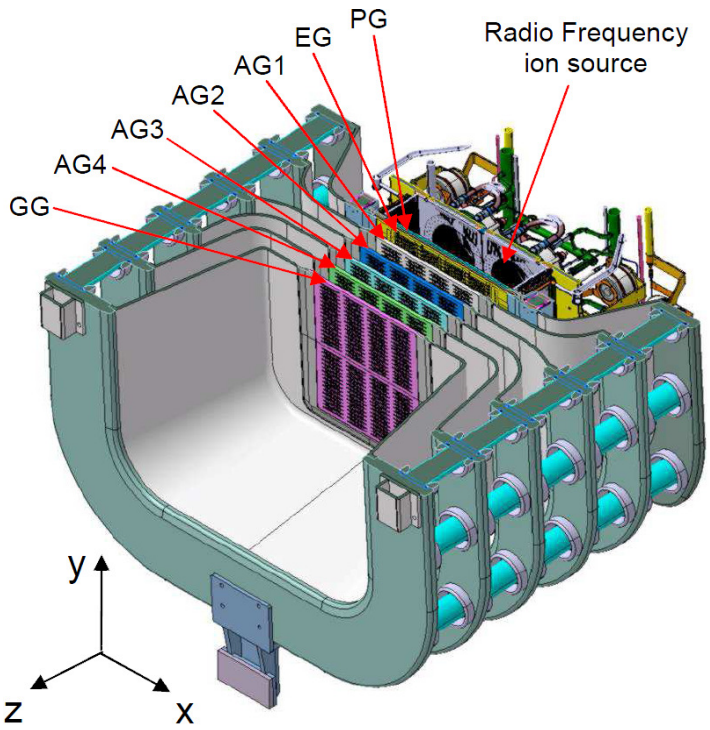

Figure 52: cut view of the MITICA accelerator, showing (right to left): RF drivers, Plasma Grid (PG), Extraction Grid (EG), Acceleration Grids (AGs) and Grounded Grid (GG). The coordinate z is parallel to the beam direction.

4.2 Optimization process and design variables

The initial accelerator "reference" configuration was that of the ITER Design Description Document DDD 5.3 [25] with important modifications derived from operational experiences of JAEA and IPP, such as equally-spaced (83 mm) acceleration grids (for better voltage holding, following new JAEA design [32]) and chamfered Plasma Grid and Extraction Grid apertures (optimized for RF source operation, according to IPP experience [33]). On this basis, several solutions have been conceived and compared for the magnetic configuration of the MITICA accelerator, with the objective of:

- reducing the heat loads due to co-extracted and stripped electrons on the grids to an acceptable level;
- minimizing the power associated with the residual electrons at the accelerator exit, which is then deposited on the beam line components;
- optimizing the ion beam optics and making more uniform beam deflection for all beamlets under a wider range of operating conditions.

There are basic differences between SPIDER and MITICA, in particular related to the higher ion energy and the resulting greater number of accelerating grid of the latter, which inevitably lead to adopt different solutions with regard the magnetic configuration. Nevertheless, it has been tried to adopt concepts as much as possible similar to those developed for the optimization of SPIDER, in order to preserve consistency between the two devices, keeping valid for MITICA the experience which will be made before on SPIDER. Flexibility and reproducibility of SPIDER-like conditions have been key criteria for MITICA optimization.

Therefore, four magnetic field contributions, originated by different sources, have been considered to influence the accelerator performances by deflecting the charged particles. In the following they are recalled:

- "Filter" field (FF) is a transverse (usually horizontal, as in SPIDER) field in the plasma source in proximity of the PG. The FF reduces the number of co-extracted electrons and also assures the best negative ion production efficiency. This field shall be small and spatially uniform (~ 5 mT on the upstream side of the plasma source), and can be produced by current flowing in the PG and in suitable bus-bars and/or by stacks of permanent magnets at the sides of the PG.
- Electron "suppression" field (SF) is a transverse field whose purpose is deflecting the co-extracted electrons onto the EG before they penetrate through its apertures and are accelerated at higher energy. The SF is produced by permanent magnets embedded in the EG between the grid apertures. These magnets constitute continuous (usually horizontal) stacks and are all magnetized along the beam axis (z) direction, however with opposite polarity from stack to stack. This configuration produces a localized transverse field (usually vertical) of about some tens of mT just upstream and downstream the EG.
- Stripped electron "suppression" field (SESF) is a transverse field in the Acceleration Grids (AGs) region, designed for dumping the stripped/secondary electrons and residual co-extracted electrons and for partially compensating the deflection of the accelerated ions caused by the SF. This field can be either "local" (produced by permanent magnets in the AGs) or "long-range" (produced by permanent magnets or coils just outside the accelerator).
- "Compensation" field (CF) in the GG is designed for completely compensating the deflection of the accelerated ions caused by the SF. This is produced by permanent magnets embedded

in the GG between the grid apertures and a ferromagnetic layer on the downstream side, as in SPIDER.

The optimization process has essentially required the pursuit of the best combination of these four contributions.

As for SPIDER, the material chosen for the permanent magnet is Samarium Cobalt (Sm_2Co_{17}), with remanence $B_0 = 1.1$ T (preferred to $SmCo_5$, $Nd_2Fe_{14}B$ and Alnico for their higher remanence and magnetization stability at high temperature).

ANSYS [29] 2D and 3D models were set up for the simulation of the various magnetic field configurations. These have been then compared by considering beamlet deflection, evaluated by numerically integrating the analytical expression of the trajectory of charged particle accelerated in a transverse magnetic field in paraxial approximation (see paragraph 3.3.3):

$$\frac{\partial^2 y}{\partial x^2} \approx \frac{q\left(B_x(z) + \frac{dy}{dz}\frac{dU}{dz}\right)}{m\sqrt{v_0^2 + \frac{2q}{m}(U_0 - U(z))}} \tag{4.1}$$

Configurations have been compared also on the basis of dumped and transmitted power due to co-extracted and stripped electrons. These quantities have been estimated by the EAMCC code [28], using the calculated magnetic field profile, the electric field profile calculated by the SLACCAD code [34] and assuming a standard pressure profile [35].

Although the performance of the initial configuration [36] was already satisfactory concerning co-extracted electron suppression, the deflection of stripped/secondary electrons was to be improved regarding both efficiency (reducing electron power at exit) and uniformity of its effects on the ion beamlets. Therefore a strategy based on the combination of the following approaches was used:

- improving the uniformity of the FF, using PG current with solenoid-like return-bars, adopting the new design developed for SPIDER;
- increasing the field in the accelerator for immediate suppression of stripped electron, either using external lateral magnets or embedded permanent magnets in the AGs, or both;
- compensating the ion deflection by improving the accelerator field uniformity and accurately calibrating the integral of the transverse field (B_x and B_y) along each beamlet in the accelerator.

Given the good perspectives in this latter regard provided by the new concept developed for SPIDER, it was considered preferable to use also in MITICA magnetic means for compensating errors of magnetic origin.

The decoupling of the magnetic field inside the ion source from that in the accelerator is considered an essential issue for a prototype device, in order to find an optimized configuration, to be then reproduced in the definitive Heating Neutral Beam (HNB) device for ITER in the simplest way. Based on IPP experience with RF sources, during the beam operations the FF inside the ion source has to be regulated in a large range. This regulation should not affect the magnetic field needed for dumping the stripped electrons in the accelerator region. As a matter of fact, the magnetic field for stripped electron dumping must be optimized to maximize its effect, without risking to have also interception of ions. For instance, considering the field produced by the PG current (according to the DDD5.3 configuration) as the only source for both FF and stripped electrons dumping, there is an optimal condition with a current of 4 kA (see Figure 53) to minimize the electrons transmitted out the accelerator. If we want to increase the FF inside the RF source, we should not be forced to increase the field also in the accelerator, where an excessive increase could lead to a lower efficiency of the field and/or an interception of the ion beamlets.

The solenoid-like return-bars configuration, developed for SPIDER, is considered better in this regard, allowing to concentrate the field inside the ion source, which can be therefore increased without the limitation due to ion beamlet interception on the grids.

In this way the magnetic field to dump the stripped electrons can be produced by other sources and thus optimized independently. Therefore, major efforts have been dedicated in this regard, finding an optimized solution in terms of:

- minimum electrons exiting the accelerator;
- better distribution of thermal loads on the different grids;
- uniformity of the field across the grids;
- minimum alternated ion deflection.

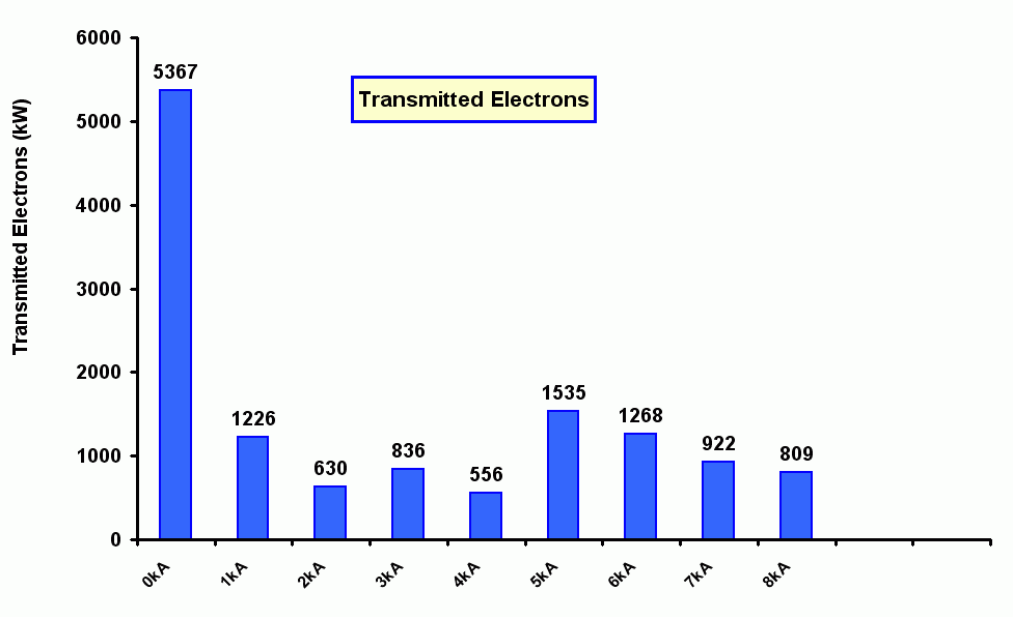

Figure 53: Amount of electrons transmitted out of the accelerator with different values of the filter field given by the PG current (from H.P.L de Esch)

4.3 Magnetic configurations: local and global approach, horizontal, vertical and diagonal field

In a first phase, attention has been placed on the optimization of the magnetic field configuration in the accelerator for the reduction of the power load on the grids and the minimization of the transmitted electrons at the exit. Only in a second stage, the uniformity of the field across the grids was carefully considered and the ion deflection compensation maximized.

Several solutions were evaluated both for physics performances and engineering robustness. It was found that magnets embedded in the AGs could provide an efficient suppression of the stripped/secondary electrons and in some cases a partial compensation of the ion deflection, with the main advantage of obtaining a more uniform magnetic field across the beam cross section with respect to a long-range approach. This implies a more uniform deflection of the 1280 beamlets and has been defined "local" approach.

On the other hand, solutions based on external field sources (such as external permanent magnets or Helmholtz coils) located outside the accelerator and for this reason defined "global approach", have been tested as well, finding in particular good results when combined with the local one.

According to the direction of the deflection field in the accelerator, three configuration families were considered:

1. vertical field configurations; local approach only;
2. horizontal field configurations; local and global approach;
3. diagonal field configurations; combined local and global.

Preliminary analyses on the different solutions have been carried out by approximated 2D models, then only the most promising will be verified in realistic 3D models, like the one built for SPIDER analysis described in paragraph 3.5.2, introducing and testing solutions for the complete beamlet deflection compensation.

4.3.1 Vertical field configurations

In this case only local magnetic configuration obtained with permanent magnets embedded in the grids have been considered and compared.

The permanent magnets in EG and AGs constitute horizontal stacks inside the grids, in between the apertures rows. While the EG magnets are always magnetized along the axial direction (z), with alternated polarity stack by stack, in order to produce a vertical field B_y in front and behind the EG beamlets apertures (like in SPIDER), two different options have been considered for the B_y field produced by the AGs:

- only upstream of the grid apertures (cases 1 and 2)
- inside the grid apertures (cases 3 to 6)

The 2D models consider a full vertical (yz) section of the accelerator. All the magnets embedded into the grids are modelled by their sections enclosed in an air region. The whole air is in turn surrounded by a ring where infinite elements are used to simulate the far-field decay.

It's worth noting that in the case of vertical magnetization, permanent magnets in adjacent rows are equally magnetized, while in the case of horizontal magnetization (i.e. along the beam direction) they have opposite sign in order to obtain a vertical magnetic field component seen by the accelerated particles. This fact may have a fundamental role on the particle deflection behaviour and on the electron power dumped onto the grids.

Figure 54 shows a sketch of the vertical section of the accelerator grids for the case 1 considered.

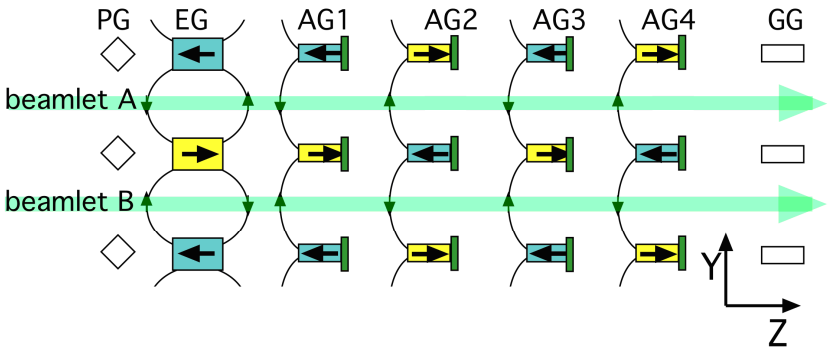

Figure 54: Sketch of the model of the case 1.

In cases 1 and 2, the magnetization of all AGs magnets is axial (z) as in the EG, and ferromagnetic layers on each AG reduce the B_y on the downstream side, as shown in Figure 57, causing a controlled horizontal (x) deflection of all particles. It is worth pointing out that horizontal deflection of beamlet A is exactly symmetrical to that of beamlet B, causing a criss-cross deflection of different beamlet layers, which can be minimized quite accurately by appropriate choice of the magnet polarization sequence (see Figure 58).

The ferromagnetic sheets on the downstream sides of the AGs, which are in direct contact with the permanent magnets, have been modelled with linear permeability, thanks to the low field values. This approximation is acceptable because the iron results far to be saturated and it allows simplifying a lot the model of the apertures with an equivalent permeability.

In Figure 55 the plot of the flux lines related to the case 1 is reported as example of the 2D models used.

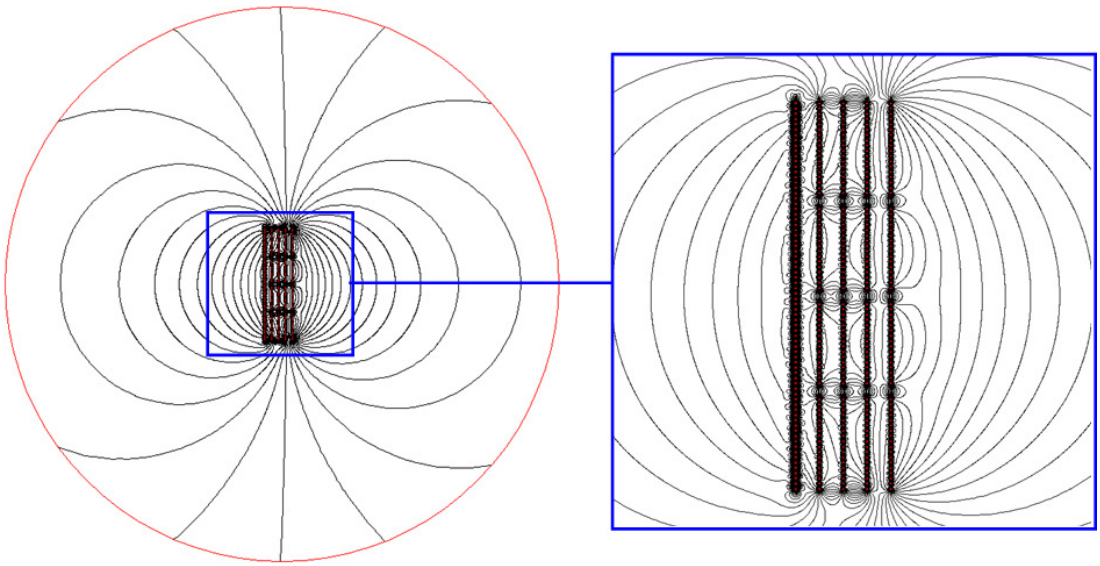

Figure 55: Magnetic flux lines in the case 6 of the vertical field configuration.

Figure 56 shows a vertical section of the accelerator grids for the case 6 considered.

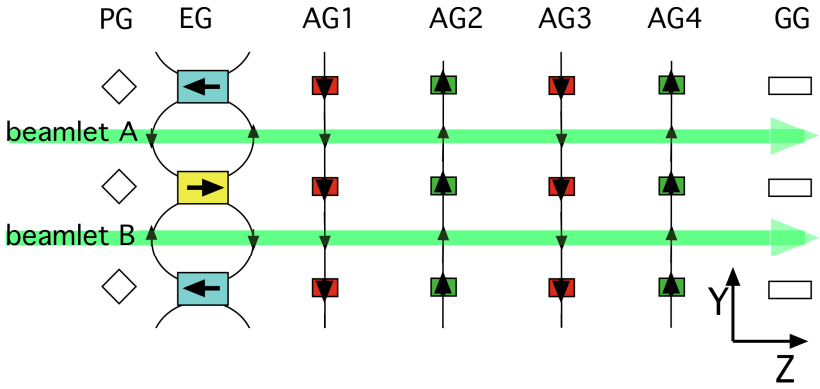

Figure 56: Sketch of the model of the case 3

In cases 3-6 the permanent magnets on AGs are vertically magnetized and no ferromagnetic layer is necessary. In these cases the deflection of beamlets A and B is not exactly symmetrical and can only be partially compensated by choosing the polarization sequence and therefore a differential deflection is inevitably introduced (see Figure 59).

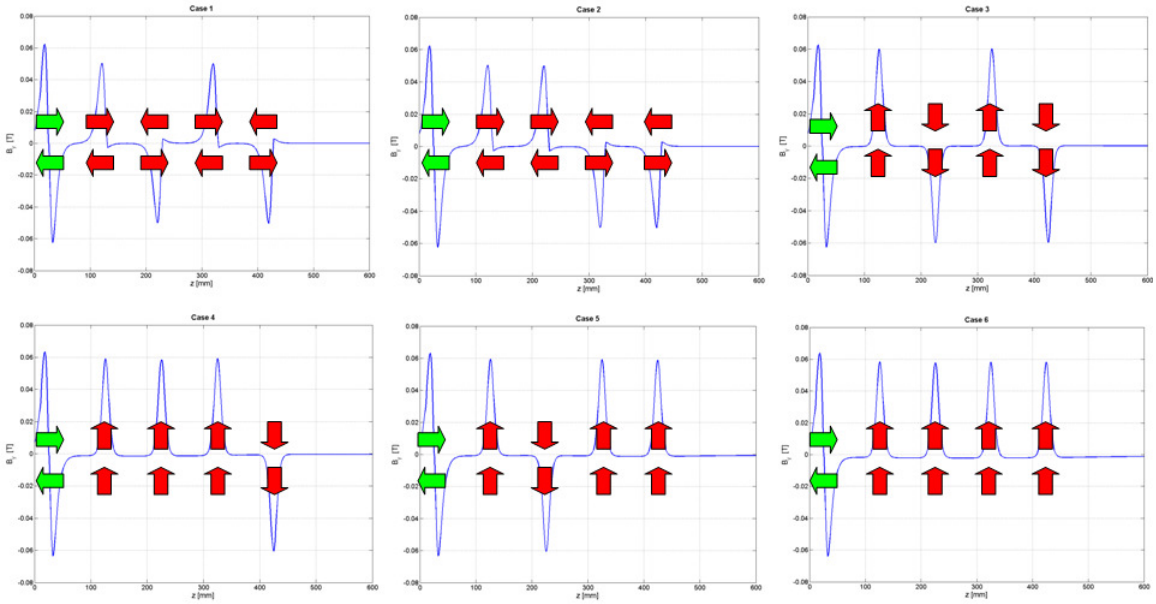

Figure 57: profiles of vertical magnetic field By along the beamlet axis for EQ_GAPS_11, cases 1-6.

The calculated heat load on the acceleration grids due to stripped electrons is considerably large, typically in the range of 1-2 MW per grid. The power related to co-extracted electrons is typically much smaller (less than 100 kW per grid). For the configurations considered, the electron loads on the grids, together with the total power related to the negative ions and to the electrons at the accelerator exit are reported in Tab 1.

	Total heat loads on the grids from stripped electrons [kW]							Power of the particles at the exit [kW]	
	EG	AG1	AG2	AG3	AG4	GG	Total on grids [kW]	D-	e-
Case 1	609	1229	1364	1189	1260	902	6553	39670	1940
Case 2	607	1245	1597	1151	1294	832	6726	39520	1470
Case 3	624	1272	1637	1568	882	928	6911	39630	1690
Case 4	610	1207	1717	1518	1025	954	7031	39390	1570
Case 5	615	1223	1588	1275	1437	940	7078	39620	1450
Case 6	609	1251	1397	1510	1483	870	7120	39510	1270

Table 7: Heat loads due to co-extracted and stripped electron on each of the accelerator grids and total power at the accelerator exit for the configurations considered, calculated with EAMCC. Also the D^- power at the accelerator exit is reported.

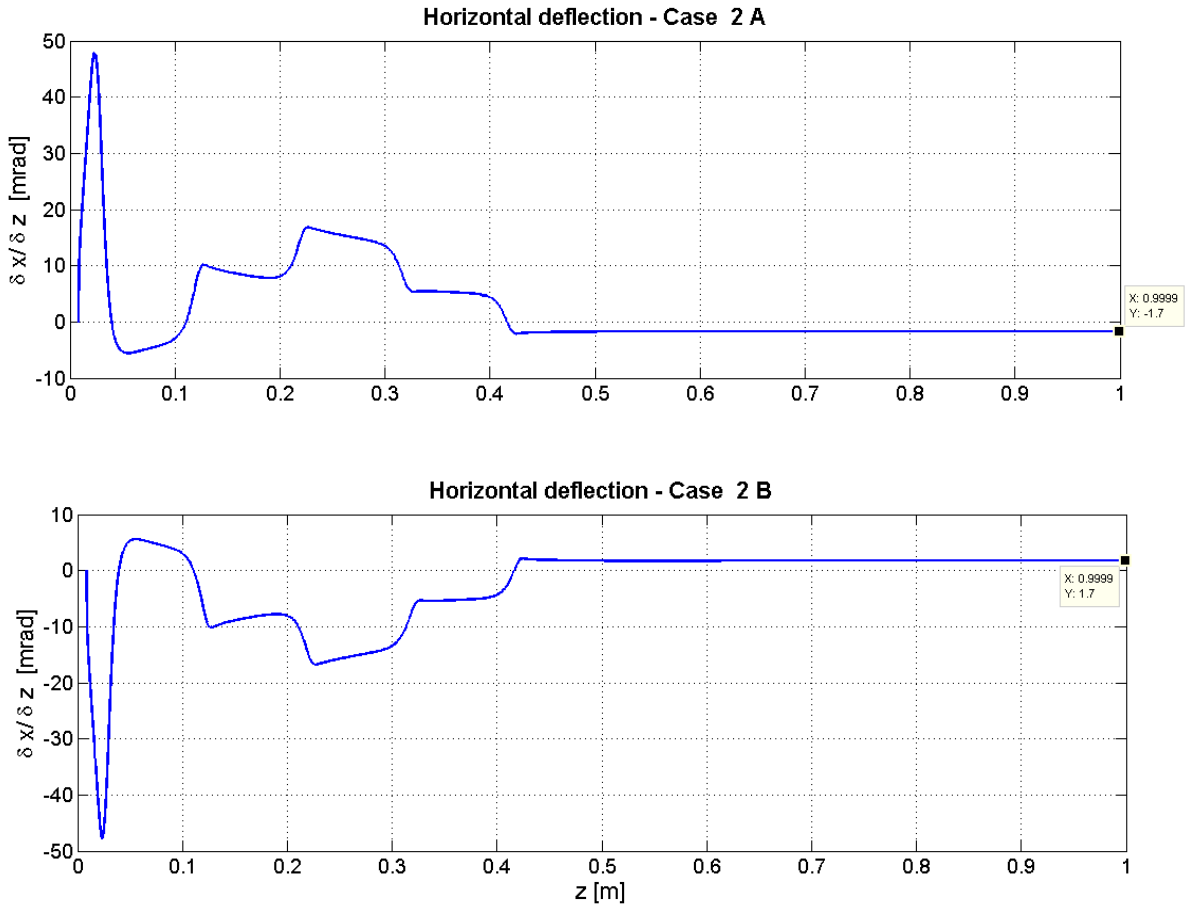

Figure 58: Ion deflection (paraxial approximation) of A and B row type beamlets produced by vertical magnetic field B_y profile for case 2.

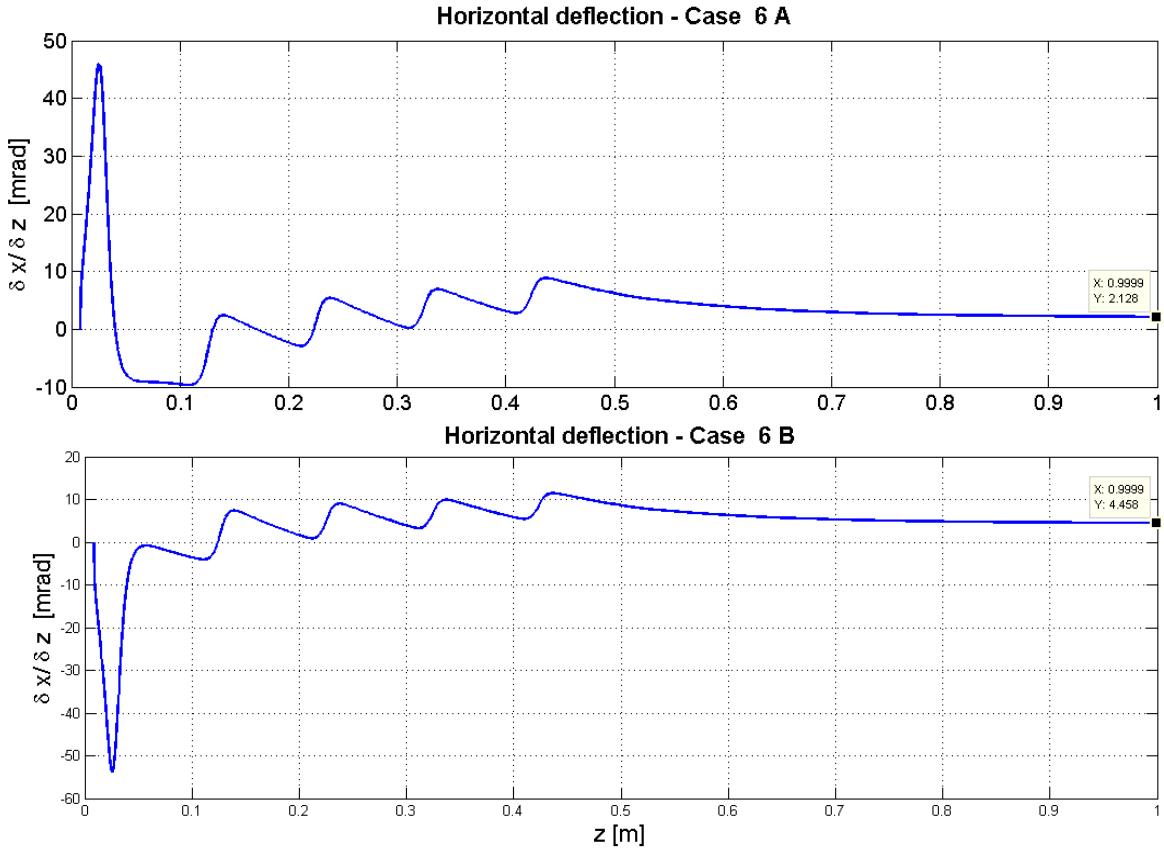

Figure 59: Ion deflection (paraxial approximation) of A and B row type beamlets produced by vertical magnetic field B_y profile for case 6.

	Deflection angle beamlet A [mrad]	Deflection angle beamlet B [mrad]	Differential deflection between beamlets [mrad]
Case 1	-1.7332	1.7332	3.4664
Case 2	-1.6998	1.6998	3.3996
Case 3	-0.4167	2.6122	3.0289
Case 4	0.372	3.4009	3.0289
Case 5	0.0961	3.125	3.0289
Case 6	2.1282	4.4583	2.3301

Table 8: Deflection of A and B row type beamlets for the six cases investigated.

The power associated to the electrons exiting the accelerator is too high for all the cases, leading to discard this configuration.

4.3.2 Horizontal field configurations

In this case both local and long-range magnetic configurations have been considered and compared, the first obtained with permanent magnets embedded into the grids and the second with permanent magnets installed on the accelerator frames.

4.3.2.1 Local approach

These configurations feature vertical magnets and horizontal cooling channels. The permanent magnets are placed in vertical stacks in the EG and AGs so as to produce a local horizontal field, as it is done in the vertical field configuration. In all cases magnets in the EG are magnetized along the beam (z) and those in the AGs along the transverse horizontal direction (x). The 2D model is the same used for the vertical field configuration, with the appropriate number of magnets, which in these cases are in between aperture columns. Figure 60 shows a sketch of the horizontal section of the accelerator for one of these cases.

A vertical deflection of the particles is obtained, which is slightly different in beamlet A from beamlet B. However, a vertical deflection is intrinsically less critical for the beam aiming, since the following beam line components consist of vertical slots, and so a precise compensation of the ion deflection is not required.

Further advantage of the configuration is that most of the deflected electrons impinge just on the horizontal cooling channels of the grid, thus improving heat removal efficiency.

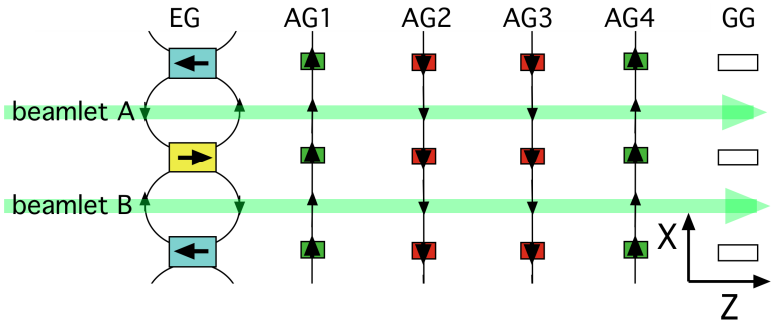

Figure 60: sketch of the horizontal cross-section of the grids for case 3, showing magnets positions and field line direction.

In Figure 61 the plot of the flux lines related to the case 1 is reported as example of the 2D models used.

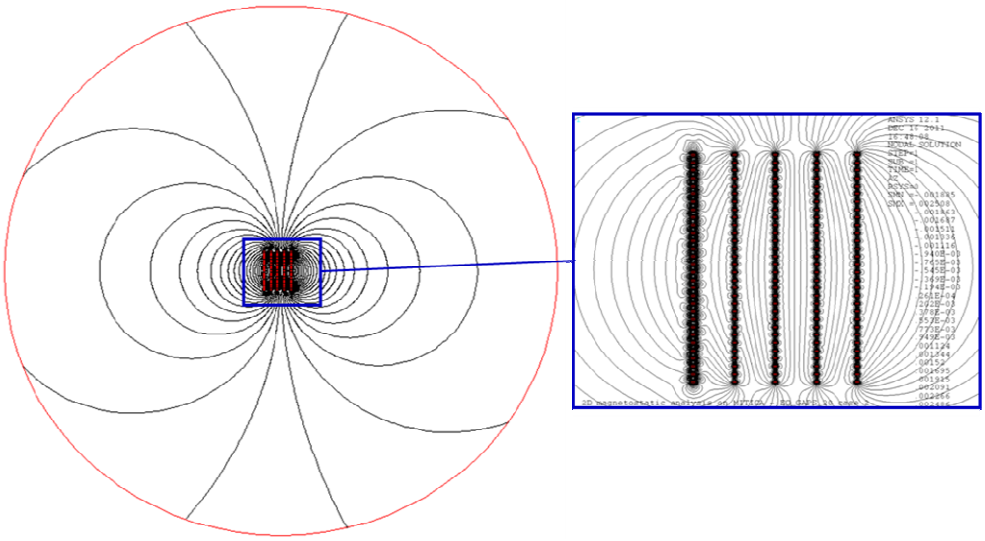

Figure 61: Magnetic flux lines in the case 1 of the horizontal local field configuration.

In Figure 62 the profile of the horizontal B_x component of the field for the three cases are reported.

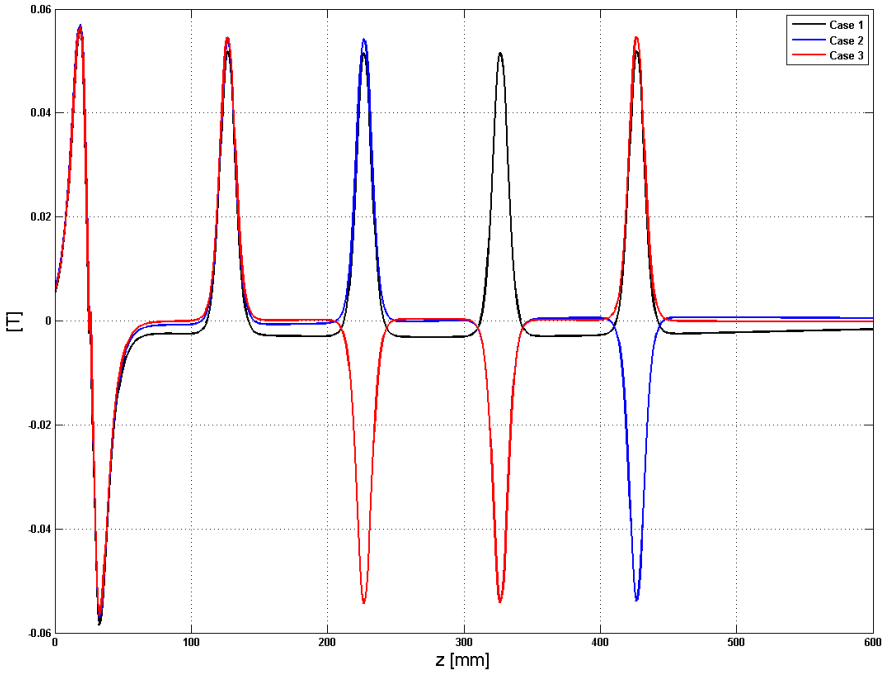

Figure 62: profiles of vertical magnetic field Bx along the beamlet axis for the three cases.

The power from the electrons exiting the accelerator, evaluated with the EAMCC code, is in the three cases of 0.97 MW, 1.62 MW and 1.82 MW, respectively.

Case 1 is particularly more efficient than any other case with vertical field, having the higher ratio between negative ions and electrons. However, this configuration featuring vertical stacks of permanent magnets magnetized in the horizontal plane has the following drawbacks:

- small copper thickness between magnets and apertures (minimum 0.7 mm instead of 1 mm in the case of horizontal magnets);
- critical thermo-mechanical behaviour, with larger temperature, stress, strain and out of plane deformation;
- a periodic modulation of the field on the PG, possibly affecting the electron and ion extraction, with the possible consequence of a worse optic, due to the superposition of the alternate horizontal field produced by the permanent magnets into the EG with the uniform FF in proximity of the PG.

More detailed analyses have been performed in order to evaluate the total field in the region of the PG, sum of the FF and the SF. Since the magnetic curve of SmCo permanent magnets can be considered linear, the total field is obtained by summing that of the previously mentioned 2D model with the FF obtained by a 3D model of the bus-bars, obtained from that built for SPIDER analysis described in paragraph 3.5.2.

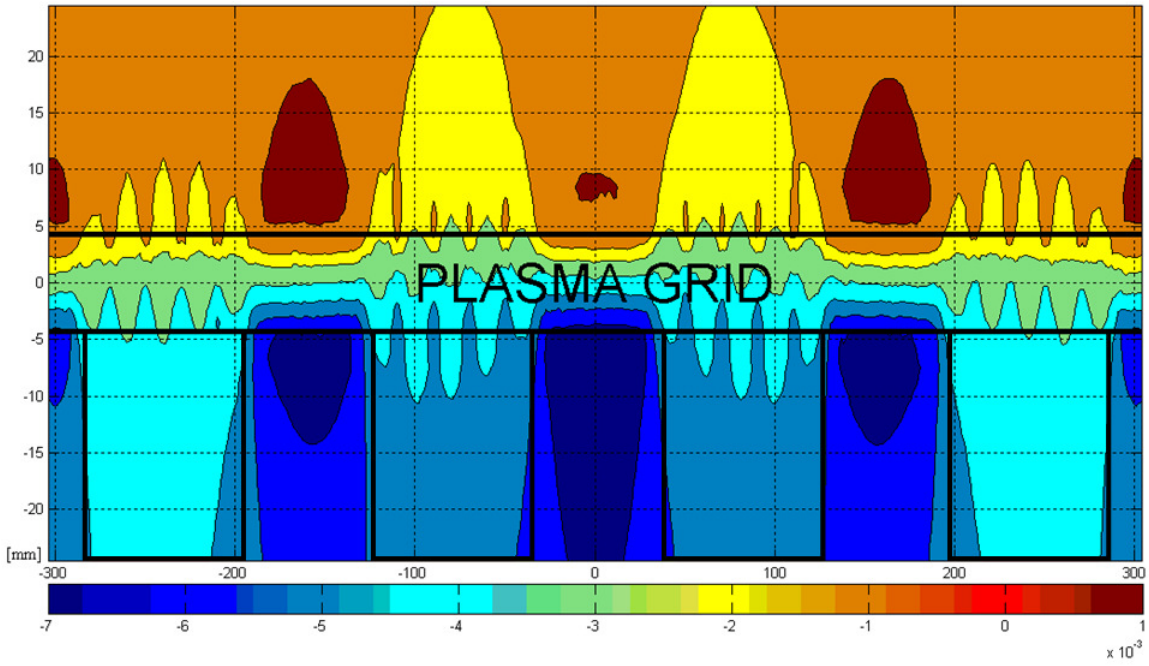

Figure 63: Contour plot of the horizontal component Bx of the magnetic field 20mm upstream and downstream the PG in case of FF (PG current) only. Black boxes highlight the regions inside the ion source in front of the four beamlet groups.

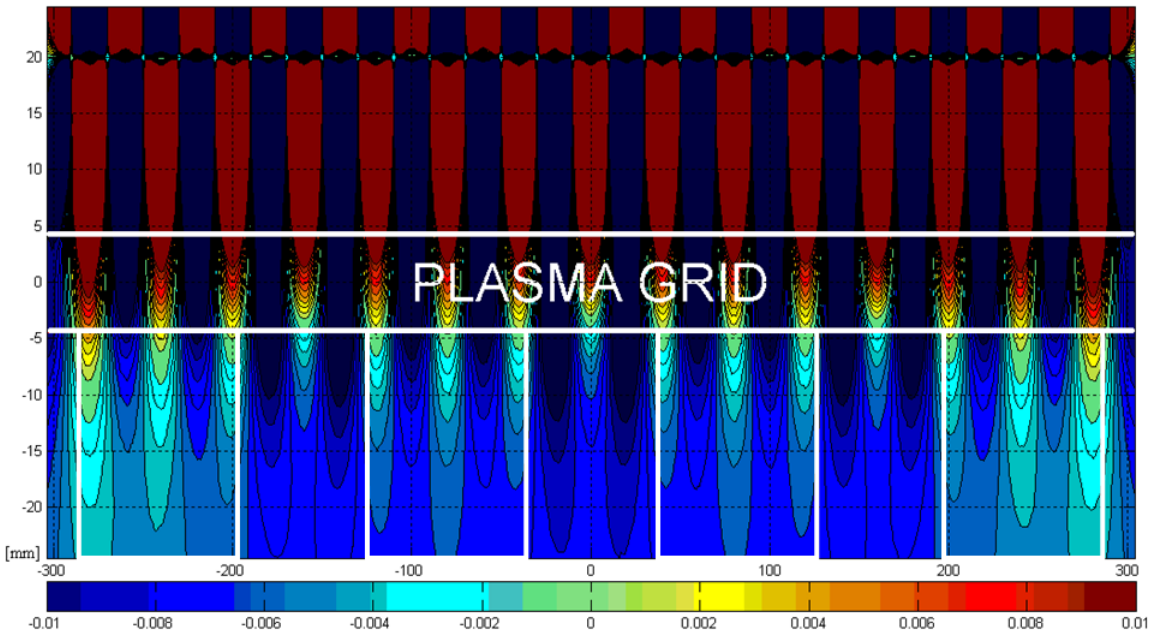

Figure 64: Contour plot of the horizontal component Bx of the magnetic field 20mm upstream and downstream the PG in case 1: superimposition of FF (PG current) and SF (EG and AGs magnets). White boxes highlight the regions inside the ion source in front of the four beamlet groups.

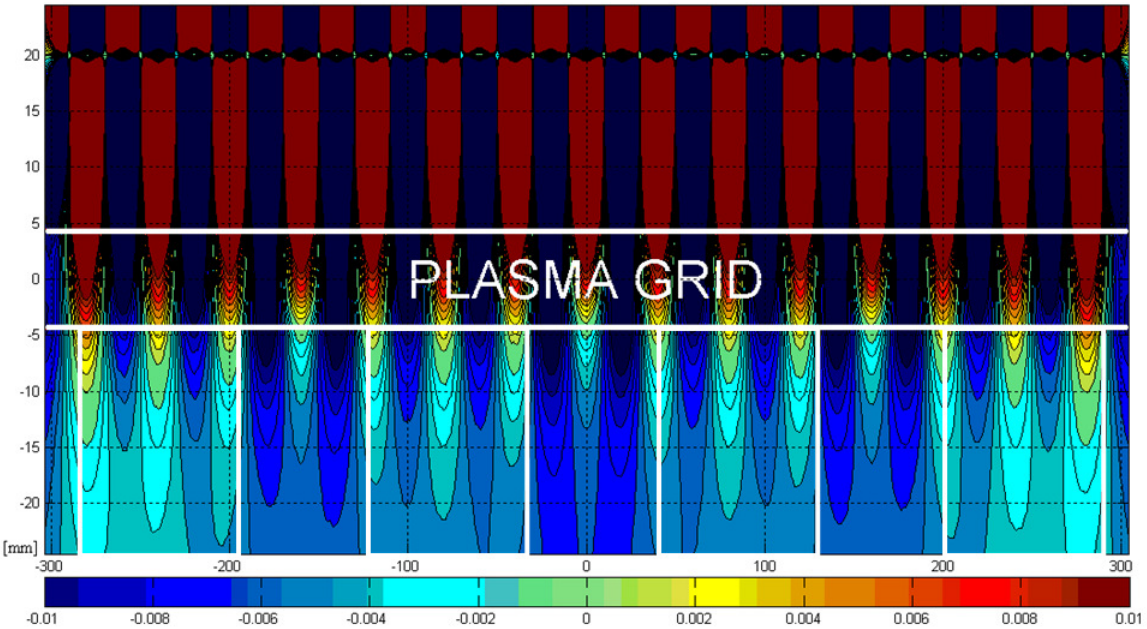

Figure 65: Contour plot of the horizontal component Bx of the magnetic field 20mm upstream and downstream the PG in case 3: superimposition of FF (PG current) and SF (EG and AGs magnets). White boxes highlight the regions inside the ion source in front of the four beamlet groups.

Figure 63 shows the contour plot of the horizontal B_x component of the FF only, that is the magnetic field produced by the PG current in absence of the suppression magnets in the EG and AGs. In this case, equivalent to have SF producing a vertical component B_y of the field, the B_x

component of the field in the region of the ion source close to the PG is always in the same direction moving parallel to the grid, with values varying at most between -3 to -6 mT.

Figure 64 and Figure 65 show the contour plot of the horizontal B_x component in case 1 and 3 with permanent magnets in the EG and AGs horizontally magnetized. The superimposition of the different contribution of magnetic field produced an unacceptable modulation of the B_x component, which even change direction in the region of 5 mm above the PG moving from beamlet to beamlet.

Despite considerable advantages of this configuration, such a lack of uniformity in the FF just upstream the PG is enough to reject this solution.

4.3.2.2 Global approach

A set of permanent magnets could be mounted on the accelerator frame to provide a long-range horizontal field inside the accelerator able to vertically deflect the electrons generated by stripping and charge exchange reactions, keeping the FF free to be varied independently. Figure 66 shows the placement of the magnets on the accelerator frames.

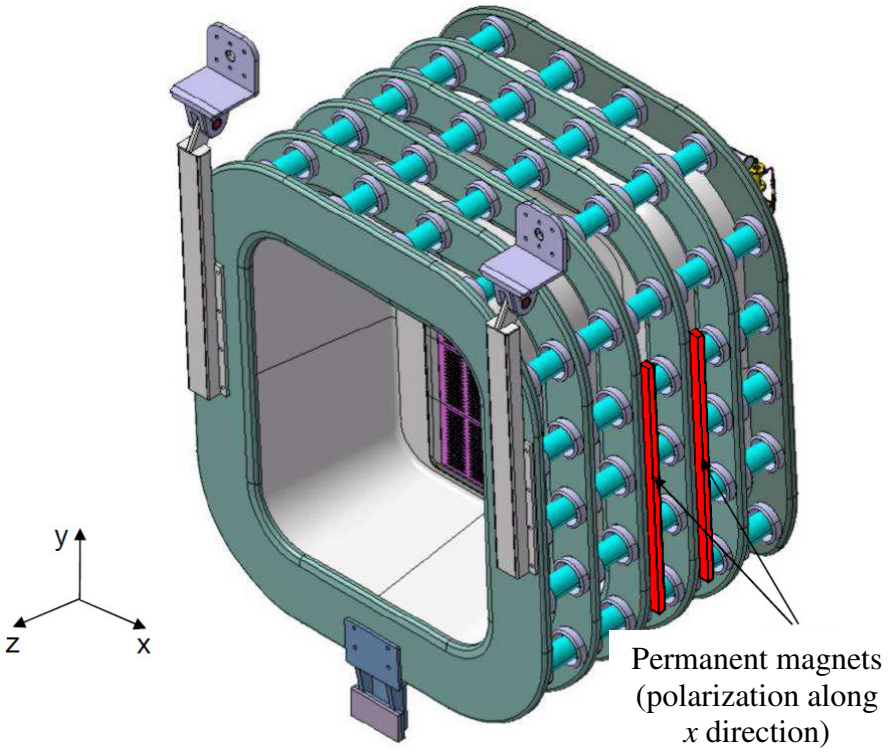

Figure 66: Possible position of lateral permanent magnets in the MITICA accelerator

Two different solutions have been tested in terms of permanent magnet dimensions, considering magnets with horizontal (xz) section of 30 x 30 mm or 60 x 40 mm respectively for the case *a* and *b*, the remanence is 1.1 T for both (Sm_2Co_{17} magnets).

The 2D model used is similar to those used in the previous cases, where only the four long range magnets are modelled; in Figure 67 the plot of the flux lines related to the case *b* is reported in order to give a sketch of the model and of the field distribution inside the accelerator; the red strip represents the footprint of the beam from the PG to the accelerator exit.

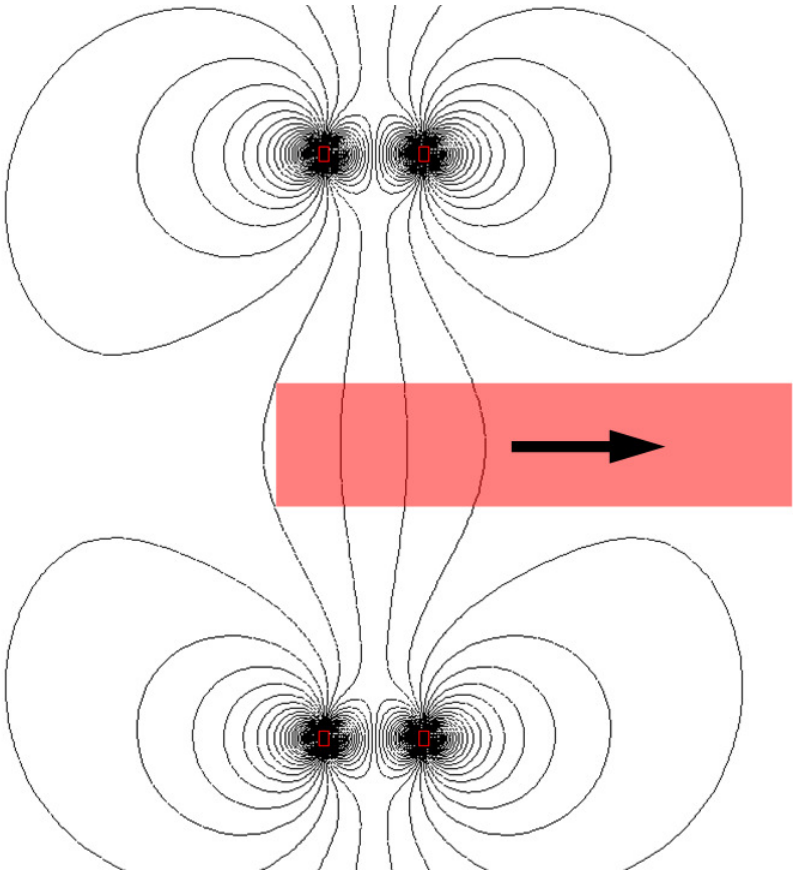

Figure 67: Magnetic flux lines in the case of 60x40 mm lateral magnets. The red strip represents the footprint of the beam from the PG to the accelerator exit.

Figure 68 shows the profiles of the B_x magnetic field component due to the lateral permanent magnets along the axis of a central beamlet.

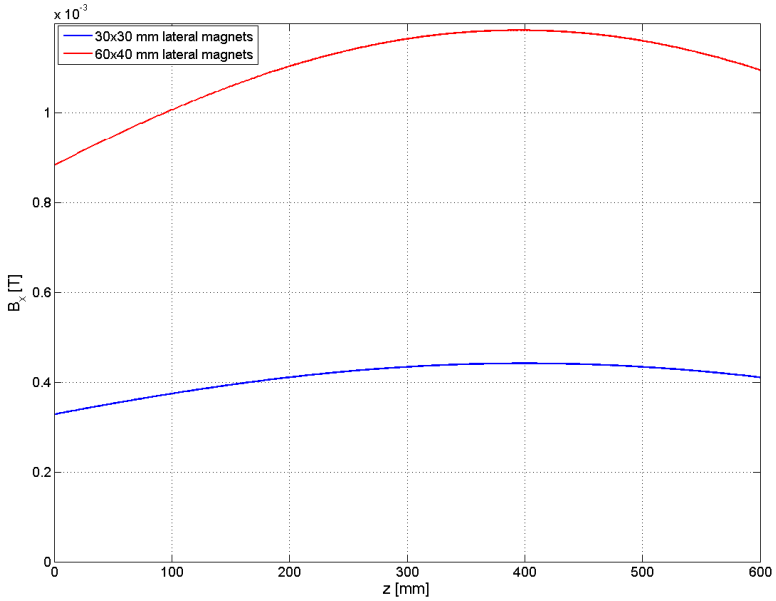

Figure 68: Profiles of magnetic field components along the beamlet axis given by the lateral permanent magnets: (blue line) 4 magnets with 30x30 cross section; (red line) 4 magnets with 60x40 cross section.

The power from the electrons exiting the accelerator is 2.44 MW in case *a* and 0.83 MW in case *b*. Giving the promising result of case *b*, a sensitivity analysis has been carried out in EAMCC to see what happens with different values of magnetic field.

The magnetic field is varied in the range between 0.4 and 1.6 times the nominal value, just by multiplying the sampled values for the relative coefficient. The corresponding profiles are shown in Figure 69.

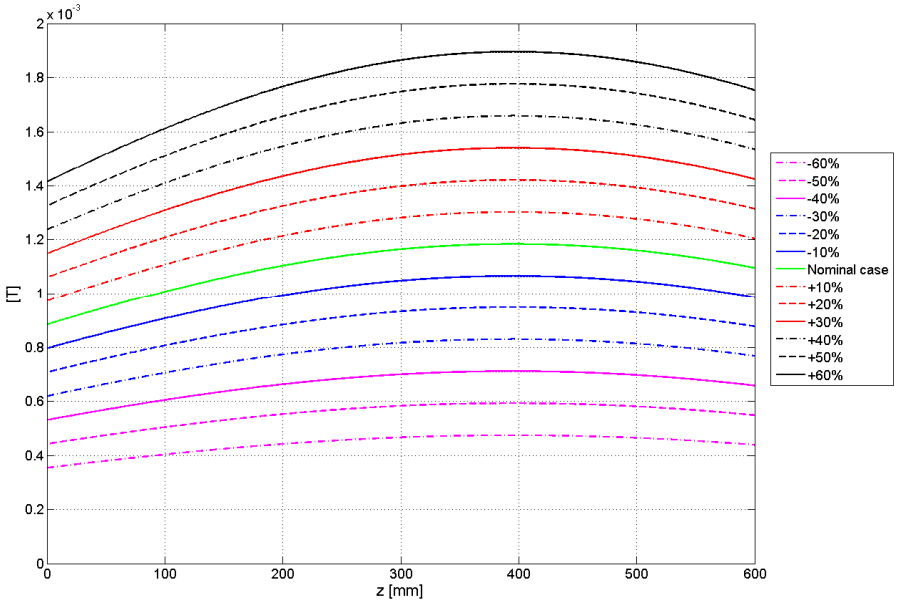

Figure 69: Profiles of the B_x components given by the lateral permanent magnets (40x60 cross section) along the accelerator, considering a variation of the magnetic field in the range ±60%.

The results in terms of heat loads on the grids and transmitted ions and electrons are summarized in Table 9. It can be observed that the best performing case is the one with a remanence of the permanent magnets of -20% the nominal value, where the power from the transmitted electrons reach the minimum (610 MW). On the other hand, the heat loads on the grids are rather high and in particular on AG3 and AG4 they are unacceptable.

	Total heat loads on the grids from stripped electrons [kW]							Power of the particles at the exit [kW]	
	EG	AG1	AG2	AG3	AG4	GG	Total on grids [kW]	D-	e-
-60%	73	1116	1420	1596	1965	1963	8133	39780	2020
-50%	70	1121	1509	1743	2111	1926	8480	39820	1270
-40%	73	1122	1576	1984	2143	1692	8590	39770	900
-30%	82	1103	1689	2212	2256	1204	8546	39750	720
-20%	77	1157	1801	2472	2074	1134	8715	39410	610
-10%	76	1129	1893	2516	1744	937	8295	39650	700
Nominal case	87	1091	1974	2621	1437	873	8083	39840	780
10%	85	1114	2007	2503	1350	922	7981	39580	950
20%	81	1087	2036	2280	1218	819	7521	39550	1360
30%	71	1071	2110	2182	1200	979	7613	39980	1500
40%	75	1101	2085	1915	1262	1003	7441	39740	1190
50%	69	1065	2119	1745	1578	1149	7725	39680	960
60%	73	1066	2052	1728	1674	955	7548	39730	950

Table 9: Heat loads due stripped electron on each of the accelerator grids and electron power at the accelerator exit for the configuration with different intensity of lateral magnets, calculated with EAMCC. Also the D^- power at the accelerator exit is reported.

The data from Table 9 are plotted for comparison in Figure 70. It can be observed there is a wave-like behaviour of the transmitted and dumped heat loads. In particular the presence of maxima and minima is clear.

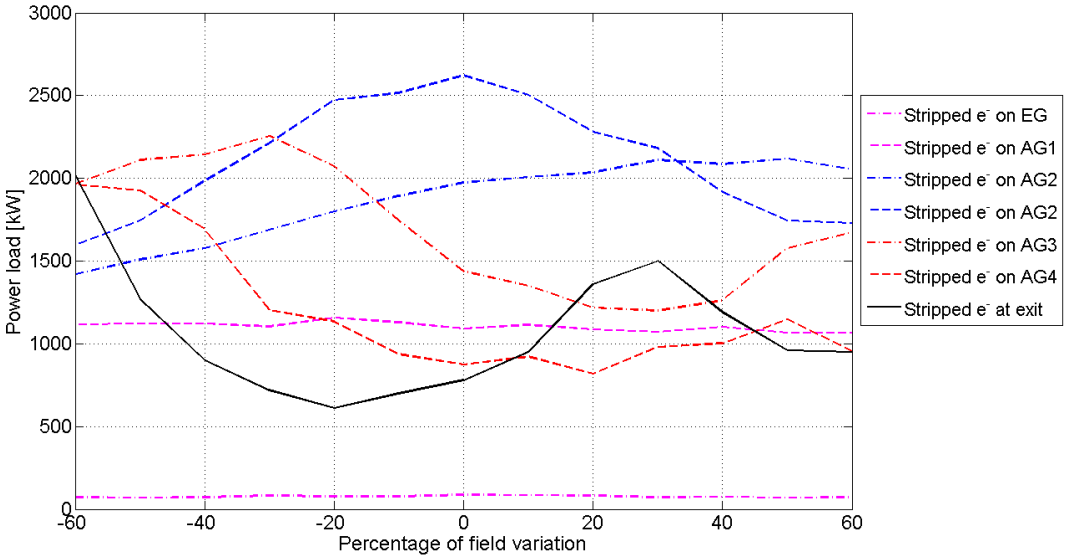

Figure 70: Amount of electrons dumped on the grids and transmitted out of the accelerator with different amounts of magnetic field by the lateral permanent magnets.

Lateral permanent magnets having a section of 60 x 32 mm can produce a field equal to the case of -20% the nominal 60 x 40 mm one, as it can be seen in Figure 71 where the two fields are compared.

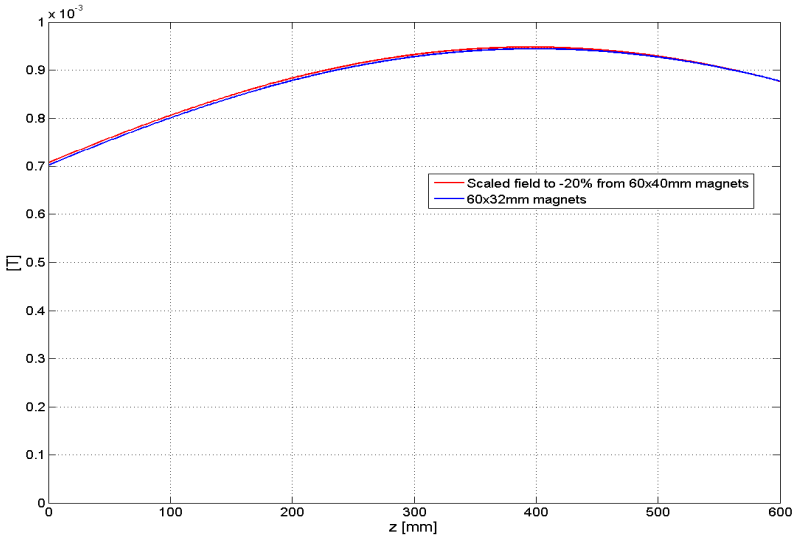

Figure 71: Comparison between fields obtained from 60x40mm magnets scaled to -20% (red line) and from 60x32mm magnets (blue line).

Similar magnetic field distribution can be obtained with coils placed outside the vacuum vessel, with advantages in terms of avoidance of very high electric field due to objects with small curvature radius which would be necessary for holding the permanent magnets and operational flexibility. In this way the field could be experimentally optimized in MITICA and eventually then reproduced with permanent magnets for a definitive implementation in the ITER HNB.

4.3.3 Diagonal field configurations

From the previous analyses, the following observations can be drawn:

- Regarding the configurations with permanent magnets embedded in the AGs, the case 1 of the horizontal field configuration is the best performing one, with an electron exiting power of 0.97 MW.
- In lateral permanent magnets approach the power from the transmitted electrons has a wave-like shape in function of the magnetic field strength. This confirms a previous result (see Figure 53) and could be due to the deflection of the electron onto the solid part of the grid (local grid power maximum) or into the neighboring apertures (local grid power minimum).
- A possibility to further increase the amount of electrons intercepted by the grids is to deflect the electrons diagonally, as schematized in Figure 72. In this way electrons would be directed to impinge on the solid region of the grid, with advantages in terms of better. This could be obtained by superimposing a horizontal magnetic field (B_x) component (for instance generated by lateral permanent magnets) and a vertical (B_y) component (for example generated by horizontal stacks of permanent magnets).

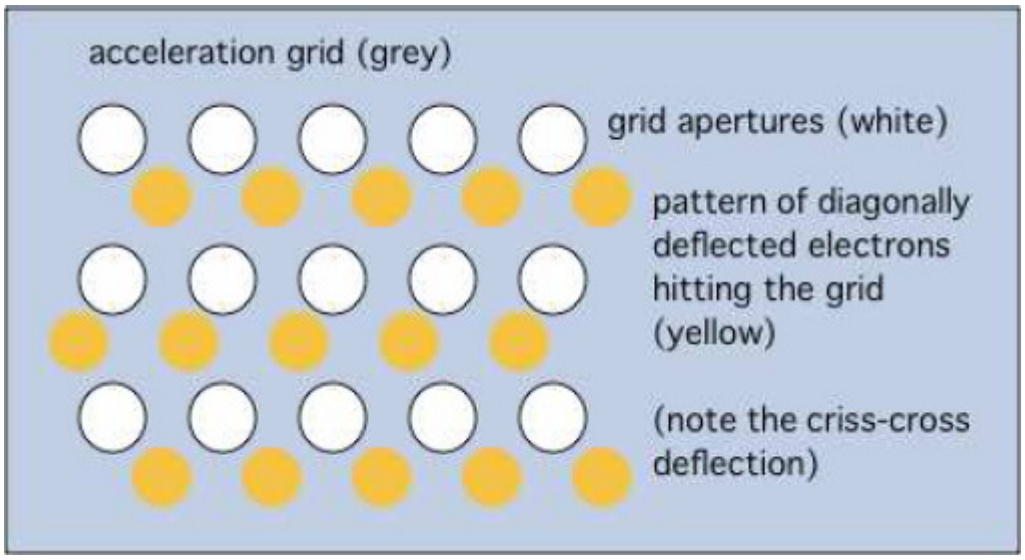

Figure 72: Sketch representing the diagonal deflection of the electrons. The footprints of the electrons, in yellow, are located in the part of the grid that is best cooled and further away from the apertures.

The combination of permanent magnets embedded into the AGs producing a local vertical (B_y) field and lateral magnets (permanent or coil) producing a horizontal long-range (B_x) field has been investigated in detail, because of its possible beneficial effects in terms of reduction of the

electrons at the accelerator exit and of more efficient electron power deposition on the grids and related cooling.

Again, comparisons have been made in terms of electron power deposition onto the grids and exiting the accelerator, with the superimposition of magnetic fields calculated with the previously described 2D models, both for the magnets embedded into the grids and those on the sides of the accelerator. This is allowed since no ferromagnetic material is present and the SmCo magnetic curve can be assumed linear with good approximation.

In particular, regarding the magnetic field profiles, for the different contributions it has been assumed:

- the B_x field produced by later magnets (uniform along x) is that corresponding to 60x32 mm permanent magnets;
- the B_y field produced by the magnets embedded in the EG is always the profile alternated from row to row;
- seven different configurations have been tested of the B_y field produced by the magnets embedded in the AGs (uniform along x):
    - 3 cases (1-3) with magnets polarized along y direction;
    - 3 cases (4-6) with magnets polarized along z direction;
    - for comparison, case 7 is considered without this contribution.

Figure 73 shows the profile of the magnetic field components for the seven configurations considered. The arrows represent the polarization of the embedded permanent magnets on two adjacent rows. The various configurations have different orientations of the AGs magnets, while the fields by the EG and lateral magnets are always the same.

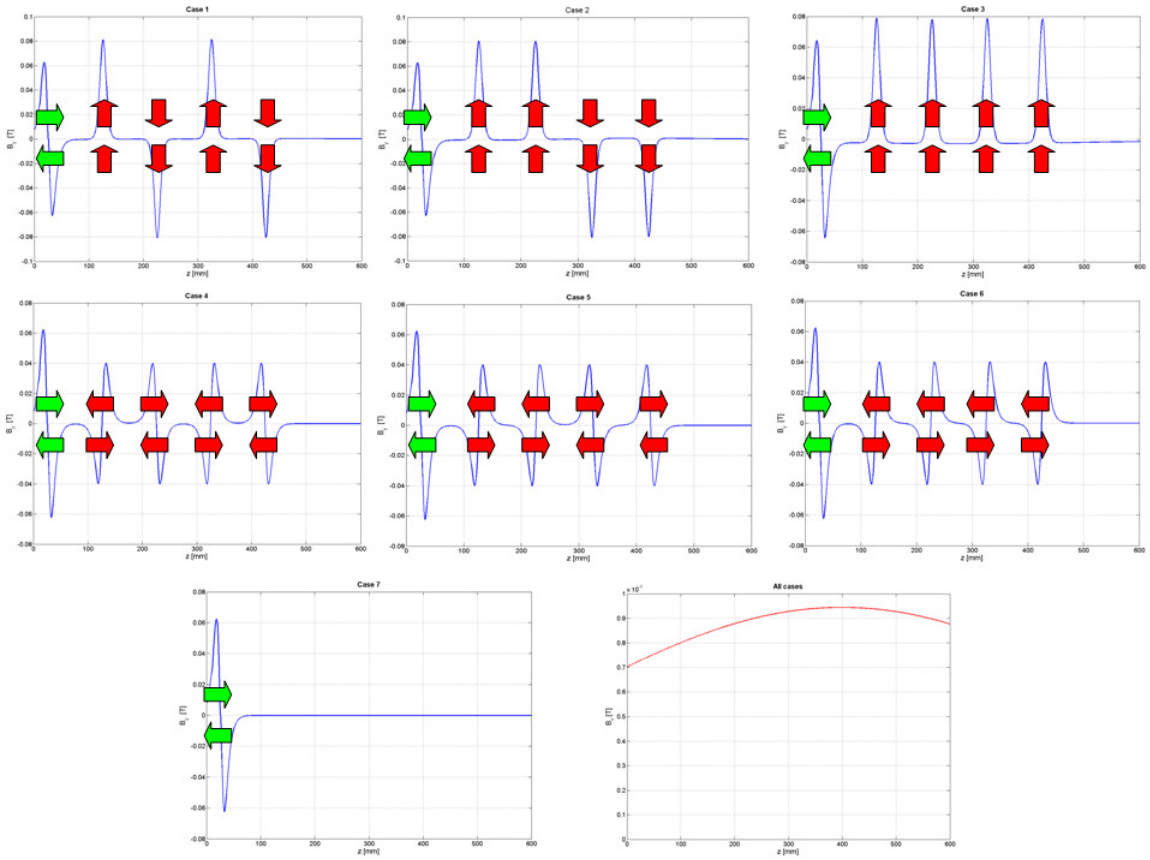

Figure 73: Bx and By magnetic field profiles along the beamlet axis calculated with ANSYS.

The main results of the heat loads on the grids and transmitted particles of the EAMCC ion simulation in the seven cases are reported in Table 10.

	Total heat loads on the grids from stripped electrons [kW]							Power of the particles at the exit [kW]	
	EG	AG1	AG2	AG3	AG4	GG	Total on grids [kW]	D^-	e^-
Case 1	75	1152	1649	1342	1119	820	6157	40080	1080
Case 2	82	1089	1759	1166	954	910	5960	40390	1010
Case 3	100	1066	1706	1442	1181	933	6428	40250	1116
Case 4	64	1485	1199	950	710	549	4957	40250	630
Case 5	85	1568	1069	1043	822	566	5153	40160	630
Case 6	88	1613	1067	955	893	751	5367	40490	460
Case 7	56	928	1868	1943	1757	866	7418	40230	410

Table 10: Heat loads due stripped electron on each of the accelerator grids and electron power at the accelerator exit for the seven configuration considered (see previous figure), calculated with EAMCC. Also the D^- power at the accelerator exit is reported.

It should be noted that the power on the grids due to co-extracted electrons is not here considered. Anyway, the heat load due to the co-extracted electrons is significant only for EG, it is not much

affected by the magnetic configuration considered and almost no co-extracted electrons can reach the accelerator exit.

It can be observed that:

- The combination of permanent magnets embedded into AGs polarized along *y* with lateral magnets (cases 1 to 3) do not bring any reduction of the transmitted electrons compared to case 7 (where there are no AGs magnets), on the contrary, it results largely increased. Nevertheless, the heat loads on the grids decreases.
- The combination of permanent magnets embedded into AGs polarized along *z* with lateral magnets (cases 4 to 6) brings a small increase of the transmitted electrons compared to case 7 (where there are no AGs magnets). The heat loads on the grids in these cases strongly decreases.
- The best performing case is number 4, where the transmitted load is low (630 kW) and the overall heat load on the grids is at the minimum (4957 kW).
- Another interesting case is number 6, where the transmitted load is lower than in case 4 (460 kW) and also the overall heat load on the grids is quite low (5367 kW).
- The minimum amount of transmitted electrons is obtained in case 7, where there are no permanent magnets embedded into AGs. But this case gives also the maximum overall heat load on the grids (7418 kW) and the maximum heat load on a single grid (1868 kW).

5 Optimization of RFX-mod MHD active control system

5.1 Introduction

The wall of any magnetic fusion device cannot be perfectly axisymmetric since it is composed of various 3D structures, such as large portholes, gaps, coil feeds, and other features. These can affect plasma stability, inducing magnetic field errors, coupling different modes, or increasing their growth rate. These effects should thus be considered and they can be mitigated by means of MHD feedback control approach. Experiments in reversed-field pinch (RFP) configuration may play an important role in this framework: due to the richer harmonic content of the edge magnetic field perturbations compared to the Tokamak, the RFP is a challenging test-bed for the development of edge magnetic field control scenarios.

The RFX-mod machine is equipped with an active control system of the MHD instabilities. Such control system has proved to be robust and well designed and to be an essential tool to improve the plasma discharge performance. In particular, the control system is extremely useful in the study of the new helical equilibrium which spontaneously appears in the RFP configuration at plasma currents above 1MA [37], being it flexible enough to apply a wide spectrum of static or time varying radial field perturbations.

It consists of 192 active coils, their independent power supply, 192 wide radial field sensors measuring the average radial magnetic field $\langle B_r \rangle$[3] and 192 small pick-up coils measuring the toroidal and poloidal components of the magnetic field. Active coils and sensors lie on toroidal surfaces and are positioned to form regular grids ($M \times N = 4 \times 48$) in the θ, φ coordinates plane. The active coils are placed outside the conducting structures which house the plasma: vacuum vessel, copper shell and supporting structure, whose non axisymmetric features shape the dynamic relation between the coils currents and the magnetic field. Therefore the feedback action is distorted by the dynamic response of the 3D wall to the externally applied fields.

[3] The average radial field is obtained dividing the flux Φ_s linked to each sensor by the sensor area.

In such conditions it may be useful to improve the quality of the radial field spatial spectrum produced by the active control system using a current distribution which reduces the side-harmonics produced by the system. Such current distribution can be obtained by making use of a simplified version of the dynamic decoupler proposed in [41], to be working on a limited subset of spatial harmonics in order to be able to run in real time with fast enough response to be integrated in a control scheme called Mode Control (MC).

Another important issue is that, because of the discrete number of actuators and sensors, the system produces an infinite number of sidebands together with the targeted harmonic of the radial magnetic field and the measures are affected by a systematic aliasing error. In order to correct this problem, currently in the control scheme is implemented a cleaning of the measured sideband content based on an analytical cylindrical model. The whole control algorithm has been called Clean Mode Control (CMC). Efforts have been undertaken also to improve the measurement cleaning, by taking into account the actual toroidal geometry of the system.

This chapter describes the analysis performed to optimize the CMC scheme through the development of a reduced dynamic modal decoupler and a new toroidal sideband cleaner. This work is based on models obtained by the use of the CARIDDI code, which allows to produce a state space representation of the system, with as many input as the actuators, as many output as the sensors and a number of states related to the FEM model discretization level, that is the number of finite elements used.

The next paragraph describes the mode coupling effect due to the toroidal geometry and 3D wall dynamic response in RFX-mod, and how this can be included in the MHD feedback control to mitigate its effects.

Paragraph 5.3 describes the models developed to carry out this work.

Paragraph 5.4 describes the steps needed to develop the reduced modal decoupler and the first results obtained in plasma discharges.

Paragraph 5.5 describes the concept behind the sideband cleaning and the method proposed to implement it in toroidal geometry.

5.2 Mode coupling effect

In the RFP configuration the tearing modes sustain the magnetic field reversal through a dynamo mechanism [38, 39] and they cannot be stabilized by magnetic feedback alone. Anyway, magnetic feedback can reduce the edge radial magnetic field of these modes to very low values, which is crucial both to avoid strong plasma–wall interaction and to reduce the core magnetic stochasticity. At high plasma current, the magnetic field configuration self-organizes into a new helical equilibrium, the so-called single-helical-axis (SHAx) state [40]. The SHAx state is characterized by the presence of a single dominant mode, with m = 1, n = −7 helicity in RFX-mod, which provides most of the dynamo. The MC scheme implemented in RFX-mod is used to apply a helical boundary condition to the edge radial field in order to keep it to low enough values and in general the plasma is also maintained into rotation.

The presence of non axisymmetric features in the conductive structures surrounding the plasma affects the dynamic relation between the MHD control coil currents and the magnetic field inside the chamber. In particular the wall equatorial gap introduces poloidal side-harmonics to the main m=1, n=-7 radial magnetic field. Such effects are due to the distortion of the eddy currents induced in the wall by time-varying currents either in the active coils or in the plasma, which depend strongly on frequency. It should be noted that the mode coupling is introduced by any non-invariance of the system, thus the poloidal non-invariance due to the toroidal geometry by itself introduces poloidal mode coupling. The non-invariance introduced by the conductive wall gaps further increases this effect.

Some results obtained in RFX-mod with and without the off-line application of the so called Dynamic Decoupler (DD) described in [41] are reported below, in order to show the distortion effect introduced by the three-dimensionality of the wall on the spatial distribution of the radial field produced by the MHD control system.

Figure 74 shows the radial magnetic field produced by a 1/-7 coil current rotating at 20Hz, as measured inside the shell in a dry shot. B_r results strongly perturbed at $\theta = 180°$ where the equatorial gap is present. As a result, spurious B_r harmonics with $m = 0,1,2$ / $n = 7$ are produced, as shown in Figure 74(c), in the time interval 0.1 - 0.2 s. It is expected that with plasma such error fields may in some way perturb the 1/-7 helical state and hence should be avoided.

Figure 74 (b) and (c) in the time interval 0.2 - 0.4s show the effect of the application of the DD in vacuum.

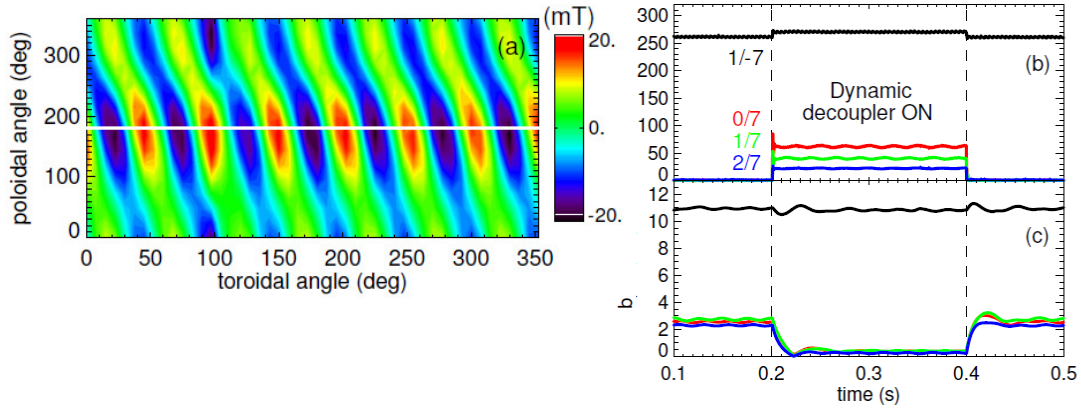

Figure 74: (a) Contour plot of the edge Br as a function of the poloidal and toroidal angles for aRFX-mod dry shot with a m=1/n=-7 coil current perturbation rotating at 20Hz. (b) Coil current and (c) B_r amplitudes of the 1/-7 (black), 0/7 (red), 1/7 (green), and 2/7 (blue) harmonics for the same dry shot. The dynamic decoupler is active in the time interval 0.2-0.4s. Courtesy of P. Piovesan [43].

The error field at the gap is strongly reduced in the time interval 0.2 - 0.4 s by a proper combination of coil current harmonics and thus a rather pure 1/-7 B_r harmonic can be produced inside the wall at the sensor radius.

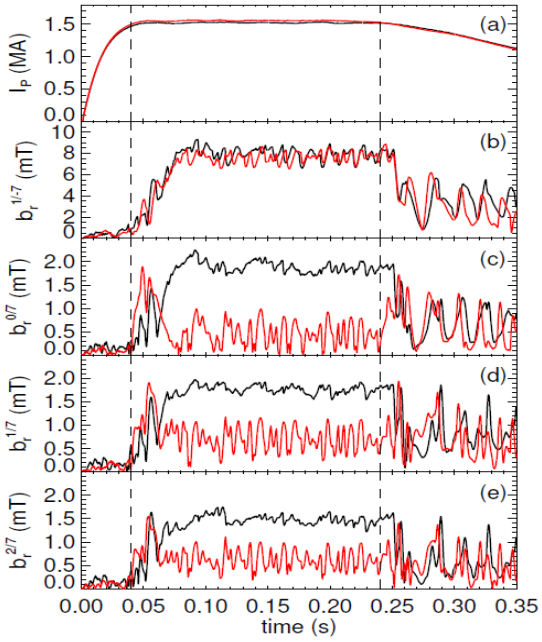

Figure 75: (a) Plasma current and Br amplitudes of the (b) 1/-7, (c) 0/7, (d) 1/7, and (e) 2/7 harmonics for two similar RFX-mod discharges with helical boundary conditions rotating at 20Hz applied from 0.05 to 0.25s. Discharge #28784 (black lines) has no dynamic decoupler, while discharge #28764 (red) has the dynamic decoupler active from 0.04 to 0.24s. Courtesy of P. Piovesan [43].

The DD has been also tested in plasma discharges where a helical boundary condition was applied to control the 1/-7 helical equilibrium, as shown in Figure 75, similarly to what described in [44]. In this case the 1/-7 mode is maintained into rotation at 20Hz in the period 0.05 - 0.25s. In discharge #28784 (black lines) no control is applied on the $m = 0,1,2 / n = 7$ error field harmonics, which have a finite amplitude. The DD is applied instead in discharge #28764 (red lines) in a pre-programmed manner and the $m = 0,1,2 / n = 7$ B_r harmonics are significantly reduced. The residual error field amplitude is probably due to variations in the 1/-7 mode amplitude, which cannot be compensated using pre-programmed waveforms. They could be further reduced by a DD running in real time with fast enough response.

5.2.1 Reduced Dynamic Modal Decoupler

The DD algorithm proposed in [41] has some disadvantages. Indeed, it requires to perform a matrix-vector product involving a matrix of size 192×576 and 384 state updates at each control step. Thus, the implementation of the DD algorithm requires too much processing power to be completed in less than 100 μs, which is about 20% of the current cycle time.

The DD was designed around the direct measurement of the input and output quantities, the currents feeding the active coils and the average radial magnetic field $\langle B_r \rangle$ signals respectively. Both of them depend on the poloidal and toroidal position of the actuator/sensor, quantities changing in time, which are said to lie in the primal space.

It is possible, in principle, to design a Dynamic Modal[4] Decoupler (DMD) considering variables in the spatial Fourier expansion of the input and output quantities, the so called dual (or modal) space, taking advantage of the spectral nature of the plasma instabilities.

As a matter of fact, if one needs to decouple a small number of modes, as it may be the case of RFX-mod or tokamaks, the dimensions of a full dynamic decoupler are excessive. Working in the dual space, a reduced DD can be obtained selecting a sub-model which contains only the relevant modes (for example m = 1, m = 0, m = -1, m = 2; n = -7), which requires a lower amount of processing power and can be run in real time. In this case the transfer function matrix is 8×8, due to the real and imaginary part of the signals, instead of 192×192, a great advantage for a real-time implementation.

[4] The term "modal" is not completely desirable, a better one would be "harmonic", since we are speaking about Fourier expanded quantities. The term "modal" has been chosen becouse the two concepts coincide in cylindrical geometry and the terminology is commonly confused by the Plasma Physics community also referring to toroidal geometry.

5.3 CARIDDI State Space model of RFX-mod MHD control system

In the past years a dynamic black-box model of the active coils and saddle probes has been developed to analyze and simulate the electromagnetic behaviour of the system. Satisfactory results were achieved in reproducing most of experimental responses and the model was used to select and test the gains of operating PID regulators. However, difficulties have emerged in reproducing some flux distributions such as those corresponding to m=0, low n current patterns.

Even though the design current of 2 MA has already been reached in several shots, a further increase in the control system performance and model accuracy is desirable, if not mandatory to study the quasi-single helicity (QSH) state. To this purpose, an activity has been started aimed at the development of a white-box model provided by the 3D finite element electromagnetic code CARIDDI (see paragraph 2.5) and its verification with experimental data.

The physical system, whose inputs are the currents I_c flowing in the saddle coils and whose outputs are the fluxes Φ_s measured by the saddle sensors, is hereafter denoted with the symbol M. The activity involves the development of a so-called white-box model M_w, the benchmark of its results against experimental data, the design of a reduced modal decoupler and the study of the side-harmonic spectrum produced by the active coils and measured by aliasing.

5.3.1 Model description

Linear time-invariant systems are typically represented as transfer function matrices or as state space models. Despite the two representations are theoretically equivalent, the former is more convenient when working in the frequency domain whereas the latter is better when working in the time domain. In the context of the present activity, the system M can be well represented as a linear time-invariant system. From an electromagnetic point of view, it is the equivalent mutual inductance matrix between active and measurement coils in presence of passive structure shielding. These conductive structures are responsible for the dynamic nature of the currents-fluxes relation, which otherwise would be static.

The model is calculated using the CARIDDI code, which applies the Galerkin's method to an integral formulation of the eddy currents problem (see paragraph 2.5). As a result of the method, the electromagnetic partial differential equations describing the eddy current problem are approximated by the matrix ordinary differential equation below:

$$\underline{\underline{L}}\frac{d\underline{I}}{dt}+\underline{\underline{R}}\underline{I}=\underline{V} \tag{5.1}$$

where $\underline{I}$ is the column vector made of the degree of freedom of the system (associated to instant values of the current), $\underline{V}$ is a column vector formed by integral quantities related to the source currents or by voltages applied to electrodes [22], $\underline{\underline{L}}$ and $\underline{\underline{R}}$ are matrices containing integral quantities representing self- and mutual-inductances among suitable current paths and their dissipative terms, respectively.

The RFX-mod model considers passive conducting structures (copper shell and mechanical structure)[5], saddle active coils and sensor coils. Figure 76 shows a portion of the optimized mesh built with Matlab® and used in Cariddi to build up the state space model. The copper shell, in red, presents a poloidal and an inner equatorial cut, which can be seen in the picture. The mechanical structure, in green, is made of two halves divided by poloidal cuts which present also an outer equatorial cut. In blue and black a number of active coils and sensors are reported.

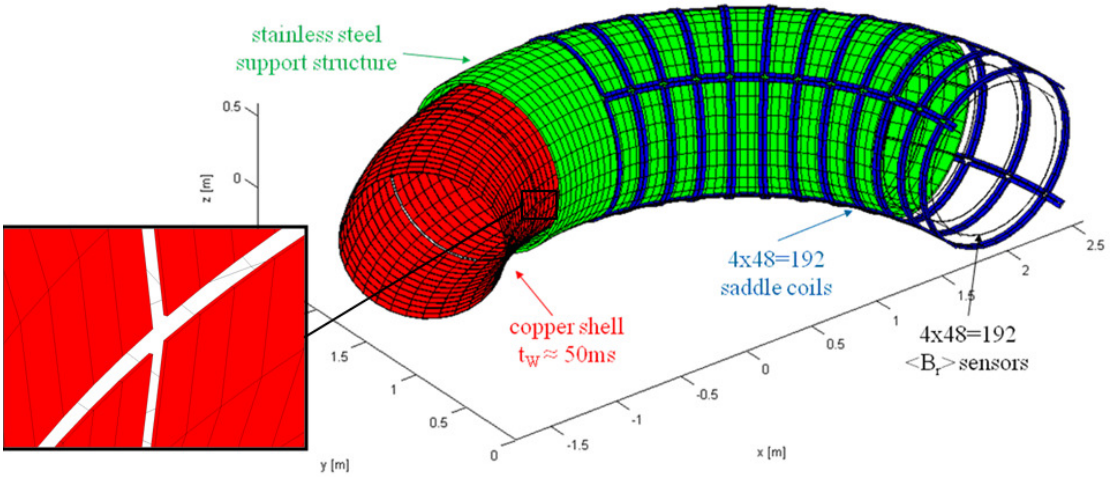

Figure 76: Portion of the mesh used in Cariddi: copper shell (red), mechanical structure (green), saddle coils and sensors (blue).

Each active coil and sensor has two electrodes, allowing to obtain a model which describes the dynamic relation among the voltages (or currents) feeding the coils and those resulting across the sensors.

The system of differential equation resulting to the application of the CARIDDI code is:

[5] The presence of the vacuum vessel proved to be superfluous in terms of the frequency response of the system (see paragraph 5.3.3.2), mainly because sensors are out of it, and therefore it was not considered in the model in order to allow a better mesh discretization of the other structures.

$$\begin{bmatrix} \underline{V}_s(t) \\ \underline{V}_c(t) \\ \underline{V}_p(t) \end{bmatrix} = \begin{bmatrix} \underline{\underline{L}}_{ss} & \underline{\underline{L}}_{sc} & \underline{\underline{L}}_{sp} \\ \underline{\underline{L}}_{cs} & \underline{\underline{L}}_{cc} & \underline{\underline{L}}_{cp} \\ \underline{\underline{L}}_{ps} & \underline{\underline{L}}_{pc} & \underline{\underline{L}}_{pp} \end{bmatrix} \begin{bmatrix} \dot{\underline{I}}_s(t) \\ \dot{\underline{I}}_c(t) \\ \dot{\underline{I}}_p(t) \end{bmatrix} + \begin{bmatrix} \underline{\underline{R}}_s & 0 & 0 \\ 0 & \underline{\underline{R}}_c & 0 \\ 0 & 0 & \underline{\underline{R}}_p \end{bmatrix} \begin{bmatrix} \underline{I}_s(t) \\ \underline{I}_c(t) \\ \underline{I}_p(t) \end{bmatrix} \tag{5.2}$$

Here the suffixes *s*, *c* and *p* stand for sensors, active coils and passive conducting structures, respectively.

Actually, no voltages or currents are applied to the coils during the CARIDDI code run, leaving to it the only task of calculating the matrices of inductances $\underline{\underline{L}}$ and resistances $\underline{\underline{R}}$, which are then elaborated in Matlab® to obtain the state space representation of the model. Since in the sensors no current flows and the current paths in the passive structure identified by the code are closed loops, $\underline{I}_s = 0$ and $\underline{V}_p = 0$.

Therefore the systems reduces to the two matrix equations below:

$$\underline{V}_s(t) = \begin{bmatrix} \underline{\underline{L}}_{sc} & \underline{\underline{L}}_{sp} \end{bmatrix} \begin{bmatrix} \dot{\underline{I}}_c(t) \\ \dot{\underline{I}}_p(t) \end{bmatrix} \tag{5.3}$$

$$0 = \begin{bmatrix} \underline{\underline{L}}_{pc} & \underline{\underline{L}}_{pp} \end{bmatrix} \begin{bmatrix} \dot{\underline{I}}_c(t) \\ \dot{\underline{I}}_p(t) \end{bmatrix} + \underline{\underline{R}}_p \underline{I}_p(t) \tag{5.4}$$

Integrating Eq. (5.3) and by simple algebraic manipulations of Eq. (5.4) the following current driven state space model is obtain:

$$\begin{cases} \dot{\underline{\Phi}}_p(t) = \underline{\underline{A}}\underline{\Phi}_p(t) + \underline{\underline{B}}\underline{I}_c(t) \\ \underline{\Phi}_s(t) = \underline{\underline{C}}\underline{\Phi}_p(t) + \underline{\underline{D}}\underline{I}_c(t) \end{cases} \tag{5.5}$$

where $\underline{\Phi}_p = \underline{\underline{L}}_{pp}\underline{I}_p + \underline{\underline{L}}_{pc}\underline{I}_c$ are the state variables, $\underline{\Phi}_s = \int \underline{V}_s dt$ are the output variables and

$$\underline{\underline{A}} = -\underline{\underline{R}}_p \underline{\underline{L}}_{pp}^{-1} \qquad \underline{\underline{B}} = \underline{\underline{R}}_p \underline{\underline{L}}_{pp}^{-1} \underline{\underline{L}}_{pc} \qquad \underline{\underline{C}} = \underline{\underline{L}}_{sp} \underline{\underline{L}}_{pp}^{-1} \qquad \underline{\underline{D}} = \underline{\underline{L}}_{sc} - \underline{\underline{L}}_{sp} \underline{\underline{L}}_{pp}^{-1} \underline{\underline{L}}_{pc} \tag{5.6}$$

Standard harmonic analysis manipulations allow to find the expression of the model transfer function matrix $\mathbf{M}_w(j\omega)$:

$$\underline{\underline{M}}_w(j\omega) = \underline{\underline{C}}\left(j\omega\underline{\underline{I}} - \underline{\underline{A}}\right)^{-1}\underline{\underline{B}} - \underline{\underline{D}} = \underline{\underline{L}}_{sc} - \underline{\underline{L}}_{sp} \frac{j\omega}{j\omega\underline{\underline{L}}_{pp} + \underline{\underline{R}}_p} \underline{\underline{L}}_{pc} \tag{5.7}$$

The number of state variables of the model has been gradually increased in order to achieve a better match with the experimental results. The optimized version of the model makes use of 12227 state variables. A model, at the limit of available computational performances, with 22771

state variables has also been examined. As its frequency response is very similar to that of the previous one, it has not been used to develop the DMD. The same model have been obtained also for virtual toroidal and poloidal pick-up sensors, exploiting the possibility of the code to calculate the three magnetic field components in a certain number of points, by integration of the singular element contribution to the current distribution, in accordance with the Biot-Savart law. The method allows getting a matrix conceptually similar to the mutual inductance matrix $\underline{\underline{L}}$, which links the magnetic field components to the current paths identified in the model. This method has also been exploited to analyze the aliasing part of the real measurements introduced by the sideband harmonic of the field, creating models with a higher number of virtual sensors with respect the actual 192 sensors. These analyses, described in detail in section 5.5, aim to verify the effect of the actual toroidal geometry on the measurement errors introduced by sidebands with respect those calculated by an analytical cylindrical model and to improve the Cleaning part of the MHD control scheme.

5.3.2 Mesh sensitivity analysis

Several meshes with different peculiarities and discretization levels have been tested in order to identify the most important features to have the more realistic model with the minimum computing resource demand. In other words, both the effect of the discretization and of distinctive features of the conductive structures have been examined. In particular the following six cases have been considered and tested, with different discretization levels:

1. meshes with only closed copper shell;
2. meshes with closed copper shell and a simplified support structure;
3. meshes with copper shell with toroidal gap and a simplified support structure;
4. meshes with copper shell with toroidal and poloidal gaps, and a simplified support structure;
5. one mesh with copper shell with gaps, a simplified support structure and vacuum vessel;
6. one mesh with copper shell with gaps and a detailed support structure.

It should be noted that this sensitivity analysis was particularly important because of the limited number of elements which was possible to adopt. Indeed, the CARIDDI code is based on an integral formulation allowing to take into account only the conductive elements in the model, without the need of meshing air regions. Consequently it calculates completely full matrices $\underline{\underline{L}}$

and $\underline{\underline{R}}$, which therefore occupy a memory proportional to the square of the number of DoF in the model. Calculating and storing an integral quantity for each element of the matrix $\underline{\underline{L}}$ and for several element around the diagonal of $\underline{\underline{R}}$, takes quite a long CPU time and may require too much memory (only one matrix occupies roughly $8 \cdot nDoF^2$ Bytes, with 20000 DoF it corresponds to 3.2 GB). Given the nature of the system to be modeled, which is purely 3D and so forbid to exploit any kind of symmetry to reduce the mesh, together with the available computer resource where the code can run (13 GB RAM), mesh convergence has not been completely met. Therefore a large part of the work was dedicated to analyze the effect of the discretization and of the presence of the gaps of the shell.

The most important features to be taken into account to get correct results are described below:

- Since the feasible discretization of the passive structures, it has to follow the presence of the saddle coils, in the sense that each coil has to "see" the same element pattern. So the number of elements of the passive structure meshes along the poloidal and toroidal direction has to be a multiple of the number of the coils (4 and 48 respectively). Otherwise the frequency responses of contiguous coils above 50 Hz can be appreciably different.
- Given the geometric approximation of the model and the need of minimizing the number of elements while obtaining the best results, the discretization of the passive structure is very critical (maximization of result quality). The surface corresponding to the coil projection has to have a number of elements high enough to allow patterns of induced currents in sufficient detail to reflect the physical reality. A too coarse discretization doesn't allow to simulate the patterns of the induced currents with sufficient accuracy to reproduce the actual cancellation at high frequency of the penetrating magnetic field which should occur in the case of closed shell. This leads to a horizontal asymptote of the frequency response of the model at high frequencies. Since we are interested to a finite bandwidth, approximately up to 200 Hz, in any case a too fine mesh is not required.
- The discretization of saddle coils and sensors has to be taken into account in order to avoid interpenetration with elements of the passive structures, in particular along the poloidal direction.

In order to perform the mesh sensitivity analysis, the configurations with closed copper shell have been used, since the behaviour of such system is expected. As a matter of fact, when sensors are placed inside a closed conductive structure, the measured magnetic field penetrating inside the structure decreases indefinitely as the frequency increases, resulting in the behaviour of a low pass filter. The sensitivity analysis has been performed comparing the frequency response of a sort of self-inductance, which is the frequency response between the currents feeding the coils and the flux measured by the underlining sensors. This has been done both in the primal and dual (modal) space. In the latter case, the compared quantities are so called harmonic self-inductance and mutual-inductance frequency responses, which are the frequency response between a current harmonic and the flux harmonic with the same harmonic number, and a current harmonic and the flux harmonic with a different harmonic number respectively. In Figure 77 the frequency response amplitude and phase (in primal space), for the different mesh discretization, are reported. Only one poloidal array has been considered, since without poloidal gap in the shell and without supporting structure the system is toroidally invariant (this concept will be clarified in paragraph 5.5.1). A toroidal position far from the poloidal gaps of the supporting structure has been chosen, in order to consider negligible their effect in those cases where the supporting structure has been implemented as well. Only the external, upper and internal coil position have been considered, since in the model of all the considered cases there is perfect symmetry between the upper and bottom position.

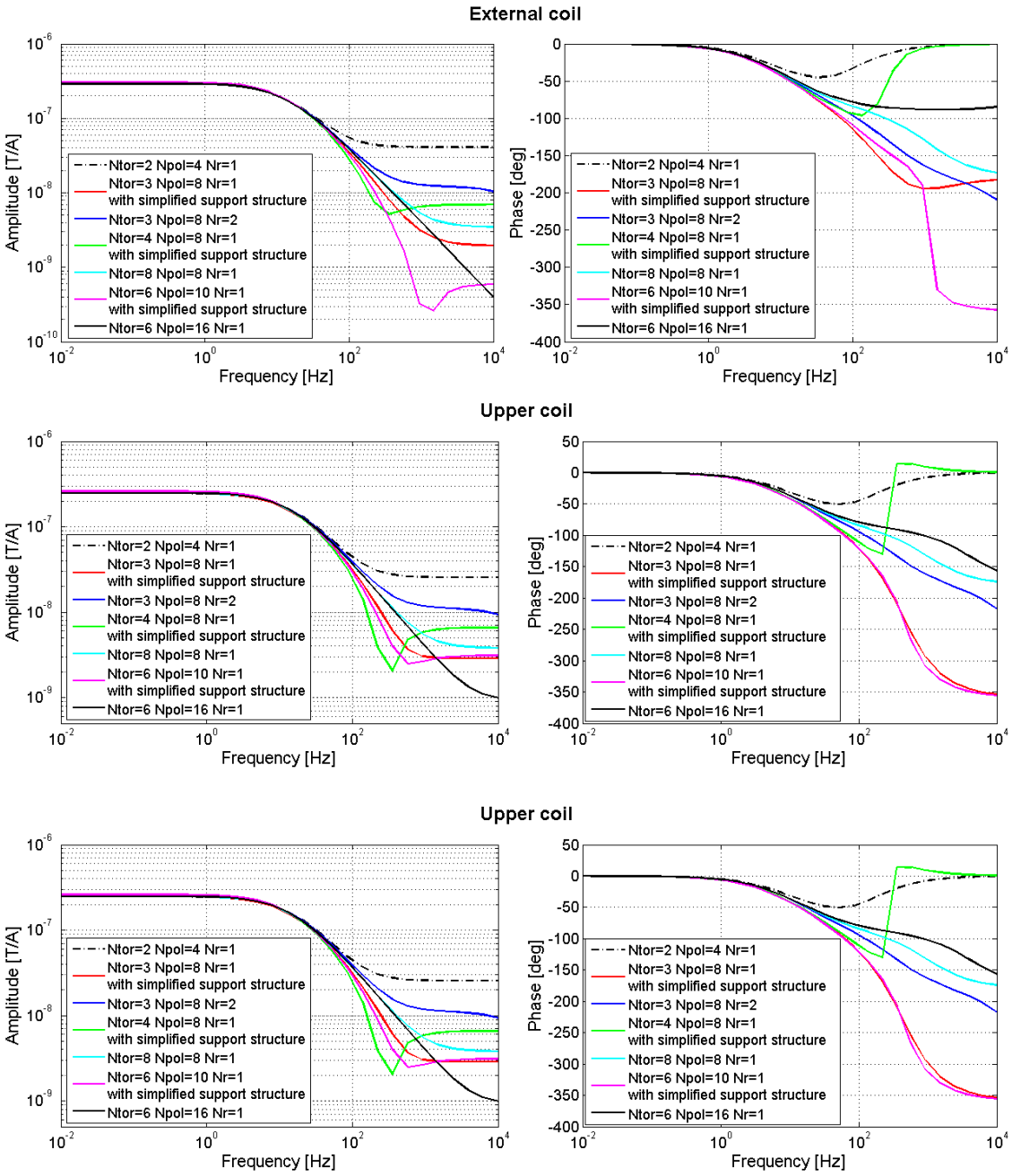

Figure 77: Comparison among the external, upper and internal coil frequency response of several closed shell model with a different degree of discretization. For each of the 48 sectors, the shell is discretized along toroidal, poloidal and radial direction respectively by: 2, 4 and 1 elements (dashed-dotted black line), 3, 8 and 1 elements with simplified support structure (red line), 3, 8 and 2 elements (blue line) 4, 8 and 1 elements with also a simplified support structure (green line), 8, 8 and 1 elements (light blue line), 6, 10 and 1 elements with simplified support structure (magenta line), 6, 16 and 1 elements (black line).

In Figure 78 the frequency response amplitude and phase of the $m = 1$, $n = -7$ harmonic self-inductance and of the poloidal mutual-inductance ($m = 0$, $m = 2$ and $m = -1$, $n = -7$) are reported.

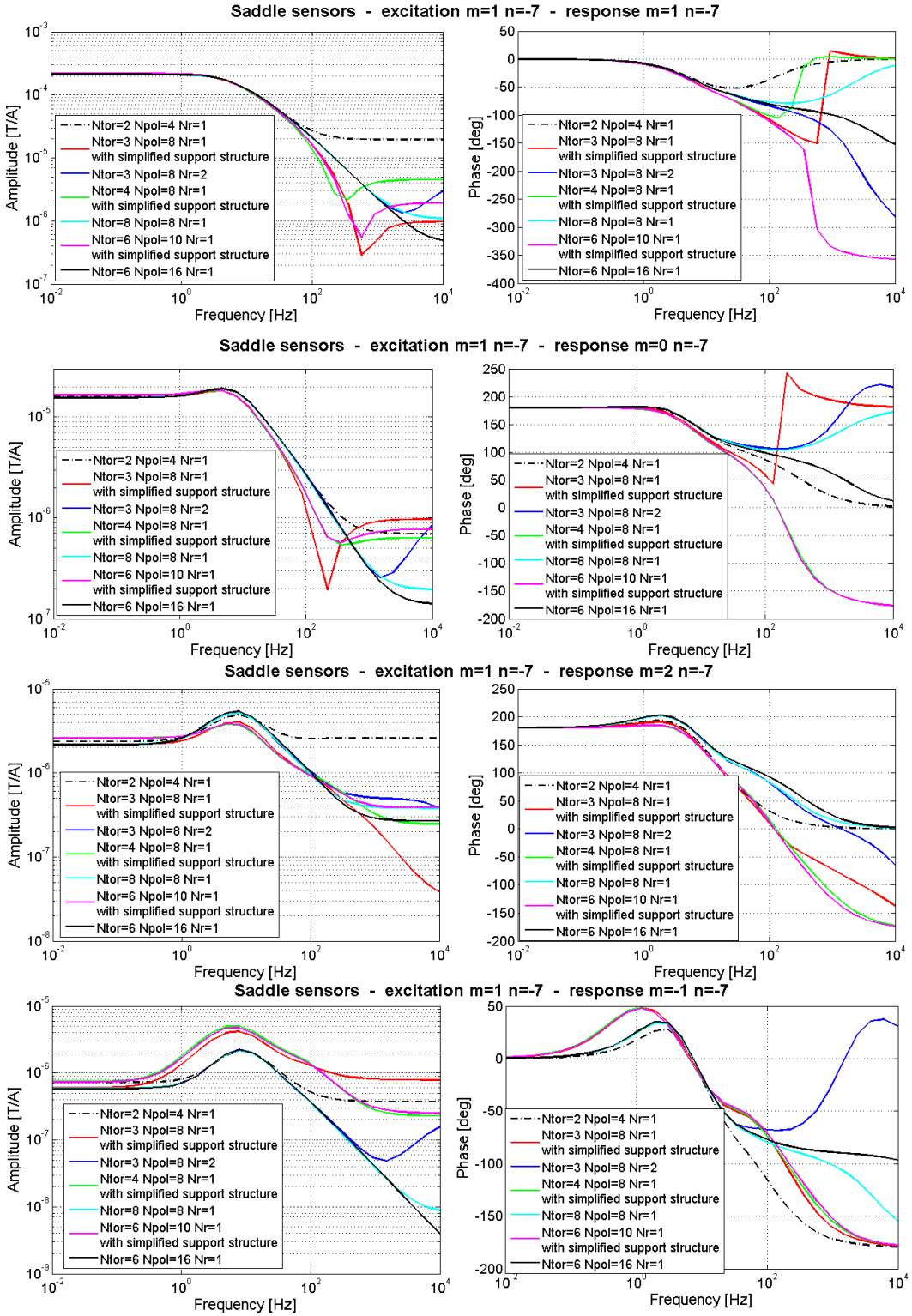

Figure 78: Comparison among the m=1, n=-7 harmonic self-inductance and relating poloidal mutual-inductance frequency response of several closed shell model with a different degree of discretization. For each of the 48 sectors, the shell is discretized along toroidal, poloidal and radial direction respectively by: 2, 4 and 1 elements (dashed-dotted black line), 3, 8 and 1 elements with simplified support structure (red line), 3, 8 and 2 elements (blue line) 4, 8 and 1 elements with also a simplified support structure (green line), 8, 8 and 1 elements (light blue line), 6, 10 and 1 elements with simplified support structure (magenta line), 6, 16 and 1 elements (black line).

As expected, the more realistic model is the one with the finest mesh, with 6 elements per toroidal sector and 16 per poloidal sector. The slope of the frequency response amplitude is the same of the other case without supporting structure, corresponding to a single-pole filter (-20 dB/decade), and it is constant up to a frequency higher than all other cases. However, in this case the number of DoF (18817) is such that the resulting matrices are already at the limit of manageability, since they have dimensions near the memory limit, without any model of the supporting structure.

As a matter of fact, the further filtering of the supporting structure is clear (see red, green and magenta cases). A sort of resonance condition would seem introduced by the presence of the supporting structure, but there is no basis to discriminate if it is the real behaviour or a numerical effect, since mesh convergence has not been achieved. Anyhow, it should be remarked that the bandwidth of interest is up to 200 Hz and this effect start just above this frequency. Considering the primal frequency responses, the case with 6 elements per toroidal sectors and 10 per poloidal sectors (magenta line in the pictures) should be chosen, but considering the dual ones, in the frequency range of interest, this model behaves very similarly to the one with 4 elements per toroidal sectors and 8 per poloidal sectors (green line in the pictures). Given the above considerations and the need of minimize the number of elements used, since the final aim of the work foresees dealing with quantities in the dual (modal) space, the mesh with 4 toroidal and 8 poloidal elements per sector has been chosen as reference for the following comparisons with experimental data.

5.3.3 Experimental benchmark

The comparison of the models with experimental data is carried out by evaluating three aspects:

a) the absolute value of the flux distribution associated with a specific coil fed with an alternate current at a given frequency;
b) the value of the parameter called modal self-inductance, as defined below;
c) the time evolution of the dominant spatial-harmonic content of the flux measures.

The choice of comparing the spatial-harmonic (modal) content of the involved quantities has been made because it is the most meaningful for the ultimate goal of these analyses and because it allows, in a sense, to mediate the local difference between models and actual system. However, it has to be pointed out that assessing the quality of the models by analysing only few cases may

be misleading. Each model can perform worse than the other in specific cases, even if the overall agreement is considered to be good.

5.3.3.1 Qualitative agreement

Figure 79 to Figure 82 show, in logarithmic scale, the amplitude of the normalised flux distribution at the sensors toroidal surface corresponding to a 20Hz alternate current in the inner coil of the 26th sector, in the following cases respectively:

1. model of closed shell and simplified supporting structure;
2. model of shell with equatorial gap and simplified supporting structure;
3. model of shell with equatorial and poloidal gaps and simplified supporting structure;
4. model of shell with equatorial and poloidal gaps, simplified supporting structure and vacuum vessel;
5. experimental data.

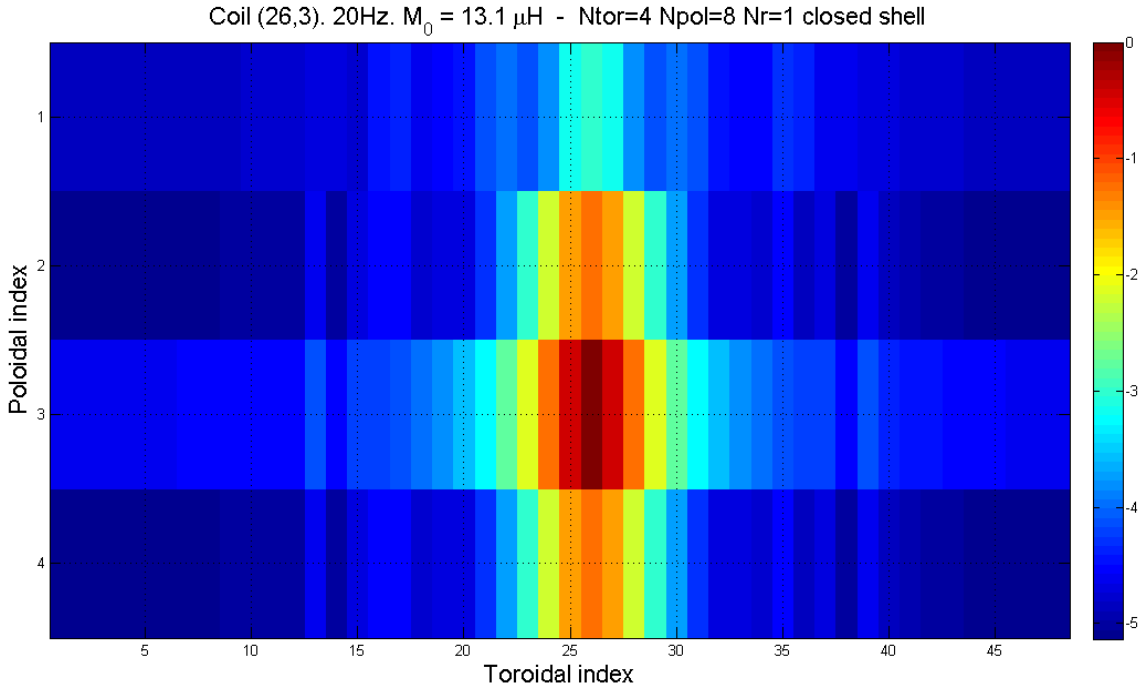

Figure 79: Normalized flux maps in the case of closed shell model. Logarithmic scale. M_0 is the inductance value corresponding to 0.

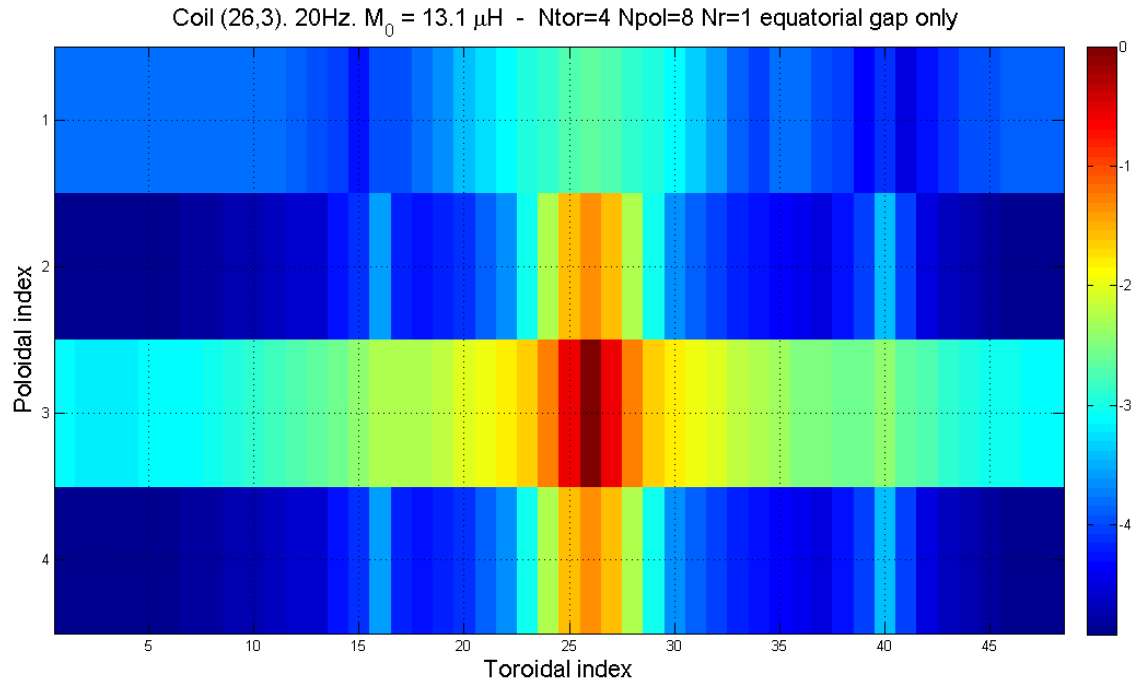

Figure 80: Normalized flux maps in the case of equatorially cut shell model. Logarithmic scale. M_0 is the inductance value corresponding to 0.

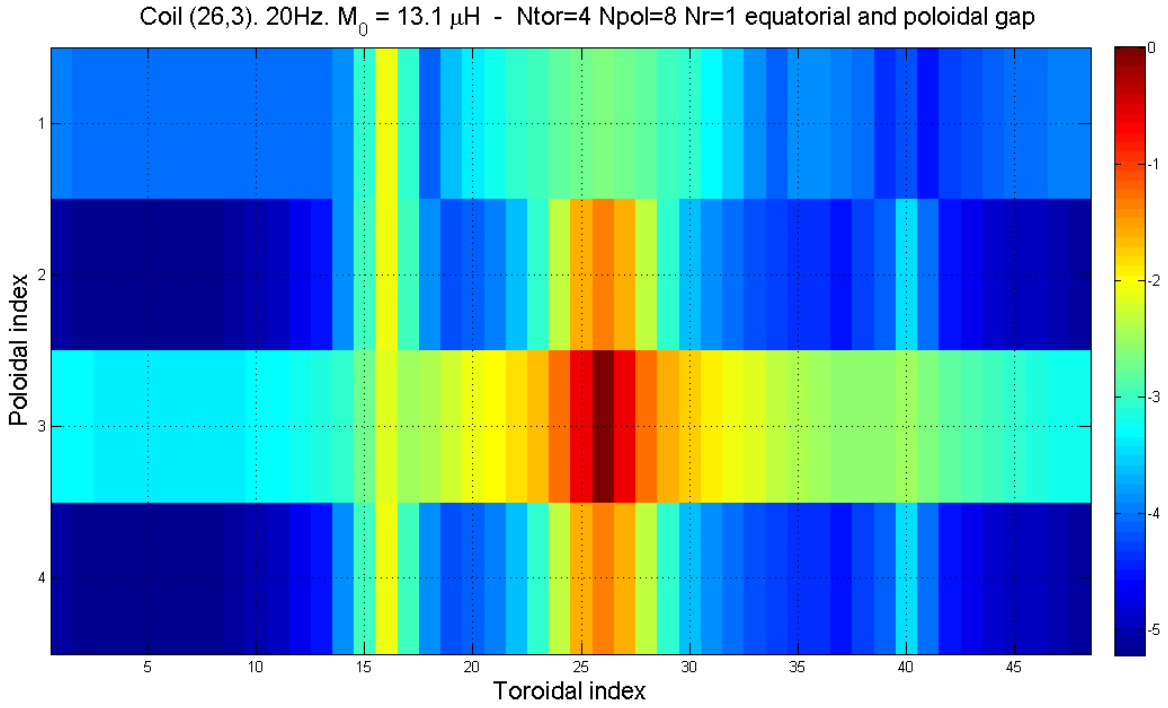

Figure 81: Normalized flux maps in the case of equatorially and poloidally cut shell model. Logarithmic scale. M_0 is the inductance value corresponding to 0.

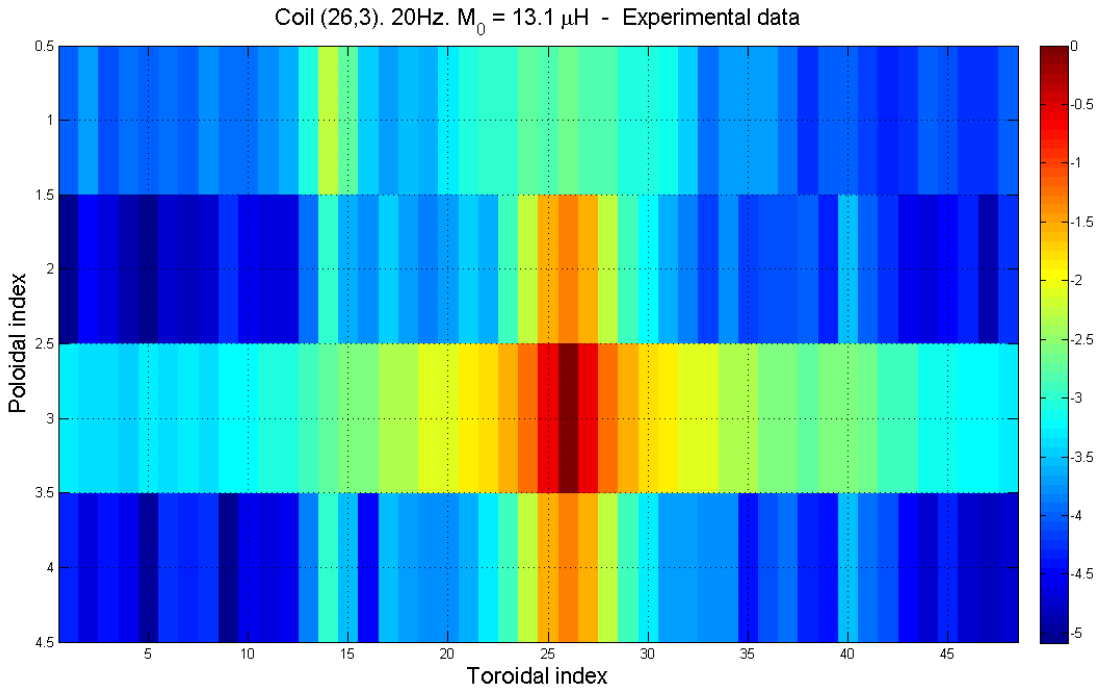

Figure 82: Experimentally estimated normalized flux maps. Logarithmic scale. M_0 is the inductance value corresponding to 0.

Even though this comparison is only qualitative, it shows how local features, such as the toroidal and poloidal gaps in the shell or in the support structure, can affect the flux distribution. The shell toroidal gap distortion is captured by the horizontal cyan line at poloidal index 3 (Figure 80 to Figure 82). The poloidal gap distortions are revealed by the yellow and light blue lines at toroidal index 16 and 40 for the models (Figure 81) and index 14 and 40 for the experimental data (Figure 82). This discrepancy is due to the fact that in the models the shell poloidal gap is simply a cut in the mesh corresponding to the 16^{th} sector, while the physical shell has two overlapping edge, separated by a dielectric layer, which cover three sectors from the 15^{th} to the 17^{th}. Thus, in the real system the flux passes in between the two edges exiting at the sensors of the 14^{th} sector.

The presence of the vacuum vessel results irrelevant when the analysis is performed on the $\langle B_r \rangle$ measured by the saddle sensors, confirming the experimental evidence (in this regard no data are reported here). A figure related to the case with the vacuum vessel results the same as the same case without vacuum vessel shown in Figure 81 and so it is not shown here.

5.3.3.2 Quantitative agreement: frequency domain

A quantitative comparison can be performed examining the frequency response of the models and of the physical system. To this end, a unitary current distribution consisting of a pure (m, n, f) harmonic is conceptually applied as an input to the models and the resulting (m, n, f) harmonic of

the flux measures is calculated. The ratio between the flux harmonic and the current harmonic is the harmonic self-inductance at the frequency *f*. It is a complex number measured in Henry but it is convenient to stress that it is not a self-inductance from an electrical point of view.

Current pure harmonics distributions are those in the form,

$$I_l = I_{m,n} \cos\left(2\pi\left(\frac{mh}{4} + \frac{nk}{48} + ft \right) + \varphi_{m,n} \right) \tag{5.8}$$

and are unitary if $\varphi_{m,n} = 0$ and $I_{m,n} = 1$. In the above equation $-23 \le n \le 24$ and $0 \le m \le 2$ are respectively the toroidal and poloidal mode numbers, $0 \le h \le 47$ and $0 \le k \le 3$ the toroidal and poloidal coil indices, *f* is the frequency and *t* is the time. Coils are indexed by $0 \le l = 4h + k \le 191$ or equivalently by the couple (*k*, *h*) itself.

Experimental harmonic self-inductance is obtained by performing the ratio between the measured flux harmonic and the current harmonic applied to the physical system. Harmonic self-inductance of the model can be calculated by evaluating the transfer function matrix $\mathbf{M}_w(j\omega)$ at the requested frequency. However, as the actual current spectrum contains a small amount of spurious harmonics, for a more meaningful comparison with experimental data, such results are instead obtained by applying experimental currents to the models. The spatial distribution in the primal space of the flux at a given frequency is obtained by multiplying the transfer function matrices $\mathbf{M}_w(j\omega)$ at that frequency for the vector of experimental currents. The spatial distribution in the dual space of the flux is then calculated by Fourier transforming the previous results. The calculated modal self-inductance is finally obtained by performing the ratio between the calculated flux harmonic and the experimental current harmonic.

Similarly it is possible to determine the cross coupling between modes, that is the ratio between the flux side harmonic and the applied current harmonic, the so called harmonic mutual-inductance. In particular the poloidal (*m*) coupling is of interest.

In the following figures the same models as before are compared to experimental data. In Figure 83 and Figure 84, respectively, the amplitude and phase of the modal self-inductance for an m = 1 n = -7 is presented. In Figure 85 to Figure 90 amplitudes and phases of the m = 0 n = -7, m = 2 n = -7 and m = -1 n = -7 side-harmonic are shown.

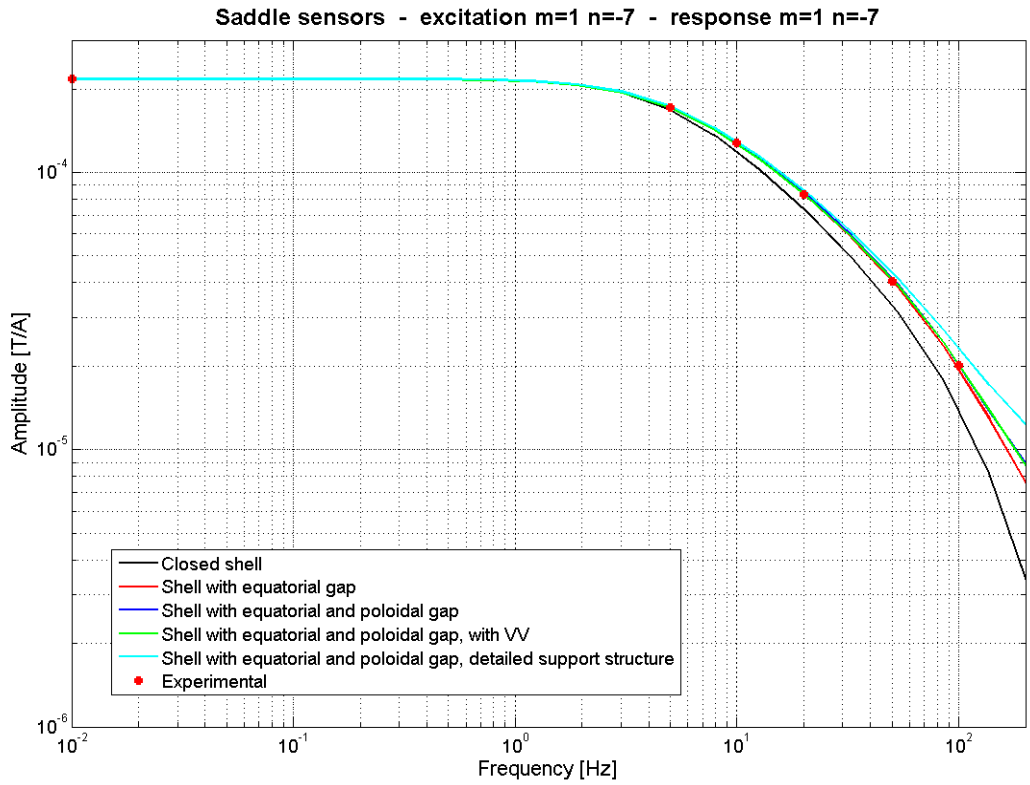

Figure 83: Amplitude of the (m = 1, n = -7) modal self-inductance as function of the frequency.

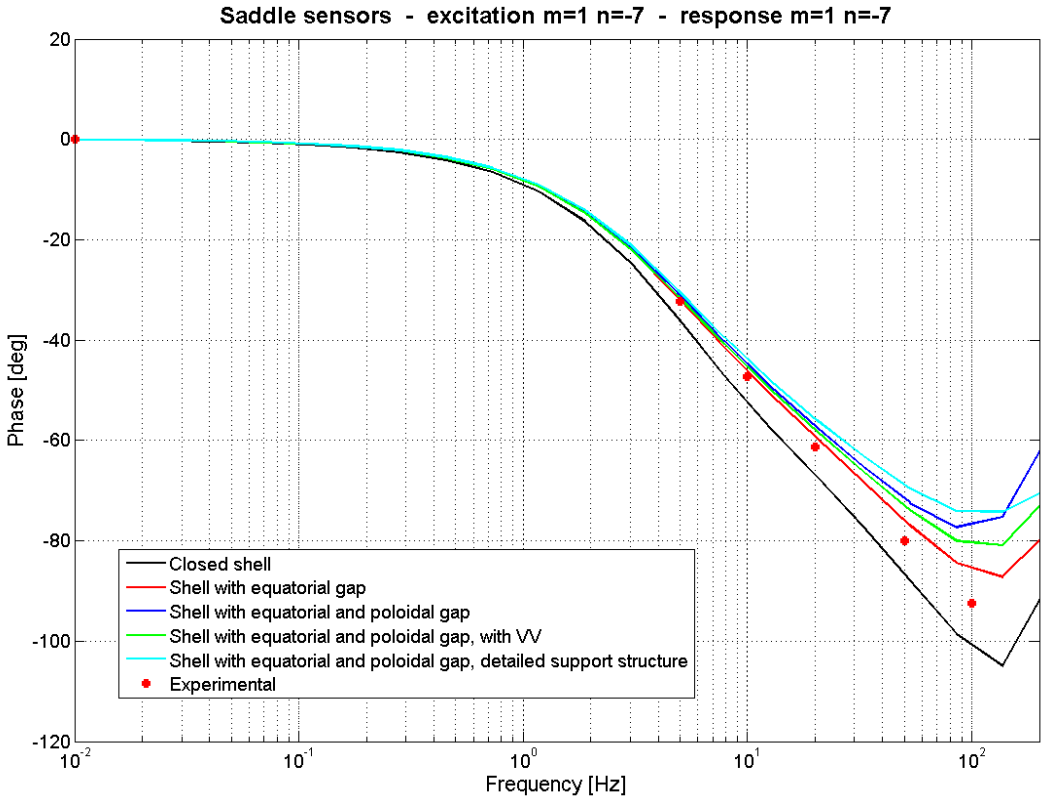

Figure 84: Phase of the (m = 1, n = -7) modal self-inductance as function of the frequency.

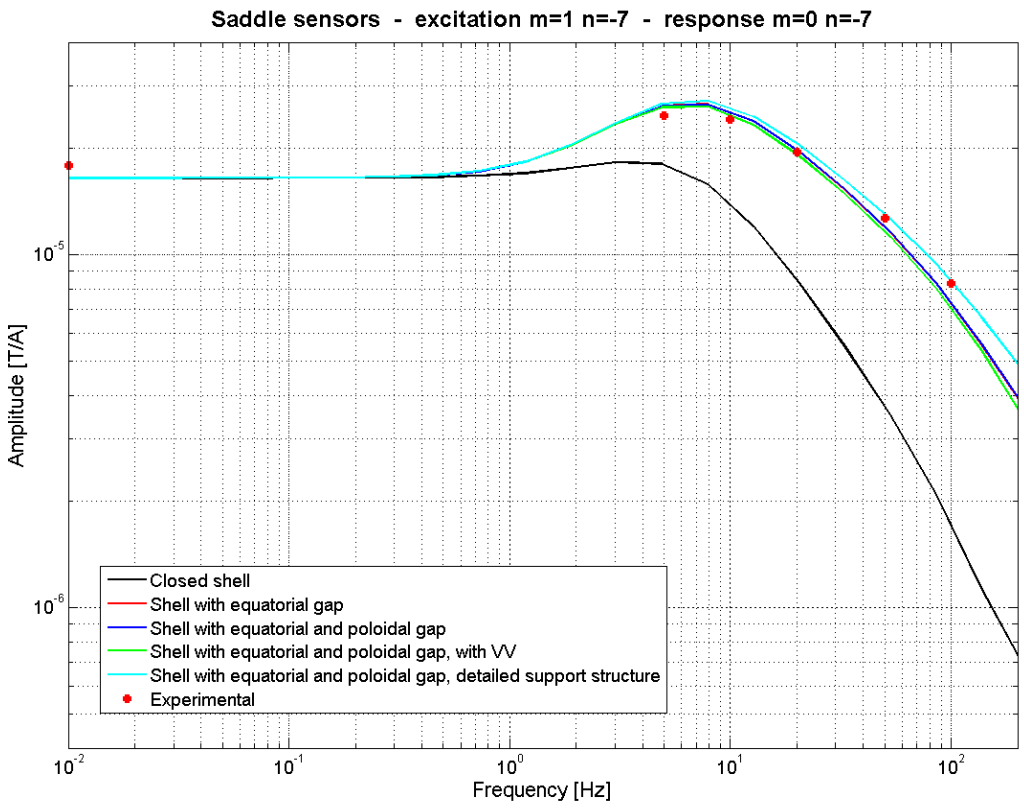

Figure 85: Amplitude of the (m = 1, n = -7) - (m = 0, n = -7) modal mutual-inductance as function of the frequency.

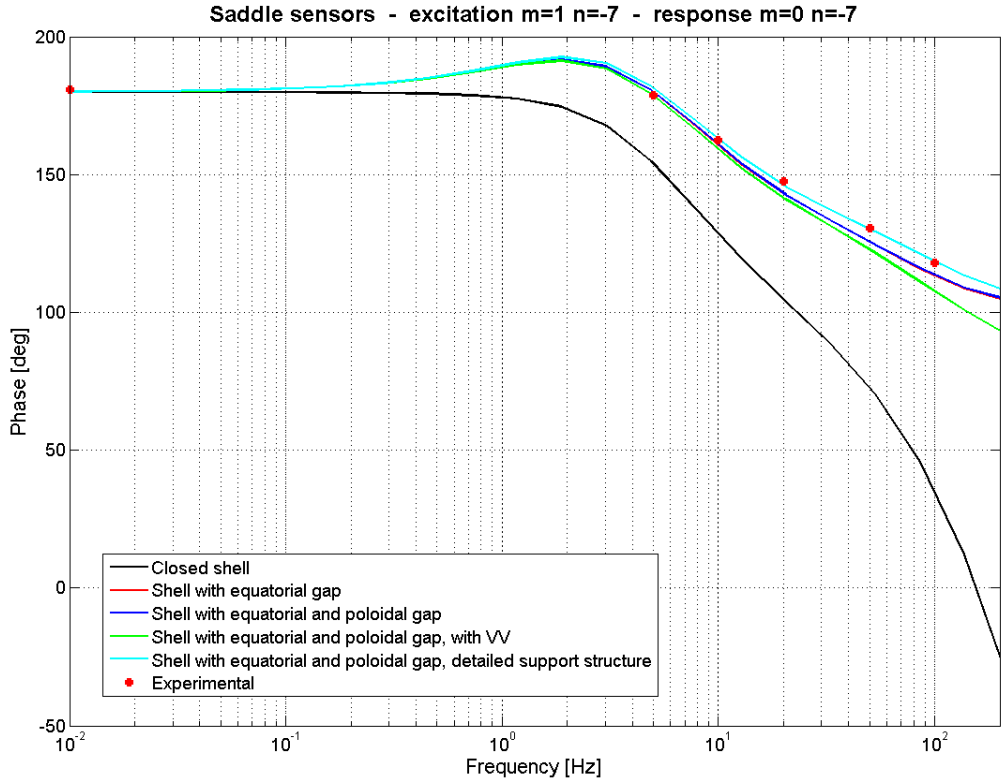

Figure 86: Phase of the (m = 1, n = -7)- (m = 0, n = -7) modal mutual-inductance as function of the frequency.

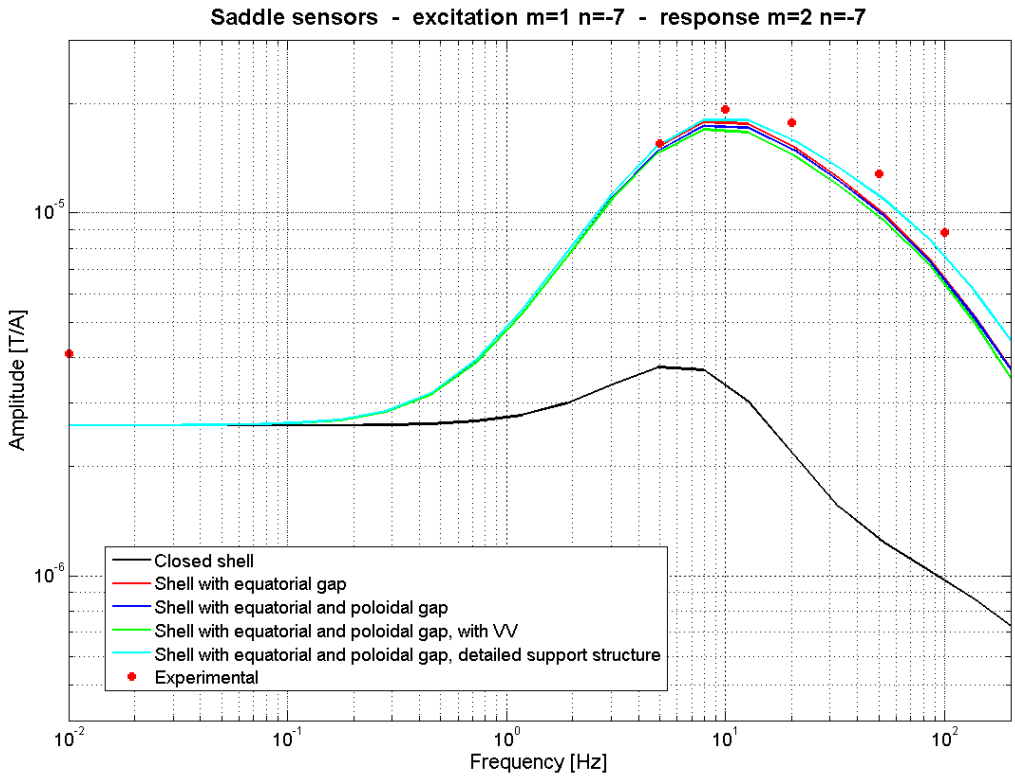

Figure 87: Amplitude of the (m = 1, n = -7) - (m = 2, n = -7) modal mutual-inductance as function of the frequency.

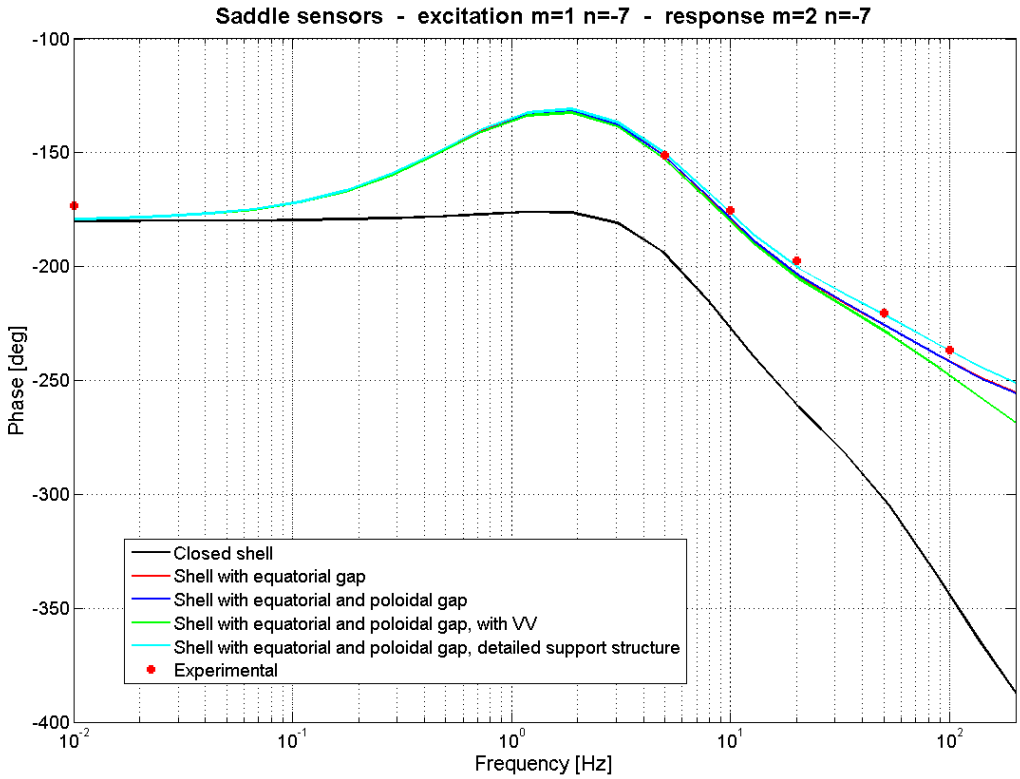

Figure 88: Phase of the (m = 1, n = -7) - (m = 2, n = -7) modal mutual-inductance as function of the frequency.

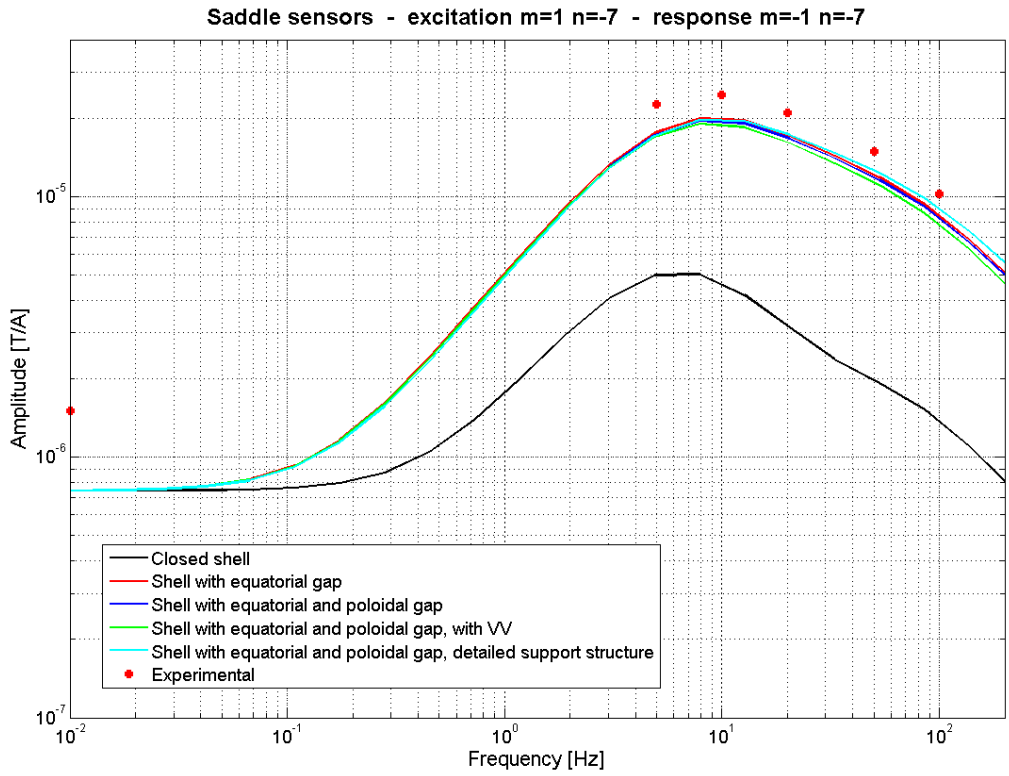

Figure 89: Amplitude (m = 1, n = -7) - (m = -1, n = -7) modal mutual-inductance as function of the frequency.

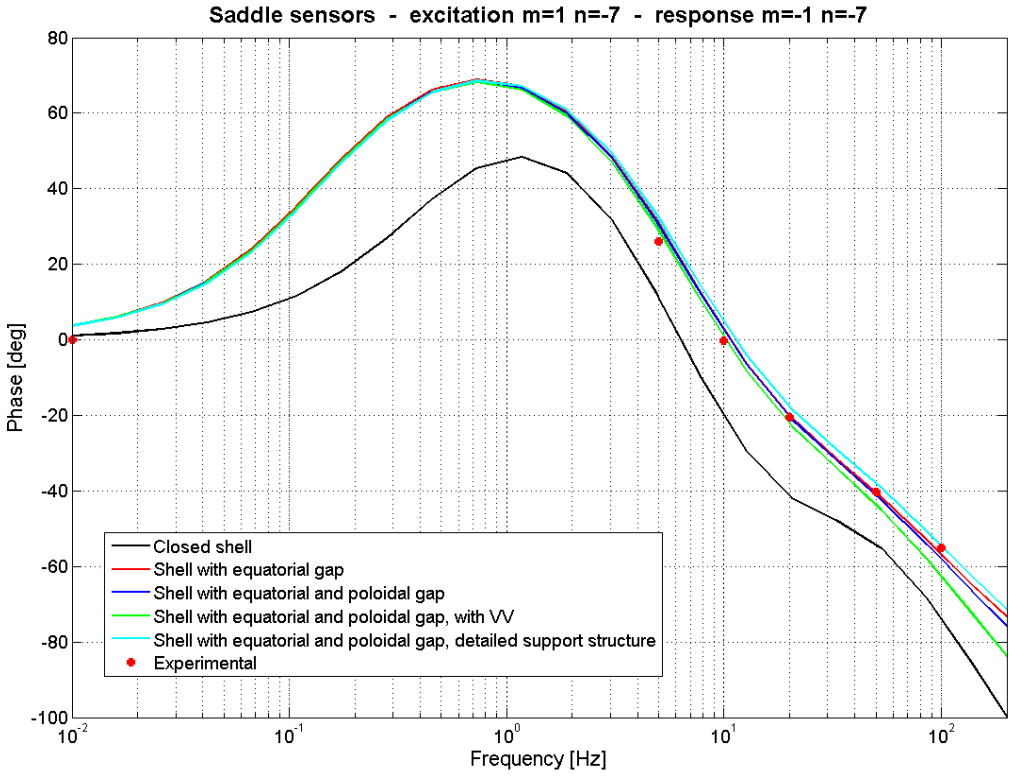

Figure 90: Amplitude (m = 1, n = -7) - (m = -1, n = -7) modal mutual-inductance as function of the frequency.

It should be noted that in the figures the frequency responses have been plotted up to 200 Hz, for two reason: this is the band of interest and the models present diverging behaviours above this frequency. Unfortunately, it is not possible to obtain experimental points to make a benchmark outside this region.

In the case of the harmonic self-inductance the agreement on the amplitude is excellent for all the models, except for the one with closed shell and that with the detailed supporting structure above 50 Hz. The agreement on the phase is quite good, degrading above 20 Hz. The experimental data are more closely reproduced by the one without the poloidal gap on the shell. It is worth recalling that the physical poloidal gap is not a simple cut on the shell, as instead it is modelled, and there is also a porthole in that position.

Regarding the side harmonics, the agreement on the amplitude is generally worse than that shown by the harmonic self-inductance, while that on the phase is quite good with a maximum deviation of about 10° for the case with vacuum vessel. We speculate this is due to the higher degree of spatial variance introduced by the real passive structures. In this case the best model seems to be that with the detailed supporting structure. In particular some models work better at low frequency, although there are exceptions. For example the model with the detailed supporting structure is better at high frequency.

What emerges from the previous figures is that probably a model with vacuum vessel, detailed support structure and a more realistic shell poloidal gap together could better match the experimental data on the whole frequency range. Since the present computer resources do not allow us to build such a model, the simplified model which reproduces better the experimental data seems to be the one with only shell equatorial gap.

The presence of the vacuum vessel seems to be necessary only if detailed support structure is adopted.

5.3.3.3 Quantitative agreement: time domain

Other interesting results obtained running simulations of the models applying experimental currents are those in time domain. These results can be directly compared against the experimental outputs of the physical system *M*, that is the spatial Fourier transformation of the measured fluxes in time. Given the large size of the models, their simulations cannot be directly performed on the continuous state space model using numerical tools like Simulink® and they required a specialized solution. The continuous state space models have been first converted into

discrete state space models and then simulated. The integration of the discrete state space can thus be performed with algebraic steps. The discrete state space representation has been obtained from the continuous one by applying the so-called bilinear or Tustin transformation [49]. The resulting discretized equations are

$$\begin{cases} \underline{\Phi}_p^{(k+1)} = \underline{\underline{A}}_d \underline{\Phi}_p^{(k)} + \underline{\underline{B}}_d \underline{I}_c^{(k)} \\ \underline{\Phi}_s^{(k)} = \underline{\underline{C}}_d \underline{\Phi}_p^{(k)} + \underline{\underline{D}}_d \underline{I}_c^{(k)} \end{cases} \tag{5.9}$$

where the superscript $^{(k)}$ represent the quantity at the k^{th} time step, which has been set at Δt = 50 μs. The above matrices are expressed in terms of those in Eq. (5.6) in the equations below:

$$\underline{\underline{A}}_d = \left(\underline{\underline{I}} + \frac{\underline{\underline{A}}\Delta t}{2} \right) \left(\underline{\underline{I}} - \frac{\underline{\underline{A}}\Delta t}{2} \right)^{-1} \qquad \underline{\underline{B}}_d = \left(\underline{\underline{I}} - \frac{\underline{\underline{A}}\Delta t}{2} \right)^{-1} \underline{\underline{B}} \sqrt{\Delta t}$$

$$\underline{\underline{C}}_d = \sqrt{\Delta t}\, \underline{\underline{C}} \left(\underline{\underline{I}} - \frac{\underline{\underline{A}}\Delta t}{2} \right)^{-1} \qquad \underline{\underline{D}}_d = \underline{\underline{D}} + \underline{\underline{C}} \left(\underline{\underline{I}} - \frac{\underline{\underline{A}}\Delta t}{2} \right)^{-1} \underline{\underline{B}} \frac{\Delta t}{2}$$

The approach is analogous to solving the ordinary differential Eq. (5.5) using a fixed step solver with a time step equal to Δt.

Because of the large size of the matrices, only the models with simplified support structure and without vacuum vessel have been discretized.

In Figure 91, (a) and (b) respectively, the amplitude and phase of the time evolution of the m=1, n = 1 harmonic of a 5Hz rotating mode simulated with the three models is compared to an experimental measure (pulse number 20110). In terms of mean amplitudes, the pictures show a good agreement between the model with both toroidal and poloidal gaps in the shell and the experimental result. The higher amplitude of the double-frequency oscillations shown by the experimental data could be due to the higher spatial variance of the actual system with respect to the models. Both the model with and without the poloidal gap in the shell are phase shifted, ahead and behind respectively, by 1.62 degrees with respect to the experimental result.

The results of pulse number 27068, shown in Figure 92, are quite different. The agreement between models and experiment in the case of a 50Hz rotating mode with m=1, n = -7 harmonic in amplitude is better for the one without poloidal gap in the shell. The model with poloidal cut is phase shifted of about 0.52 ms, while the one with toroidally continuous shell presents a 0.22 ms phase lag.

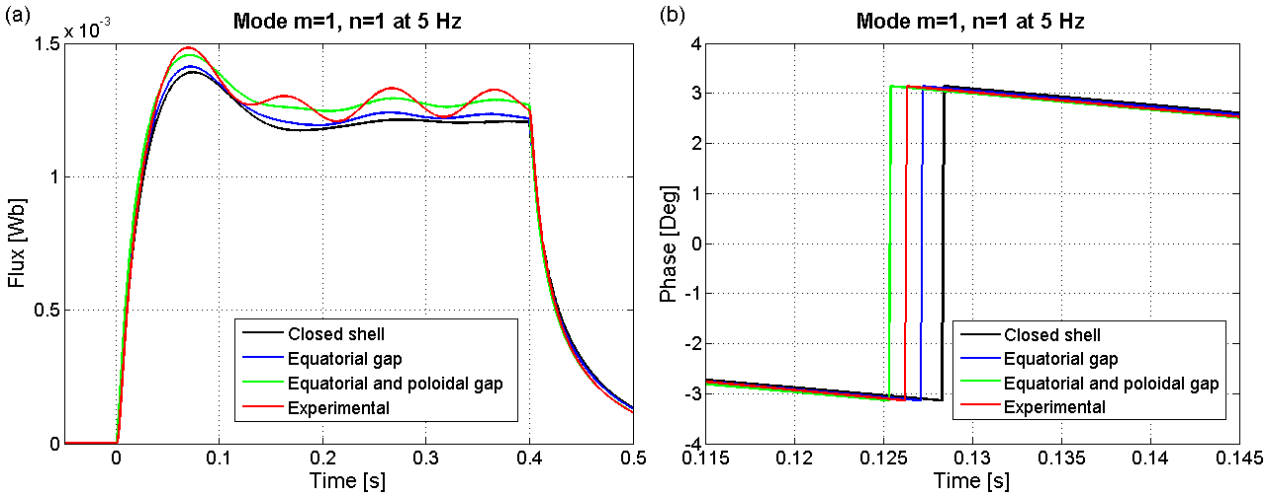

Figure 91: m=1, n=1 harmonic of shot number 20110: (a) amplitude and (b) phase.

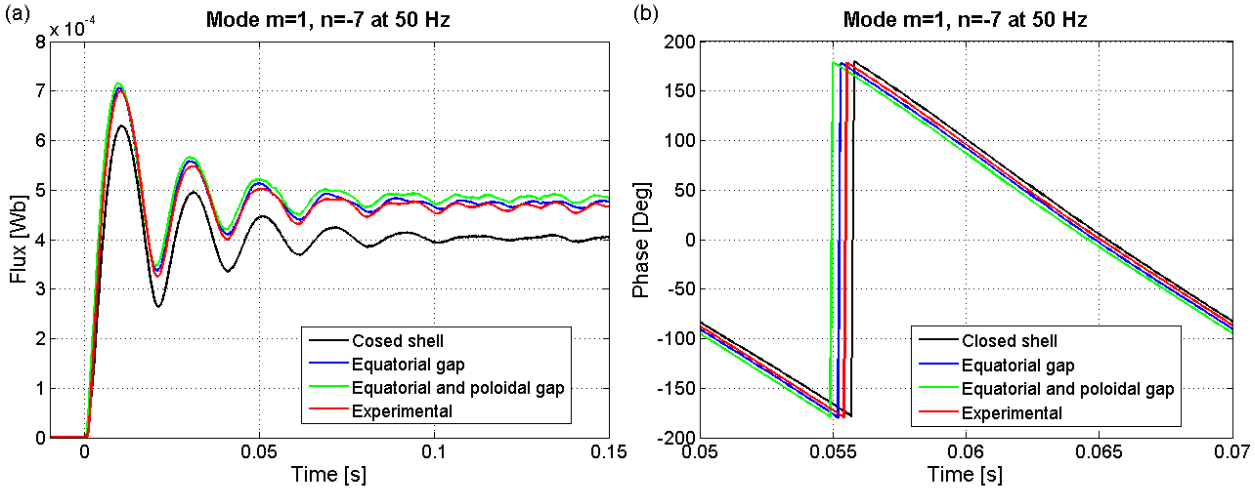

Figure 92: m=1, n=-7 harmonic of shot number 27068: (a) amplitude and (b) phase.

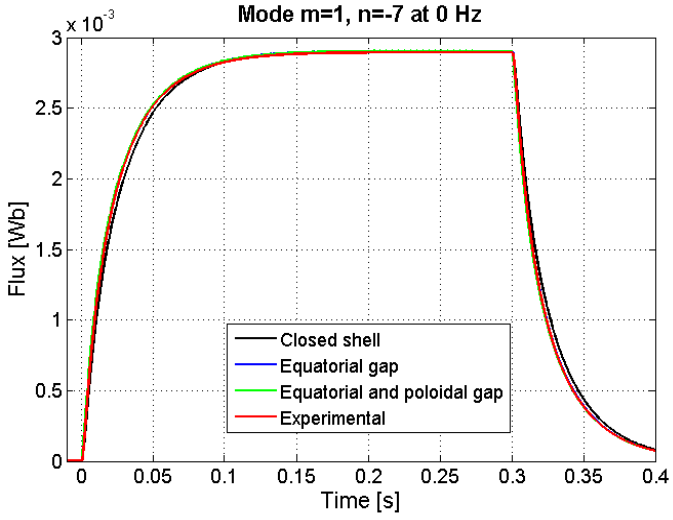

Figure 93: m=1, n=-7 harmonic of shot number 27082.

In Figure 93 the results of the m = 1, n = -7 harmonic of a static mode are shown (pulse number 27082). In the steady state part all models correctly coincide and reproduce very well the experimental result.

Both the models with and without poloidal gap in the shell reproduce fairly well the measures in several experimental conditions. Taking into account both results in the time and in the frequency domain, the model considered reproducing better the physical system, at least in the framework of the development of a reduced dynamic modal decoupler for the dominant m = 1, n = -7 mode, is that without the poloidal gap in the shell. However, there is still margin for improvements, as in some cases experimental results are not well reproduced. In particular a more detailed modelization of the shell edges overlapping which constitute the poloidal gap might lead to a better matching to experimental results in any operation conditions.

5.4 Dynamic Modal Decoupler: development and implementation

The idea behind the dynamic decoupler is the following. Having a system Σ, an approximation of its inverse Σ^{-1} is constructed so that, up to a frequency $f \leq f_0$, the series with the system is an approximation of the identity, as illustrated in Figure 94.

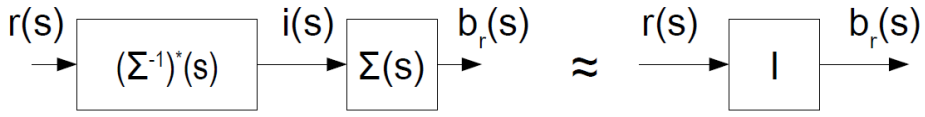

Figure 94: Scheme of the dynamic decoupler concept.

In our framework the system Σ is the MHD control system, in vacuum, and its inverse Σ^{-1} allows to reduce the spurious harmonics produced by itself by finding those currents which flowing in the coils produce a radial field $b_r(s)$ approximately equal to the reference r(s).

The decoupler $(\Sigma^{-1})^*$ can be designed using mathematical models of the MHD control system only, as a linear time invariant Multiple-Input Multiple-Output system. A first design has been performed using the black-box model developed in 2006 [41]. As already mentioned in section 5.2.1, this dynamic decoupler (DD) correspond to the pseudo-inverse of the entire system, implemented in primal space. This means that it requires the spatial distribution of the mean value of the radial field as input and produces the current values to feed the coils as outputs. To be completed in real time, this implementation of the DD algorithm requires more processing power than available in the present control system. Indeed, it has to perform a matrix-vector product involving a complex matrix of size 192x576 and 384 state updates at each control step.

The possibility of reducing the problem stems from the spectral nature of the plasma instabilities, whose proper representation considers variables in the spatial Fourier expansion of the input and output quantities. As a matter of fact, the problem can be strongly reduced inverting the system in dual space form and selecting only the small number of modes one needs to decouple. This is correct if the toroidal coupling is negligible.

The design process of such a modal decoupler consists of several steps. Once performed the preliminary step of obtaining a good mathematical model of the system Σ, described in paragraph 5.3, ideally one could proceed indifferently in the following two way:

- inverting the full model, Fourier transforming the inverted model and selecting the interesting modes only;

- Fourier transforming the direct model, selecting the interesting modes and inverting the obtained sub-model.

In both cases, the last step is a model reduction in order to limit the states of the model and thus to be implemented in real time.

This would be true if the inverted system Σ^{-1} maintained stability, which is not the case, since the system Σ is like a low-pass filter. It has been tried to follow these steps with different sequences in order to find a way to do it automatically, without success, just for the nature of the system. The only way to set up a dynamic decoupler is that of following the same sequence used in [41] passing through the calculation of the transfer function matrix of the system in a number of frequency samples. The entire design process can be summarized as follow:

1. Obtain a good mathematical (state space) model of the system Σ;
2. evaluate the system transfer function matrix in the frequency domain of interest $\Sigma(j2\pi f)$;
3. Fourier transform in spatial domain each transfer function matrix to get their dual representation;
4. perform the inversion of the transfer function matrix at each frequency sample;
5. select the proper sub-matrix of required modes,
6. shape the inverted transfer function matrix at high frequency in order to be compatible with a causal system;
7. perform a parametric identification of the so shaped inverted transfer function matrix in the frequency domain, in order to obtain a real-time implementable (state-space) form of the decoupler.

As already mentioned and widely described in paragraph 5.3, the first two steps have been accomplished creating a numerical model by the use of the FEM code CARIDDI, which has been then elaborated in Matlab® to get its state space form and so to calculate its transfer function matrices $\mathbf{M}_w(j\omega)$ in 30 frequency samples, logarithmically distributed in a range between 10^{-2} and 10^4 Hz.

Each transfer function matrix has then been spatially (2D) Fourier transformed into the dual domain. At this stage a formal mathematical description of the system representation in primal and dual spaces is mandatory.

5.4.1 Systemic description of the RFX-mod active control system

The system input (currents) and output (fluxes) quantities are described as real signals over the domain $I_\vartheta \times I_\varphi \times \mathbb{R}$ (denoted by $u, y : I_\vartheta \times I_\varphi \times \mathbb{R} \to \mathbb{R}$) where $I_\vartheta = \mathbb{Z}(1/M)/\mathbb{Z}(1)$ and $I_\varphi = \mathbb{Z}(1/N)/\mathbb{Z}(1)$ are quotient groups and $\mathbb{Z}$(T) denotes the algebraic group consisting of integer multiples of the real number T. The first two domains describe the poloidal and toroidal spatial dimensions, respectively, while the third represents the time. *M* is the number of input and output along the poloidal dimension and *N* along the toroidal one. The relation between input and output is described by the following integral [42]:

$$y(i,j,t) = \int_{I_\vartheta \times I_\varphi \times \mathbf{R}} g(i,j,h,k,t-\tau)u(h,k,\tau)dhdkd\tau \tag{5.10}$$

with $i,k \in I_\vartheta$, $j,h \in I_\varphi$ and $t,\tau \in \mathbb{R}$.

The kernel function $g : I_\vartheta \times I_\varphi \times I_\vartheta \times I_\varphi \times \mathbb{R} \to \mathbb{R}$ describes a space-variant time-invariant linear system. The spatial variance of the system arises from its toroidal geometry and from the presence of local features such as the gaps in the shell and in the support structure. The presence of poloidal gaps give rise to toroidal spatial variance, which is the reason why it was necessary to make the mesh of the whole system and it was not possible to reduce the model to only one poloidal sector.

Therefore, one has to distinguish between the 2D spatial Fourier transformation of the system and the temporal one. Consequently two different operators are applied to variables, separately or as a whole. Both temporal and spatial transformations imply that both the transformed signal and the transformed kernel take values into the complex field **C**. The dual domain $\hat{I}_\vartheta$ and $\hat{I}_\varphi$ are $\mathbb{Z}(1)/\mathbb{Z}(M)$ and $\mathbb{Z}(1)/\mathbb{Z}(N)$, respectively.

The 2D spatial Fourier operator is defined as follow:

$$F_{p,l} = e^{-j2\pi\left(\frac{k\cdot m}{M}+\frac{h\cdot n}{N}\right)} \tag{5.11}$$

where *k* and *h* represent poloidal and toroidal spatial index, respectively, *m* and *n* poloidal and toroidal harmonic numbers, respectively, and $p = nM + m$ and $l = hM + k$.

As well as in the primal space, when the kernel is variant the output spectrum results to be a convolution between the signal and the kernel in dual space, whose derivation is straightforward [50] and gives the following result:

$$\hat{y}(m,n,f) = \int_{\hat{I}_\vartheta \times \hat{I}_\varphi} \hat{g}(m,n,-l,-r,f)\hat{u}(l,r,f)\,dl\,dr \tag{5.12}$$

With the given choice of domains, *f* represents time-frequency, *l* and *r* input poloidal and toroidal harmonic numbers respectively, and m and n output poloidal and toroidal harmonic numbers respectively. The fact that the output spectrum is the result of a convolution implies the presence of coupling between different harmonics, as shown in Figure 95.

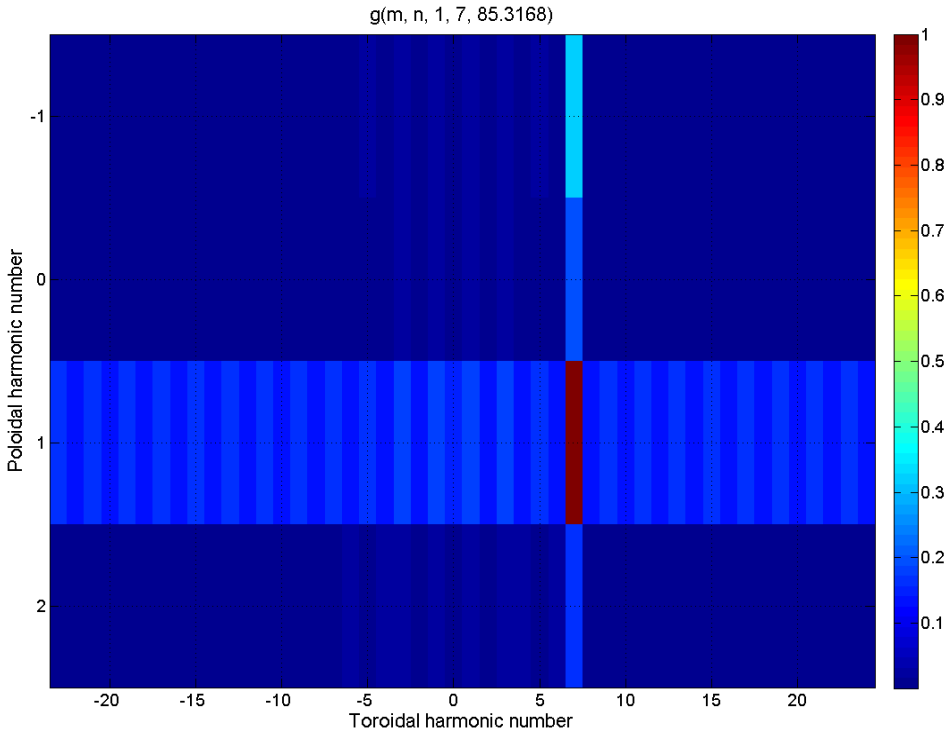

Figure 95: Normalized spectrum of the l=1, r=7, f=85 Hz harmonic

The excitation of a current mode, in this case the m = 1 n = 7, implies a rich magnetic field harmonic spectrum is produced. As already mentioned, the poloidal coupling is an intrinsic consequence of the toroidal geometry and it is further stressed by the presence of equatorial gaps, while the toroidal coupling is due only to the presence of poloidal gaps in the shell and in the supporting structure. As a matter of fact, at zero frequency the RFX-mod system is toroidally invariant, since the source of spatial non-invariance along the toroidal direction are induced currents flowing in the passive structure with non invariant geometry. The lack of symmetry due to the poloidal gaps causes the harmonic coupling along the toroidal direction. Figure 96

represents the normalized field spectrum due to an $m = 1$ $n = 7$ current harmonic exited at 0 Hz and confirms the statements above. In absence of non-invariant induced current distribution there is no harmonic coupling along toroidal direction at all, while along poloidal direction is strongly reduced but it is still present.

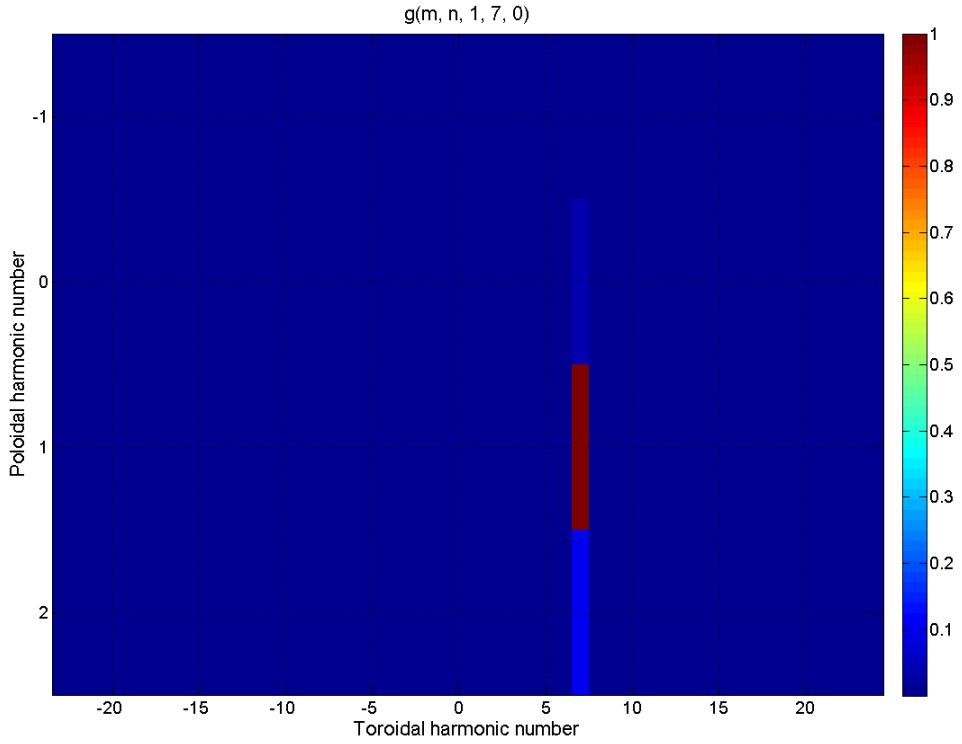

Figure 96: Normalized spectrum of the l=1, r=7, f=0 Hz harmonic

5.4.2 Reduced dynamic modal decoupler synthesis

What allowed implementing a sort of dynamic decoupling in real-time has been its harmonic representation, the following selection of a sub-set of these harmonics and finally its reduction in terms of number of states used.

Therefore, first step has been to determine a pseudo inverse of the frequency response matrix of the model at each frequency sample, $\mathbf{W}(j\omega) = \mathbf{M}^{-1}(j\omega)$. Even if $\mathbf{M}(j\omega)$ could be an invertible matrix numerically, its inverse has been calculated through its Singular Value Decomposition (SVD), in order to obtain a kind of decoupler able to project the direct model onto the space of the magnetic distributions which satisfy the flux conservation condition [50].

The resulting frequency response matrices have been Fourier transformed into their dual (spatial) representation; then only a few number of these harmonics have been selected in order to obtain matrices with reduced dimensions. In particular, starting from the 192×192 frequency response matrices, 4×4 matrices with only the four poloidal $n = -7$ harmonics have been selected. These

matrices represent the n = -7 harmonic components of the inverse 3D wall frequency response, representing the relation between an external n = -7 magnetic fields (or better the coil currents to produce it) required to obtain a particular poloidal spectrum of the field penetrated inside the wall at each sampled frequency.

$$\begin{pmatrix} W_{0,-7}^{0,-7} & W_{0,-7}^{1,-7} & W_{0,-7}^{2,-7} & W_{0,-7}^{-1,-7} \\ W_{1,-7}^{0,-7} & W_{1,-7}^{1,-7} & W_{1,-7}^{2,-7} & W_{1,-7}^{-1,-7} \\ W_{2,-7}^{0,-7} & W_{2,-7}^{1,-7} & W_{2,-7}^{2,-7} & W_{2,-7}^{-1,-7} \\ W_{-1,-7}^{0,-7} & W_{-1,-7}^{1,-7} & W_{-1,-7}^{2,-7} & W_{-1,-7}^{-1,-7} \end{pmatrix} \begin{pmatrix} B_r^{0,-7} \\ B_r^{1,-7} \\ B_r^{2,-7} \\ B_r^{-1,-7} \end{pmatrix} = \begin{pmatrix} I^{0,-7} \\ I^{1,-7} \\ I^{2,-7} \\ I^{-1,-7} \end{pmatrix} \tag{5.13}$$

The above equation clearly shows as, likewise what happens for the direct system, or that by exciting an m = 1 n = -7 current harmonic a full poloidal harmonic spectrum of the magnetic field is produced, in order to obtain a pure m = 1 n = -7 magnetic field harmonic, a full poloidal harmonic spectrum of coil currents is required. This is schematized by equation (5.14):

$$\begin{pmatrix} I^{0,-7} \\ I^{1,-7} \\ I^{2,-7} \\ I^{-1,-7} \end{pmatrix} = \overline{M}^{-1} \begin{pmatrix} 0 \\ B_r^{1,-7} \\ 0 \\ 0 \end{pmatrix} = \overline{W} \begin{pmatrix} 0 \\ B_r^{1,-7} \\ 0 \\ 0 \end{pmatrix} \tag{5.14}$$

The simply inverted frequency responses have to be pre-conditioned before to be used for implementing the decoupler, since the inverse of a strictly proper system (all the physical systems) is not a proper system. This would indeed be the case. In other words, such an inverted system corresponds to a derivative action and so it can work only up to a certain frequency, which is limited by our power supply and coil system to less than 100 Hz.

The main issue of the implementing procedure was the state space realisation of the decoupler starting from the so shaped inverted frequency responses. This has been done by performing a parametric identification of the inverted transfer function matrix in the frequency domain. Each one of the elements of $\mathbf{W}(j\omega) = \mathbf{M}^{-1}(j\omega)$ could be reasonably approximated in a fairly wide frequency range I_f (from 0 to 200 Hz) by a simple transfer function having just two zeros. Three poles were also added outside the frequency range of interest in order to assure the physical realisability of the decoupler obtaining a strictly proper transfer function.

The location of the zeros has then been found by fitting the frequency response of each harmonic transfer function with the following second order model:

$$k\frac{(s\theta_1+1)(s\theta_2+1)}{(s\tau_p+1)^3} \tag{5.15}$$

using a least square procedure. In the above model the gain k and the pole $1/\tau_p$ were fixed parameters not affected by the fitting procedure, whereas θ_1 and θ_2 were the parameters to be identified. To the parameter τ_p has been assigned the value $1/(2\pi 500)$ in order to reduce the additional phase lag in the band 0-100 Hz. The gain of each transfer function has been calculated evaluating the inverted frequency response elements at $\omega = 0$, whereas for τ_p has been used an equal value for each transfer function, chosen to lie outside the frequency range of interest. The result of the fitting procedure is an approximation $\tilde{\mathbf{W}}(j\omega)$ of the decoupler such that $\tilde{\mathbf{W}}(j\omega) \approx \mathbf{W}(j\omega)$ over the frequency range I_f.

Actually, the dual transfer function matrices above are 4×4 matrices with complex elements, while a real time implementation needs to work with real numbers. Therefore, the identification procedure has been done on the associated 8x8 real matrices, whose elements are the real and imaginary part of the original ones.

5.4.3 Controller synthesis

Because of the derivative nature of the dynamic decoupler, doubts raised about the opportunity of using it directly in the feedback loop. Thus, it has been implemented to work in the following control scheme:

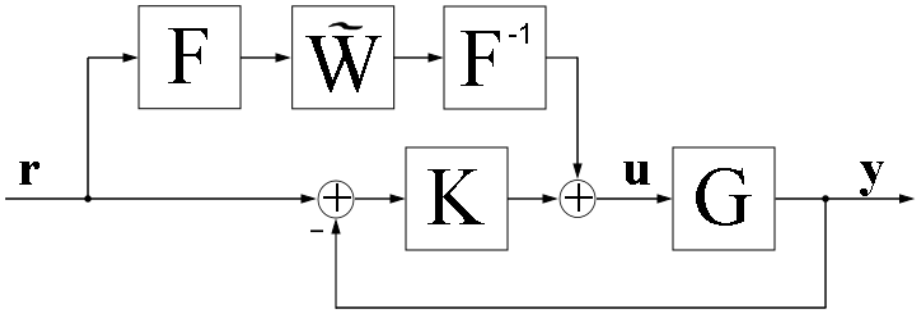

Figure 97: Scheme of the control loop.

where **G** is the plant, **K** represent the controller, $\tilde{\mathbf{W}}$ is the decoupler, **F** and $\mathbf{F^{-1}}$ are the Fourier operator defined in Eq. (6.11) and its inverse respectively. In this way the decoupler acts in feedforward, generating those current reference values which reduce the poloidal side-harmonic of the main mode to be produced, on which acts the feedback controller.

5.4.4 Preliminary results

A simulation of the decoupler implemented in the control scheme of RFX-mod has been done and results are reported in and Figure 98. An $m = 1$, $n = -7$ mode rotating at 20Hz of unitary amplitude has been generated with a sample time corresponding to the actual experimental sample frequency. This mode represents the reference radial magnetic field distribution which is requested to be generated by the MHD control system. The matrix formed by the 192 vectors of time samples of the field which would be measured by the sensors is spatially Fourier transformed and the only four interesting modes are then selected. These are the inputs of the modal decoupler, whose outputs are the four current harmonics which generate the required field if they are inputted to the direct model of the machine. Before being given as inputs to the direct model, the four currents harmonics time vectors are inserted into a matrix formed by 192 vectors, where the vector elements corresponding to the other harmonics are all zero vectors. This matrix is Fourier anti-transformed in primal space and then it is given as input to the direct model.

The model used to implement the decoupler contains also the model of the so called sideband cleaner, which will be described in details in the next paragraph. In this way the decoupler works in order to minimize the cleaned poloidal side-harmonic, not the raw ones. As it can be seen in the figures, after a short transient, the cleaned main harmonic reproduce very well the reference both in amplitude and in phase, and the cleaned poloidal side-harmonic amplitudes are almost zeroed.

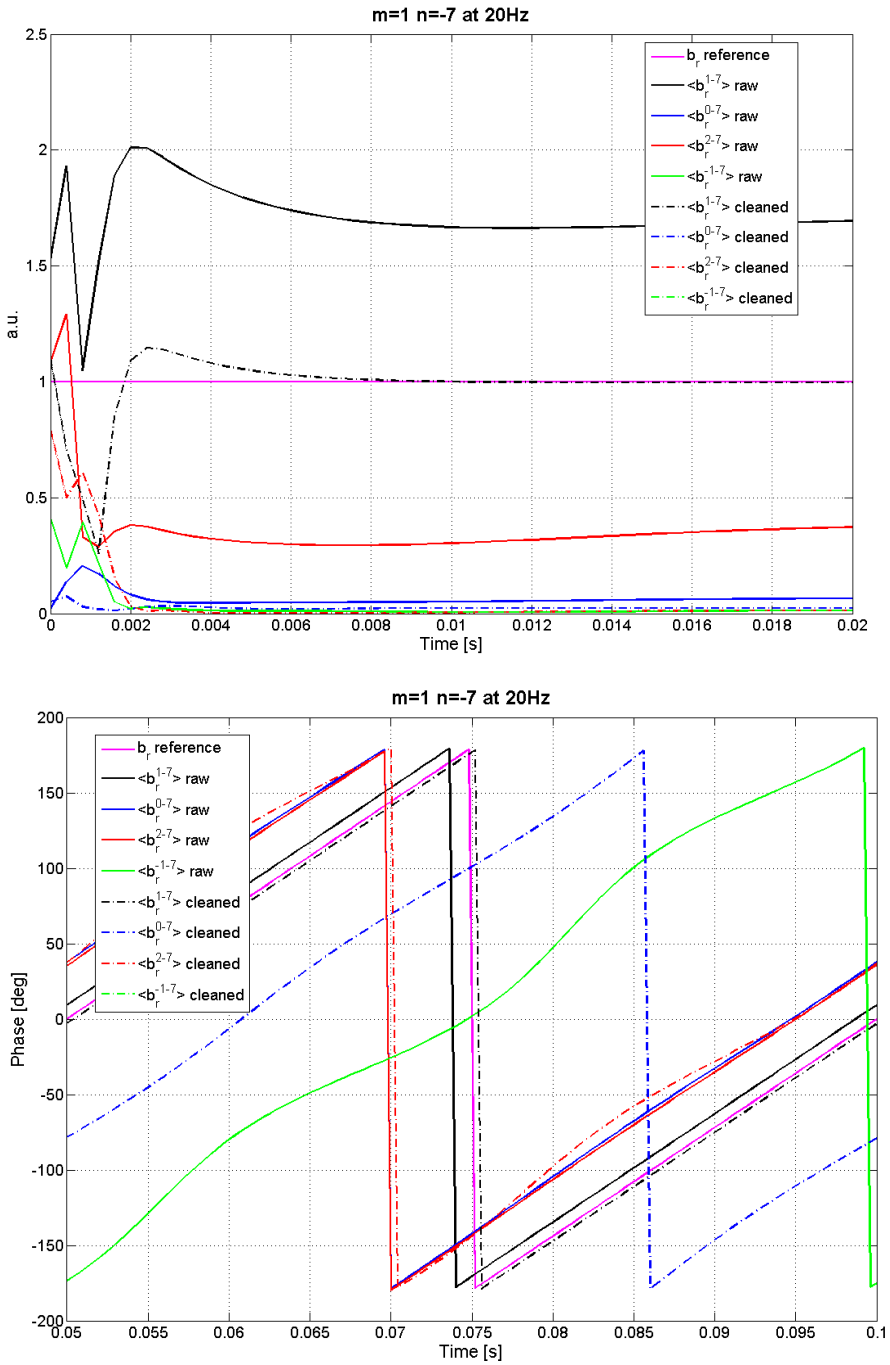

Figure 98: Discrete time modal decoupler simulation of an m = 1, n = -7 rotating mode at 20Hz in vacuum. Amplitude and phase of the main harmonic m = 1, n = -7 (black line) and coupled poloidal harmonic m = 0 (blue line), m = 2 (redline) and m = -1 (green line). Continuous lines refer to raw quantities, dashed-dotted lines to cleaned quantities. Magenta line is the reference, input of the decoupler.

The reduced modal dynamic decoupler has been then tested in plasma discharges where, similarly to what described in [44], a helical boundary condition was applied to control the 1/-7 helical equilibrium, as shown in Figure 99.

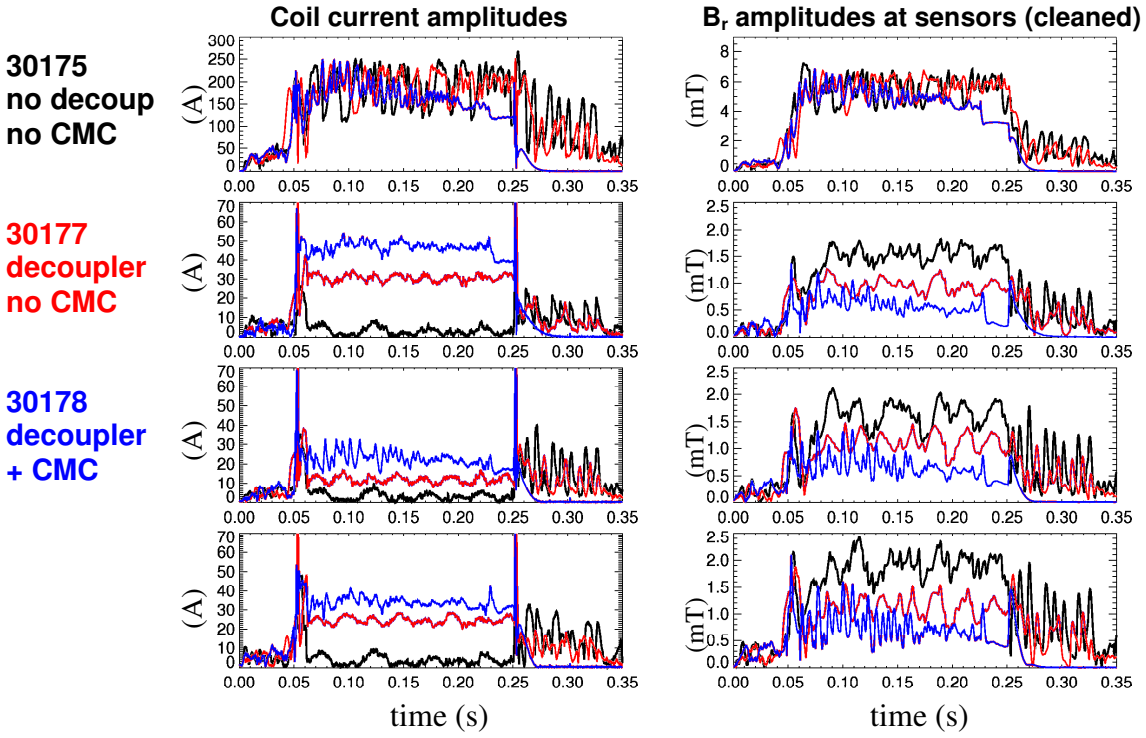

Figure 99: Coil current and Br amplitudes of the 1/-7, 0/7, 1/7, and 2/7 harmonics for three similar RFX-mod discharges with a helical b.c. rotating at 20Hz applied from 0.05 to 0.25s: discharge #30175 (black lines) has no dynamic decoupler and no Mode Control, discharge #30177(red line) has dynamic decoupler active and no MC, while discharge #30178 (blue line) has both dynamic decoupler and MC active (courtesy of P. Piovesan).

In this case the 1/-7 mode is maintained into rotation at 20Hz in the period 0.05-0.25s. In discharge #30175 (black lines) no feedback control on the error field is applied and the feed-forward references correspond to current harmonic; in discharge #30177 the dynamic decoupler is active in order to minimize the $m = 0,1,2/n = 7$ error field harmonics without feedback action, finally in discharge #30178 both the dynamic decoupler and the Clean Mode Control are active.

In both cases where the decoupler is active, the $m = 0,1,2/n = 7$ error field harmonic amplitudes are more than halved, when the two actions are both active the amplitude of the poloidal side-harmonic are almost one third of those which otherwise would be present.

5.5 Improved sideband cleaning

5.5.1 Theoretical framework

In a discrete grid made up of a finite number of $M \times N$ saddle coils (M along the poloidal and N along the toroidal direction) the production of each harmonic component B_{mn} ($|m| < M/2$ and $|n| < N/2$) of the magnetic field distribution is accompanied by an infinite number of sidebands $B_{m',n'}$ according to the equation $m' = m \pm hM$, $n' = n \pm kN$ (h, k integer). A set of sensors arranged in the same $M \times N$ grid causes the aliasing of the whole sideband spectrum which brings about a systematic error in the Fourier analysis of the measurements. This is indeed the case of the radial magnetic flux (saddle) and poloidal and toroidal pick-up sensors sets in RFX-mod.

A real-time correction algorithm to subtract the sideband effect is currently used to obtain "clean" feedback signals. Different versions have been worked out making possible to feed back the control system with the corrected signals evaluated either at the sensor radius (0.507m) or at the first wall radius, i.e. at the plasma boundary (0.459 m). In the latter case the measures of the toroidal components provided by the 4×48 pick-up coils placed on the shell inner surface are used to obtain the extrapolated radial component.

This correction algorithm is based on a cylindrical, thin shell approximation, where the diffusion of the (m,n) components of the magnetic field is described by 1st order differential equations. The cylindrical approximation greatly simplifies the problem since it admits analytical solution expressed in terms of the modified Bessel function [45 - 48].

Since the control algorithms works on radial and toroidal field signals and the radial field measurements are values obtained by averaging flux measures on areas extended on $\Delta\theta=\pi/2$ along poloidal direction and $\Delta\varphi=\pi/48$ along toroidal direction, in order to be compared with the field harmonics calculated with the model, the harmonics calculated by the Fourier analysis of these measurements have to be divided by the form factor $f(m,0,n,0)$ defined as [47]:

$$f(m,0,n,0) = \frac{\sin\left(m\frac{\Delta\theta}{2}\right)}{m\frac{\Delta\theta}{2}} \frac{\sin\left(n\frac{\Delta\varphi}{2}\right)}{n\frac{\Delta n}{2}} \tag{5.16}$$

On the other hand, each calculated sideband harmonic has to be multiplied by the form factor $f(m,h,n,k)$ defined below, in order to be compared to the measured harmonic.

$$f(m,h,n,k)=\frac{\sin\left[(m+hM)\frac{\Delta\theta}{2}\right]}{(m+hM)\frac{\Delta\theta}{2}}\frac{\sin\left[(n+kN)\frac{\Delta\varphi}{2}\right]}{(n+kN)\frac{\Delta\varphi}{2}} \tag{5.17}$$

It's worth noting the form factor $f(m,0,n,0)$ takes into account the fact that the radial field measurement are averaged and not point quantities, while the form factor $f(m,h,n,k)$ is required to take into account of the actual discretization of the current density distribution, which flows inside the saddle coils in the real machine, while is assumed as a uniform distribution in the cylindrical model used to calculate the sideband content. The form factor $f(m,0,n,0)$ is not necessarily a particular case of $f(m,h,n,k)$, they could be in general different. In this case they correspond because both of them have been determined assuming filamentary coils, which is true only for the sensors. Anyway, the use of more precise factors for the active coils produces very similar results.

The measurement correction algorithm currently calculates the cleaned harmonic as difference of the raw measured harmonic and the sideband components up to a certain harmonic order, according to the equation below:

$$b_r^{m,n}=\frac{1}{f(m,0,n,0)}\left[b_{r,DFT}^{m,n}-\sum_{l,k}b_{r,c}^{m+hM,n+kN}f(m,h,n,k)\right] \tag{5.18}$$

where $b_r^{m,n}$ is the cleaned (m,n) harmonic, $b_{r,DFT}^{m,n}$ is the raw (m,n) measured harmonic and $b_{r,c}^{mhlM,n+kN}$ is the (m,n) sideband harmonic of poloidal order h and toroidal order k.

In cylindrical geometry, the study of the magnetic field penetration dynamics in terms of Fourier components assumes a diagonal structure model, overcoming the considerable electromagnetic coupling between each coil and many underlying sensors. As it has been shown in the previous paragraphs, in the case of RFX-mod, the toroidal geometry of the machine and the presence of gaps in the shell and the support structure brings about a non-negligible coupling between different (m,n) modes. For this reason the cylindrical cleaning works quite well for specific modes and frequency, worse for others.

Figure 100 to Figure 103 show the time evolution of the raw measured main radial field harmonic (red line), the main harmonic calculated with the cylindrical model (green line) and the cleaned measures (blue line), for four vacuum shots where different rotating modes at different frequency

have been excited. It has been considered sidebands up to the second toroidal order ($k = \pm 1, \pm 2$) and the third poloidal order ($l = \pm 1, \pm 2, \pm 3$).

It is easy to see in the figures as in the case of the $m = 1$, $n = -7$ rotating mode at 10 Hz the cleaned measure and the calculated main harmonic are in good agreement, while the same is not true for the static and 20 Hz $m = 1$, $n = -7$ mode, as well as for the $m = 1$, $n = 1$ rotating mode at 5 Hz. It should be noted that the cleaned measures are anyhow closer to the calculated pure main harmonic than the raw ones.

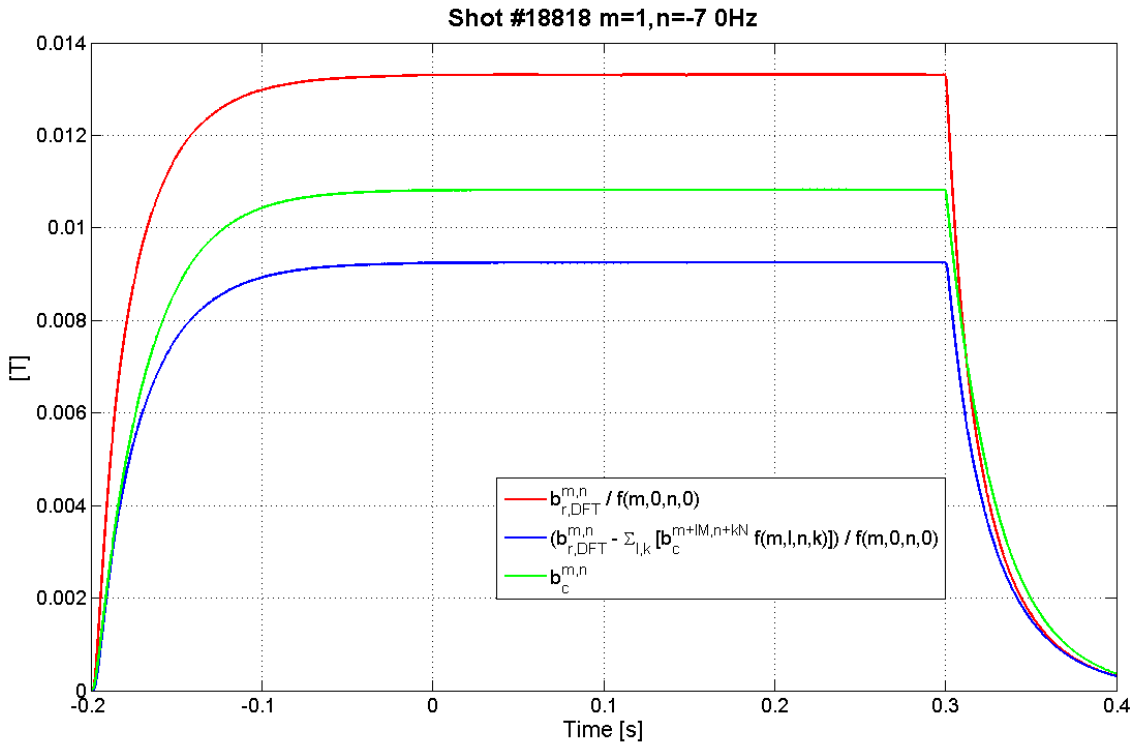

Figure 100: Time evolution of the m=1, n=-7 radial field harmonic amplitude of shot number 18818: raw measures (red line), calculated with the cylindrical model (green line) and the cleaned measures (blue line).

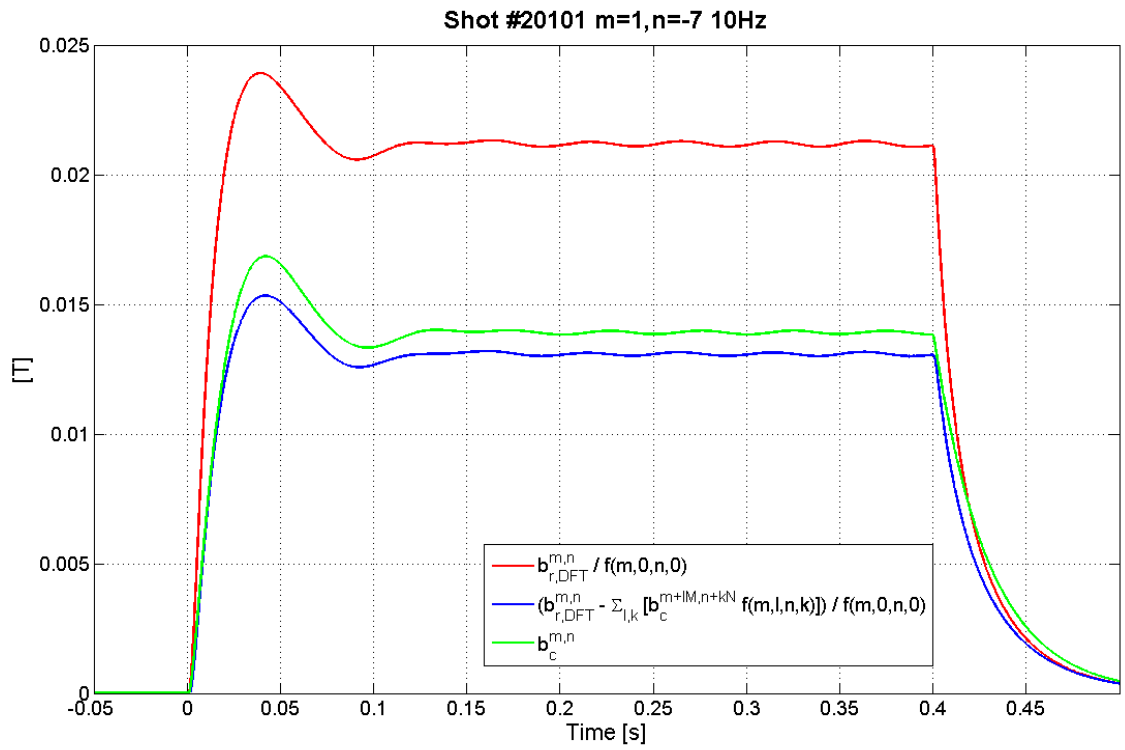

Figure 101: Time evolution of the m=1, n=-7 radial field harmonic amplitude of shot number 20101: raw measures (red line), calculated with the cylindrical model (green line) and the cleaned measures (blue line).

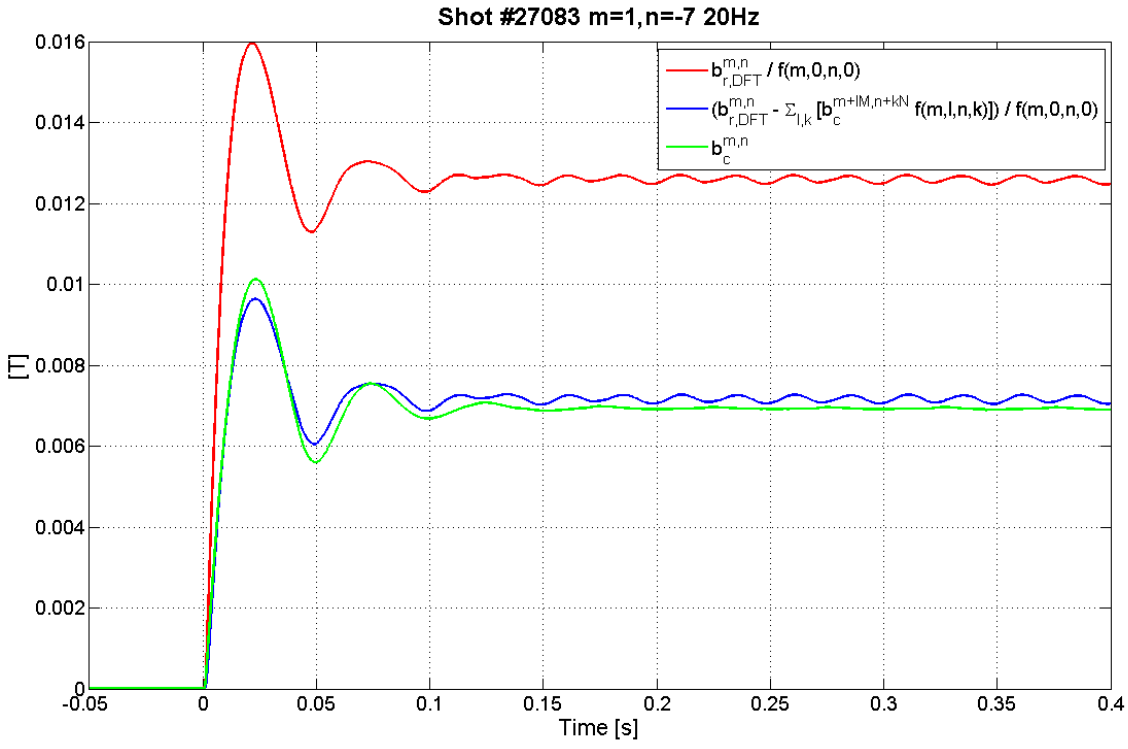

Figure 102: Time evolution of the m=1, n=-7 radial field harmonic amplitude of shot number 27083: raw measures (red line), calculated with the cylindrical model (green line) and the cleaned measures (blue line).

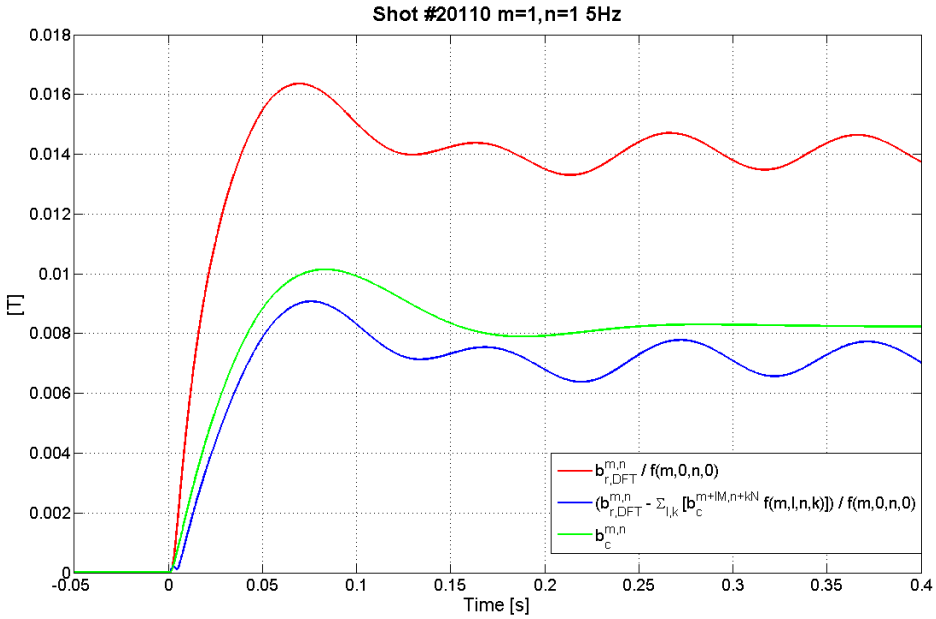

Figure 103: Time evolution of the m=1, n=-7 radial field harmonic amplitude of shot number 18818: raw measures (red line), calculated with the cylindrical model (green line) and the cleaned measures (blue line).

5.5.2 Sideband cleaning in toroidal geometry

The models developed with the CARIDDI code are also useful to estimate the sideband measured signal contents in toroidal geometry, taking into account the effect introduced by the gaps in the shell and the support structure as well. Indeed, models with a higher number of virtual sensors than the actual set of 192 sensors have been developed, which allow evaluating higher order harmonics with increasing precision as the sensor number increases. The possibility of introducing ideally as many sensors as desired has allowed to verify if the evaluated sideband component converges by increasing the number of sensors, and to try the effect of using a number of sensors co-prime with respect that of actuators.

In the latter case it is indeed expected the first aliased harmonic is that of order $N_a \times N_s$, where N_a is the number of actuators and N_s the number of sensors. Therefore, a co-prime sensor array allows getting a very precise value of the main harmonic produced, employing a quite low number of sensors. However, while an array of sensors arranged in a grid made up of $F \times G = hM \times kN$ elements, multiple of the actuators, provides information on the whole spectrum up to the $F/2$ poloidal harmonic and the $G/2$ toroidal harmonic, that is also about the close to the dominant sideband content of the coupled modes, the co-prime sensor set has the drawback of providing precise information only about the targeted harmonic, as it is described in the next section.

5.5.2.1 Spatial sampling and aliasing

In order to provide a more precise description of the concepts just asserted, let's introduce the first order diofantine equations. These are equations in the form:

$$ax + by = c \tag{5.19}$$

where a, b and c are all integer numbers, and we search for integer solutions.

Such equations have a solution (x_0, y_0) if and only if c is divisible by the Greatest Common Divisor (GCD) of a and b. If this is the case, the equation has infinite solutions, in the form ($x_0 + nb/d$, $y_0 - na/d$), with n integer and d = GCD(a, b).

Now consider, for purposes of simplification, a one-dimensional arrangement of actuators and sensors. N_a is the number of actuators and N_s the number of sensors.

If a harmonic h_0 is produced by the discrete grid of actuators, together with the sideband spectrum $h_0 \pm lN_a$ (with l integer different from zero), the sideband harmonics which add by aliasing to measured harmonic k_0 are those solving the equation below:

$$h_0 + N_a x = k_0 + N_s y \tag{5.20}$$

for x,y integers. Eq. (5.20) corresponds to a linear diofantine equation with $a = N_a$, $b = -N_s$ and $c = k_0 - h_0$.

If $N_s = N_a$ and the harmonic to be measured is the same as the main one produced ($k_0 = h_0$), all produced harmonics ($h_0 \pm nN_a$) are summed in the measure. This case corresponds to have $a = -b = N_a$, which admits the infinite solutions $h_0 \pm nNa$. Whether N_s and N_a are instead co-prime numbers, the only solutions of equation (5.20) are those for $x = nN_s$, $y = nN_a$, with n integer. This means the aliased sideband harmonics are only those which are multiple of the product between the actuator and sensor numbers, $h_0 \pm nN_aN_s$.

If $N_s = N_a$ and the measured harmonic k_0 is generic ($k_0 \neq nh_0$), there is aliasing only if N_s divides ($k_0 - h_0$). In fact, if N_s does not divide ($k_0 - h_0$) Eq. (5.20) has no solutions and so there isn't aliasing. Instead, if the k_0 harmonic is produced through a coupling mechanism by the main one, its measurement is affected by the aliasing according to Eq. (5.20) having infinite solutions $h_0 \pm nNa$.

Whether N_s and N_a are instead co-prime numbers, the equation again has infinite solutions, but they depend on both the numbers of actuator N_a and sensors N_s. In other words, the measurement of the coupled harmonic k_0 is affected by the spectra of other (coupled) harmonics if present. Let's clarify the concept, considering the following example.

Suppose that an $n = 7$ harmonic is produced with $N_a = 48$ actuators and it is measured with $N_s = 48$ sensors. The measurements would then be aliased by the harmonics $7 \pm k48$. If, for instance, also an $n = 8$ coupled side harmonic is present, it would be aliased by the harmonics $8 \pm k48$. If indeed the $n = 8$ harmonic is not coupled to the $n = 7$, the measurements related to the $n = 8$ are equal to zero.

Instead, the measurement performed with $N_s = 49$ sensors of an $n = 7$ harmonic produced with $N_a = 48$ actuators results aliased by the harmonics $7 \pm k \cdot 48 \cdot 49$, while that of the $n = 8$ harmonic is aliased by the harmonics $8+48 \cdot [-1; 48; -50; 97; -99; 146; -148; 195; -197; 244; -246; \ldots]$, which are obtained by the solution of the diofantine equation (5.19) through the extended Euclidean algorithm.

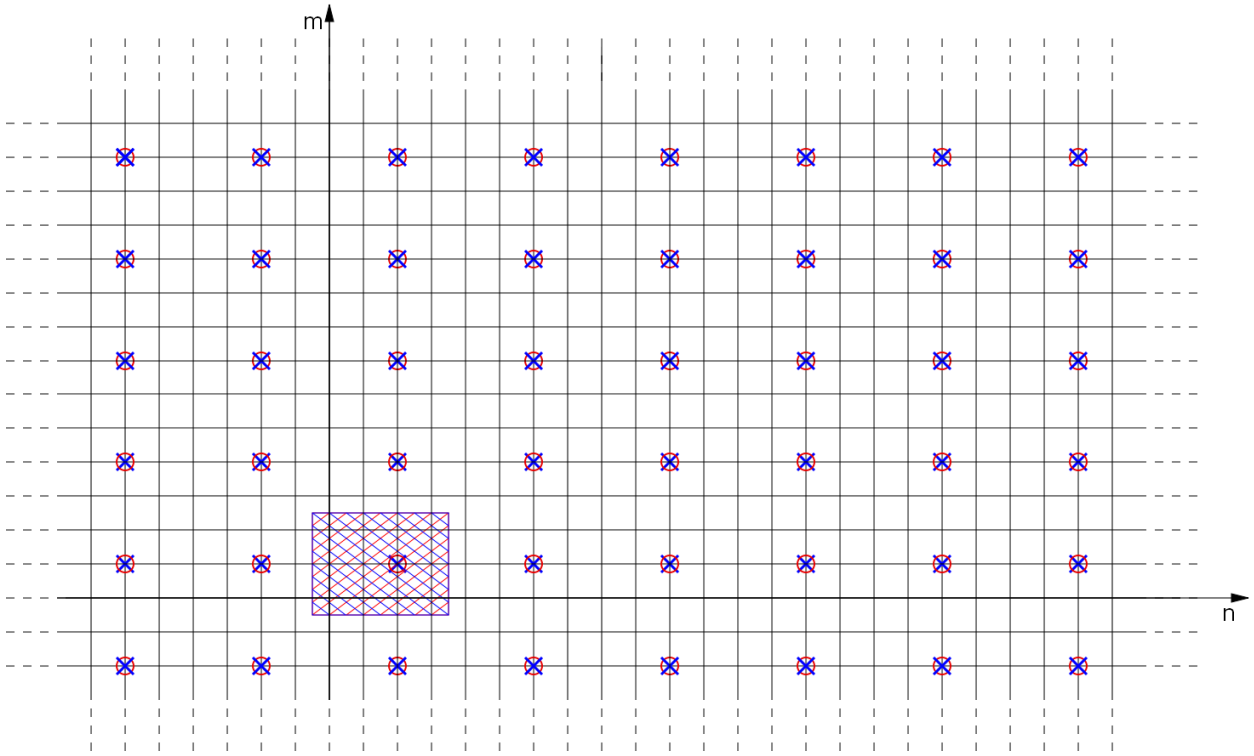

Figure 104: Graphical interpretation of produced (red circles) and aliased (blue crosses) harmonics in the case of equal number of actuators and sensors ($M_s = M_a = 3$, $N_s = N_a = 4$). The red and blue cross-hatched rectangles represent the actuator and sensor grid respectively. Measure is aliased by the whole spectrum since all blue crosses overlap red circles.

Figure 104, Figure 105 and Figure 106 give a graphical bi-dimensional interpretation of what mentioned above. Red circles represent the harmonic content of the spectrum produced by actuators (the principal harmonic is inside the hatched region), blue crosses are those harmonics which affect the measurement (harmonic desired to be measured is inside the hatched region) and green squares are the harmonic coupled to the main one with its spectrum. The abscissas

represent the toroidal harmonic numbers, the ordinates the poloidal ones. The red cross-hatched rectangle represents the grid of actuators (3×4) and the blue one represents the grid of sensors. In all the figures it is assumed that an $m = 1$, $n = 2$ harmonic is produced. If measured harmonics overlap produced ones, these are all summed up to that measured.

If the sensor grid is the same of that of actuators, the entire spectrum produced with the coils is summed up in the measure by aliasing, as the case represented in Figure 104 where all the blue crosses overlap the red circles (and the blue grid match the red one). When the sensors are arranged in a grid of dimensions corresponding to co-prime numbers with respect that of the actuators, only the harmonic ($m \pm lM_aM_s$, $n \pm kN_aN_s$) are aliased; this is the case represented in Figure 105, where a sensor grid of 4×5 is used and therefore only the blue crosses corresponding to the 4^{th} poloidal ($7 = 1 + 2 \times 3 = m_0 + M_aM_s$) and 5^{th} toroidal ($14 = 2 + 3 \times 4 = n_0 + N_aN_s$) produced harmonics are overlapped to red circles.

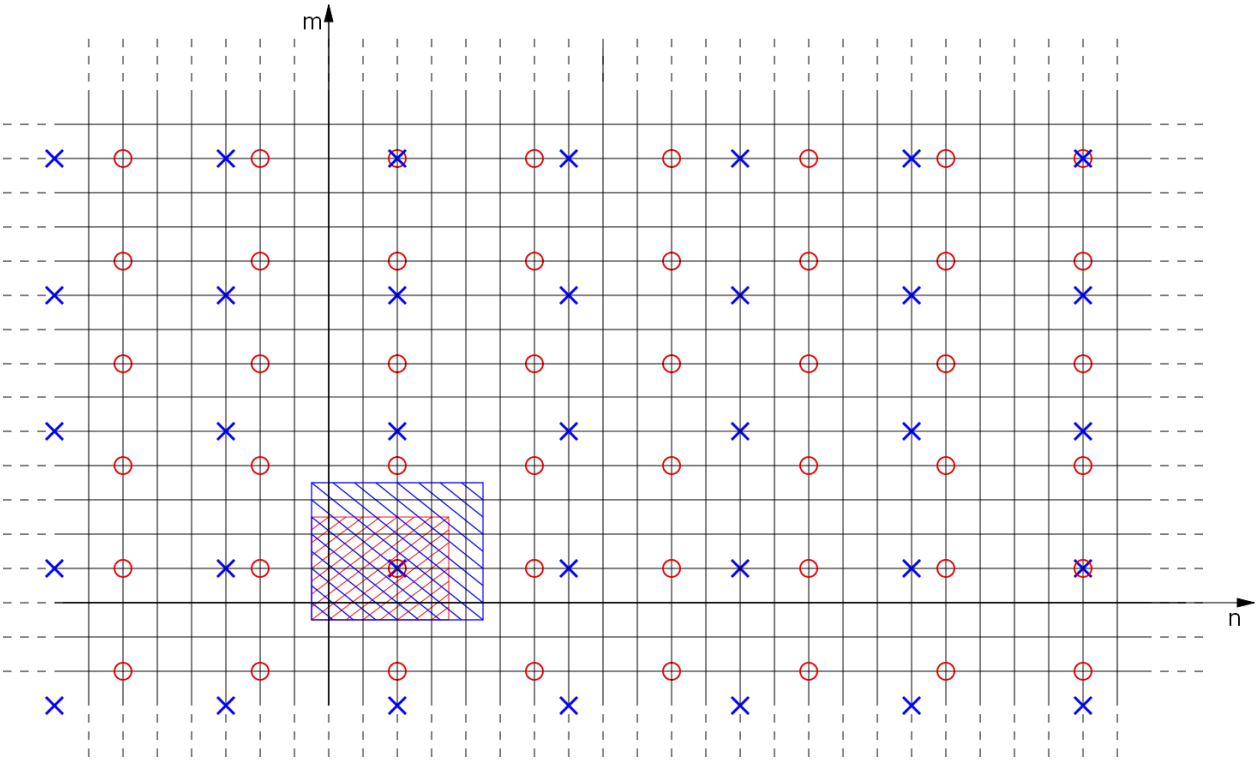

Figure 105: Graphical interpretation of produced (red circles) and aliased (blue crosses) harmonics in the case of co-prime number of actuators and sensors ($M_a = 3$, $M_s = 4$, $N_a = 4$, $N_s = 5$). The red and blue cross-hatched rectangles represent the actuator and sensor grid respectively. The only blue crosses overlapping red circles are those corresponding to the $m \pm lM_aM_s$, $n \pm kN_aN_s$ harmonics and result summed up to the main harmonic in the measurements.

Figure 106 instead shows a case when the measurement of a side harmonic by coupling (green squares) is considered. Again the whole sideband spectrum is summed up by aliasing. In order to

filter lower number sideband harmonic, a grid of sensors in number equal to a integer multiple of the actuators has to be used.

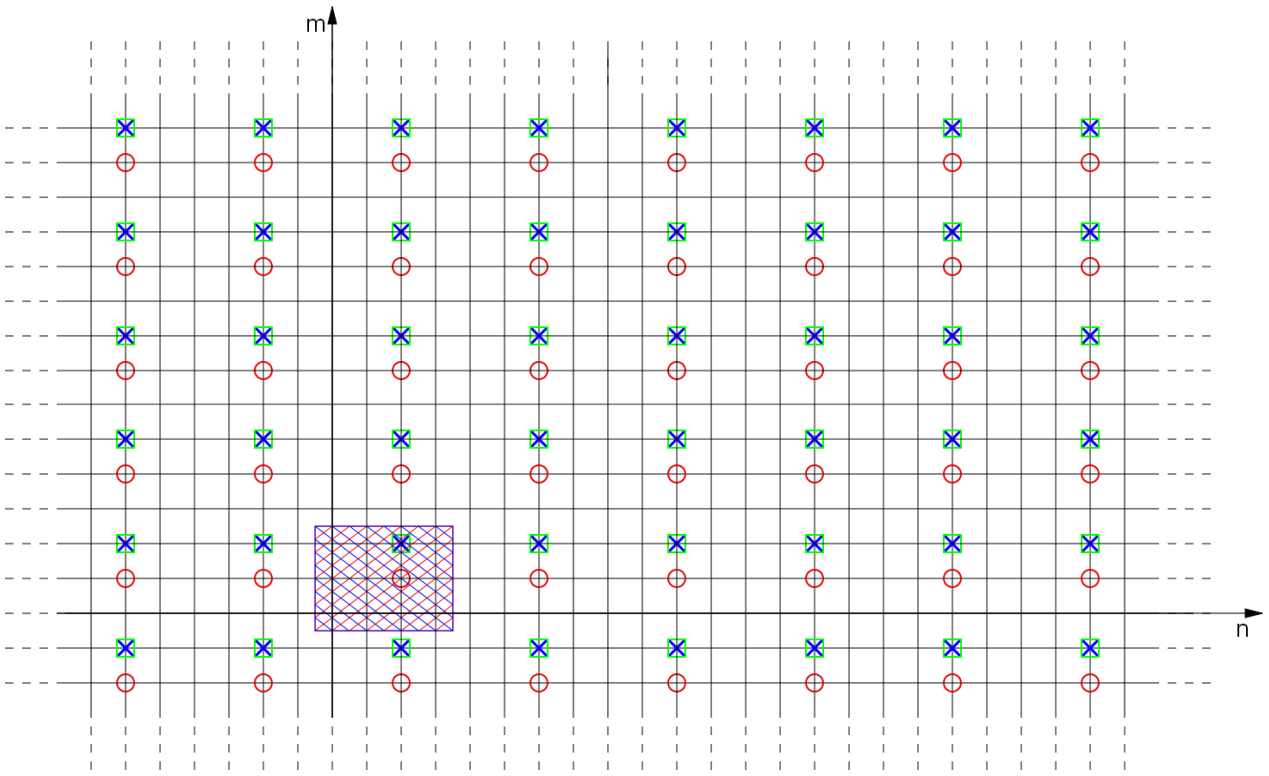

Figure 106: Graphical interpretation of produced (red circles), coupled (green squares) and aliased (blue crosses) harmonics in the case of equal number of actuators and sensors ($M_s = M_a = 3, N_s = N_a = 4$). The red and blue cross-hatched rectangles represent the actuator and sensor grid respectively. A coupled side harmonic is measured with its own harmonic number, but all ots spectrum is summed aliased.

It must be stressed that the presence of what has been called coupled side harmonic and their spectrum are due to the toroidal geometry and possible 3D features, which break the spatial invariance of the system. In cylindrical geometry, if $N_s = N_a$ the measurement of a side harmonic results equal to zero, if instead N_s and N_a are co-prime numbers the measurement of a side harmonic results aliased by a subset of the main spectrum, as it is schematized in Figure 107.

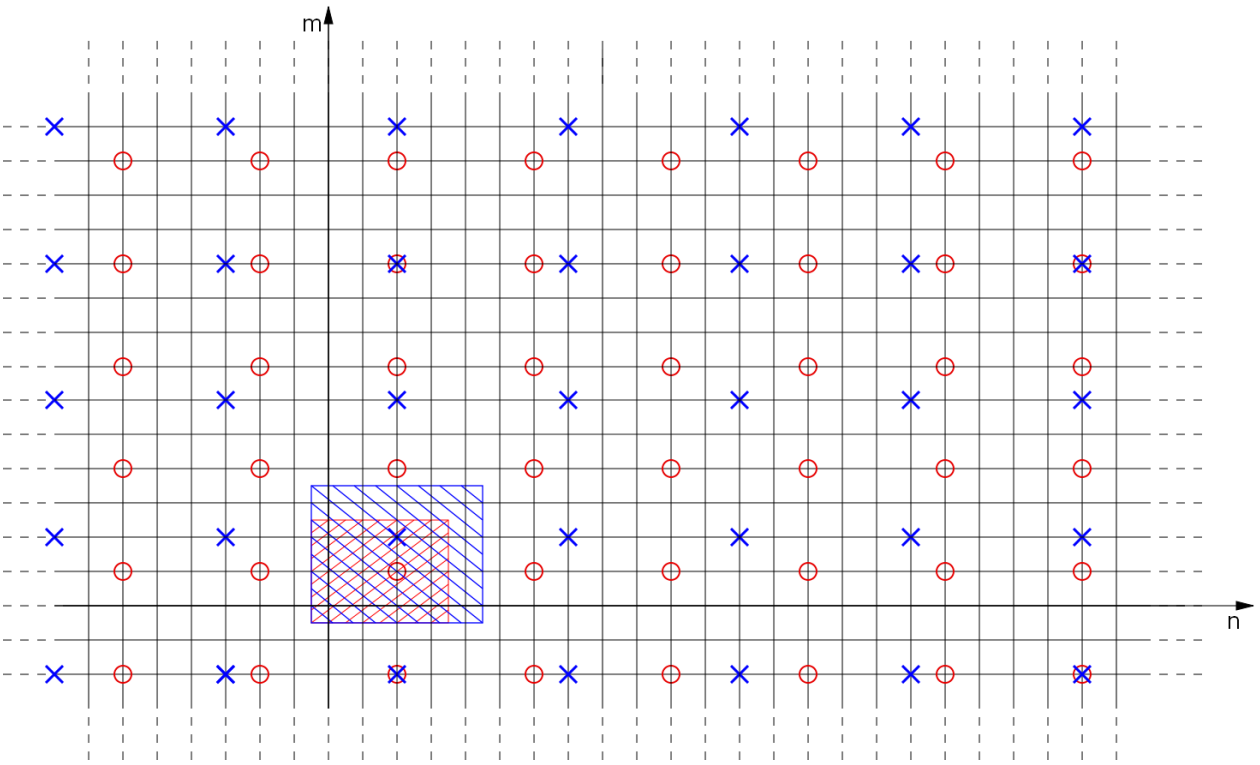

Figure 107: Graphical interpretation of produced (red circles) and aliased (blue crosses) harmonics in the case of co-prime number of actuators and sensors (M_a = 3, M_s = 4, N_a = 4, N_s = 5), measuring a side harmonic. The red and blue cross-hatched rectangles represent the actuator and sensor grid respectively. The only blue crosses overlapping red circles in the figure are those corresponding to the m +M_a (M_a ± lM_s), m +N_a (N_a ± lN_s) harmonics and result summed up to the side harmonic in the measurements.

Therefore, if one is interested in evaluating the sideband contents of the whole coupled spectrum, necessarily a grid of sensors in number multiple of the actuators has to be used. In this case to have precise information the number of sensors has to be much larger than that of actuators. If instead one is interested in evaluating very precisely only the main produced harmonic, the choice of a co-prime number of sensors allows using a number of sensors similar to that of actuators, for example just picking the first co-prime number bigger the number of actuators.

5.5.2.2 Sideband analysis results

Figure 108 to Figure 111 show the time evolution of radial field rotating modes at several frequency exited during distinct dry shots, calculated by different model or experimentally measured. In particular, simulated and experimental measurements of the raw mean radial field harmonic, principal harmonic of the cylindrical model and the data from models with different grid of virtual pick-up sensors are compared.

The very good agreement between the simulated and experimental raw measures proves the goodness of the model used. The comparison of data obtained by the same toroidal model with

different grids of virtual pick-up sensors shows as, by increasing the number of sensors, the calculated main harmonic oscillates and then converges to a value quite different from that calculated by the cylindrical model. As already mentioned, this difference depends on the frequency and on the excited mode, since the cylindrical model approximates better in some conditions and worse in other. The oscillating convergence is due to the fact that some sideband harmonics adds to the main one, other reduce it.

The figures show there is a good convergence both for the amplitude and the phase, and the idea of using co-prime set of sensors works well just with a number of sensors 6 times higher, versus at least 50 times more sensors in the case of no co-prime grids. In particular, the poloidal number of sensors has to be increased more than the toroidal, since poloidal sideband harmonic contribute more than the toroidal ones in the measurement error.

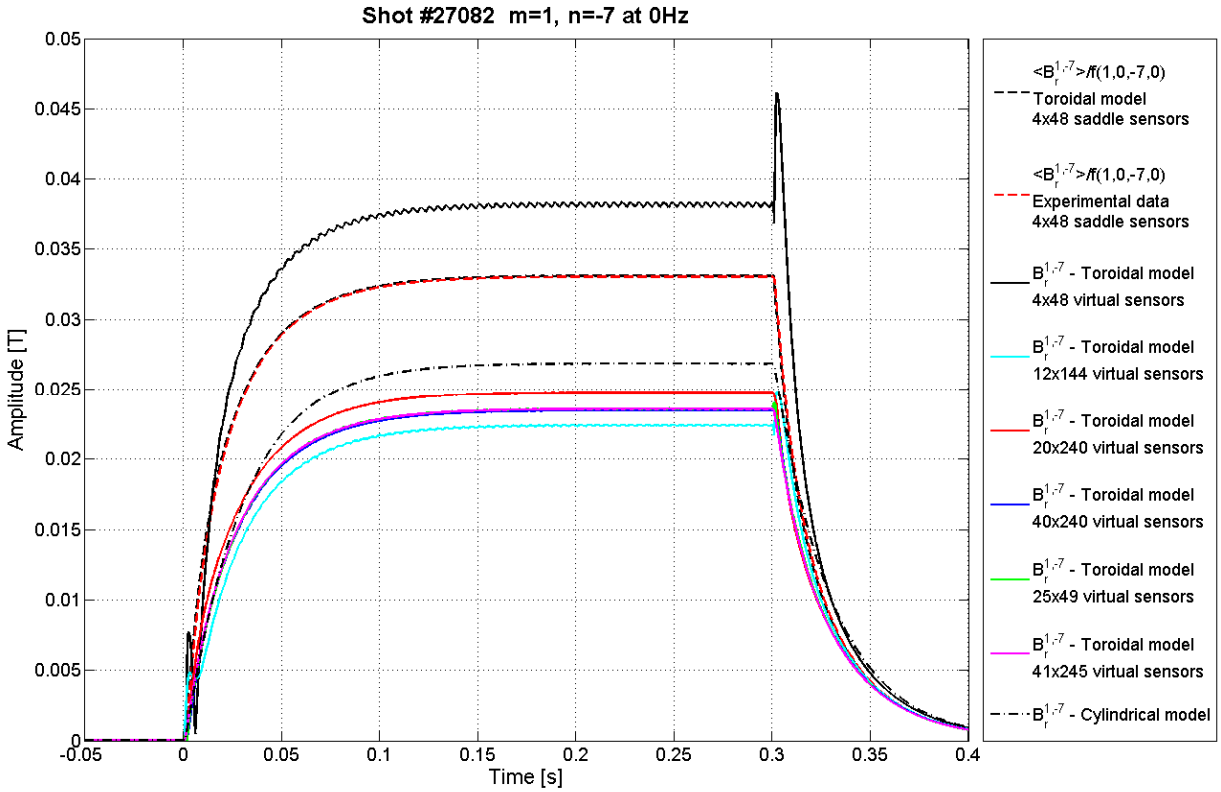

Figure 108: Time evolution of the m=1, n=-7 radial field harmonic of shot number 27082: simulated mean radial field measures (black dashed line), experimental mean radial field measures (red dashed line), calculated with the cylindrical model (black dashed-dotted line) and with virtual sensors respectively in a grid of (M×N): 4×48 (black line), 12×144 (light blue line), 20×240 (red line), 40×240 (blue line), co-prime 25×49 (green line), co-prime (magenta line).

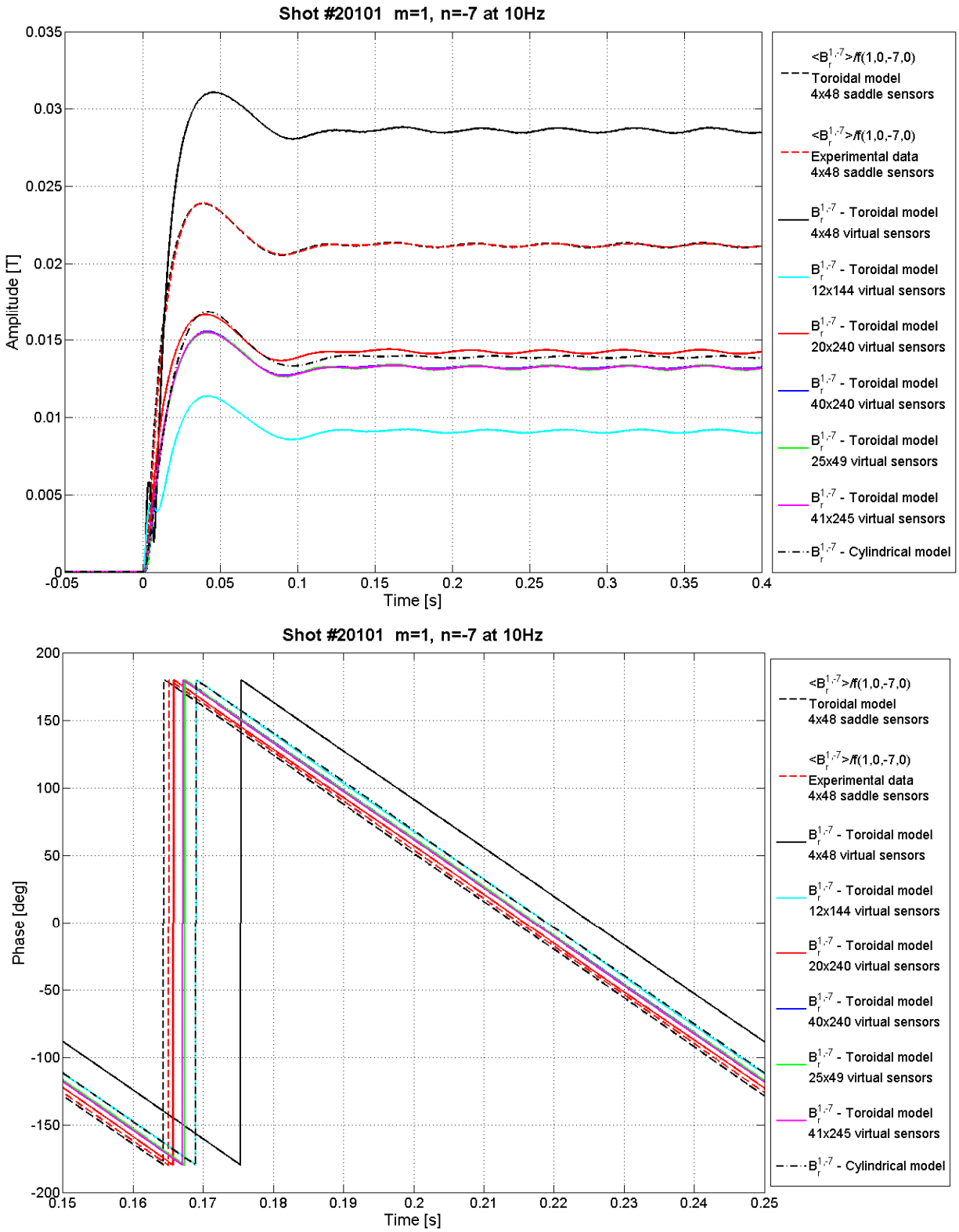

Figure 109: Amplitude and phase of the time evolution of the m=1, n=-7 radial field harmonic rotating at 10 Hz of shot number 20101: simulated mean radial field measures (black dashed line), experimental mean radial field measures (red dashed line), calculated with the cylindrical model (black dashed-dotted line) and with virtual sensors respectively in a grid of (M×N): 4×48 (black line), 12×144 (light blue line), 20×240 (red line), 40×240 (blue line), co-prime 25×49 (green line), co-prime (magenta line).

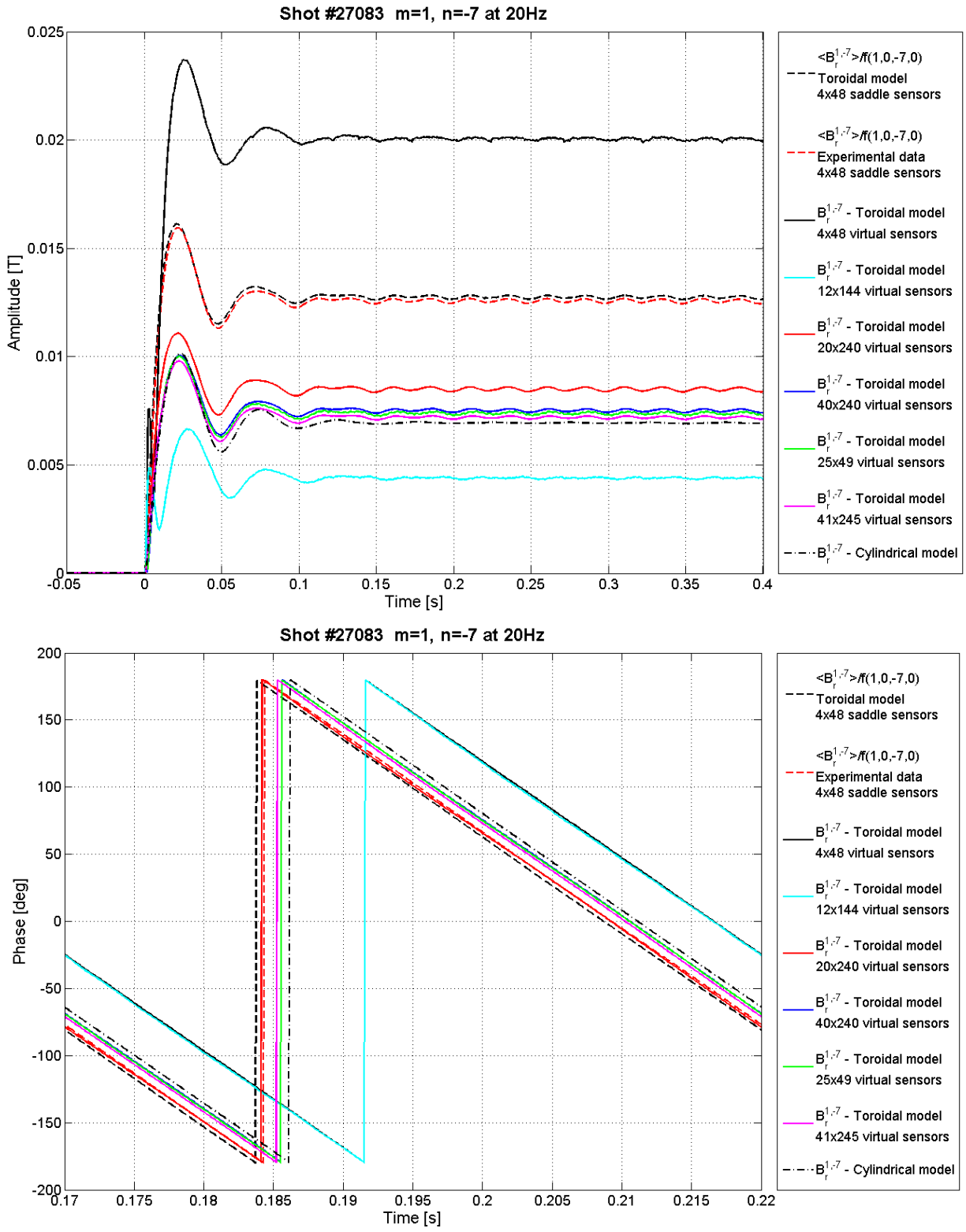

Figure 110: Amplitude and phase of the time evolution of the m=1, n=-7 radial field harmonic rotating at 10 Hz of shot number 20101: simulated mean radial field measures (black dashed line), experimental mean radial field measures (red dashed line), calculated with the cylindrical model (black dashed-dotted line) and with virtual sensors respectively in a grid of (M×N): 4×48 (black line), 12×144 (light blue line), 20×240 (red line), 40×240 (blue line), co-prime 25×49 (green line), co-prime (magenta line).

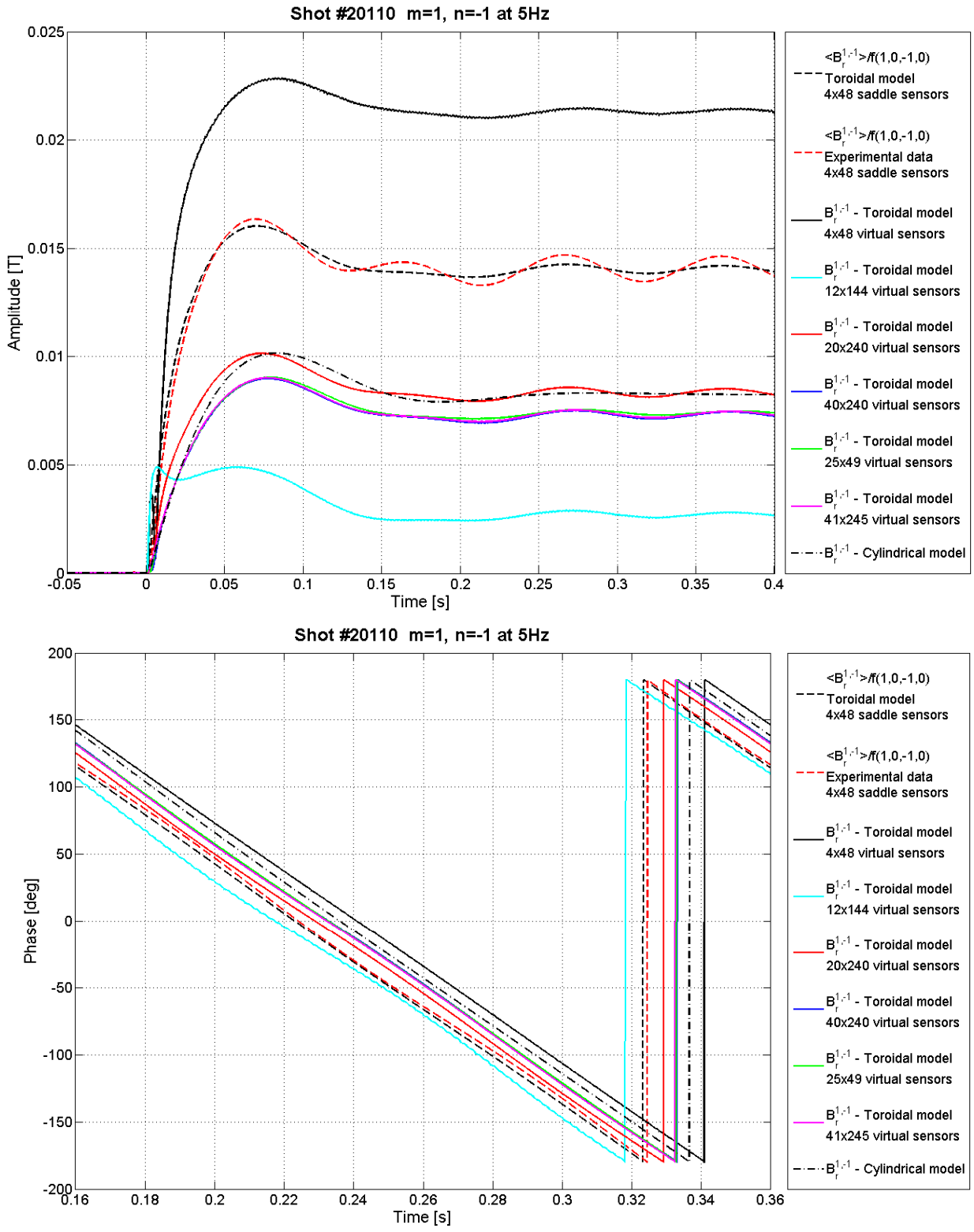

Figure 111: Amplitude and phase of the time evolution of the m=1, n=- radial field harmonic rotating at 5 Hz of shot number 20110: simulated mean radial field measures (black dashed line), experimental mean radial field measures (red dashed line), calculated with the cylindrical model (black dashed-dotted line) and with virtual sensors respectively in a grid of (M×N): 4×48 (black line), 12×144 (light blue line), 20×240 (red line), 40×240 (blue line), co-prime 25×49 (green line), co-prime (magenta line).

An analysis has been carried out in order to verify the consistency between the magnetic flux values obtained by the modeled saddle sensors and the radial field values from the virtual pick-up sensors. A static $m = 1$, n = -7 harmonic has been excited and the values of the mean radial field $\langle b_r \rangle$ determined both from the saddle sensors and the pick-up sensors have been compared. The quantities from the saddle sensors have been calculated simply dividing the flux measures by the saddle sensor areas. The quantities from the virtual pick-up sensors have been calculated dividing by the saddle sensor areas an equivalent flux, obtained by summing the equivalent flux contributions relating to each pick-up underlying a saddle sensor, which in turns are the product between the point field value and the area equal to the saddle sensor area divided by the number of pick-up per saddle sensor.

Figure 112 shows the results of this analysis, where black lines represent the $\langle b_r \rangle$ values calculated from saddle sensors, blue lines represent values calculated from virtual pick-up sensors arranged in a grid of 10 poloidal and 5 toroidal points per saddle coil, and red lines is the case of a grid of 50 poloidal and 20 toroidal points per coil.

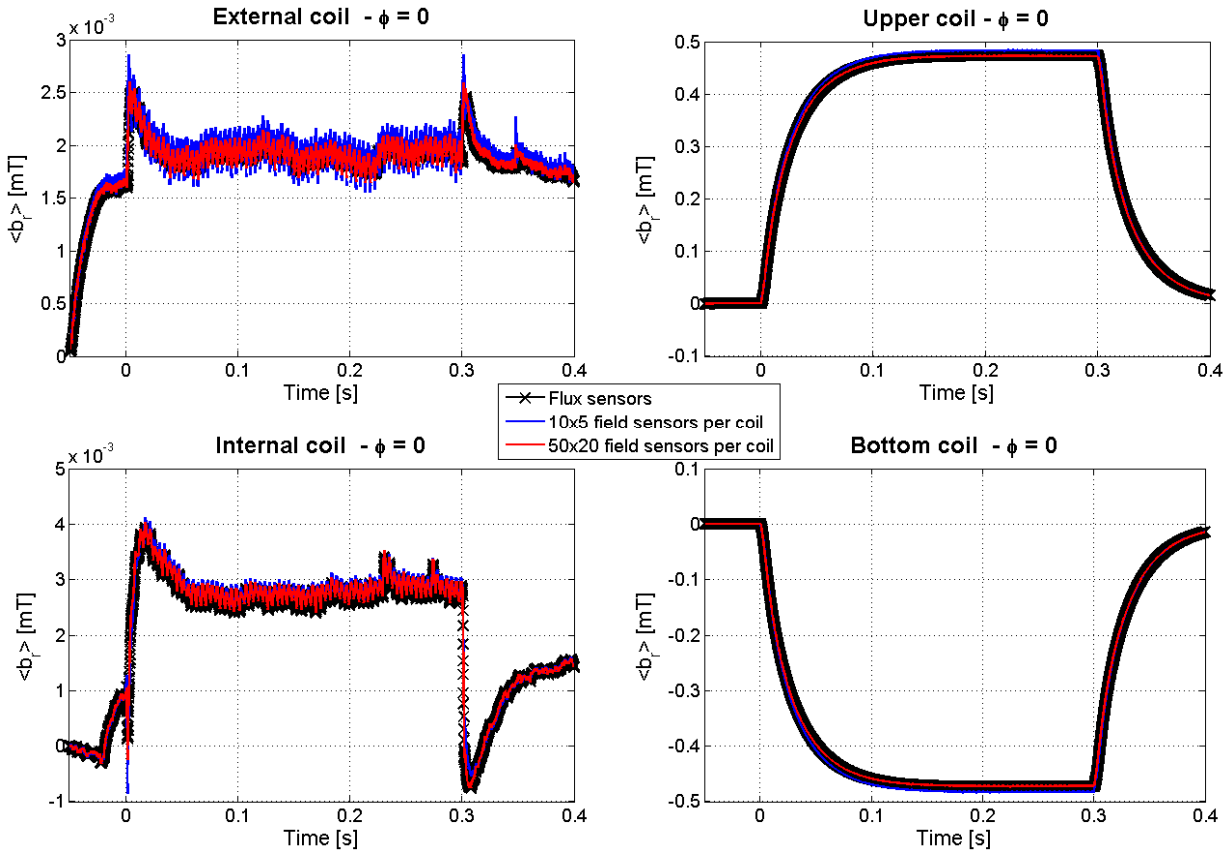

Figure 112: Consistency analysis results. Time evolution of the mean values of the radial field $\langle b_r \rangle$ from saddle sensors (black lines), from a grid of 10×5 virtual pick-up sensors per saddle coil (blue lines) and from a grid of 50×20 (red lines), calculated from a static m=1, n=-7 *excited mode.*

The waveforms in the case of a grid of 50×20 points per coils perfectly overlap those from saddle sensors, but just with the grid of 10×5 the agreement is quite good. Therefore, the results mentioned above, related to the possibility of distinguishing the main harmonic produced from the sideband contribution in realistic toroidal conditions, may be considered well-founded.

5.5.2.3 Toroidal sideband cleaning synthesis

The sideband cleaning of the measures enters in the feedback control scheme as shown in the block diagram below;

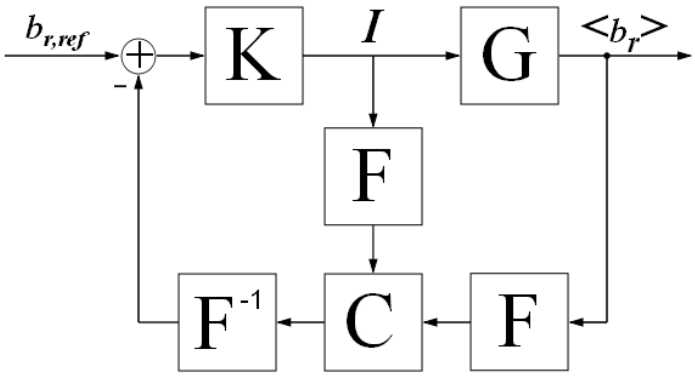

Figure 113: Scheme of the cleaned control loop.

where ***I*** is the vector of saddle coil currents, **G** is the plant, **K** represent the controller, **F** is the Fourier operator and **C** is the cleaning block, currently based on the cylindrical model. It should be noted that the radial magnetic field measures $\langle \boldsymbol{b_r} \rangle$ are not point quantities but averaged on the saddle sensor areas.

The proposed toroidal cleaning block is schematized as in Figure 114:

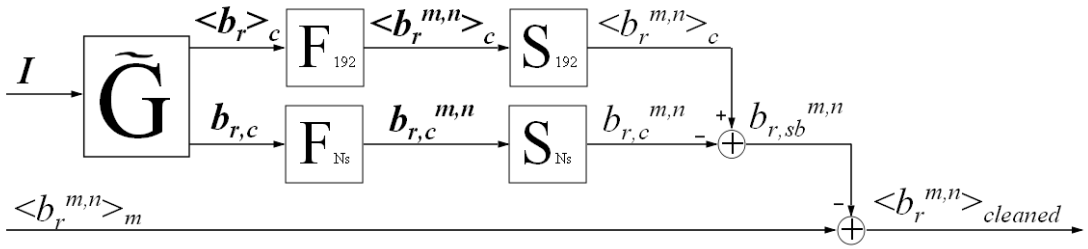

Figure 114: Scheme of the toroidal cleaning block.

The measurements of the current flowing into the saddle coils are given as input to the model $\check{\mathbf{G}}$ which considers 192 saddle sensors and N_s virtual sensors. The outputs of $\check{\mathbf{G}}$ are 192 values of the mean radial field $\langle \boldsymbol{b_r} \rangle_c$, which correspond to the real measures $\langle \boldsymbol{b_r} \rangle_m$, and N_s point values of radial field $\boldsymbol{b_{r,c}}$, which correspond to "virtual" pick-up radial sensors arranged in a grid of N_s

elements. These are then multiplied for the relative Fourier operator $\mathbf{F}_{192}$ and $\mathbf{F}_{Ns}$ of dimensions 192×192 and N_s×N_s, respectively, to obtain the vectors of the calculated radial field harmonics $\langle \boldsymbol{b_r}^{\boldsymbol{m,n}} \rangle_{\boldsymbol{c}}$ and $\boldsymbol{b_{r,c}}^{\boldsymbol{m,n}}$. The target raw harmonic $\langle b_r^{m,n} \rangle_c$ and pure harmonic $b_{r,c}^{m,n}$ are then selected through the selector matrices $\mathbf{S}_{192}$ and $\mathbf{S}_{Ns}$. The selectors are matrices, of dimensions 192×192 and N_s×192, respectively, with all the coefficients equal to zero except those corresponding to the harmonic of interest, where they are equal one. The difference between the raw harmonic $\langle b_r^{m,n} \rangle_c$ and the pure harmonic $b_{r,c}^{m,n}$ is the sideband component $b_{r,sb}^{m,n}$, which is then subtracted to the raw measured field harmonic $\langle b_r^{m,n} \rangle_m$, giving the cleaned measured field harmonic $\langle b_r^{m,n} \rangle_m$.

The whole cleaning scheme can be set up with a single block which implements the following state-space model:

$$\begin{cases} \dot{\underline{x}}(t) = \underline{\underline{A}}\,\underline{x}(t) + \underline{\underline{B}}\,\underline{I}(t) \\ b_r(t) = \left(\underline{\underline{S}}_{N_s}\,\underline{\underline{F}}_{N_s}\,\underline{\underline{C}}_{N_s} - \underline{\underline{S}}_{192}\,\underline{\underline{F}}_{192}\,\underline{\underline{C}}_{192}\right)\underline{x}(t) + \left(\underline{\underline{S}}_{N_s}\,\underline{\underline{F}}_{N_s}\,\underline{\underline{D}}_{N_s} - \underline{\underline{S}}_{192}\,\underline{\underline{F}}_{192}\,\underline{\underline{D}}_{192}\right)\underline{I}(t) \end{cases} \tag{5.21}$$

Therefore, the related block diagram becomes the following:

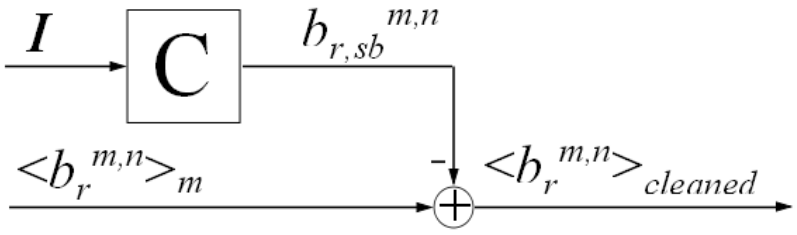

Figure 115: Compact scheme of the toroidal cleaning block.

For a real-time implementation the dynamic system must consider at most few hundreds of states can be used. Unfortunately , since the model has tens of thousands of states, such an algorithm cannot be implemented in real time anyway. However, a similar procedure to that used for reducing the decoupler can be adopted also in this case. By neglecting the toroidal cross-coupling of the modes, one can use as input the current harmonics of interest relating to the poloidal coupled modes and a (spatial) Fourier transformed version of the state-space model **C**. The resulting model could then be reduced in terms of state variables; again, this can be done by the use of some direct model reduction techniques (as for instance the Hankel singular value decomposition), or via the calculation of the frequency responses in a number of frequency samples and the following parametric identification of the model through simple transfer functions with few zeros and poles (as seen in paragraph 5.4).

6 Conclusions and further developments

This thesis describe most of the work done during the doctoral period, which covers many of the issues in numerical magnetic analysis and their critical states, dealing with various kinds of problems and different tools to treat them. In particular, the use of both multi-purpose commercial FEM software and dedicated custom code has allowed an in-depth investigation and understanding of the methods implemented, evidencing advantages and drawbacks of both. The wide range of possible formulations, whose choice is particularly important considering the numerical point of view, make the solution of magnetic problems particularly tricky and thus their in-depth knowledge is essential.

6.1 SPIDER and MITICA magnetic configuration optimization

Magnetic field configuration inside the SPIDER source and accelerator assumes great importance, being required to maximize negative ion production by allowing an electron separation between two thermal populations inside the source and to efficiently filter the electrons extracted together with negative ions.

The numerical simulation and optimization of the final 3D magnetic configuration of SPIDER has required developing numerical models capable of representing with sufficient accuracy the magnetic field features on different scales of magnitude, from the local configuration inside a single aperture to the global non-uniformity effects near the external edges of the device. Being the magnetic field produced by a combination of bus-bars and permanent magnets, together with a current-carrying grid and a ferromagnetic grid (both having complex geometry with 1280 beamlet apertures) the development of such models was not straightforward.

The optimized final design of the accelerator holds the following innovations:

- a magnetic filter in the ion source produced solely by a suitable arrangement of electrical currents, featuring also a very low magnetic field outside the source;

- compensation of the alternate deflection of negative ion trajectories due to the SF by means of permanent magnets and ferromagnetic material in the GG;
- reduction of the long-range magnetic field downstream of the accelerator and of the resulting vertical ion deflection.

These modifications, not only improve the uniformity of the beam and increase the ratio of expected negative ions to co-extracted electrons, but also allow a greater flexibility. Producing the FF only by electrical currents will allow varying its intensity maintaining the same spatial distribution. The new proposed approach to compensate the crisscross ion deflection will allow maintaining much more similar conditions in a wider voltage range with respect the classical electrostatic solution.

This concept is particularly well suited for a prototype device, whose main purpose is to investigate different operating condition in order to find an optimum.

A thorough exploration of many magnetic configurations for MITICA has been carried out, having flexibility and reproducibility of SPIDER-like conditions as design guidelines in order to preserve consistency and the experience acquired. The most promising design concepts have been compared, in terms of capability to dump the co-extracted and stripping electrons.

The best performing design solutions found are those characterized by the combined use of permanent magnets on the accelerator frames, mainly producing a long-range horizontal field component, and magnets embedded in EG and AG1-AG4 with vertical field orientation, arranged in horizontal stacks which are useful both for suppression of co-extracted and stripped electrons and for partial beamlet deflection compensation. In particular, the best case features a quite low and uniform overall heat load on the grids and a very low transmitted load (460 kW). Hence, this solution is proposed as the reference one.

In order to come to a definitive design, the following further development steps have to be done:

- precise evaluation of the possibility to compensate the alternate deflection of the beamlets by means of proper compensation magnets and ferromagnetic layer on the downstream side of the GG;
- investigation of the possibility to use coils instead of permanent magnets to produce the long range field inside the accelerator. A possible design foresees two coils located externally outside of the beam line vessel. The first simulations carried out shows that such solution provides a fairly uniform B_x magnetic field inside the accelerator, very

similar to the one provided by permanent magnets on the accelerator frames. The main advantage of using coils instead permanent magnets would be that the magnetic field could be varied without substitution of magnets located in vacuum environment.

6.2 Reduced Modal Decoupler and Toroidal Cleaning

Finite element models which reasonably reproduce the dynamic response of the RFX-mod MHD active control system have been successfully developed. They have been useful to understand the effect of different components, and of their features, which form the conductive structure whose presence shape the dynamic relation between the coil currents and the magnetic field inside the plasma chamber.

They have been used to develop a modal decoupler, which is an evolution of the dynamic pseudo-decoupler proposed in [41] which exploits the spectral nature of the plasma instability to reduce its dimensions, allowing its real time implementation. First encouraging experimental results show it actually acts in reducing the poloidal side-harmonic which are otherwise unavoidably coupled to any harmonic produced by the saddle coil system.

There still exist margins for improvement: the model could be improved including all the structure with higher degree of detail and the plasma response could be consider by the use of the CarMa code, or making the spatial Fourier transformation in flux coordinates. Both solutions required more powerful computer architecture for a precise solution.

The developed models have been also used to study the sideband effect observed when non-zero saddle coil currents are applied in toroidal geometry, which introduces by aliasing a systematic error in the field measurements. A new cleaner algorithm based on the developed CARIDDI model has been proposed to be implemented in the machine to perform the measurement cleaning in toroidal geometry with the purpose of testing if it can improve the performances.

References

[1] Global Energy Futures and Human Development: A Framework for Analysis, October 2000; can be downloaded from www.llnl.gov/tid/lof/documents/pdf/239193.pdf

[2] O. Fukamasa et al., Identification of caesium effect on enhancement of H^- production in a volume negative ion source. Review of Scientific Instruments, 2009.

[3] G. Serianni et al, Compensation of ion deflection and disposal of electrons in the ion source test facility for ITER neutral beam injectors, Proc. of the EPS2009 conference, Sofia, Bulgaria, July 2009

[4] B. Heinemann et al., Design of the "half-size" ITER neutral beam source for the test facility ELISE, Fusion Engineering and Design 84 (2009), 915–922.

[5] J. Pamela. The physics of production, acceleration and neutralization of large negative ion beams, Plasma Phys. Control. Fusion 37 (1995) 325-336.

[6] T. Inoue, M. Taniguchi, T. Morishita, M. Dairaku, M. Hanada, T. Imai, M. Kashiwagi, K. Sakamoto, T. Seki and K. Watanabe, R&D on a high energy accelerator and a large negative ion source for ITER. Nucl. Fusion 45 (2005) 790-795.

[7] Y. Takeiri, O. Kaneko, K. Tsumori, Y. Oka, K. Ikeda, M. Osakabe, K. Nagaoka, E. Asano, T. Kondo, M. Sato and M. Shibuya, High-power and long-pulse injection with negative-ion-based neutral beam injectors in the Large Helical Device. Nucl. Fusion 46 (2006) 119-210.

[8] Ikeda, N. Umeda, N. Akino, N. Ebisawa, L.Grisham, M. Hanada, A. Honda, T. Inoue, M. Kawai, M. Kazawa, K. Kikuchi, M. Komata, K. Mogaki, K. Noto, F. Okano, T. Ohga, K. Oshima, T. Takenouchi, Y. Tanai, K. Usui, H. Yamazaki and T. Yamamoto. Present status of the negative ion based NBI system for long pulse operation on JT-60U. Nucl. Fusion 46 (2006) 211-219.

[9] R. S. Hemsworth et al., Neutral beams for ITER, Rev. Sci. Instr. 67, Issue 3, 1120 (1996).

[10] P.L. Mondino, P. Bayetti, E. Di Pietro, R.S. Hemsworth, H. Iida, T. Inoue, K. Ioki, G. Johnson, A.I. Krylov, V.M. Kulygin, P. Massmann, K. Miyamoto, Y. Okumura, A.A. Panasenkov, R.T. Santoro, M. Sironi, Y. Utin, K. Watanabe and M. Yamada. ITER neutral beam system. Nuclear Fusion, Vol. 40, No. 3Y.

[11] P. Franzen et al., Progress of the development of the IPP RF negative ion source for the ITER neutral beam system, Nucl. Fusion 47 (2007) 264-270.

[12] http://www.fieldp.com/cpa.html

[13] P. Sonato et al., Machine modifications for active MHD control in RFX. Fusion Engineering and Design, 66-68:161–168, September 2003.

[14] R.D. Pillsbury Jr., "A three dimensional eddy current formulation using two potentials: the magnetic vector potential and the total magnetic scalar potential", RAL 3-D Eddy Current Seminar, April 1982.

[15] C. R. I. Emson and J. Simkin, "An Optimal Method for 3-D Eddy Currents", IEEE Trans Magn, 6, 2450-2452, 1983.

[16] O. Biro et al., "Numerical Analysis of 3D Magnetostatic Fields", IEEE Transaction on Magnetics, Vol. 27, No. 5, pp. 3798-3803 (1991).

[17] A. Bossavit, “A rationale for “Edge-Elements”, IEEE Trans Magn., 24, 74–79, 1988.

[18] R. Albanese and G. Rubinacci (1998) “Finite element methods for the solution of 3D eddy current problems” in Advances in Imaging and Electron Physics, Academic Press, Vol. 102, pp. 1-86.

[19] R. Albanese, R. Fresa, G. Rubinacci, S. Ventre, F. Villone, Cariddi Users Guide, draft final report, EFDA study contract 02-699, Part 1, April 2004

[20] R. Albanese and G. Rubinacci (1988) “Integral formulation for 3D eddy-current computation using edge elements”, IEE Proc., Vol. 135, Pt. A, 457-462.

[21] R. Albanese and G. Rubinacci (1998), “Solution of three dimensional eddy current problems by integral and differential methods”, IEEE Trans Magn. 24, 98-101.

[22] Rubinacci G., Tamburrino A., Villone F., “Circuits/Fields Coupling and Multiply Connected Domains in Integral Formulations”, IEEE Trans Magn., 38, 581 –584, 2002.

[23] ITER Technical Basis - ITER EDA Documentation Series No. 24, IAEA, Vienna 2002

[24] R.S. Hemsworth et al., Rev. Sci. Instrum. 79, 02C109 (2008).

[25] ITER Technical Basis 2002, “Neutral beam heating & current drive (NB H&CD) system”, Detailed Design Document (section 5.3 DDD5.3) (Vienna: IAEA)

[26] Tobari H. et al. “Uniform H- ion beam extraction in a large negative ion source with a tent-shaped magnetic filter” Rev. Sci. Instrum. 79, 02C111 (2008)

[27] Nocentini R., et al., “Plasma grid design for optimised filter field configuration for the NBI test facility ELISE”, SOFT conference 2008, published in Fusion Eng. Des.

[28] G. Fubiani, et al., Modeling of secondary emission processes in the negative ion based electrostatic accelerator of the International Thermonuclear Experimental Reactor. Phys. Rev. STAB 11, 014202 (2008).

[29] ANSYS Manual, ANSYS Inc. , (2009), http://www.ansys.com/.

[30] R. Hemsworth, et al., Status of the ITER heating neutral beam system, Nucl. Fusion 49 (2009) 045006.

[31] P. Sonato et al. Fusion Engineering and Design, Vol. 84, 269-274 (2009)

[32] M. Kashiwagi, T. Mizuno, N. Umeda and T. Inoue, "Physics design of 1 MeV D MAMuG accelerator for H&CD NB", 1st Intermediate Report, ITER Task No. C53TD48FJ.

[33] P. Franzen et al.: Continuation of the Development for the RF Ion Source, Final Report of Contract F4E-2008-GRT-07 (RFSDE)

[34]J. Pamela, A model for negative ion extraction and comparison of negative ion optics calculations to experimental results. Rev. Sci. Inst. 62 (1991) 1163.

[35] A. Krylov and R.S. Hemsworth, Gas flow and related beam losses in the ITER neutral beam injector, Fusion Eng. Des. 81 (2006), p. 2239

[36] P. Agostinetti et al.: "F4E-2009-GRT-032-PMS-H.CD Task T6.1 and 6.2 – Physics and engineering analyses on the MITICA accelerator” - Final report Contract F4E-2009-GRT-032.

[37] Rita Lorenzini et Al., Self-Organized helical equilibria as a new paradigm for ohmically heated fusion plasmas, NATURE PHYSICS, Vol. 5, pag. 570-574, 2009

[38] Ortolani S. and Schnack D.D. 1993 Magnetohydrodynamics of Plasma Relaxation (Singapore: World Scientific)

[39] Cappello S. and Paccagnella R. 1992 Phys. Fluids B 4 611

[40] Lorenzini R. et al 2009 Nature Phys. 5 570

[41] Anton Soppelsa et Al., Design of a new controller of MHD modes in RFX-mod, FUSION ENGINEERING AND DESIGN, vol. 83, pag. 224-227, 2008

[42] Gianfranco Cariolaro, La teoria unifiacta dei segnali, UTET, 1991

[43] P. Piovesan et al., Inclusion of 3D wall effects in MHD feedback control for RFP and tokamak plasmas, 38th EPS Conference on Plasma Physics, Vol. 35G

[44] P. Piovesan et al., Influence of external 3D magnetic fields on helical equilibrium and plasma flow in RFX-mod, Plasma Phys. Control. Fusion 53, 084005 (2011)

[45] P.Zanca, G.Manduchi, G.Marchiori, RFX internal document FC-NT-69 (2006)

[46] P.Zanca, FC-NT-70 (2006)

[47] P.Zanca, L. Marrelli, RFX internal document FC-NT-73revised (2006)

[48] P.Zanca, , RFX internal document FC-NT-80 (2011)

[49] GF Franklin, JD Powell and ML Workman, Digital Control of Dynamic Systems, 3rd Edition, Addison Wesley, 1998.

[50] Anton Soppelsa, Aspects of Electromagnetic Modelling for Multiple-Input Multiple-Output Control of MHD Modes in RFX-mod, Phd Dissertation, PADOVA UNIVERSITY, 2008

Publications

{1} P. Agostinetti, N. Marconato, et al., Optimisation of the magnetic field configuration for the negative ion source of ITER neutral beam injectors, Proceedings of ITC18 (2008)

{2} G. Serianni, N. Marconato, et al., Compensation of ion deflection and disposal of electrons in the ion source test facility for ITER neutral beam injectors, 36th EPS Conference on Plasma Phys. Sofia, June 29 - July 3, 2009 ECA Vol.33E, P-4.171 (2009)

{3} G. Serianni, N. Marconato, et al., Secondary particles in the acceleration stage of high current, high voltage neutral beam injectors: the case of the injector of the thermonuclear fusion experiment ITER, Proceedings of IPAC'10, Kyoto, Japan (2010)

{4} N. Marconato, et al., Simulation, code benchmarking and optimization of the magnetic field configuration in a Negative Ion Accelerator, Fusion Eng. Des. (2011)

{5} P. Agostinetti, N. Marconato, et al., Physics and engineering design of the accelerator and electron dump for spider, Nucl. Fusion 51 063004, (2011)

{6} G. Chitarin, N. Marconato, et al., Experimental Mapping and Benchmarking of Magnetic Field Codes on the LHD Ion Accelerator, SECOND INTERNATIONAL SYMPOSIUM ON NEGATIVE IONS, BEAMS AND SOURCES. AIP Conference Proceedings, Volume 1390, pp. 381-390 (2011).

{7} A. Soppelsa, N. Marconato, et al., Modeling of spatial harmonic transfer functions and its application to the decoupling of the RFX-mod active control system, 38th EPS Conference on Plasma Physics (2011) P5.106

{8} P. Piovesan, N. Marconato at al, Inclusion of 3D wall effects in MHD feedback control for RFP and tokamak plasmas, 38th EPS Conference on Plasma Physics (2011) O2.105

{9} S. Peruzzo, N. Marconato, et al., "Integrated procedure for halo current reconstruction in ITER", proceedings of the 24th Symposium on Fusion Engineering (SOFE), Chicago, USA, 26-30 June 2011, 29/06/2011, extended version submitted to IEEE Transactions on Plasma Science

{10} P. Agostinetti, N. Marconato et al., RFX-SPIDER-TN-011: Optimisation of magnetic field across SPIDER beam source. Results of 2D computations, Technical report, Consorzio RFX, 2009.

{11} P. Agostinetti, N. Marconato, et al., RFX-SPIDER-TN-016: Studies on electron dump for SPIDER, Technical report, Consorzio RFX, 2009.

{12} P. Agostinetti, N. Marconato, et al., RFX-SPIDER-TN-050rev3: Analysis and Design of the updated SPIDER Extractor/Accelerator system and Electron Dump, Technical report, Consorzio RFX, 2009.

{13} P. Agostinetti, N. Marconato, et al., RFX-SPIDER-TN-083: Physics and engineering design of the Accelerator and Electron Dump for SPIDER, Technical report, Consorzio RFX, 2010.

{14} P. Agostinetti, N. Marconato, et al., RFX-SPIDER-TN-094rev2: Optimization of magnetic field for SPIDER, Technical report, Consorzio RFX, 2011.

{15} P. Agostinetti, N. Marconato, et al., RFX-SPIDER-TN-110: Experimental mapping and benchmarking of magnetic field codes on the LHD NBI BL2, Technical report, Consorzio RFX, 2011.

{16} P. Agostinetti, N. Marconato, et al., RFX-SPIDER-TN-121rev2: Choice of the permanent magnets for the SPIDER and MITICA beam sources, Technical report, Consorzio RFX, 2011.

Acknowledgments

Alla fine la parte più difficile… non dimenticare nessuno sarà piuttosto arduo, visto quante sono le persone che vorrei ringraziare per questi anni passati ad RFX: da tutte le persone che hanno contribuito pesantemente alla realizzazione del mio lavoro e alla mia crescita professionale, a chi con un semplice sorriso a reso piacevole ogni giorno passato in questo locus amoenus della zona industriale di Padova.

Un grazie infinito va sicuramente a Bepi, al quale devo l'opportunità di aver fatto questo dottorato. Grazie per la professionalità, l'infinita disponibilità e voglia dimostrate nel spiegarmi le cose, anche se ripetute più e più volte. Grazie in particolare per l'apprezzamento dimostrato nei miei confronti e nel mio lavoro, cosa che certamente fa molto bene a un giovane alle prime armi e che non credo sia molto frequente.

Tante e tante grazie a Gianluigi, per l'indispensabile contributo tecnico, per la gentilezza e disponibilità, ma ancora di più per i preziosissimi consigli dati in questi anni.

Non potrei assolutamente dimenticare Anton, eclettico informatico e fonte inesauribile di conoscenze tecniche e non solo. Più che dire grazie, sottinteso, forse dovrei chiedere scusa per tutte le volte che ho interrotto i mille impegni che affollano le sue giornate per chiedere e richiedere che mi spiegasse concetti che solo la sua brillante bravura è riuscita a farmi entrare in testa.

Un grazie particolare va anche a Simone e Paolo Bettini che, oltre a mille consigli e chiacchierate, mi hanno spinto a fare la bellissima esperienza napoletana, dove ho conosciuto tante altre persone eccezionali, talmente tante che sicuramente dimenticherei qualcuno… grazie a tutti!

Grazie a Giuseppe Marchiori, Paolo Piovesan e Lionello Marrelli per gli spunti, i contributi e gli aiuti vari.

Grazie ai compagni di ufficio Antonio (peccato che te ne sei andato) e Giovanni (meno male che sei arrivato), e a tutti i compari di merenda, pranzo e trasferte varie, insomma grazie a tutti gli amici di RFX, troppi in numero da elencare.